UC San Diego
UC San Diego Electronic Theses and Dissertations

Title

Advancements in Blast Simulator Analysis Demonstrated on a Prototype Wall Structure

Permalink

Author

Freidenberg, Aaron

Publication Date

2013

Peer reviewed|Thesis/dissertation

UNIVERSITY OF CALIFORNIA, SAN DIEGO

**Advancements in Blast Simulator Analysis Demonstrated on a
Prototype Wall Structure**

A dissertation submitted in partial satisfaction of the
requirements for the degree
Doctor of Philosophy

in

Structural Engineering

by

Aaron Freidenberg

Committee in charge:

Professor Gilbert Hegemier, Chair
Professor David Benson
Professor Hyonny Kim
Professor Vlado Lubarda
Professor Vitali Nesterenko

2013

The dissertation of Aaron Freidenberg is approved, and it is acceptable in quality and form for publication on microfilm and electronically:

_____

_____

_____

_____

_____
Chair

University of California, San Diego

2013

TABLE OF CONTENTS

LIST OF FIGURES

LIST OF TABLES

ACKNOWLEDGEMENTS

I am extremely grateful to my parents for encouraging me to use my imagination, and for forcing me to do my chores, eat my vegetables, do my homework, and all that other stuff that's so important during those formative years. It is because of this that I know the value in working hard and with purpose. I am also grateful for the continued support of my family throughout my adult life.

I would like to thank my advisor, Gil Hegemier, as well as Lauren Stewart and Peter Huson, for taking the initiative in recruiting me to the blast group. At the time, I was fairly clueless about PhD student life and beyond, but I have learned a great deal during my time here. Prof. Hegemier, (Prof.) Lauren, Peter; your guidance was essential.

Thanks to the ESEC staff, in particular Lonnie, Alex, Steve, and Hector. I know how hard you all work, and it was a pleasure "taking care of business" with you on the various projects.

I've been fortunate to have access to teachers and scholars that are unrivaled in their fields of interest. Professor Vlado Lubarda and David Benson taught me many of the fundamentals that I needed in order to conduct my research. Thanks to Professor Hyonny Kim, as well as Daniel, Zhi, and Jen, who were all generous with their time and their lab space. Professor Vitali Nesterenko and ChienWei contributed significant time to assisting me with testing and paper writing; it was truly a pleasure working with the both of you. Other professors I would like to acknowledge who didn't directly assist with information contained in this thesis, but who were nevertheless extremely important to the completion of my degree include Professor Robert Asaro and Anne Conn.

Thanks to Ady, Ron, Carl, and Tyler for their innovative design ideas, and their commitment to making the most of every Blast Simulator test. Brad, thanks for being such a dependable office and lab companion. Lastly, Maryanne, thanks for being the yin to my yang. Ultimately, the completion of my degree and this thesis was made more enjoyable and otherwise facilitated by all of you. My experience at UCSD has exceeded my expectations, and has truly taught me the value of lifelong learning.

VITA

2007	B. S. in Civil Engineering, University of Southern California
2009	M. S. in Civil Engineering, Princeton University
2013	Ph. D. in Structural Engineering, University of California, San Diego

ABSTRACT OF THE DISSERTATION

Advancements in Blast Simulator Analysis Demonstrated on a Prototype Wall Structure

by

Aaron Freidenberg

Doctor of Philosophy in Structural Engineering

University of California, San Diego, 2013

Professor Gilbert Hegemier, Chair

It has been demonstrated that the UCSD Blast Simulator has the capability of generating repeatable heavy impact loading on large structures. The pulse shape and duration of the impact from the hydraulic rams is tailored by careful regulation of the hydraulic pressures (the *punch*) and additionally by the presence of a particular rubber material (the *programmer*) at the front of hydraulic rams. A systematic approach was undertaken in order to meet the challenges of incorporating these unique characteristics of the *punch* and the *programmer* into experimental data processing and high fidelity computer models of Blast Simulator tests. These new methods were then validated through a test series consisting of ten prototype wall tests and corresponding computer simulations. Additionally, important insight was gained with regard to the effectiveness of this particular prototype wall system as a hardening strategy, and in further demonstrating the capability of the Blast Simulator in generating blast-like loading on wall systems.

Chapter 1

Introduction

One of the threats to civil structures and their occupants is blast. Blast can come either as a result of a high explosive detonation typically associated with terrorism, or as a result of accidental ignition of a fuel source. There is increasing interest in investigating the behavior of structures under blast loads in order to develop strategies that ensure occupant safety from the shockwave and from flying debris, and in order to develop strategies to prevent progressive collapse of the structure. In order to achieve a better level of understanding of the response of structures to these kinds of transient dynamic loads and develop general methodologies to effectively harden structures specifically for blast, large-scale testing must be conducted and predictive models validated. At UCSD we are able to simulate these events using the Blast Simulator, a large experimental apparatus that uses hydraulics, rather than explosives, to impart blast-like loads.

The first half of this dissertation will provide some general background relating to blast effects, followed by a detailed description of several systematic improvements to the methods that are used for Blast Simulator experimental data processing and computer simulation. The first major improvement is a new methodology for determining experimental pressure-time histories and impulses that are imparted to Blast Simulator test articles. These pressures and impulses can be calculated from accelerometer and hydraulic data that is known post-test. Additional major improvements include a new method for modeling the load application within computer simulations and the characterization of a rubber material

model that is used to simulate an important material located at the front of the impact rams in the Blast Simulator. This material plays a vital role in tailoring the loads that are generated from the impact rams and is ultimately one of the key features of the Blast Simulator that enable it to achieve *blast-like* loads.

The second half of the dissertation will consider a particular prototype wall system that is being employed as a blast retrofit strategy as well as in new construction. Various Blast Simulator tests will be discussed in this dissertation, but the major test series on these prototype walls will be the primary focus. This test series served three important purposes. First, it validated the major changes that have been made with respect to Blast Simulator data analysis, further demonstrating the capability of the Blast Simulator to generate tailored, repeatable, heavy dynamic loading for large scale structures. Secondly, the wall system was shown to be an effective retrofit strategy, and the Blast Simulator testing provided considerable insight into the effectiveness of the many unique features of this particular wall system. Thirdly, the prototype wall test series provided sufficient data to validate high fidelity computer models, including some new material models, that can now be used in order to predict the response of untested specimens to a wide range of blast threats.

A brief description of each of the chapters will now be given, starting with Chapter 2, which describes the UCSD Blast Simulator. Chapter 2 will discuss the capabilities and the special characteristics of the Blast Simulator that make it possible to achieve blast-like loads. Major previous research will also be discussed in Chapter 2.

Chapter 3 provides some background relating to blast design. In particular, chapter 3 will focus on the principles of blast design that make it unique, compared to static or cyclic structural loading, which are more commonly considered by structural engineers. Chapter 3 will introduce some of the common design charts and will conclude with design examples.

Chapter 4 focuses on a major change to the way that accelerometer data is post-processed and a new methodology for including hydraulic data into the calculation of experimental impulse. Additionally, chapter 4 will describe an improved

method for modeling Blast Simulator impacts, which makes use of the experimental hydraulic data. Two blast simulator tests will be discussed in chapter 4, which will serve to validate the new data processing and modeling methods.

Chapter 5 deals with the rubber material that is located at the front of the impact rams in the Blast Simulator. The focus in chapter 5 is on characterizing a particular material model that is capable of accurately simulating the behavior of this rubber material using the finite element analysis (FEA) software LS-DYNA. The theoretical foundations of this rubber material model will be discussed in detail, followed by test results from a variety of materials tests, and then chapter 5 will conclude with a comparison between the new material model and the old material model.

Chapter 6 provides the test descriptions and test results from 12 tests that were performed in the Blast Simulator on a series of prototype wall systems. These wall systems consisted of light-gauge high strength steel studs, along with a special kind of cement-board paneling and a unique semi-rigid connection system. Experimental pressure and impulse is found by using a new method that includes both hydraulic and accelerometer data, the details of which are provided in Chapter 4.

Chapter 7 gives the results of computer simulations for the prototype wall tests. These computer simulations serve to validate all of the new methods relating to hydraulic data processing, material modeling, *etc.*, as outlined in chapters 4 and 5. These computer simulations are presented in the order that they were performed, rather than in the order that the experimental tests were performed. All computer simulations give satisfactory results.

Chapter 8 summarizes the major research findings that are presented in this dissertation, including the important conclusions that can be drawn from the computer simulations of the prototype wall tests. Chapter 8 concludes with some recommendations for future work. Appendices are provided at the end of the text, which include some of the common design tables and charts to supplement the design examples of chapter 3, along with some theoretical information on elasticity to provide background for chapter 5.

Chapter 2

Blast Simulator

The UCSD Blast Simulator [21] is a US Federal Government-sponsored apparatus that utilizes hydraulic actuators in order to simulate blast-like events. Powerful hydraulic actuators accelerate masses, ranging up to several thousand pounds, to target velocities that range up to 50 meters per second. The impacts are tailored such that peak forces with time durations that are nearly identical to those of blast loads are imparted. While several actuators can be used simultaneously in order to generate large pressures that are distributed over a large area, each actuator, referred to as a Blast Generator (BG), is independently controlled.

The actuators react against a "strong-wall" as shown in Fig. 2.1. The specimen is connected to a separate reaction wall, but both reaction walls are fixed to a common foundation that is base isolated, as shown in Fig. 2.1 and described in detail in [48]. Specimens of different sizes can be accommodated and the actuators can be adjusted accordingly, as they are connected to the reaction wall *via* rails that permit vertical adjustment.

The ability for the blast simulator to impart "blast-like" loads is possible primarily because of two unique characteristics. The first is that the impact is *not* a projectile-type impact. While impact masses are placed at the front of the actuators as shown in Fig. 2.2b, they are not simply "pushed." Rather, these impact masses are fixed to the hydraulic pistons and the impact is classified as a "punch." The hydraulic pressures and valve timings are controlled in a manner to ensure that a singular "pulse" is delivered, which in practice usually requires that
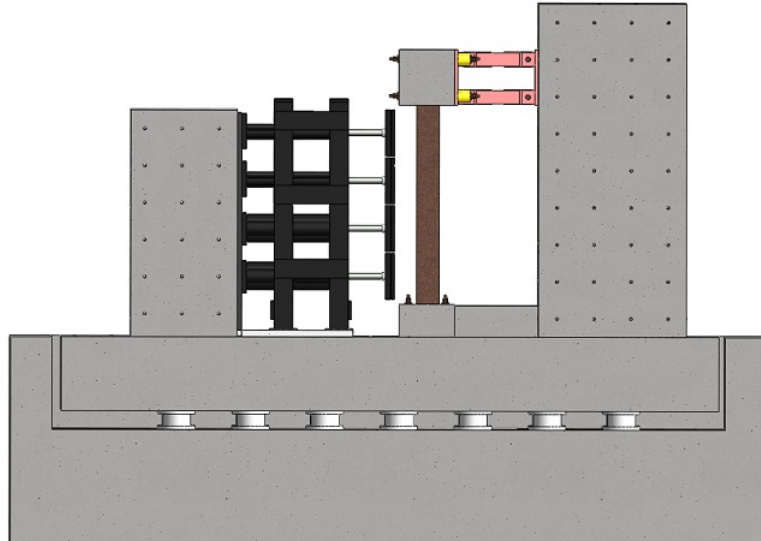
Figure 2.1: Base Isolated Foundation

the actuators "pull" on the impact masses during the collision.

Nitrogen is first pumped into an accumulator where a volume of oil is compressed to high pressure (5000 psi). The oil flow into the acceleration ("charge") port of the actuator is regulated through high speed servo controlled poppet valves. The poppet valves are opened and the pressurized oil drives the piston assembly, which includes the impact mass, toward the specimen. At a desired time, such as at impact, a separate servo controlled poppet valve opens, and a deceleration ("return") chamber fills with pressurized nitrogen in order to slow down and retract the impact mass. Pressure transducers within the actuator along with magnetostrictive position sensors on the impact mass give precise feedback. User supplied inputs such as initial impact mass position, total assembly mass, initial chamber pressures, and valve openings/closings all play critical roles in tailoring the impact.

A second unique characteristic of the Blast Simulator that enables the impact masses to deliver "blast-like" loads is the presence of an elastomer called the "programmer," which is bolted to the front of the impact masses as show in Fig. 2.2b and Fig. 2.3. The material of this elastomer is Adiprene L-100/MOCA, which is Adiprene that has been cured with MOCA(methylene bis-orthochloroaniline) [48]. While most of the mass of the collision comes from the aluminum portion
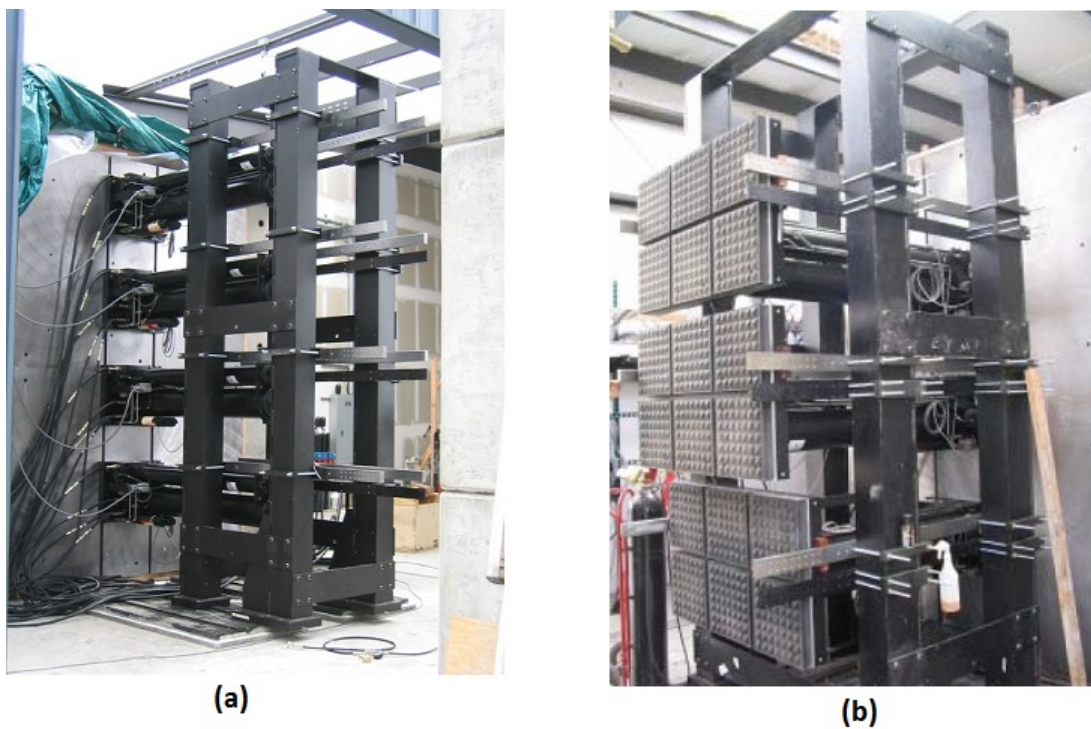
Figure 2.2: (a) Four actuators arranged in "stacked" configuration. (b) Three impact masses.

of the impact masses, the programmer is the material that makes actual contact with the specimen. The pyramidal geometry of the programmer eliminates high frequencies in the load application and the viscoelastic material properties of the programmer determine the shape of the imparted pulse.

The shape of the pulse is asymmetric, just like the loading from blast events. In particular, it is well known that the shape of loading from blast has a long decay relative to the rise-time portion of the loading [37] [57]. This is also true for rubber materials under impact, where the decompression phase is longer than the increasing portion of the compression loading. The programmer's material properties are essentially tailored so that the impacts produce not only a "blast-like" loading shape, but also peak forces and time durations that are blast-like. The "punch" and the "programmer" are the two key features of the Blast Simulator, and will also be the major topics in this thesis.
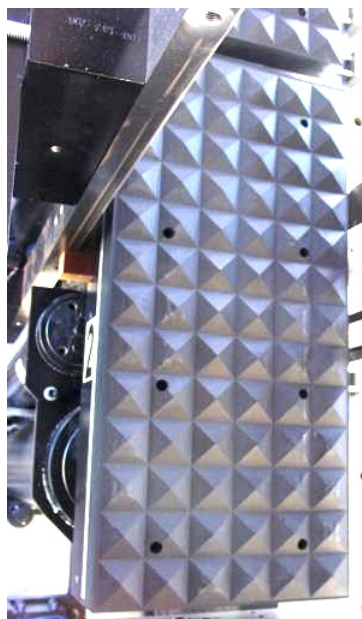
Figure 2.3: Urethane polymer programmer

The Blast Simulator has a number of advantages over explosive field testing. The primary advantage is that the behavior of the specimen is not obscured by the presence of a "fireball." High speed video footage of tests conducted at the

Blast Simulator allows researchers to see the behavior of specimens under blast loads, which is not possible when actual explosives are used. The Blast Simulator has been used to observe the response of vehicle sized blast loads to a variety of structural elements commonly used in civil structures, as well as evaluate the effectiveness of blast retrofitting technologies. The initial test series was conducted in 2006 by Rodriguez [48], which studied the response of reinforced concrete columns (Fig. 2.4) to blast loads.

Additionally, a variety of tests were conducted on masonry walls, by Oesterle [44]. One such masonry wall test is shown in Fig. 2.5. Steel columns were studied as well, by Stewart [59], as shown in Fig. 2.6. These tests were important because they validated the capabilities of the Blast Simulator for simulating blast loads. These tests also developed many of the procedures and protocol for laboratory testing and data collection that were used in the tests conducted by the author, which will be described in detail later on in this thesis. Additionally, the configuration of the series of tests by Oesterle [44], in particular, is similar to the setup of the tests that will be discussed in this thesis. For example, many of the same reaction fixtures and BG impact mass elements are the same.
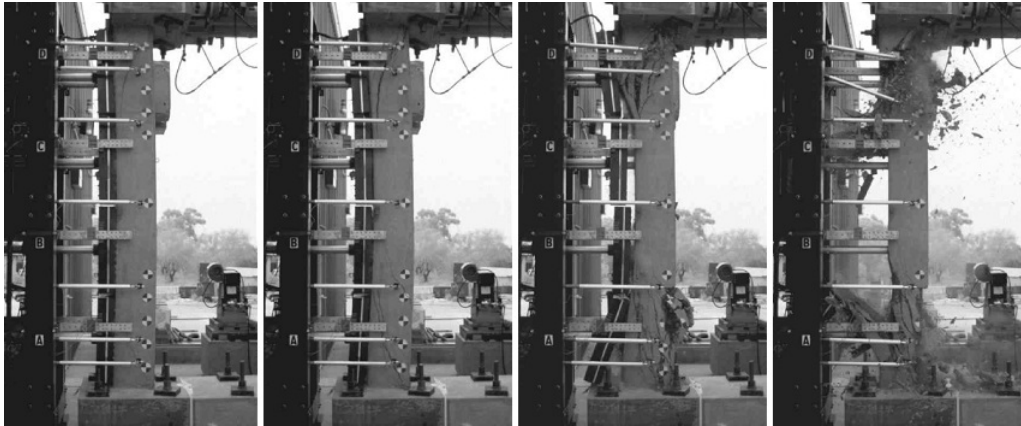
Figure 2.4: Simulator Test of RC Column - Damage Evolution [48]

While the Blast Simulator, like field testing with explosives, is a vital research tool, much of the actual blast design and materials research is done with
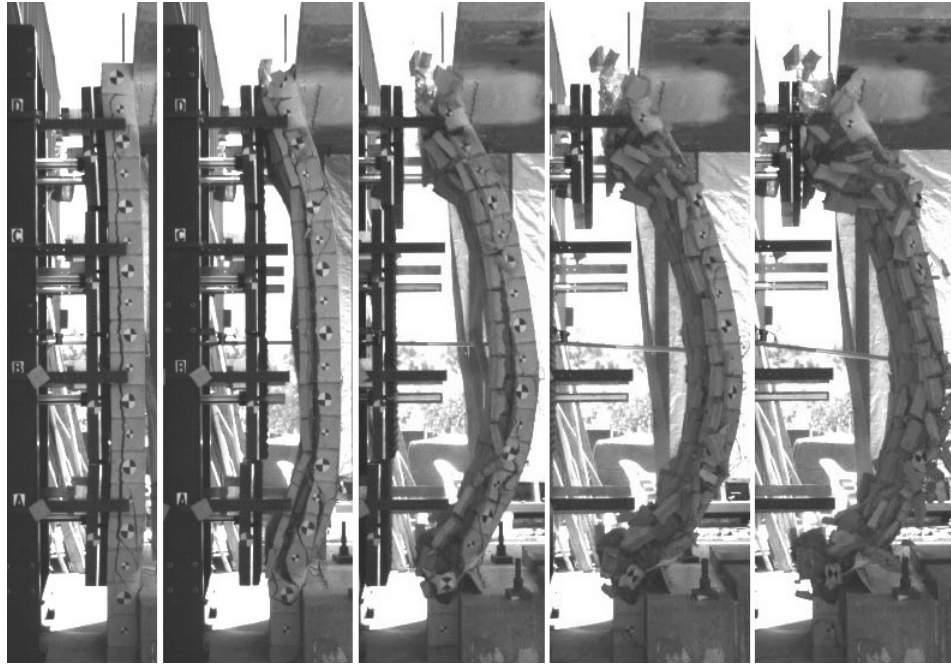
Figure 2.5: Simulator Test of Masonry Wall - Damage Evolution [44]
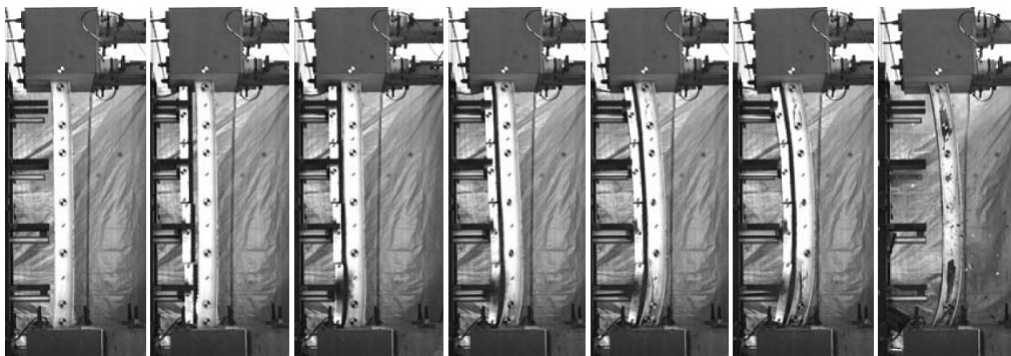
Figure 2.6: Simulator Test of Steel Column Strong Axis - Damage Evolution [59]

computer simulations. Experimental tests at the Blast Simulator are conducted, in many circumstances, in order to acquire a sufficient number of data points to calibrate the computer models. Computer simulations can then be run in order to compare various designs that cannot realistically all be tested, experimentally. In order for this process to be successful, however, the computer models must be capable of simulating behavior to a high degree of precision. As the Blast Simulator had begun operation only four years before the author joined the group, the computer modeling and post-processing of data collected from the Blast Simulator was not yet well developed. For example, the "punch" effect of the actuators had not been incorporated into any of the calculations or computer models, and the material model of the "programmer" lacked the ability to capture actual observed behavior. The Blast Simulator is a one-of-a-kind testing apparatus and is the only testing option, besides field testing with explosives, that can deliver blast like loads on large structures.

The first requirement for a test apparatus designed to simulate blast effects is to that it must have the capability of delivering a uniform load. Test systems that are capable of imparting uniform pressure over large areas include loading trees (see DiPaolo [12]) and vacuum chambers (see Salim [49]). These systems, however, typically apply the loading quasi-statically and do not have the capability of applying transient, high rate loading. Another test method is the shock tube, which is capable of applying dynamic, uniform, loading on structures. Some shock tube tests on large structures are described by Sunshine [61], Schleyer [54], and Lacroix [29], where it is demonstrated that shock tubes can generate blast-like loading for certain far field threat-levels.

Several kinds of test methods are used to impart transient dynamic loads on structures. Projectiles from a gas gun can impart the kind of strain rates of interest for blast. However, the gas gun is typically used for materials characterization of the projectile or for ballistic response of the target, as described in Bourne [8], rather than for applications such as blast that require a uniform load. Additionally, the pulse delivered from a projectile is inherently less tailorable than a hydraulic punch and the gas gun cannot apply high rate loading over a large area.

Heavy dynamic loading on large structures that is approximately uniform can perhaps be achieved by using sleds and impact trolleys as is done in crashworthiness testing. These full-scale crash tests are projectile-like impact, as described by Versmissen [62] and Johnsen [26]. The use of polymers or aluminum foam as energy absorbing materials at the front of impact trolleys as a means of tailoring the impact has been investigated by Massenzio [35] and Zaouk [67]. The use of a hydraulic punch to tailor impact has also been studied by Liu [31] and Morris [40], but only for smaller applications. The Blast Simulator is currently the only system that incorporates both an energy absorbing material at the front of impact ram and a hydraulic punch in order to deliver uniform pressures on large structures over. It is the only test apparatus, besides field testing with explosives, that is capable of generating such pressures over blast-like time-durations.

Chapter 3

Blast Design Fundamentals

The intent of this chapter is to introduce the basic concepts that underlie any investigation into the response of civil structures to transient dynamic loading. In particular, it will be shown that the blast response of a structure with known structural properties can be reasonably predicted if the pressure and impulse demands are known, and a simplified shape of the pressure-time history is assumed. The chapter will conclude with a discussion of the P-I diagram and two blast design examples.

3.1   Loads

The load demands from a charge depend on a number of factors. A non-exhaustive list of such factors is provided:

- Size of the charge (typically expressed in the number of equivalent pounds of TNT)

- Distance from the target (distance has more influence than charge size)

- Spherical or hemispherical wave propagation

- Open or enclosed area

- The strength of the cladding (assuming the structure has cladding) can influence the effective tributary area of the loading

- Geometry of the structure (an angle of incidence of 0° results in the highest load)

The demand also depends on the deformation of the structure, though this is often ignored since the time duration of the structural response is usually much longer than the time duration of loading. In most cases, the above list of factors is sufficient to estimate the force *vs.* time load demand acting on the structure. For structures with simple geometries, charts can be used to determine this force-time loading. For structures with more complex geometries, a hydrocode can be used to determine the load demands [10]. Hydrocodes are typically Eulerian-type software that make use of "adaptive" meshing techniques to precisely capture behavior at the shock front [10][38].

In typical, uncoupled, analyses, the force-time history can be "applied" to the structure, and the structure's behavior (deflection, damage, *etc.*) can then be determined using analytical formulae if the structure is simple and idealized, or a Lagrangian-type software if the structure is complex and insight into detailed behavior is required. Only for very light structures, such as blast "catcher" structures, would a fully-coupled "fluid-structure interaction" analysis be deemed necessary.

3.2   Work, Energy, and Impulse

For problems of relatively simple geometries, basic structural response can be approximated by hand. Boundary conditions can be simplified to be fully pinned or fully fixed, and material strengths can be increased by an amplification factor to account for strain-rate effects. In blast design, unlike earthquake engineering, mass is beneficial. The blast response of structures is often governed by the following fundamental relations:

- Net impulse, I, equals change in momentum, Δv

- Change in kinetic energy, $m(\frac{v_2^2}{2} - \frac{v_1^2}{2})$, equals net internal work, W

- Work (external or internal) $\leftrightarrow$ strain energy

In classical structural analysis, where loads are applied quasi-statically, we essentially use something like:

$$\int_0^x F_{net} dx = \frac{1}{2} * K * x^2 \tag{3.1}$$

For static problems, some form of eq. (3.1) might be used, with "F" applied as a linear ramping function, suggesting that the load is applied quasi-statically. Later on, we will use eq. (3.1) with a different kind of ramping function, and an equivalent stiffness, "K", to solve for our "worst-case" dynamic load factor - *i.e.* the dynamic load factor for a "pressure" type response.

For impulse-controlled problems, we are also interested in the strain energy developed in the structure. However, in place of the direct work/strain energy relation (eq. (3.1)), the dominant relation, here, will be kinetic-energy/work or kinetic-energy/strain energy, where the kinetic energy can be estimated based on the impulse. Thus, we need to know two additional relations. The first relation is familiar:

$$\int_0^t F_{net} dt = \int_0^t m * a \, dt = m * v \tag{3.2}$$

Eq. (3.2), of course, represents the familiar impulse/momentum relation, for an object initially at rest. As we can see, this relation follows directly from the balance of linear momentum (Newton's 2nd Law). The second relation we need is work/kinetic energy. This will be quickly derived, as follows.

$$\int_{x_1}^{x_2} F_{net}(x) dx = \int_{x_1}^{x_2} m * a(x) dx \tag{3.3}$$

In eq. (3.3), we can then use the common integration by substitution (change of variables) rule:

$$\int_{x_1}^{x_2} m * a(x)dx = \int_{t_1}^{t_2} m * a(t) * \frac{dx}{dt}(t)dt = \int_{t_1}^{t_2} m * a * v dt \qquad (3.4)$$

Then, we can consider:

$$\frac{d}{dt}(\frac{1}{2}m * v^2) = \frac{1}{2}m \underbrace{\frac{d}{dv}(v^2)\frac{d}{dt}(v(t))}_{\text{chain rule}} \qquad (3.5)$$

But eq. (3.5) reduces to:

$$\frac{d}{dt}(\frac{1}{2}m * v^2) = m * v * a \qquad (3.6)$$

From eq. (3.3), eq. (3.4), and (3.6) we arrive at the desired result, *viz.*

$$\int_{x_1}^{x_2} F_{net}(x)dx = \frac{1}{2}m * (\Delta v)^2 \qquad (3.7)$$

note: the "Δv" in eq. (3.7) pops up as we invoke the Fundamental Theorem of Calculus when taking the integral of both sides of eq. (3.6)

If the response of a structure is truly impulsive, then perhaps one can find the initial velocity of the structure that occurs as a result of the applied blast impulse, *via* the impulse momentum equation (eq. (3.2)). Then, ignoring any deflection that occurs during the impulse, one can calculate the deflection of the structure by assuming:

$$\text{kinetic energy} \longrightarrow \text{internal work} \longrightarrow \text{strain energy} \qquad (3.8)$$

In other words, one can assume that "x_1" in eq. (3.7) is zero, then plug in the previously found velocity to solve for "x" from eq. (3.1). This is a reasonable estimation of "x" if the response of the structure is truly impulsive. If the response

is governed by "pressure," rather than impulse, then we know that we can use the work-strain energy equation (eq. (3.1)) directly:

$$\text{external work} \longrightarrow \text{strain energy} \tag{3.9}$$

We need to know when we can use eq. (3.8), eq. (3.9), or if neither are valid. In other words, we need a methodology to determine the type of response that we can expect. The quantity $\frac{t_d}{T}$, where t_d is the duration of the force-time loading history and T is the natural period of the structure, will be a quantity of particular interest.

3.3   Response: Dynamic Load Factor

Since the response of the structure is inherently dynamic, the static deflection, "F/k", must be modified (either amplified or reduced) by a "dynamic load factor." It can be shown that this "dynamic load factor" is small for structural response that is dominated by impulse/momentum-type behavior, and large (up to a factor of "2") for structural response that is dominated by "pressure" or work/strain energy-type behavior. In between these two extremes would be the "dynamic" or "pressure-time" realm, where the equation of motion can be solved in order to calculate the "dynamic load factor."

> note: Though the ideas in this chapter fundamentally apply to any blast-like problem, the equations and plots that will be shown can be used only for structures where single-degree-of-freedom (SDOF) equivalency is possible

Impulsive response occurs for $\frac{t_d}{T} \leqslant .1$, where we can find the deflection of the structure from eq. (3.8), if the force-time loading history is known and the equivalent mass and stiffness of the structure are known. "Pressure" response occurs for $\frac{t_d}{T} \geqslant 2$, where we can find the deflection of the structure from eq. (3.9), if the force-time loading history is known and the equivalent stiffness of the structure

is known. In between these two values, which is the "dynamic" or "pressure-time" realm, we can fit a curve. Even without having the force-time loading history, or the structure's equivalent mass and stiffness, we can plot the dynamic load factor as a function of $\frac{t_d}{T}$, as follows.

Consider a block pulse of magnitude F, where the time duration of the load, t_d, is long. Since t_d is long, we can assume that the structure depends only on the load F, and is not impulsive. Thus from eq. (3.9), we can say,

$$F * x_m = \frac{1}{2} K x_m^2 \tag{3.10}$$

Since F/K is the static deflection, and solving for x_m from eq. (3.10) results is $x_m = 2 * F/K$, we can say that the dynamic load factor, here, is "2."

$$\frac{x_m}{F/K} = \frac{x_m}{x_{st}} = 2 \tag{3.11}$$

Next, consider a pulse where the time duration, t_d, is small, and the impulse can be expressed as $\frac{1}{2} * F * t_d$ (triangular pulse). From $I = mv$ (eq. (3.2)) we can find the velocity of the structure from the external work (ignoring any structural stiffness). Substituting this value of velocity into the equation for kinetic energy, $KE = \frac{1}{2} m v^2$, we get:

$$KE = \frac{I^2}{2m} \tag{3.12}$$

From eq. (3.8), we can find the strain energy (*i.e.* the deflection of the structure) if we know the equivalent mass and stiffness of the structure, and so long as we ignore any structural deflection that occurs during the impulse. Accordingly, we can set the kinetic energy from eq. (3.12) equal to the strain energy:

$$\frac{I^2}{2m} = \frac{1}{2} K * x_m^2 \tag{3.13}$$

We know that I is a triangular pulse, so we have:

$$\frac{(\frac{1}{2}F*t_d^2)^2}{2m} = \frac{1}{2}K*x_m^2 \longrightarrow \frac{x_m^2}{\frac{1/4*F^2}{K}} = \frac{\frac{1}{4}t_d^2}{2m} \longrightarrow \frac{x_m^2}{F^2/K^2} = \frac{1}{4}*K*m*t_d^2$$

$$\frac{x_m}{F/K} = \frac{x_m}{x_{st}} = \frac{1}{2}\omega t_d \tag{3.14}$$

where ω, in eq. (3.14), is $\sqrt{K/M} = \frac{2*\pi}{T_n}$.

Remember, our goal was to be able to plot the dynamic load factor as a function of $\frac{t_d}{T}$ (or ωt_d). Eq. (3.11) and eq. (3.14) give us two asymptotes, between which, we can presumably fit a line (Fig. 3.1).
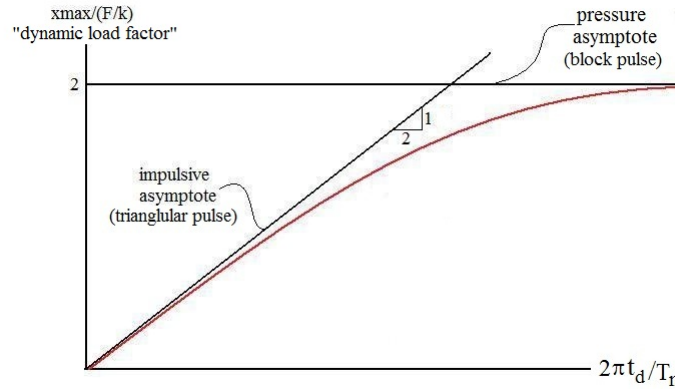
Figure 3.1: Graphical representation of "dynamic load factor" *vs.* ωt_d

Plots such as Fig. 3.1 are common, though the horizontal axis may be t_d/T_n, in which case our slope would need to be multiplied by $2*\pi$. One or both of the asymptotes may also change if the shape of the impulse is different than what was previously assumed. It was previously stated that values of $\frac{t_d}{T_n} \leqslant .1$ can be approximated as "impulsive" while values of $\frac{t_d}{T_n} \geqslant 2$ can be assumed to be "pressure" controlled. These values were conservative. It should be additionally noted that the shape of the plot in between the asymptotes was not drawn precisely. To obtain a precise curve, the equation of motion must be solved, which we have avoided doing. The purpose of Fig. 3.1 is to illustrate the idea of "dynamic load factors," conceptually.

3.4   P-I Diagram

Instead of graphically depicting the "dynamic load factor" as a function of natural frequency, we can plot some function of pressure *vs.* impulse. It is important to recognize that Fig. 3.1 can predict whether our structure will experience some form of "damage," if, in addition to K, t_d, *etc.*, we also know the displacement capacity of the structure. While the true capacity of the structure is a function the structure's material strength and geometry, conservative limits on displacement capacity have been codified to some extent, and we will deal with such approximate limits in the examples of the next chapter. So, if we know the displacement capacity of the structure, we can predict the "x_m" demand from Fig. 3.1 and compare to the capacity. In this way, Fig. 3.1 can tell us something about damage or failure. With the idea of damage in mind, we can instead develop a different, graphical, approach, called a Pressure-Impulse (P-I) Diagram, as follows.

First, we can re-write eq. (3.11) as $\frac{2F}{Kx_m} = 1$. This will be our horizontal asymptote for our P-I diagram.

Next, we can re-write the equation that describes our diagonal asymptote in Fig. 3.1, *viz.*

$$\frac{x_m}{F/K} = \frac{1}{2}\omega t_d \longrightarrow \frac{Ft_d/(Kx_m)}{\sqrt{K/M}} = 2 \rightarrow \frac{2I}{x_m\sqrt{KM}} = 2 \tag{3.15}$$

Eq. (3.15) can be re-written as:

$$\frac{I}{x_m\sqrt{KM}} = 1$$

Now we have our vertical asymptote for our P-I diagram. This diagram is shown

in Fig. 3.2.
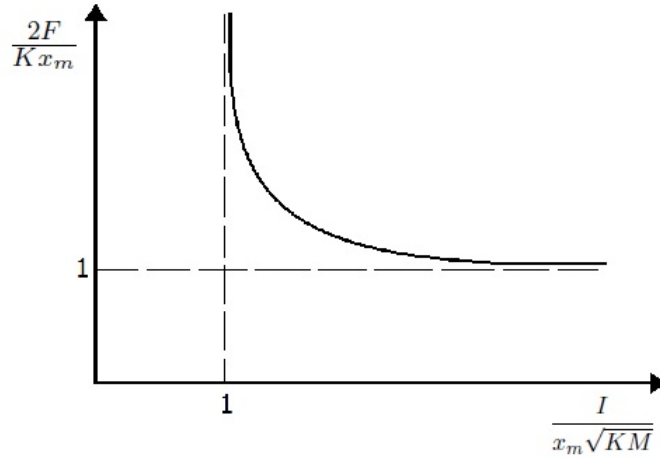
Figure 3.2: Pressure-Impulse (P-I) Diagram

Fig. 3.2 is useful because it allows us to see what combinations of F and I cause damage. Assuming we know the mass and stiffness of our structure, as well as the displacement capacity (here, defined as x_m), then any combination of F and I that result in a point to the right and above our P-I curve, will cause damage (*i.e.* would cause a displacement demand that exceeds the capacity). Remember, the curve shown is Fig. 3.2 is for illustrative purposes only and would also change significantly if the shape of the impulse is not triangular, with a peak of "F," as we assumed.

We'll see in examples to follow that the displacement capacity is simply defined in terms of support rotations (ranging from 2º to 4º) for typical blast design problems. The following examples will look at structural behavior in somewhat more detail than what we've done so far, though the basic ideas presented in this chapter will still be valid as the SDOF idealization will still be assumed. While the examples are done in a purely analytical, simplified, manner, we will see that such analytical methods are important for preliminary design of structural elements. This is, however, only the first step, since this treatment only considers single, isolated, structural members. Robustness at a systems level would be necessary

to prevent progressive collapse, whether such robustness is achieved through prescriptive "tying" methods or through direct consideration of alternate load paths [10].

3.5   Simple Design Examples

3.5.1   Light, stiff, steel, structure

The first design example, from [37], deals with a blast load on a relatively light, stiff, steel column, such that the load-structure behavior shows a "pressure-time" response rather than the "impulsive" response more commonly seen in heavier, more flexible, concrete structures.
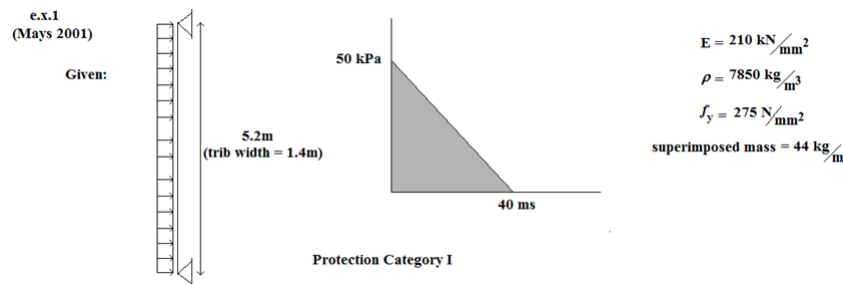
Figure 3.3: Steel Column Design Example

Fig. 3.3 shows the force-time history of the loading, along with some basic geometry and boundary conditions of the structure.

We need to first determine a column section size that we think will work, assuming elastic behavior only, and a dynamic load factor (DLF) of "1." Then, we will check that our column can withstand the true demands from the load, which will likely require a dynamic amplification since the load is in the "pressure-time" realm (*i.e.* it is not impulsive), where dynamic effects typically amplify the response rather than reduce it. This dynamic amplification factor will be found by

using charts in the Appendix. We will also consider the capacity of the column beyond the elastic limit, by using another set of charts from the Appendix.

Assuming a DLF of 1, we can make the following simple calculations:

Beam Load $= 50\frac{kN}{m^2} * 1.4m = 70\frac{kN}{m} = $ "p"

$M = \frac{(70kN/m)(5.2m)^2}{8} = 236.6kN*m$

Conservatively assume that $M = M_p = f_{dy} * S_{req'd}$, where $f_{dy} = $ "dynamic" yield stress $= 1.2 * 1.2 * 275\frac{N}{mm^2} * S_{req'd}$ per Appendix A.1, for structural steel $\leqslant 50ksi$, that is in bending.

$236.6kN*m * 10^6 \frac{N*mm}{kN*m} = 1.1 * 1.2 * 275\frac{N}{mm^2} * S_{req'd}$

$\longrightarrow S_{req'd} \geqslant 652 * 10^3 mm^3$

Try 356 x 127 x 39 kg/m universal beam (W14 x 26)
($I = 100.87 * 10^6 mm^4$; $S = 654 * 10^3 mm^3$; $M = 1.1 * 1.2 * 275 * 654 * 10^3 = 237 * 10^6 N * mm = 237kN * m$)

"r_u" $= \frac{8M_p}{L^2} = \frac{8*237*10^3}{5.2^2} = 70.1 kN/m$ (slightly larger than "p", as expected)

$\boxed{\text{note: we'll use } \frac{r_u}{p} \approx 1 \text{ later when we enter the charts}}$

Next, we find the mass, load, and stiffness factors from Appendix B.1. Such factors are derived in [57].

$(k_M)_{elast} = .5$; $(k_M)_{plast} = .33$
$(k_L)_{elast} = .64$; $(k_L)_{plast} = .50$
$(k_S)_{elast} = .64$; $(k_S)_{plast} = .50$

$\longrightarrow (k_{LM})_{elast} = \frac{(k_M)_{elast}}{(k_L)_{elast}} = .78 \quad ; \quad (k_{LM})_{plast} = .66$

Use average $k_{LM} = \frac{(k_{LM})_{elast} + (k_{LM})_{plast}}{2} = .72$

To find "T", we also need the elastic spring stiffness and the total mass:

$k_E = \frac{384EI}{5L^4} = 2.225 * 10^6 N/m$ (*i.e.* stiffness per unit length that, when multiplied by uniform load, w, produces mid-span deflection)

mass (per unit length) $= m = 39kg/m + 44kg/m = 83kg/m$, where, recall from Fig. 3.3, that "$44kg/m$" is the superimposed mass.

$$T = 2\pi\sqrt{\frac{k_{LM} * m}{k_E}} = 2\pi(\frac{.72 * 83}{2.225 * 10^6})^{1/2} = .0326s = 32.6ms \qquad (3.16)$$

Eq. (3.16) was not derived, but a similar result can be obtained from:

$$T = 2\pi\sqrt{\frac{[(k_M)_{elast} + (k_M)_{plast}]/2 * m}{[(k_S)_{elast} + (k_S)_{plast}]/2 * k_E}} = .0327s \qquad (3.17)$$

Note that in eq. (3.17), $(k_S)_{plast} = (k_L)_{plast}$ was assumed.

With $\frac{r_u}{p} \approx 1$ and $\frac{t_d}{T} = \frac{40}{32.6} \approx 1.2$, we can enter the chart in Appendix C.1.

$\longrightarrow \frac{x_{max}}{(F/K)} = \frac{x_m}{x_E} = 2.1$, where "$x_m$" and "$x_E$" are commonly used variables in [37], and their ratio is not necessarily greater than unity.

From Appendix A.2, for Protection Category 1, $2.1 \leqslant 10 \longrightarrow$ OK

$x_m = 2.1* \text{ "}x_E\text{"} = 2.1 * \frac{70.1*10^3 N/m}{2.225*10^6 N/m/m} = .0662m$

$$tan\phi = \frac{x_m}{(L/2)} = \frac{.0662}{(5.2/2)} \rightarrow \phi = tan^{-1}(\frac{.0662}{5.2/2}) = 1.46^{\circ}$$

From Appendix A.2, for Protection Category 1, $1.46^{\circ} \leqslant 2^{\circ} \rightarrow$ OK

Lastly, from Appendix C.2, $\frac{t_m}{t_d} = .51$; $.51 < 3 \longrightarrow$ "pressure-time" or "dynamic" loading (as opposed to "impulsive" loading) $\rightarrow$ OK

note: Shear not checked.

3.5.2   Heavy, flexible, concrete, structure

This design example will consider a concrete cantilevered wall structure subjected to a short duration shock. The behavior of such a heavy structure under short duration loading is determined primarily from the impulse that is imparted. This design example is adapted from [37].
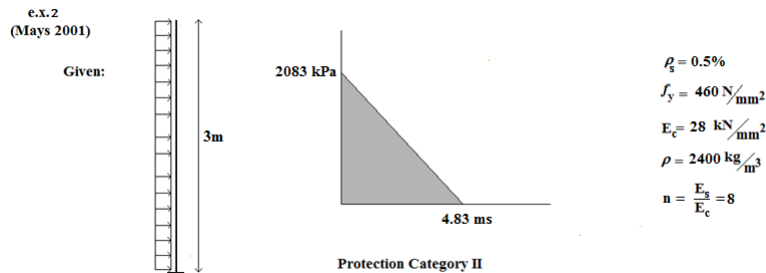
Figure 3.4: Concrete Wall Design Example

Fig. 3.4 shows the pressure-time history of the loading, along with some basic geometry and boundary conditions of the structure. The specific impulse is found to be $5030kPa - ms$.

With the reinforcement ratio known, the load known, and the basic properties of the steel and concrete known, we have all of the information that we need in order to determine a required wall depth. We will assume that the response is

purely impulsive.

We can approximate the moment capacity per unit width of wall as:

$$M_n = \rho_s f_{ds} d_c^2 \tag{3.18}$$

The resistance can be expressed as $r_u = \frac{2M_n}{H^2}$. So,

$$r_u = \frac{2}{H^2} \left(\rho_s f_{ds} d_c^2 \right) \tag{3.19}$$

In eq. (3.19), $f_{ds} = f_{dy} + \frac{f_{du} - f_{dy}}{4}$ (Appendix A.3)

where, from Appendix A.1:

$$f_{dy} = 1.20 * 460 = 552 N/mm^2$$

$$f_{du} = 1.05 * 550 = 578 N/mm^2$$

So,

$$f_{ds} = 560 N/mm^2 = 560 * 10^6 N/m^2$$

r_u can now be written as a function solely of d_c:

$$r_u = \frac{2}{(3m)^2} \left(.005 * 560 * 10^6 \frac{N}{m^2} \right) d_c^2 = \left(622 * 10^3 d_c^2 \right) N/m^2 \tag{3.20}$$

The elastic displacement capacity can also be written as a function of d_c, if the elastic stiffness of the wall is known:

$$x_E = \frac{r_u}{k_E} \qquad (3.21)$$

In eq. (3.21), k_E can be taken as $k_E = 8EI/H^4$ per Appendix B.3

From Appendix C.3 we can see that $I = Fbd^3$, where F for our $n = 8$ and reinforcement ratio of .005 gives $F = .0245$

So, for k_E, we get:

$$k_E = \left(\frac{8*28*10^9 \frac{N}{m^2}*.0245*1m}{(3m)^4} d_c^3 \right) N/m^2 (\text{per meter})$$

and

$$x_E = \frac{r_u}{k_E} = \frac{9.2*10^{-3}}{d_c} meters$$

The difference between our elastic displacement capacity, x_E, and the true maximum displacement, x_m (from Appendix A.2), gives us the displacement that occurs post yield but prior to failure.

$x_m = H tan 4º = .21 meters$ (Appendix A.2, for Protection Category 2)

Now, we have everything that we need. We can write our impulse formula, which is based on $\frac{i^2}{m} = kx_m^2$ (eq. (3.13)) as derived previously. We can then solve for d_c, which is the depth of the wall that is required in order to resist the given impulsive load.

Let's define "m" to be $m = \rho d_c = 2400 d_c$ (kg/m^2)

$$\frac{i^2}{2k_{LM}m} = \frac{r_u x_E}{2} + r_u(x_m - x_E) \qquad (3.22)$$

Plugging in all values, noting that k_{LM} is equal to 0.66 from Appendix B.1, and simplifying:

$$413.8 = 10^6 d_c^3 - 9.06 * 10^6 d_c^2 = 25.3 * 10^6 \tag{3.23}$$

Solving for d_c from eq. (3.23), we get: $d_c = .4\ meters$

If this were a pure analysis problem and the depth was already known, then one way to check against demands would be to solve for x_m from eq. (3.22) and compare to $(x_m)_{\text{allow}}$. One final step remains, and that is to check that the impulsive loading assumption was valid.

Taking the time to reach max displacement, t_m, as $t_m \approx \frac{i}{r_u}$, we find that $t_m = 50.5ms$. We know the time duration of loading to be 4.83ms. So, we can solve for $\frac{t_m}{t_d}$:

$$\frac{t_m}{t_d} = \frac{50.5}{4.83} = 10.5 \quad ; \quad 10.5 > 3 \longrightarrow \text{``impulsive'' loading (as opposed to}$$
(``pressure-time'' or ``dynamic'' loading) $\rightarrow$ OK

note: Shear not checked.

Chapter 4

Accelerometer and Hydraulic Pressure Data

This chapter will first describe the methodology for determining the hydraulic pressure time histories applied to the actuators in the Blast Simulator. This is data that is needed for performing computer simulations of the Blast Simulator tests as well as for calculating the experimental impulses that are applied to test articles in the Blast Simulator. This discussion of hydraulic pressures will be followed by a detailed description of a methodology that can be used for post-processing accelerometer data from the impact masses. In order to determine the force-time history that an impact mass applies to a specimen in the Blast Simulator, the procedure is to obtain the net force on the impact mass, which can be found from the accelerometer data, and then subtract the corresponding hydraulic force that acts on the mass.

4.1   Blast Simulator Net Hydraulic Force

The hydraulic actuators in the Blast Simulator consist of two pressure chambers: the deceleration chamber and the acceleration chamber. The importance of post-processing the hydraulic forces will be described and the procedure for calculating the "net hydraulic force" will be provided. Lastly, the procedure is validated by carefully investigating the hydraulic data output for a particular Blast Simula-

tor test.

4.1.1   "flyer" *vs.* "punch" (BG Equation of Motion)

The force-time history delivered to specimens in the Blast Simulator depends on the mass and stiffness of the specimen, and other related properties. The impact that simulates the "blast" is not purely elastic due, in part, to the rubber programmer attached to the front of the impact mass that dissipates much of the energy in the collision. Thus, the force-time history to be delivered to the specimen is difficult to predict *a priori*. To conduct basic research in the field of blast, the ability to predict response is ultimately the goal, but most of the experimentation at the Blast Simulator involves prototype testing wherein a series of similar tests are performed in order to conduct parameter studies and validate computer models. This kind of research requires only that one can precisely obtain force-time history data post-test. This data can then be used in the computer simulations, and the structural behavior can then be compared to other kinds of measured experimental data, such as strain.

As the Blast Simulator had been in existence for only four years when the author began his Ph.D. research on the subject, the ability to obtain force-time history data from the Blast Simulator, post-test, needed improvement. The primary way of obtaining force-time data was from an accelerometer that was placed on the the impact mass (blast generator). If the blast generator (BG) is a "flyer" - that is, if the hydraulics serve only to push the impact mass up to its target speed (and then detach prior to the collision), then the only force acting on the impacting mass, during the collision, is the force from the specimen. Thus, if the acceleration-time history (or, more precisely, the deceleration) of the impacting mass is known, then the force on the specimen can be calculated.

The other, more common, type of test performed in the Blast Simulator is the "punch" test. In a "punch," the hydraulics are connected to the impact mass throughout the collision. In a "punch," the hydraulics should begin to "pull back" on the impact mass near the end of the collision, in order to prevent a "double-hit." Even though the net force acting on the impact mass, during a collision, is a

result of both the hydraulics and the contact with the specimen, common practice at the Blast Simulator had been to ignore the contribution of the hydraulics. In other words, with the mass of the impactor, m, known, and the accelerometer time history, $a(t)$, known as well, the force-time history delivered to the specimen, $F(t)_{specim}$ was taken as $F(t)_{specim} = m * a(t)$.

However, the correct formula for the impacting mass is:

$$F(t)_{net} = m * a(t) = F(t)_{specim} - F(t)_{hydraul} \qquad (4.1)$$

If one seeks to calculate the magnitude of the force, $F(t)_{specim}$, from eq. (4.1), then the sign conventions should be such that the magnitude of the force, $F(t)_{hydraul}$, shall be "added" to the magnitude of $m * a(t)$, if the impact mass is being "pushed" by the hydraulics. Since the purpose of the "punch" is to prevent a double-hit, it is common for the hydraulic to be "pulling" on the impacting mass, near the end of the collision, in which case the magnitude of the force, $F(t)_{hydraul}$, should be subtracted from $m * a(t)$ in order to calculate the magnitude of the force delivered to the specimen.

Ignoring the contribution of $F(t)_{hydraul}$ can result in errors in excess of 100% in extreme cases, as we'll see in the next two sections.

> Note that eq. (4.1) is only correct if the programmer is absent. It is true that the mass of the programmer is negligible compared to the mass of the rest of the blast generator (BG) assembly. However, the force at the backside of the programmer, which is precisely $F(t)_{specim}$ in eq. (4.1), is <u>not necessarily</u> the same as the force at the front side (impact face) of the programmer, due to the unique properties of the programmer material. Thus, $F(t)_{specim}$, as calculated from eq. (4.1), may underestimate the force imparted to the specimen if the programmer is present and no modification factors are applied to eq. (4.1).

Figure 4.1: Schematic of hydraulic system for a single impacting mass

4.1.2 "oil charge" *vs.* "deceleration" pressure

Hydraulic force is not provided from the Blast Simulator, directly. After a test, the Blast Simulator outputs the deceleration pressure (Fig. 4.1) and the "oil charge" pressure, which is the pressure inside the "acceleration chamber" in Fig. 4.1 (the deceleration pressure is zero during a "flyer" test). From this figure we can see that the net hydraulic force acting on the impacting mass (the piston rod) is the difference between the force on the piston rod from the pressure in the acceleration chamber and the force on the piston rod from the pressure in deceleration chamber. We can also see from the schematic that the pressure in the acceleration chamber (the "oil charge pressure") acts over a larger area compared to the pressure from the deceleration chamber (the "decel pressure").

The area of the hydraulic piston can be found, circled, in the "velocity generator specifications" in Fig. 4.1. In the field, the pressure within this chamber is often referred to as the "oil charge pressure." The area on which the pressure in the deceleration chamber acts is the area of the "piston rod" subtracted from the total area of the hydraulic piston. This result, which is typically called the "decel pressure," is labeled the "nitrogen piston area" in the velocity generator specification table (Fig. 4.1). These areas were also verified in the field by direct measurement. Once we have these pressures, and their associated areas, we can find $F(t)_{hydraul}$.

In eq. (4.1), one proper sign convention would be to assume that $F(t)_{hydraul}$ is positive to the left, $F(t)_{specim}$ (always $\geqslant 0$) contacts the impacting mass at the location of the "programmer" and acts to the right, while the acceleration is positive to the right (negative as the impacting mass gets up to speed; positive during impact). We will further explore the implications of incorporating hydraulic pressure into our net force calculations, by looking at some actual "decel pressure" and "oil charge pressure" test data, along with the accelerometer data for the same test. In addition, a load cell was placed at the front of the specimen (in between the impacting mass and the specimen), which was possible only due to the relatively small loads generated in this particular test. In total, we will look at three different ways to estimate the force delivered to the specimen, for this particular test, and

look at general advantages and disadvantages of each method.

4.1.3 Validation of hydraulic force in LS-DYNA
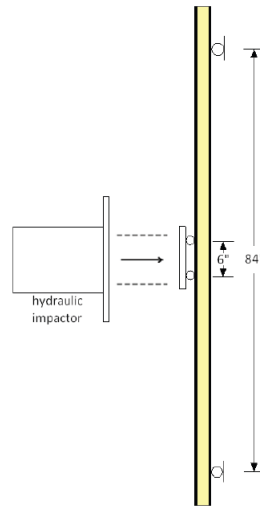
Figure 4.2: Schematic of Blast Simulator tests on long 7-ft sandwich beams. The tests were conducted as 4-point bend tests.

This section will show that the basic equation of motion for the blast generator impact mass (BG), eq. (4.1), can determine the force imparted to a specimen in a given test in the Blast Simulator. It should be emphasized, however, that eq. (4.1) is strictly-speaking correct only if the accelerometer data retrieved from the experiment is good. This is sometimes not the case, which would then require that eq. (4.1) or some of the parameters within eq. (4.1), be modified in an *ad hoc* fashion, or alternative data and methods would have to be used. In addition, this section will show that LS-DYNA [19] modeling can produce a near perfect simulation of the experiment, so long as the hydraulic data is good and the material models used in the simulation are good. The material model used for the programmer, for example, will be discussed in detail in later chapters.

The test involves an 7ft "beam" specimen, shown in Fig. 4.2. This specimen is impacted by a steel plate that is connected to the impacting mass (no rubber programmer pad was used for this test). A four-point bending response was desired

in order to isolate the bending mode of failure at mid-span. Some additional details of the test are shown in Figs. 4.3a,b. The specimen is supported *via* an aluminum frame as seen in Fig. 4.3a that has, at its ends, "rollers" to produce moment free simple support. More information on the material properties, experimental description, *etc.*, for this test series can be found in Whisler *et al.*, 2012 [64].

Dynamic load cells were fixed to the back of the aluminum frame so that accurate loads imparted to the assembly could be recorded. The impacting mass was instrumented with an accelerometer and at the front of the beam was placed a load cell. All sensors were time synchronized with the hydraulic pressure data to provide a complete record to be compared to numerical simulation. In addition, the entire sequence of events was recorded by Phantom high speed cameras (also synchronized), which provide a detailed view of the bending process and damage, as well as provide an accurate measurement of impact velocity and specimen displacement. Figure 4.3b shows 4 snapshots of the beam at time (measured in ms) as indicated on the figure on each frame. The strain rates induced in these tests were in the range $0.5\text{-}1s^{-1}$. More information on the instrumentation and data obtained from these tests can be found in Whisler [64].

For our purposes, consider that the objective of this test is to see if we can simulate the test in LS-DYNA [19], given that we already know, precisely, the geometries and materials of all of the components involved in the test. Thus, all that remains is a logical way to subject the specimen to the correct force-time history, in LS-DYNA. One way to do this (call this *method 1*) would be to take the data obtained from the front load cell (recall that a load cell was placed in between - but essentially left "unattached" to - the impacting mass and the specimen) and apply this force-time history to the specimen in the computer simulation. This, however, is not recommended, despite the load cell producing very clean results (Fig. 4.4), because one would have to model the load cell itself in the LS-DYNA simulation, which would require significant additional research relating to the material properties of the load cell, *etc.*.

Essentially, the front load cell measures force at the interface between the load cell and the impacting mass. Depending on the mass of the load cell, as well
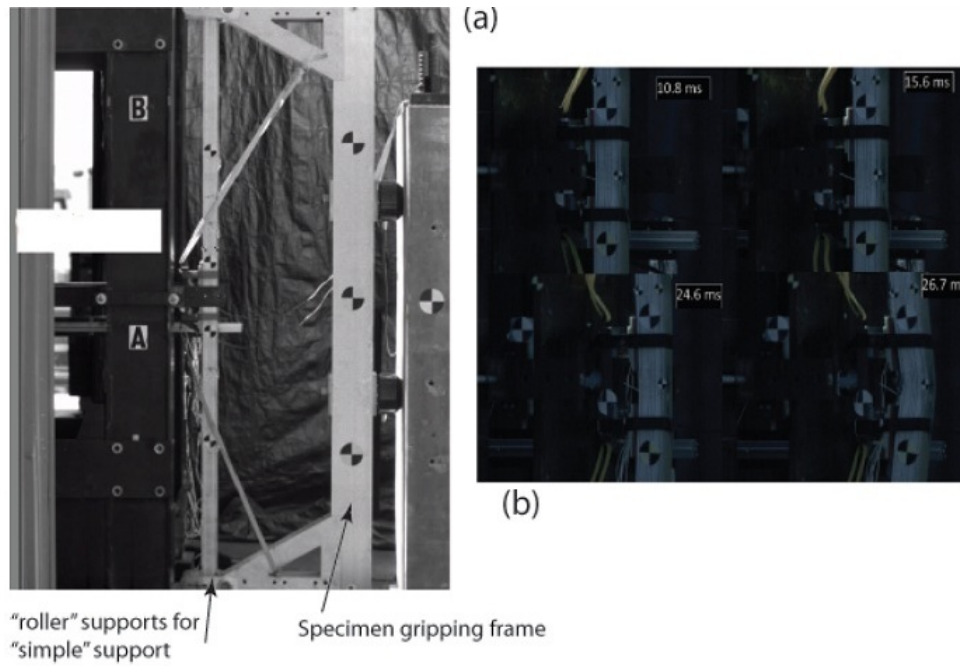
Figure 4.3: (a) Photo of Blast Simulator test configuration on long 7ft sandwich beams. (b) Four snapshots of beams under loading.
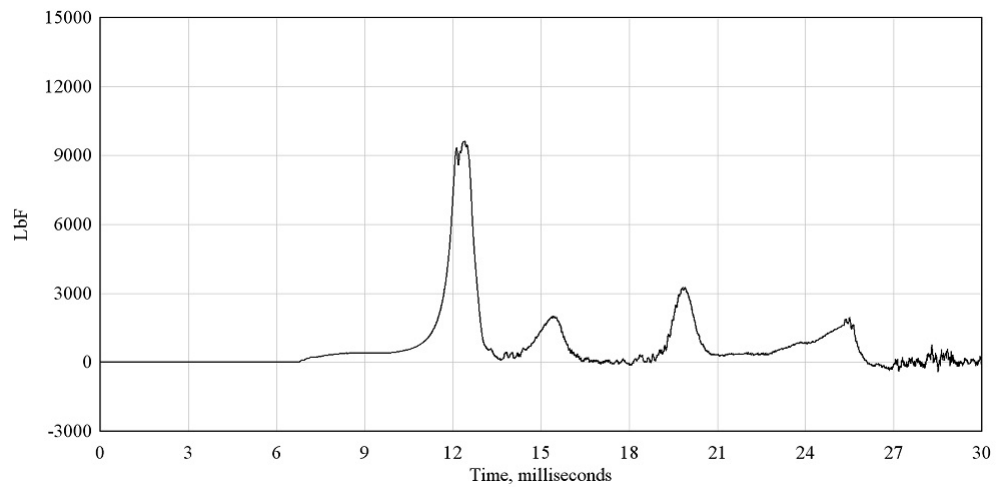
Figure 4.4: Force *vs.* time data from "front load cell"

as its stiffness and geometry, there could be a large disparity between the force measured and the force at the opposite interface - *i.e.* the contact between the backside of the load cell and the specimen. For this test, the difference between the force measured by the front load cell and the force that we're interested in - the force on the backside of the load cell - is approximately 40%. The front load cell could possibly be flipped, though this would have required modification as the load cell was mounted with a ball attachment that is appropriate for the steel impact mass interface, but not ideal for contact with the material of the specimen. Furthermore, were the programmer present in this test, the front load cell would cause additional complications.

A second way to determine the force-time history that is imparted to the specimen (*method 2*), would be to use the hydraulic data in combination with the accelerometer data from the impacting mass and solve for $F(t)_{specim}$ from eq. (4.1).
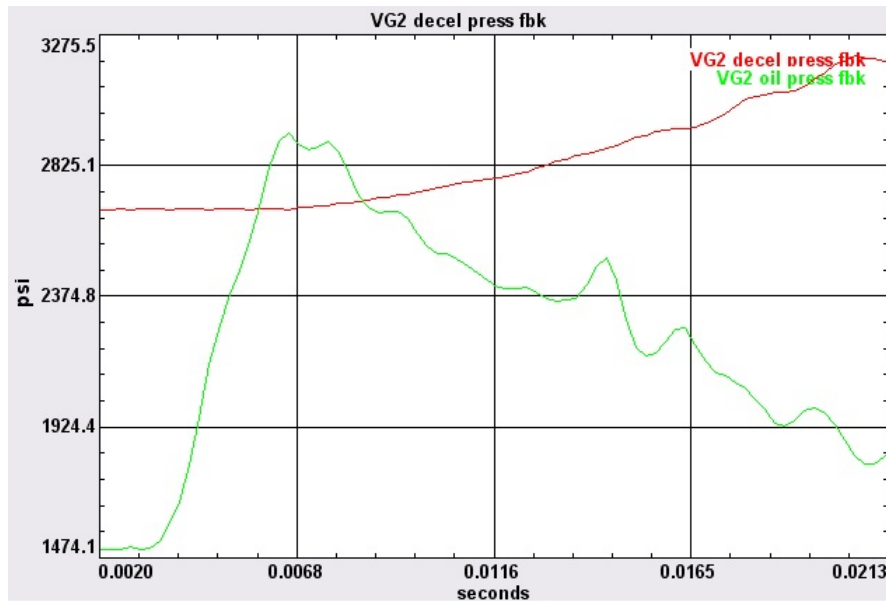
Figure 4.5: Relevant hydraulic pressure data

This is, in fact, what should be done for commissioning tests at the Blast Simulator - *i.e.* if no computer simulation is required, but an approximation of the force-time history delivered to the specimen is desired. The way this should be done is to first acquire the "oil charge pressure" and "decel pressure" time

histories, post-test (Fig. 4.5). Then, one can find the associated forces (from the areas shown in Fig. 4.1) and take a difference to find the net hydraulic force, which we simply called $F(t)_{hydraul}$ in eq. (4.1). This process is shown graphically in Fig. 4.6.

Notice that the "oil charge" and "decel" curves have appeared to shift (translate vertically) with respect to each other in Fig. 4.6a, compared to Fig. 4.6b (of course, first note the difference in vertical scale between the two figures). This is because the "decel pressure" is multiplied by a much smaller area to obtain force, compared to the "oil charge pressure," which is multiplied by the entire hydraulic piston area (Fig. 4.1). The yellow line of Fig. 4.6c is the force that is of particular interest to us - "$F(t)_{hydraul}$" in eq. (4.1). Now we can find $F(t)_{specim}$, shown in Fig. 4.7, along with the accelerometer data that has been converted to units of force. Also note that for this particular test, the impacting mass "punch" is "pushing" up until about $20ms$, which it turns out was at the very end of the first collision (recall that we want to begin "pulling" prior to the end of the collision; there was a slight "double-hit" on this test).

We can see in Fig. 4.7 that the estimation of force imparted to the specimen assembly (this includes the presence of the front load cell) using this method has peaks that are about the same as those obtained using the first method (Fig. 4.4). It must be emphasized, though, that the high frequency "noise" in the accelerometer data was filtered, in an *ad hoc* manner. Essentially, the data was filtered using a frequency cut-off of about 1500 Hz for this particular data set, and then the data was "smoothed" in DPlot [25]. "Smoothing" is not usually necessary, but this set of accelerometer data is particularly poor. Low pass filtering, on the other hand, is often required, and will be discussed in a later section devoted to accelerometer post-processing.

This particular set of data, even after being filtered and smoothed (Fig. 4.7) is relatively messy compared to the front load cell's output, because this accelerometer data is displaying oscillations (resonance) of the impacting mass along with oscillations of the accelerometer itself. The latter accelerations can be mostly filtered out. However, since the natural frequency of the impacting mass is
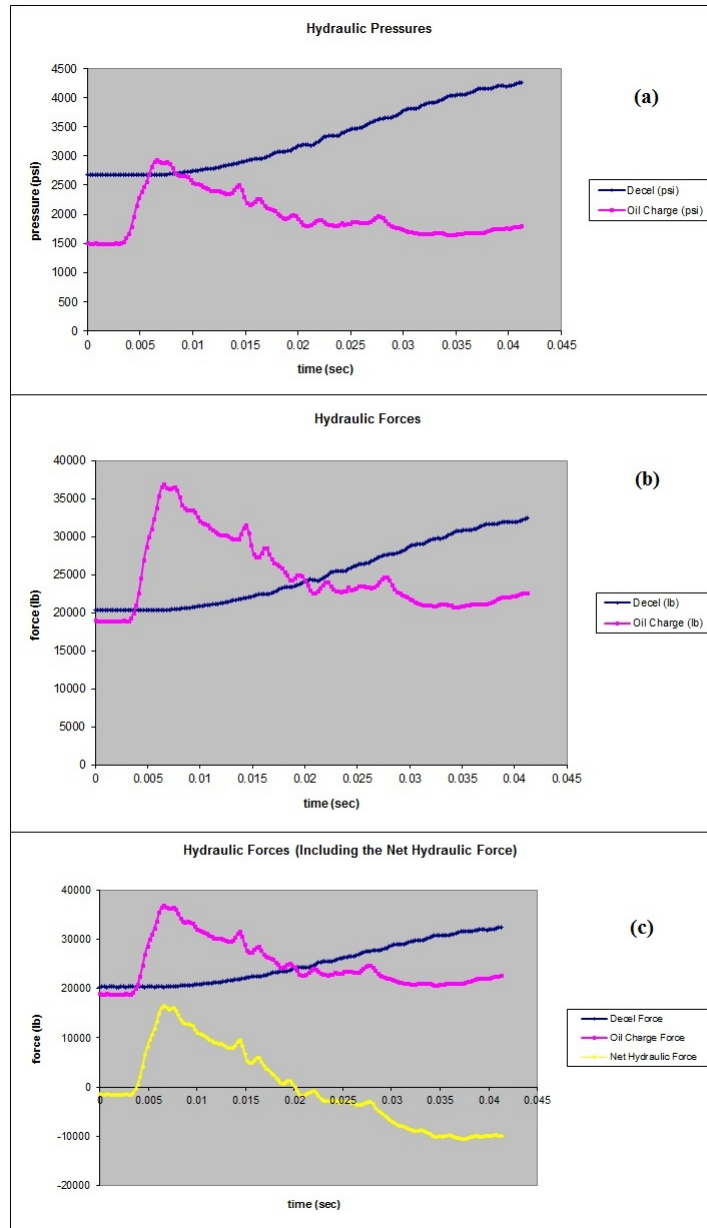
Figure 4.6: Hydraulic "oil charge" and "deceleration" pressures and forces (and combined)
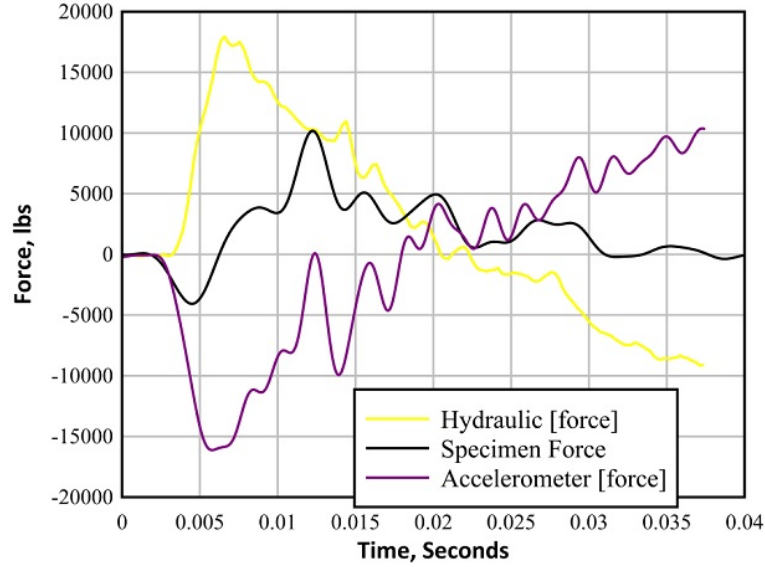
Figure 4.7: Estimation of force imparted to specimen

often similar to the time duration of the collision, a "filter" cannot be used in order to eliminate such oscillations. These impacting mass oscillations are particularly apparent, here, since a rubber programmer was not used, which would have helped to damp out some of this unwanted behavior, and also since the force imparted to the specimen is relatively small. Still, we can see that the specimen force is zero before impact and zero after impact, as expected.

Method 2 also has the same problem as method 1, in that the front load cell would ultimately have to be modeled in the computer simulation, since the net force shown in Fig. 4.7 occurs at the interface with the impacting mass and not necessarily at the direct interface with the specimen. In addition, it should be mentioned that the presence of a programmer may affect one's ability to find the force imparted to the specimen by solving for $F(t)_{specim}$ from eq. (4.1). $F(t)_{specim}$ is the force at the backside of the programmer. The force at the programmer's impact side, which is what we want, may be reduced. While the programmer is known to be viscoelastic and its presence known to reduce the coefficient of restitution of the impact with the specimen, the difference in force between the front and backside of the programmer is a separate issue. Even though the programmer is highly viscoelastic it is certainly possible that it can transmit 100% of the force

through its thickness. Various programmer material models will be discussed in a later chapter that is devoted to the issue of viscoelasticity. Transmitted force will be addressed in the following section devoted to accelerometer post-processing.

For this "beam" test, which was modeled in LS-DYNA, neither method 1, nor method 2, was used. Whereas the first two methods would require that the forces imparted to the specimen be input into LS-DYNA as a force-time history, a third method that will be presented instead requires that we model the mass itself. *Method 3* will be discussed for the remainder of this section. The LS-DYNA model was a continuum model that primarily incorporated "TYPE 1" solid elements.

In the experiment, the impactor was placed at an initial position one inch away from contacting the front load pad. The impactor in the simulation, shown in Figure 4.8b, does not incorporate all of the complex geometries of the actual hydraulic actuator used in the Blast Simulator. For the purposes of the LS-DYNA simulation, the impactor's geometry was simplified and the density scaled in order to match the total weight of the actual impactor. Figure 4.8b shows this initial location of the impactor at time 0, in LS-DYNA and Fig. 4.8c is a screen-shot of the simulation at time 26 milliseconds, just prior to failure. Note that the force from the hydraulics is the force that drives the impactor in the Blast Simulator, and will be the force that drives the LS-DYNA simulation, as shown in Figure 4.8b.
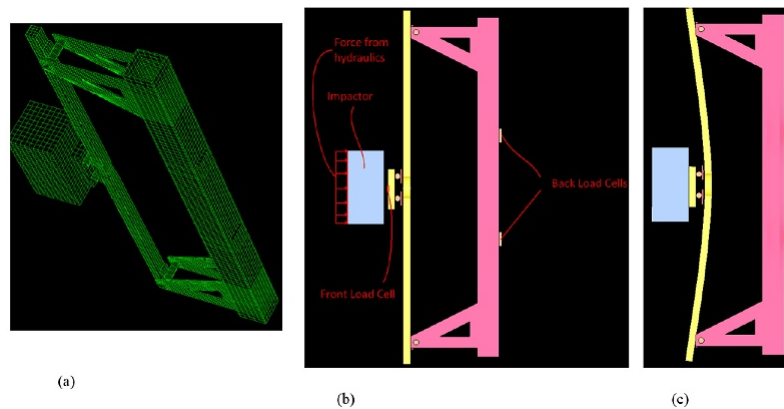
Figure 4.8: (a) LS-DYNA model mesh for an 7 ft beam simulation (b) Model prior to impact (impactor, hydraulic forces, and locations of load cells are shown) (c) Time = 26 milliseconds, just prior to failure

The pressure-time history on the impactor is one of the data retrieved from the Blast Simulator, as described previously (Fig. 4.6c), and is, accordingly, loaded as input into LS-DYNA. This is the force that drives the simulation. Other forces of interest, such as the force at the locations of the the back load cells, or at the interface between the contact pads at the specimen, can be post-processed from LS-DYNA and plotted against data retrieved from the experiment, where applicable. The center displacement of the beam can also be verified.

The two parameters that will be considered, here, are the load at the location of the back load cells and the center displacement of the specimen. These experimental values are plotted as a function of time, alongside the values from the LS-DYNA simulation, in Figure 4.9. Recall that the displacement at the center of the specimen was obtained from high-speed camera footage, and the forces at the backside of the aluminum frame were measured using 50 kip load cells. The experimental forces are plotted against the total LS-DYNA "contact" force at the back of the aluminum frame, in Figure 4.9. In addition, the experimental displacement versus time of the center of the specimen is plotted against the LS-DYNA displacement at the same location. These displacements are shown in Figure 4.9 as well (see right vertical axis for displacement). Figure 4.9 shows that plots of displacement versus time for the experiment and for the simulation match closely, and failure occurs between 26 and 27 milliseconds. The force-time history at the back of the frame also match closely.

It's interesting to note that the mass and stiffness of the "front load cell" have very little influence on the behavior of the specimen in the simulation, using the third method - *i.e.* modeling the actual impact mass itself within the model. In fact, the front load cell was not modeled at all, despite it weighing slightly more than the specimen (excluding the reaction frame). In fact, it is because the mass of the front load cell is greater than the specimen (but less than the impacting mass), and also because the test was governed mostly by impulse-momentum (eq. (3.2) and eq. (3.8)), that it was possible to neglect the front load cell altogether. This can be easily proven by lining up three billiard balls of masses $m_1 \geqslant m_2 \geqslant m_3$, where it can be shown that the presence of the second billiard ball, m_2 is irrelevant
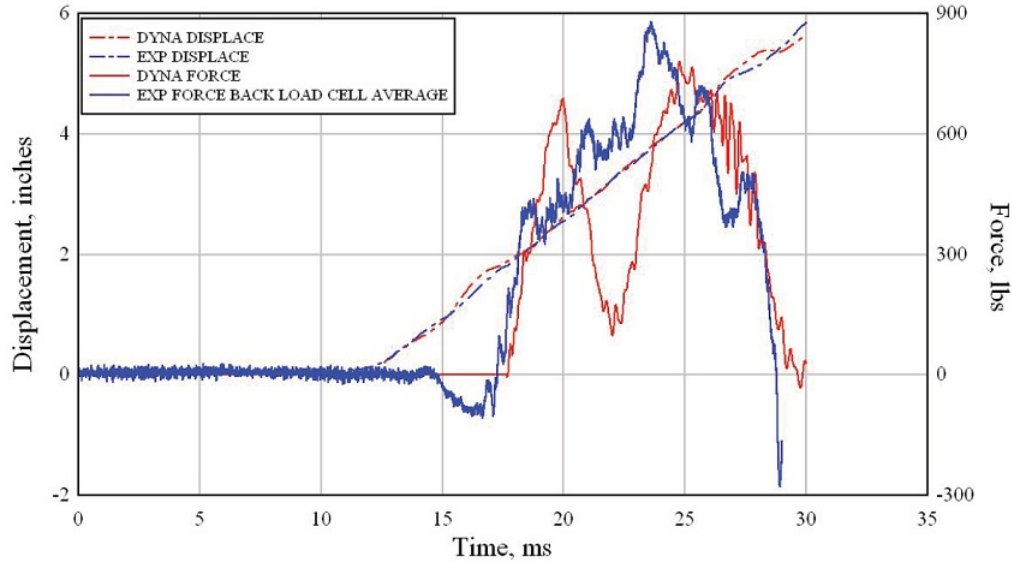
Figure 4.9: Back load cell force and displacement versus time comparison between experiment and computer simulation for 7 ft bend test

to the *impulse* delivered to m_3. Recall that the billiard ball analogy is valid because the front load cell is not "attached," *per se*, to either the impacting mass or the specimen, and the collision is governed mostly by impulse.

We already know, on the other hand, that consideration of the front load cell is essential if one seeks to run the LS-DYNA simulation by applying force output from the experimental front load cell (method 1) or from the net force method (method 2). This was described in detail previously, where it was noted that the presence of this front load cell can make it difficult to obtain precise results if method 1 or method 2 are used. Method 3, however, produced excellent results as we can see in Fig. 4.9, without considering the mass and stiffness of the front load cell. Thus, modeling the impactor in LS-DYNA, as described in method 3, rather than "applying" loads in LS-DYNA using front load cell data (or the net force method), allows for a high level of precision in the simulation without having to model all of the less important components involved in the test - at least, in many cases. Method 3 should be used whenever possible to obtain force-time load demands on specimens (and to model specimen behavior, when needed), though, method 2 can often give a reasonable estimate - in particular method 2 can be

useful for estimating force-time demands for cases where a computer simulation is not performed. Placing a front load cell at the interface between the impacting mass and the specimen is not recommended, as the *impacting mass - programmer - specimen* physical behavior will be altered. More information about these "beam" tests can be found in Huson [24].

4.2 Accelerometer Post-Processing

There are many circumstances at the Blast Simulator where we, or our clients, desire the pressure-time history imparted to a particular specimen, post-test, from experimental data. Sometimes the output from a computer simulation will suffice, but experimental results are usually most desirable. In cases where the computer simulations are not fully validated, experimental pressure data can be particularly vital, for all parties involved. In the previous section, "method 2" addressed the basic idea of using acceleration-time histories of the impact masses, along with the hydraulic force-time histories, to estimate the pressure-time history imparted to a specimen. This section will expand on this idea.

4.2.1 Pressure-time *vs.* Impulsive Behavior

In general, it is good practice to filter the accelerometer data in order to eliminate high frequency "noise." It is also essential to include the contribution of the hydraulics for "punch" type tests, where the hydraulics are actively influencing the behavior of the collision. To illustrate an important point, consider two extreme cases. In case 1, the natural period of the specimen is very small, like the time duration of impact, and so the specimen is driven by "pressure-time." In case 2, the natural period of our specimen is large, compared to the time duration of impact, and so the specimen behaves "impulsively."

In case 1, the peak pressure is the most important parameter, and the filtering of accelerometer data is critical. To see the significance of filtering on peak

pressure, see Fig. 4.10. Often, the peak forces from the hydraulics are quite small compared to the peak forces imparted to the specimen, and so, perhaps, the contribution of the hydraulics can be ignored for case 1. However, it is recommended that the contribution of the hydraulics be incorporated into the calculations wherever possible.
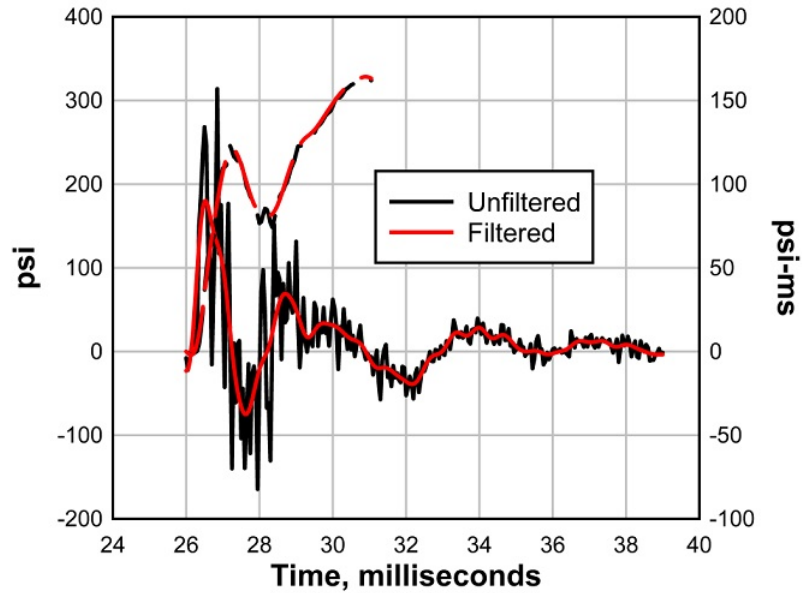
Figure 4.10: Filtered *vs* unfiltered pressures and impulses

Case 2 (impulsive behavior) is much more common in the Blast Simulator. Here, total impulse imparted to the specimen is the most important parameter (for design calculations, for example); the peak pressure is less important. While the filtering of data significantly affects peak pressure, it does not much affect total impulse. The lack of effect on total impulse is illustrated in Fig. 4.10. We can see that the impulse of the filtered data is identical to the unfiltered data, despite the very large differences in peak pressures between the two curves. So, for typical tests in the Blast Simulator (case 2), which are impulse-controlled, the filtering of accelerometer data may not be necessary. If a proven method for low-pass filtering exists, then it is recommended. The specific low pass filter used for this thesis is a function in DPlot [25] called "Option 2 low-pass," which essentially eliminates frequencies above approximately 2000 Hz for the history shown in Fig. 4.10.

Of much more consequence than filtering is the contribution of the hydraulics. The contribution of the hydraulics for case 2 "punch" tests is essential to include (so long as the hydraulics are connected - *i.e.* if the "break away" bolts fail, then the hydraulic data should only be included up until said failure). To illustrate just how important it is to include the hydraulics, consider Fig. 4.11.
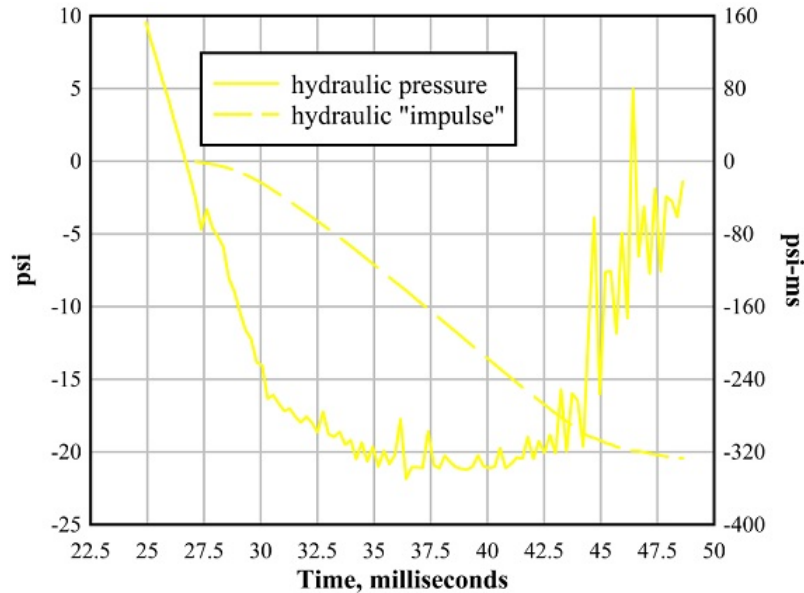
Figure 4.11: "Impulse" from hydraulics illustrated

Fig. 4.11 shows the hydraulic force and impulse data for the same test as Fig. 4.10. For this BG, the collision began at 26.25ms, and so we begin looking at the hydraulic force at 26.25ms. We can see that although the pressure values from the hydraulics are relatively small, the "impulse" is very large, and in fact would be even larger if the BG impacted at zero acceleration (zero pressure from the hydraulics), as is normally the objective (impacting at zero acceleration is arbitrary, but is desirable merely for Blast Simulator operator consistency purposes). Fig. 4.12 also shows the importance of including the hydraulics. From computer simulations and from correctly post-processed experimental data, it is known that the collision is over at about 31ms for the test depicted in these figures. We can see in Fig. 4.12 that at 31ms, the error is just over 10%. Worse yet, if we neglect the hydraulics, the impulse continues to increase, such that one may be led to believe

that the collision duration is much longer and the impulse much greater.
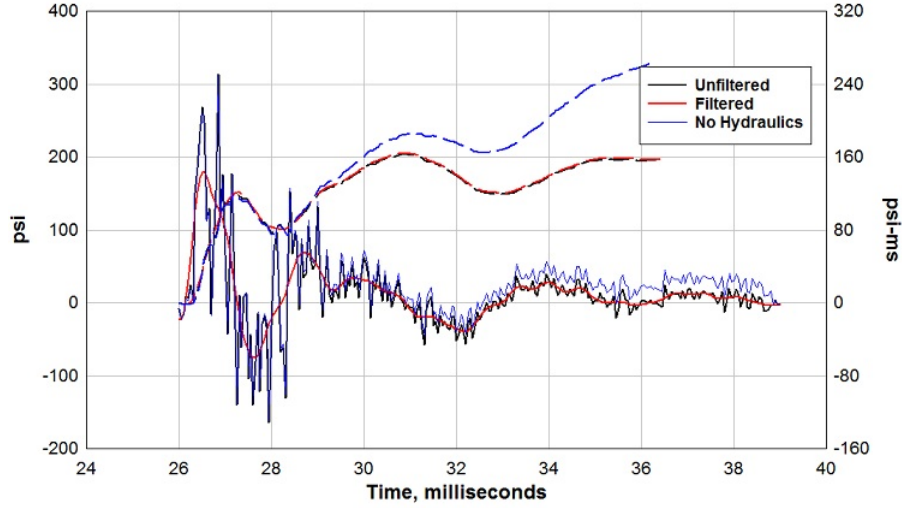
Figure 4.12: Comparison of impulse with and without hydraulic contribution

So, from Figures 4.11 and 4.12 it should now be clear that were we to obtain the net force from the accelerometer data recordings, which includes any contribution from the hydraulics, and then simply set this net force to be equal to the imparted impulse on the specimen, then this estimation of imparted impulse would potentially have an error greater than 100%. We *must* consider the contribution of the hydraulics in deriving imparted impulse (and peak pressure, to a lesser extent), as explained in the previous section.

4.2.2   Pressure and Impulse Estimation Procedure

In order to obtain the pressure-time history imparted to the specimen, we must use data obtained from the accelerometers on the BGs, along with hydraulic data. Fig. 4.13 depicts the important data from a BG. Specifically, Fig. 4.13 shows the net hydraulic force, as discussed in the previous section, along with the net force from the BG accelerometer. Prior to impact, these curves should exactly cancel, since the net hydraulic force is the only force acting on the BG, prior to impact. In other words, the value of $F(t)_{specim}$, in eq. (4.1), should be zero prior

to impact.
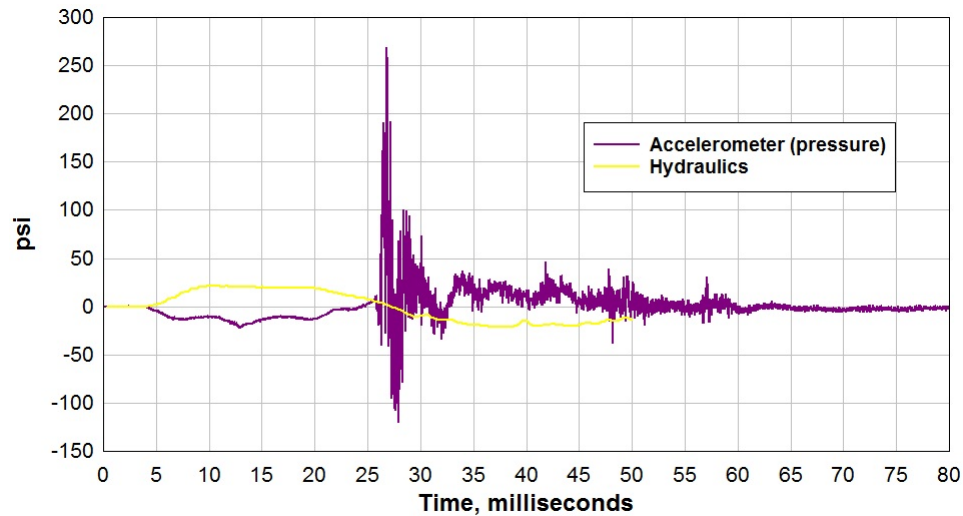
Figure 4.13: Hydraulic and accelerometer data converted to BG demands

We can see that the curves do not yet cancel each other exactly. The net force magnitudes obtained from the accelerometer are underestimated in Fig. 4.13 due to unknown influences from the mass of the oil behind the actuator (recall, one of the pressures involved in the motion of the actuator is "oil charge pressure"), friction of the piston, and any badness in the hydraulic pressure data itself. The way these factors will be accounted for is by placing an *ad hoc* factor on the actuator mass such that the two curves of Fig. 4.13 exactly cancel. Fig. 4.14 includes this factor (factors generally range from 1.0 to 1.4). The resulting imparted specimen pressure can then be found, and was shown in full (along with impulse) in Fig. 4.10.

Mid-frequency oscillations are the greatest problem with this type of procedure, though they are less of a problem when larger forces are imparted. In fact, in typical tests, mid frequency oscillations are not much of an issue. Recall, however, the example in the previous section, where the peak pressure (and impulse) was relatively small and therefore heavily influenced by mid-frequency oscillations. High frequency oscillations are an issue as well, though we already saw (Fig. 4.10) that such oscillations are so short in duration that they do not affect impulse.
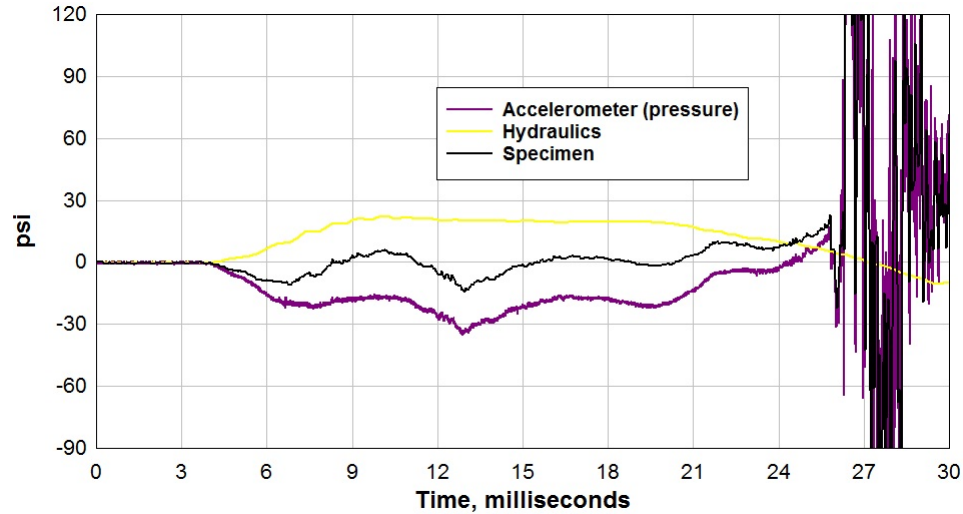
Figure 4.14: Hydraulic, accelerometer, and specimen pressure generated from BG

A second problem is unknown influences from the mass of the oil behind the actuator, friction of the piston, and any badness in the hydraulic pressure data itself. As previously stated, these influences are essentially accounted for with an *ad hoc* factor on the actuator mass. In reality, though, it is unknown whether the aforementioned issues do indeed effectively "add" to the mass of the actuator or if the hydraulic data itself should be modified. Experience and comparisons to LS-DYNA models suggests that the correct procedure is to "add" to the mass to account for oil interaction, friction, *etc.*, as discussed. Additionally, we've seen that the imparted specimen force is near zero at the beginning and at the end of the collision, which is expected, and gives confidence in the procedure.

Other issues: Most tests have several impact masses, rather than just one single mass. We therefore must determine a systematic approach for obtaining some sort of "average" pressure-time history, since this is what is usually desired by clients. The recommended approach is to sum the force-time histories imparted to the specimen, from each impact mass, and then divide by the total area of all of the masses. Lastly, most tests in the Blast Simulator use rubber "programmer" pads at the impact face of each impact mass. Loss of transmitted force through the thickness of the programmer is a potential issue that must be addressed, since

acceleration-time histories of the impact masses do not provide an estimate of net force at the contact surface, but instead provide an estimate of the net force acting on the backside of each programmer. The assumption is that the force history on the front and the back of the programmer pad is the same, although there could be some through-thickness variation in force within the programmer. To investigate this issue, a test was done (Fig. 4.15) to determine the amount of transmitted force variation that occurs through the thickness of our two-inch programmer pads. Fig. 4.15 shows this programmer pad being impacted by a flyer. The programmer pad is sandwiched by the test apparatus in such a way that the force on the non-impact face of the programmer can be measured. Unfortunately, in this particular test, a significant amount of force was delivered to the boundary conditions of the test apparatus, which was not measured. Since the force history on the front and back side of the programmer pad could not be measured, the results were inconclusive.

However, a comparison of the results of the test that is shown in Fig. 4.15 to a "baseline" test on a thin steel plate was performed, which showed close agreement for all measured parameters. This may suggest that the force variation through the thickness of the programmer is similar to the force variation through the thickness of a thin steel plate, which we know to be negligible. Thus, the methodology for using acceleration-time histories of the impact masses to provide an estimate of the net force acting on the backside of each programmer can be used to estimate the net force at the contact surface, as previously assumed. Additionally, we will verify later on (in the chapter related to programmer material modeling) *via* drop tower tests that the force-time histories for each side of the two faces of the programmer are approximately equal during heavy impact events. The problem with using drop tower test data to prove negligible through-thickness force variation of a programmer pad is that the programmer samples in the drop tower tests are not the full thickness of a programmer pad, nor do they contain pyramids.

The low-pass filtering of data was mentioned previously, and it was emphasized that such filtering does not significantly affect total impulse. Since impulse is unaffected, and since most of the tests in this thesis are impulse-controlled, we will use raw, unfiltered, data, most of the time. However, the occasion may arise
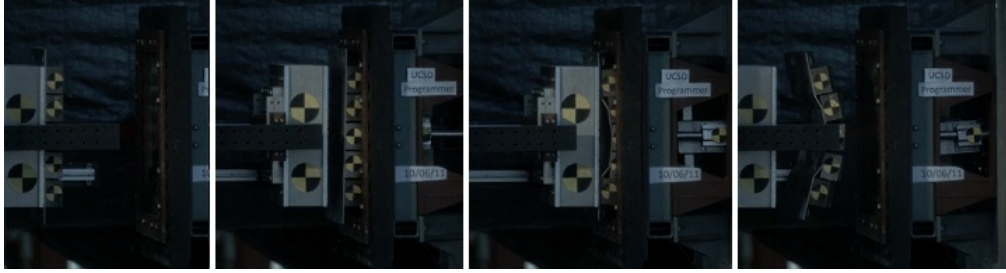
Figure 4.15: Experiment to measure the through-thickness force variation of the programmer

where the client will request the value of peak pressure, even if the behavior of the specimen is impulsive. In fact, what the client often wants is a simplified pressure-time history that captures the peak pressure, total impulse, and time duration. In order to capture all three of these parameters, the "simplified" pressure-time history needs to be nonlinear. Eq. (4.2) can be used to estimate the positive phase portion of a blast demand. This is the so-called modified Friedlander equation [5].

$$P(t) = P_{s0}[1 - (t - t_A)/t_0]e^{-(t-t_A)/x}, \text{ for } t \leqslant t_A + t_0 \tag{4.2}$$

The variables in eq. (4.2) are shown in Fig. 4.16. For the wall tests in this thesis, eq. (4.2) will yield a reasonable value of impulse, using filtered peak pressure and experimental time duration, if the value of "x" is varied by trial and error between 1.10 and 1.30.

Our previous example (Fig. 4.10) shows a filtered pressure of about 180 psi with a time duration of about 4.6ms, and a start time of about 26.4ms. Plugging into eq. (4.2) with "x" equal to 1.29 yields the curve shown in Fig. 4.17. We can see that we get a value of impulse from the simplified pressure-time history that is a slight overestimate, in this case. In order to achieve the exact impulse, using our simplified demand formula, "x" would have to be decreased *ad hoc* when plugging into eq. (4.2).
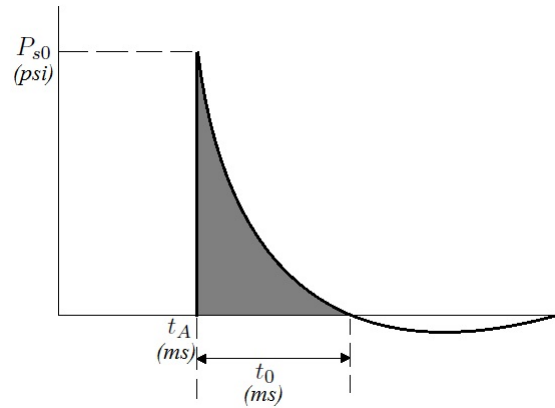
Figure 4.16: Simplified pressure-time history
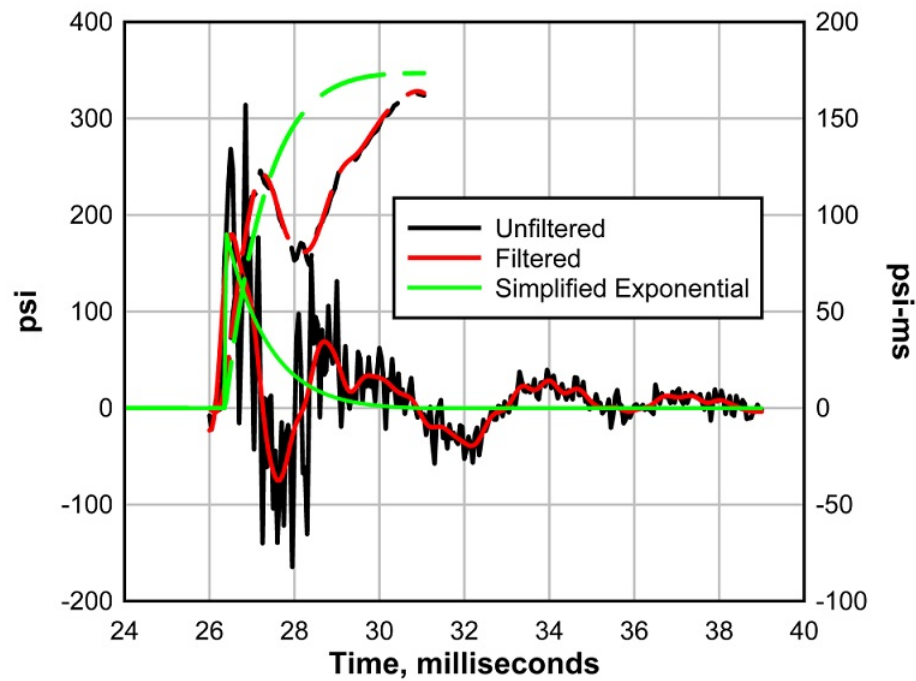
Figure 4.17: Simplified pressure-time history for our example

Chapter 5

Programmer Material Modeling

The programmer material is Adiprene L-100/MOCA, which is Adiprene that has been cured with MOCA(methylene bis-orthochloroaniline) [48]. This material is a kind of elastomer that is a nearly incompressible and is "rubbery" in the sense that it behaves hyperelastically when loaded and unloaded infinitesimally slow (nonlinear elastic relaxed equilibrium response), and viscoelastically under realistic loads. In LS-DYNA [19], there exists a wide variety of material models. Some models contain hyperelasticity in a purely phenomenological sense (e.x. Blatz-Ko "rubber"), while others are based on micro-mechanical properties (e.x. Arruda-Boyce "rubber"). Viscoelasticity is treated differently depending on the chosen model as well. Some of the LS-DYNA rubber models contain no viscoelastic capability at all (e.x. Blatz-Ko "rubber").

Since large hysteretic losses are observed in our programmer under the kinds of loads that it is subjected to in daily operation, a model must be chosen that can handle viscoelastic effects, even if only in a phenomenological sense. These viscoelastic effects are not only unavoidable, but also desirable, since the "decompression" part of the impact is longer than the "compression" part of the impact - similar to the behavior observed in actual "blast" pulses, where the increasing portion of the imparted force is steep and is often ignored.

Thus, a "tabulated" material model in LS-DYNA, called *MAT_057 or *MAT_LOW_DENSITY_FOAM is what was ultimately decided upon, prior to the author's arrival at UCSD. It turns out that this model is a poor choice, due to its

lack of incompressibility, as well as its lack of both physical hyperelasticity and viscoelasticity. An alternative rubber model will be described and validated in this thesis.

5.1 *MAT_057

*MAT_057, also known as *MAT_LOW_DENSITY_FOAM is a material model that was chosen by Oesterle [44] for the purpose of modeling the Blast Simulator "wall programmer" in LS-DYNA. The model is based on data from a compression test that was performed on a 16in. x 16in. programmer "pad," as described by Rodriguez [48] and shown in Fig. 5.1. The original purpose of this test was to obtain global compression data for this programmer "pad," rather than to obtain *material* compression data.

Moreover, the material that was tested in Fig. 5.1 is the first programmer material that was used in the Blast Simulator. The "wall programmer" material used by Oesterle (and subsequently by the author) is a different material. In fact, the actual wall programmer material exhibits a decreasing tangent stiffness within the strain ranges that are depicted in Fig. 5.1, as we will see later on in this chapter. Thus, *MAT_LOW_DENSITY_FOAM is based on incorrect material data.
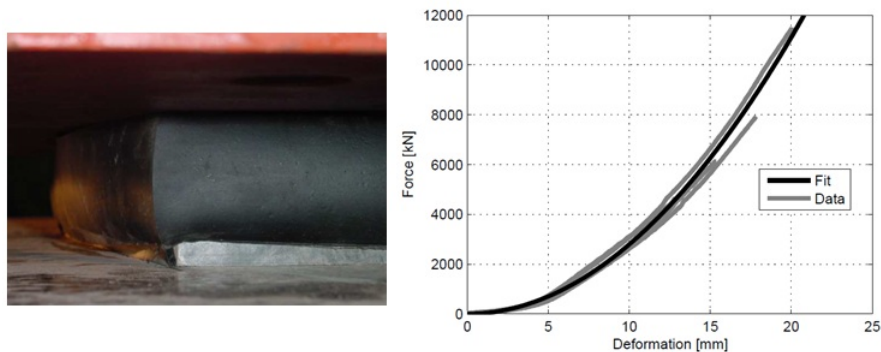
Figure 5.1: Compression test on programmer "pad" [48]

*MAT_LOW_DENSITY_FOAM contains a constitutive relation to describe loading behavior that is based on the uniaxial tabulated experimental data shown in Fig. 5.1. This relation is shown in eq. (5.1).

$$\sigma_i = \frac{\sigma_0(\lambda_i - 1)}{\lambda_j \lambda_k} \qquad (5.1)$$

λ_1, λ_2, λ_3 are the principal stretches, which are found from actual loading. $\sigma_0(\lambda_i - 1)$ is the engineering (nominal) stress, as a function of the engineering strain, $\lambda_i - 1$, which comes from tabulated uniaxial test data.

σ_1, σ_2, σ_3 are the principal Cauchy stresses.

This relation is *not* based on hyperelasticity. Rather, it is only valid for uniaxial loading, in the longitudinal direction. It is not work conjugate, nor correct under any loading except for uniaxial loading. This is easily seen by observing the simulation of the behavior of a cube of programmer under compression that has been modeled using *MAT_LOW_DENSITY_FOAM, as shown in Fig. 5.2. In this case the "correct" behavior simulation was performed using a simple "Blatz-Ko Rubber" model, a well-known hyperelastic model. Later on, we will see actual images of this "barreling" behavior from photos of quasi-static and drop tower test experiments.

*MAT_LOW_DENSITY_FOAM contains a simple treatment for viscoelasticity. The loading behavior is defined by eq. (5.1), while the unloading is determined in a manner such that the total area enclosed by a loading/unloading hysteretic closed loop is held constant. The result is that energy dissipation is independent of strains or strain rates. The way that this energy dissipation is defined is described in the LS-DYNA Manual [19], but this nonphysical behavior is easily observed by simulating a variety of impacts and noting that the coefficient of restitution is independent of mass and impact velocity. This is fundamentally flawed, since we know viscoelastic effects to be highly dependent on strain and strain rate.

In summary, *MAT_LOW_DENSITY_FOAM is a simple model. While
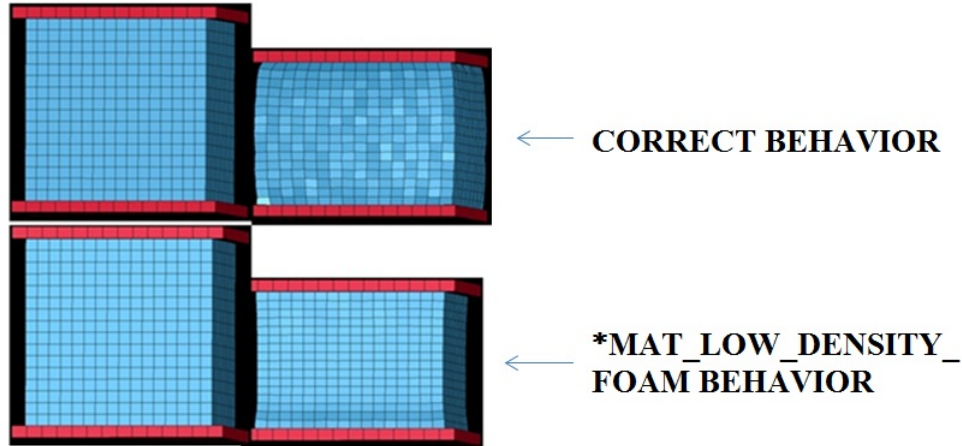
Figure 5.2: *MAT_LOW_DENSITY_FOAM incorrect behavior

the *MAT_LOW_DENSITY_FOAM "wall programmer" model was "calibrated" by Oesterle for a series of impacts on masonry walls [44] and therefore performs adequately under such impacts, it is not, in general, a good model. *MAT_LOW_DENSITY_FOAM lacks the capability to adequately capture physical hyperelastic behavior or viscoelastic behavior.

Another LS-DYNA model had been previously considered by Sallay and Gurtman of SAIC [52]. This model was the Arruda-Boyce Model [2], which in LS-DYNA is called *MAT_ARRUDA_BOYCE_RUBBER. The LS-DYNA version of this model contains a hyperelastic component along with a viscoelastic component. The hyperelastic component is characterized by two material constants and the viscoelastic component is characterized by an additional two material constants. Sallay and Gurtman [52] characterized this model for our programmer based solely on coefficient of restitution data, which was apparently known from a series of early programmer tests. Since Sallay and Gurtman did not know the stress-strain behavior of the programmer, they provided us with a four different sets of material constants, each set providing the best possible fit to our COR data for a particular initial shear modulus. Unfortunately our initial shear shear modulus for the wall programmer falls well outside the range of values that they considered. In addition, the Arruda-Boyce model is a micromechanical model that in general exhibits a stress-strain response with an increasing tangent modulus in compression. Our

wall programmer exhibits a decreasing tangent modulus in compression in the range of strains that we're interested in (only up to 30%). For these reasons, *MAT_ARRUDA_BOYCE_RUBBER will not be considered for the material model of the wall programmer.

This "wall programmer" model will be replaced by a more sophisticated (but still computationally cheap) model called *MAT_SIMPLIFIED_RUBBER _WITH_DAMAGE. *MAT_SIMPLIFIED_RUBBER_WITH_DAMAGE is based on so-called Ogden hyperelasticity, though *MAT_SIMPLIFIED_RUBBER_WITH _DAMAGE, like *MAT_LOW_DENSITY_FOAM, is a "tabulated" model. In addition, *MAT_SIMPLIFIED_RUBBER_WITH_DAMAGE incorporates a somewhat more sophisticated treatment for unloading behavior, compared to *MAT _LOW_DENSITY_FOAM.

5.2 Hyperelasticity

Ogden hyperelasticity is one of the more advanced ways of handling hyperelasticity. It will be discussed, following a brief review of hyperelasticity. Understanding the foundations of hyperelasticity, as it pertains to continuum mechanics and 3D "solid" elements in finite element analysis, is crucial, since this is how the programmer material models are treated in LS-DYNA simulations.

Observing Fig. 5.3, consider that we will be interested in the following strain tensors:

$\mathbf{F}$ = "deformation gradient" tensor

$$\mathbf{F} = \begin{bmatrix} \frac{\partial x_1}{\partial X_1} & \frac{\partial x_1}{\partial X_2} & \frac{\partial x_1}{\partial X_3} \\ \frac{\partial x_2}{\partial X_1} & \frac{\partial x_2}{\partial X_2} & \frac{\partial x_2}{\partial X_3} \\ \frac{\partial x_3}{\partial X_1} & \frac{\partial x_3}{\partial X_2} & \frac{\partial x_3}{\partial X_3} \end{bmatrix} \tag{5.2}$$

note: $\mathbf{F}^T \cdot \mathbf{F} = \mathbf{C}$ = "Right C - G" (Cauchy - Greene) deformation tensor
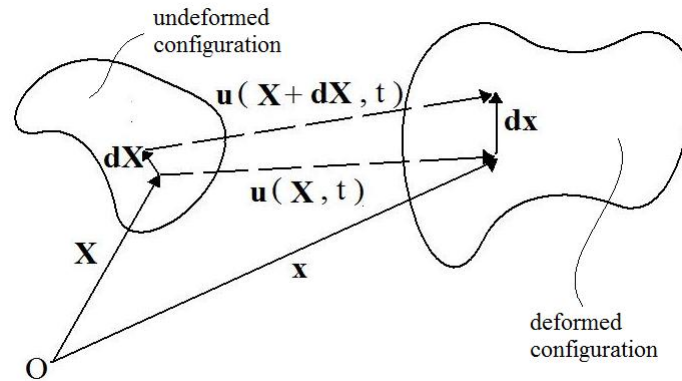
Figure 5.3: Strain potato

$\mathbf{E} =$ Lagrangian Strain Tensor $= \frac{1}{2}(\mathbf{F}^T \cdot \mathbf{F} - \mathbf{I})$

or

$$\mathbf{E} = \frac{1}{2}(\mathbf{C} - \mathbf{I}) \tag{5.3}$$

or

$$E_{ij} = \frac{1}{2}\left(\frac{\partial u_i}{\partial X_j} + \frac{\partial u_j}{\partial X_i} + \frac{\partial u_k}{\partial X_i}\frac{\partial u_k}{\partial X_j} \right) \tag{5.4}$$

> note: Although some authors insist that the "dot product" operator must always produce a scalar [23], most of the literature in solid mechanics uses a "dot" to signify a product between tensors that produces a tensor. This distinction is important in particular when deriving identities and quantities using indices, where the placement and function of a "dot" is more than just a notation.

> note: $\mathbf{F} \cdot \mathbf{F}^T = \mathbf{B} =$ "Left C-G" tensor

$\mathbf{e} =$ Eulerian Strain Tensor $= \frac{1}{2}(\mathbf{I} - \mathbf{F}^{-T} \cdot \mathbf{F}^{-1})$

or

$$\mathbf{e} = \frac{1}{2}(\mathbf{I} - \mathbf{B}^{-1}) \tag{5.5}$$

or

$$\mathbf{e} = \frac{1}{2}(\delta_{ij} - B_{ij}^{-1}) = \frac{1}{2}\left(\frac{\partial u_i}{\partial x_j} + \frac{\partial u_j}{\partial x_i} - \frac{\partial u_k}{\partial x_i}\frac{\partial u_k}{\partial x_j}\right) \tag{5.6}$$

If only infinitesimal deformation, $E_{ij} \approx \epsilon_{ij} = \frac{1}{2}(\frac{\partial u_i}{\partial X_j} + \frac{\partial u_j}{\partial X_i})$

$e_{ij} \approx \epsilon_{ij}$ as well, unless significant rigid body rotations is present.

Constitutive relations between stress and strain simply require that the stress-strain pair be work-conjugate - *i.e.* behave similarly under rigid body rotation. In hyperelasticity, this means that we can either use the Second-Piola Kirchhoff stress tensor, $\hat{\boldsymbol{\sigma}}$, with the Right C-G tensor, $\mathbf{C}$, or, alternatively, we can use the Cauchy stress tensor, $\boldsymbol{\sigma}$, with the Left C-G tensor, $\mathbf{B}$. The former stress - strain pair is invariant to rigid body motion. $\boldsymbol{\sigma}$ and $\mathbf{B}$, however, are each defined in a spatial frame of reference, and so each will change, accordingly, with rigid body rotation. Still, $\boldsymbol{\sigma}$ and $\mathbf{B}$ are perfectly work-conjugate with each other, which permits a constitutive relation to be formed using this stress - strain pair if we choose.

Consider that:

$$\boldsymbol{\sigma} = g(\mathbf{B}) \tag{5.7}$$

Specifically, it turns out, that:

$$\boldsymbol{\sigma} = \frac{1}{det\mathbf{B}^{1/2}}\left(\mathbf{B}\frac{d\phi}{d\mathbf{B}} + \frac{d\phi}{d\mathbf{B}}\mathbf{B}\right) \tag{5.8}$$

Now, say we know that for isotropy [55]: $\phi = \phi(I_B, II_B, III_B)$

where I_B, II_B, III_B are the three invariants of tensor $\mathbf{B}$. If λ_1, λ_2, λ_3 are the three eigenvalues of $\mathbf{B}$, then we know that:

$I_B = \lambda_1 + \lambda_2 + \lambda_3$

$II_B = \lambda_1\lambda_2 + \lambda_2\lambda_3 + \lambda_3\lambda_1$

$III_B = \lambda_1 * \lambda_2 * \lambda_3$

We can also define the invariants in a different way, *viz.*:

$I_B = tr\mathbf{B}$

$II_B = \frac{1}{2}\left[(tr\mathbf{B})^2 - tr(\mathbf{B^2})\right]$

$III_B = det\mathbf{B} = \frac{1}{3}\left[tr(\mathbf{B}^3) - \frac{3}{2}tr(\mathbf{B})tr(\mathbf{B}^2) + \frac{1}{2}(tr\mathbf{B})^3\right]$

Now, from the chain rule (multivariable):

$$\longrightarrow \frac{d\phi}{d\mathbf{B}} = \frac{\partial\phi}{\partial I_B}\frac{dI_B}{d\mathbf{B}} + \frac{\partial\phi}{\partial II_B}\frac{dII_B}{d\mathbf{B}} + \frac{\partial\phi}{\partial III_B}\frac{dIII_B}{d\mathbf{B}} \tag{5.9}$$

We need to determine $\frac{dI_B}{d\mathbf{B}}$, $\frac{dII_B}{d\mathbf{B}}$, and $\frac{dIII_B}{d\mathbf{B}}$:

Appendix D.1 contain the complete derivations of $\frac{dI_B}{d\mathbf{B}}$, $\frac{dII_B}{d\mathbf{B}}$, and $\frac{dIII_B}{d\mathbf{B}}$.

$$\frac{dI_B}{d\mathbf{B}} = \mathbf{I} \tag{5.10}$$

$$\frac{dII_B}{d\mathbf{B}} = I_B\mathbf{I} - \mathbf{B} \tag{5.11}$$

$$\frac{dIII_B}{d\mathbf{B}} = \mathbf{B}^2 - I_B\mathbf{B} + II_B\mathbf{I} \tag{5.12}$$

Eq. (5.10), Eq. (5.11), Eq. (5.12) $\longrightarrow$ Eq. (5.9)

$$\longrightarrow \frac{d\phi}{d\mathbf{B}} = \frac{\partial\phi}{\partial I_B}\mathbf{I} + \frac{\partial\phi}{\partial II_B}(I_B\mathbf{I} - \mathbf{B}) + \frac{\partial\phi}{\partial III_B}(\mathbf{B}^2 - I_B\mathbf{B} + II_B\mathbf{I}) \tag{5.13}$$

Recall $\boldsymbol{\sigma} = \frac{1}{det\mathbf{B}^{1/2}}(\mathbf{B}\frac{d\phi}{d\mathbf{B}} + \frac{d\phi}{d\mathbf{B}}\mathbf{B})$

We can substitute and go through the algebra. We would also have to make use of the Cayley-Hamilton Theorem.

i.e.

$$\mathbf{B}^3 - I_B\mathbf{B}^2 + II_B\mathbf{B} - III_B\mathbf{I} = 0 \tag{5.14}$$

What we would get, is:

$$\boldsymbol{\sigma} = \frac{2}{det\mathbf{B}^{1/2}}[(III_B\frac{\partial\phi}{\partial III_B} + \frac{\partial\phi}{\partial II_B}II_B)\mathbf{I} + (\frac{\partial\phi}{\partial I_B})\mathbf{B} - (III_B\frac{\partial\phi}{\partial II_B})\mathbf{B}^{-1}] \tag{5.15}$$

Sometimes in other literature (see [3] [34] [32]) II_B is taken as $\frac{1}{2}[tr(\mathbf{B^2}) - (tr\mathbf{B})^2]$ instead of $\frac{1}{2}[(tr\mathbf{B})^2 - tr(\mathbf{B^2})]$. If this is the case, then the last term in eq. (5.15) would be added instead of subtracted, the Cayley-Hamilton Theorem would become $\mathbf{B}^3 - I_B\mathbf{B}^2 - II_B\mathbf{B} - III_B\mathbf{I} = 0$ instead of $\mathbf{B}^3 - I_B\mathbf{B}^2 + II_B\mathbf{B} - III_B\mathbf{I} = 0$, and any strain energy functions that are a function of II_B would also need to be modified accordingly.

Incompressibility:

$det\mathbf{F} = 1(III_B = 1)$; $\phi = \phi(I_B, II_B)$

$$\boldsymbol{\sigma} = -\rho_0\mathbf{I} + 2\underbrace{\left[\frac{\partial\phi}{\partial II_B}II_B\mathbf{I} + \frac{\partial\phi}{\partial I_B}\mathbf{B} - \frac{\partial\phi}{\partial II_B}\mathbf{B}^{-1}\right]}_{\text{stress for given deformation}} \tag{5.16}$$

The underbraced expression is what you would set as the stress for a <u>given</u> deformation. But we can always superimpose an arbitrary pressure (e.x. hydrostatic) to the body without causing deformation. Thus, the basic constitutive expression doesn't uniquely specify stress ∴ we introduce ρ_0 - TBD by boundary conditions.

Note, however, that in eq. (5.16), the first term in the square brackets influences all σ_{ii} (diagonal) terms equally just as ρ_0 does. Thus, this first term can be thought of as another pressure, and can, accordingly, be lumped together with ρ_0.

So,

$$\boldsymbol{\sigma} = -\rho_0 \mathbf{I} + 2 \left[(\frac{\partial \phi}{\partial I_B}) \mathbf{B} - (\frac{\partial \phi}{\partial II_B}) \mathbf{B}^{-1} \right] \tag{5.17}$$

We can limit further discussion to phenomenological models only, for now. The simplest such model is the Blatz-Ko model. Blatz-Ko Foam [7], for example, requires the determination of a single material constant. A somewhat more complex model is the Mooney-Rivlin model [39] [47], which contains two material constants. The Ogden model [45] contains an arbitrarily large number of constants, though the Mooney-Rivlin model can be obtained from the Ogden model when only two constants are desired. A classic Blatz-Ko model and a classic Mooney-Rivlin model are described in detail in Appendix D.2 and Appendix D.3. *MAT_SIMPLIFIED_RUBBER_WITH_DAMAGE is based on the Ogden model but is "tabulated" and so will be presented in its own section, following the discussion of the more traditional Ogden model.

The Mooney-Rivlin examples in Appendix D.3 are shown in order to illustrate the complexity involved in obtaining unique material constants from multiple material experiments. While the Ogden model is not necessarily "better" than the Mooney-Rivlin model, as both are used extensively in practice, the advantage of the Ogden formulation that is used by *MAT_SIMPLIFIED_RUBBER_WITH_DAMAGE is that material "constants" do not need to be determined. *MAT_

SIMPLIFIED_RUBBER_WITH_DAMAGE is characterized from "tabulated" uniaxial data, automatically. Characterizing a material from uniaxial data alone is nothing new. In practice, uniaxial data is often used by itself and all material constants are determined based solely on uniaxial data. *MAT_SIMPLIFIED_RUBBER _WITH_DAMAGE is quite unique, however, in its ability to function as a "tabulated" model. *MAT_SIMPLIFIED_RUBBER_WITH_DAMAGE is based on the Ogden model, so the next section will describe the Ogden model, in its traditional form.

5.2.1   Ogden Rubber

The Ogden strain energy function is often written in terms of principal stretches, rather than the Right or Left C-G Deformation Tensor. These "principal stretches," λ, are the eigenvalues of the Right or Left Stretch Tensor, which come from Polar Decomposition:

$$\mathbf{F} = \mathbf{V} \cdot \mathbf{R} = \mathbf{R} \cdot \mathbf{U} \tag{5.18}$$

$\mathbf{U}$ and $\mathbf{V}$ are called the Right Stretch Tensor and Left Stretch Tensor due to their respective positions (relative to $\mathbf{R}$) in eq. (5.18).

$\mathbf{V} = \mathbf{V}^T$ (symmetric)
$\mathbf{U} = \mathbf{U}^T$ (symmetric)
$\mathbf{R}^T = \mathbf{R}^{-1}$ (orthogonal)

$$\mathbf{C} = \mathbf{F}^T \cdot \mathbf{F} = \mathbf{U} \cdot \underbrace{\mathbf{R}^T \cdot \mathbf{R}}_{\mathbf{I}} \cdot \mathbf{U} = \mathbf{U}^2 \tag{5.19}$$

$$\mathbf{B} = \mathbf{V}^2 \tag{5.20}$$

The Left Stretch Tensor, $\mathbf{V}$, in principal stress space:

$$[\mathbf{V}]_{\mathbf{n}} = [\mathbf{\Phi}]^T[\mathbf{V}][\mathbf{\Phi}]$$

$$\text{where } [\mathbf{\Phi}] = [\mathbf{\Phi}]_{\mathbf{V}} = \begin{bmatrix} (n_1)_{\lambda_1} & (n_1)_{\lambda_2} & (n_1)_{\lambda_3} \\ (n_2)_{\lambda_1} & (n_2)_{\lambda_2} & (n_2)_{\lambda_3} \\ (n_3)_{\lambda_1} & (n_3)_{\lambda_2} & (n_3)_{\lambda_3} \end{bmatrix}$$

$$[\mathbf{\Phi}]^T[\mathbf{V}][\mathbf{\Phi}] = \begin{bmatrix} \lambda_1 & 0 & 0 \\ 0 & \lambda_2 & 0 \\ 0 & 0 & \lambda_3 \end{bmatrix}$$

The following general result can be shown:

$$\mathbf{\Phi}^T\boldsymbol{\sigma}\mathbf{\Phi} = \frac{2}{\lambda_1\lambda_2\lambda_3}\mathbf{\Phi}^T \cdot \mathbf{V} \cdot \mathbf{\Phi}\frac{\partial\phi}{\partial\mathbf{\Phi}^T \cdot \mathbf{V}^2 \cdot \mathbf{\Phi}}\mathbf{\Phi}^T \cdot \mathbf{V} \cdot \mathbf{\Phi} \tag{5.21}$$

By making several useful observations - namely:

$$\frac{\partial\phi}{\partial\boldsymbol{\lambda}} = \frac{\partial\phi}{\partial f(\boldsymbol{\lambda})}\frac{\partial f(\boldsymbol{\lambda})}{\partial\boldsymbol{\lambda}} \rightarrow \frac{\partial\phi}{\partial f(\boldsymbol{\lambda})} = \frac{1}{\frac{\partial f(\boldsymbol{\lambda})}{\partial\boldsymbol{\lambda}}}\frac{\partial\phi}{\partial\boldsymbol{\lambda}}$$

$$\frac{\partial f(\boldsymbol{\lambda})}{\partial\boldsymbol{\lambda}} = \frac{\partial\boldsymbol{\lambda}^2}{\partial\boldsymbol{\lambda}} = 2\boldsymbol{\lambda}$$

$$\frac{\partial\phi}{\partial\boldsymbol{\lambda}} = \frac{\partial\phi}{\partial\boldsymbol{\lambda}}\mathbf{I} = \frac{\partial\phi}{\partial\lambda_{ii}}\delta_{ij}\mathbf{e_i}\mathbf{e_j}$$

$$\boldsymbol{\lambda} \cdot \boldsymbol{\lambda} = \lambda^2\mathbf{I} = \lambda_{ii}^2\delta_{ij}\mathbf{e_i}\mathbf{e_j}$$

Eq. (5.21) becomes

$$\sigma_i = \frac{2}{\lambda_1\lambda_2\lambda_3}\lambda_i^2\left(\frac{1}{2\lambda_i}\frac{\partial\phi}{\partial\lambda_i}\right) = \frac{1}{\lambda_j\lambda_k}\frac{\partial\phi}{\partial\lambda_i} \tag{5.22}$$

Eq. (5.22) is a general hyperelastic constitutive relation that relates principal Cauchy stress to principal stretch. This relation is equivalent to eq. (5.15), but in principal stress space. In eq. (5.22), i, j, k are used as subscripts to indicate eigenvalues 1, 2, 3 of the Left Stretch Tensor, where j and k are the directions perpendicular to i.

The strain energy density function for an Ogden material [45], is given by

$$\phi = \sum_{n=1}^{3}\sum_{s=1}^{m}\frac{\mu_s}{\alpha_s}(\lambda_n^{*\alpha_s}-1)+K(III_{\mathbf{V}}-1-\ln III_{\mathbf{V}}) \tag{5.23}$$

In eq. (5.23), μ_s and α_s are material constants.

$\lambda_n^* = \lambda_n * III_{\mathbf{V}}^{-1/3}$ and $III_{\mathbf{V}} = \lambda_1\lambda_2\lambda_3$

Eq. (5.23) is valid for nearly incompressible materials.

Since $\sigma_i = \frac{1}{\lambda_j\lambda_k}\frac{\partial\phi}{\partial\lambda_i}$, we need to find $\frac{\partial\phi}{\partial\lambda_i}$ for the Ogden model.

We note the following:

$$\frac{\partial\left(\sum_{n=1}^{3}\frac{\mu_s}{\alpha_s}\lambda_n^{*\alpha_s}\right)}{\partial\lambda_i} = \frac{\partial\left(\sum_{n=1}^{3}\frac{\mu_s}{\alpha_s}\lambda_n^{\alpha_s}III_{\mathbf{V}}^{-\frac{\alpha_s}{3}}\right)}{\partial\lambda_i} = \overbrace{\frac{\mu_s\alpha_s\lambda_i^{\alpha_s-1}}{\alpha_s}III_{\mathbf{V}}^{-\frac{\alpha_s}{3}}}^{\text{only one term since }\frac{\partial\lambda_n^{\alpha_s}}{\partial\lambda_i}=\delta_{in}}$$

$$+\overbrace{\sum_{n=1}^{3}\frac{\mu_s\lambda_n^{\alpha_s}}{\alpha_s}(-\frac{\alpha_s}{3})III_{\mathbf{V}}^{(-\frac{1}{3}\alpha_s-1)}\lambda_j\lambda_k}^{\text{3 terms since nonzero for all values of n}}$$

$$= \mu_s\frac{\lambda_i^{\alpha_s}}{\lambda_i}III_{\mathbf{V}}^{-\frac{\alpha_s}{3}} - \sum_{n=1}^{3}\mu_s\frac{\lambda_n^{\alpha_s}}{3}III_{\mathbf{V}}^{(-\frac{1}{3}\alpha_s-1)}\lambda_j\lambda_k$$

$$\frac{\partial(\sum_{n=1}^{3}\frac{\mu_s}{\alpha_s}\lambda_n^{*\alpha_s})}{\partial\lambda_i} = \mu_s\frac{\lambda_i^{*\alpha_s}}{\lambda_i} - \sum_{n=1}^{3}\mu_s\frac{\lambda_n^{*\alpha_s}}{3}III_{\mathbf{V}}^{-1}\lambda_j\lambda_k \tag{5.24}$$

We further note that:

$$\frac{\partial K(III_{\mathbf{V}}-\ln III_{\mathbf{V}})}{\partial\lambda_i} = K\left(\frac{\partial III_{\mathbf{V}}}{\partial\lambda_i} - \frac{\partial\ln III_{\mathbf{V}}}{\partial\lambda_i}\right) = K\left(\lambda_j\lambda_k - \frac{1}{III_{\mathbf{V}}}\lambda_j\lambda_k\right)$$

$$\frac{\partial K(III_{\mathbf{V}}-\ln III_{\mathbf{V}})}{\partial\lambda_i} = K\lambda_j\lambda_k\frac{(III_{\mathbf{V}}-1)}{III_{\mathbf{V}}} \tag{5.25}$$

eq. (5.24) and eq. (5.25) $\longrightarrow$ eq. (5.22), where ϕ is given by the Ogden formula (eq. (5.23)), yields the following result:

$$\sigma_i = \sum_{s=1}^{m}\frac{\mu_s}{III_{\mathbf{V}}}\left[\lambda_i^{*\alpha_s} - \sum_{n=1}^{3}\frac{\lambda_n^{*\alpha_s}}{3}\right] + K\frac{III_{\mathbf{V}}-1}{III_{\mathbf{V}}} \tag{5.26}$$

Eq. (5.26) is the traditional constitutive relation for Ogden hyperelasticity, in terms of principal stretches and principal Cauchy stress. *MAT_183, also known as *MAT_SIMPLIFIED_RUBBER_WITH_DAMAGE uses a "tabulated" version of the Ogden model, as will be discussed in the next section.

5.3   *MAT_183

*MAT_183, also known as *MAT_SIMPLIFIED_RUBBER_WITH_DAMAGE is an LS-DYNA material model developed by Stefan Kolling of Daimler AG, in collaboration with P.A. Du Bois of LSTC and David Benson of UCSD [28]. It is based on Ogden hyperelasticity, but can fit uniaxial experimental data exactly. Whereas the traditional Ogden model contains experimental constants that must be found from experimental data (axial data is the most common), *MAT_SIMPLIFIED_RUBBER_WITH_DAMAGE uses uniaxial data directly, in its tabulated form - namely, engineering stress, σ_0, vs. engineering strain, $\lambda_i - 1$. Thus, *MAT_SIMPLIFIED_RUBBER_WITH_DAMAGE is similar to the existing programmer model, *MAT_LOW_DENSITY_FOAM, in that it is a "tabulated" model.

The other material models that have been presented so far, such as the Blatz-Ko model and the traditional Ogden model, were developed for relatively soft elastomers at relatively large strains. Soft elastomers at large strains typically display an increasing tangent modulus in compression, whereas the "wall programmer" displays a decreasing tangent stiffness, as shown in Fig. 5.4. Fig. 5.4 depicts the loading portion of a displacement-controlled compression test on a 2in. cube of "wall programmer" that was loaded at a rate of .394in (10mm) per second.

It is worthwhile to note that this test was not uniaxial ("pure" compression), since barreling is clearly present. The uniaxial data can be easily back-calculated by applying a "shape factor" to the test data [17], and the resulting uniaxial engineering stress vs. engineering strain is essentially what is shown in Fig. 5.4. This stress-strain data will be validated in the next few sections.

While the Blatz-Ko model and the traditional Ogden model can be characterized very well using uniaxial data since they do not depend on higher order invariants, these models, as well as the Mooney-Rivlin model, are all incapable of providing a suitable "fit" to the data shown in Fig. 5.4, due to the decreasing tangent stiffness - a phenomenon sometimes referred to as "small-strain softening" [6]. A uniaxial "tabulated" approach, like the one that is used in *MAT_SIMPLIFIED_RUBBER_WITH_DAMAGE can fit uniaxial experimental data exactly, and so the small strain softening behavior exhibited by the "wall programmer" is not an issue at all when using *MAT_SIMPLIFIED_RUBBER_WITH_DAMAGE.
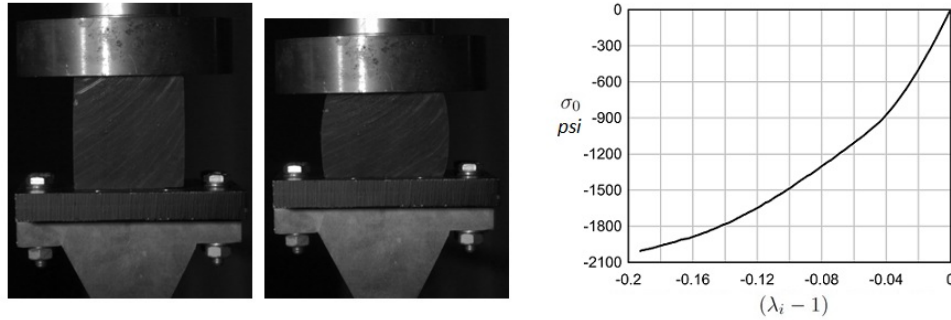
Figure 5.4: Compression test on "wall programmer" cube

*MAT_SIMPLIFIED_RUBBER_WITH_DAMAGE is based on Ogden hyperelasticity - eq. (5.26). The following derivation of the hyperelastic component of *MAT_SIMPLIFIED_RUBBER_WITH_DAMAGE is adapted from *A tabulated formulation of hyperelasticity with rate effects and damage* [28].

Let's define a function:

$$f_0(\lambda) = \sum_{s=1}^{m} \mu_s \lambda^{*\alpha_s} \tag{5.27}$$

eq. (5.27) $\longrightarrow$ eq. (5.26) yields:

$$\sigma_i = \frac{1}{III_{\mathbf{V}}} \left(f_0(\lambda_i) - \frac{1}{3} \sum_{n=1}^{3} f_0(\lambda_n) \right) + K \frac{III_{\mathbf{V}} - 1}{III_{\mathbf{V}}} \tag{5.28}$$

Recall from the first Mooney-Rivlin example, that for an incompressible material under uniaxial test conditions, $\lambda_j^* \approx \lambda_k^* \approx \lambda_i^{*-1/2}$ $(\lambda_j \approx \lambda_k \approx \lambda_i^{-1/2})$, where the subscripts j and k refer to the two coordinate directions perpendicular to i, just as before.

The engineering stress, which would be commonly retrieved from a uniaxial test, is the nominal stress for a hyperelastic material:

$$\boldsymbol{\sigma}^0 = III_{\mathbf{V}} \mathbf{F}^{-1} \cdot \boldsymbol{\sigma} \tag{5.29}$$

eq. (5.29) then yields:

$$\boldsymbol{\sigma}^0 = \lambda_i \lambda_j \lambda_k \begin{bmatrix} \frac{1}{\lambda_i} & 0 & 0 \\ 0 & \lambda_i^{1/2} & 0 \\ 0 & 0 & \lambda_i^{1/2} \end{bmatrix} \cdot \begin{bmatrix} \sigma_{11} & 0 & 0 \\ 0 & 0 & 0 \\ 0 & 0 & 0 \end{bmatrix}$$

$$\longrightarrow \sigma_{11}^0 = \lambda_j \lambda_k \sigma_{11}$$

Eq. (5.28), for uniaxial load under the Ogden model, will be expressed as $\sigma_1 = \sigma_{11} = \text{``}\sigma(\lambda_i)\text{''}$. So, $\sigma(\lambda_i)$ is a particular value of longitudinal Cauchy stress under uniaxial loading, using the Ogden model, which corresponds to a particular value of the longitudinal stretch, λ_i.

We'll introduce a new variable, ϵ_{0i}, which is the engineering strain in a uniaxial test - *i.e.* $\epsilon_{0i} = \lambda_i - 1$ for a hyperelastic material if λ_i is some longitudinal stretch that occurred during the uniaxial test. Presumably, we have an experimental curve of uniaxial engineering stress, which we will from now on call σ_0, as a function of the longitudinal engineering strain $\big(i.e.\ \sigma_0(\epsilon_{0i})\big)$.

With our new notation: $\sigma_{11}^0 = \sigma_0(\epsilon_{0i}) = \sigma_0(\lambda_i - 1) = \lambda_j \lambda_k \sigma(\lambda_i)$

Noting that $\frac{1}{3} \sum_{n=1}^3 f_0(\lambda_n) = \frac{1}{3} \left[\sum_{s=1}^m \mu_s \lambda_i^{*\alpha_s} + 2 \sum_{s=1}^m \mu_s \lambda_i^{-\frac{\alpha_s}{2}} \right]$,

we get $\rightarrow \sigma_0(\lambda_i - 1) = \lambda_i \lambda_k \sigma(\lambda_i) = \frac{\lambda_k \lambda_j}{III_\mathbf{v}} \left(\frac{2}{3} f_0(\lambda_i) - \frac{2}{3} f_0(\lambda_i^{-1/2}) + K \frac{III_\mathbf{v}-1}{III_\mathbf{v}} III_\mathbf{v} \right)$

$= \frac{1}{\lambda_i} \left(\frac{2}{3} f_0(\lambda_i) - \frac{2}{3} f_0(\lambda_i^{-1/2}) - pIII_\mathbf{v} \right)$

$$\lambda_i \sigma_0(\lambda_i - 1) + p = \frac{2}{3} f_0(\lambda_i) - \frac{2}{3} f_0(\lambda_i^{-1/2}) \tag{5.30}$$

$III_\mathbf{v}$ was eliminated from eq. (5.30) since we are going to limit our discussion to nearly incompressible materials only.

Note that "p" is really a hydrostatic term since it depends on a value of "K" that is very large for our nearly incompressible material. Simply striking the term would not stay true to the Ogden function and could cause undesirable behavior. However, we can eliminate the term through consideration of boundary conditions.

For uniaxial stress, $\sigma(\lambda_j) = \sigma(\lambda_k) = 0$.

Eq. (5.28) yields:

$0 = \frac{1}{3} f_0(\lambda_i^{-1/2}) - \frac{1}{3} f_0(\lambda_i) + \underbrace{K \frac{III_\mathbf{v} - 1}{III_\mathbf{v}}}_{p}$

$$p = \frac{1}{3} f_0(\lambda_i) - \frac{1}{3} f_0(\lambda_i^{-1/2}) \tag{5.31}$$

Eq. (5.31) $\longrightarrow$ eq. (5.30) yields:

$$\lambda_i \sigma_0(\lambda_i - 1) = f_0(\lambda_i) - f_0(\lambda_i^{-1/2}) \tag{5.32}$$

We can substitute consecutive values of the principal stretch into eq. (5.32).

i.e.

$\lambda_i^{-1/2} \sigma_0(\lambda_i^{-1/2} - 1) = f_0(\lambda_i^{-1/2}) - f_0(\lambda_i^{1/4})$

$\lambda_i^{1/4} \sigma_0(\lambda_i^{1/4} - 1) = f_0(\lambda_i^{1/4}) - f_0(\lambda_i^{-1/8})$

.

.

etc.

In general,

$$\lambda_i^{(-1/2)^{r-1}} \sigma_0 \left(\lambda_i^{(-1/2)^{r-1}} - 1 \right) = f_0 \left(\lambda_i^{(-1/2)^{r-1}} \right) - f_0 \left(\lambda_i^{(-1/2)^r} \right) \tag{5.33}$$

Since $\lim_{r \to \infty} f_0 \left(\lambda_i^{(-1/2)^r} \right) = f_0(1)$, where $f_0(1) = \sum_{s=1}^m \mu_s$

We get: $\sum_{r=1}^{\infty} \lambda_i^{(-1/2)^{r-1}} \sigma_0 \left(\lambda_i^{(-1/2)^{r-1}} - 1 \right) = f_0(\lambda_i) - f_0(1)$,
where all terms on the right hand side cancel, except for the first and last.

So, $f_0(\lambda_i) = f_0(1) + \lambda_i \sigma_0 (\lambda_i - 1) + \lambda_i^{-1/2} \sigma_0 (\lambda_i^{-1/2} - 1) + \lambda_i^{1/4} \sigma_0 (\lambda_i^{1/4} - 1) + \ldots$

Writing this as concisely as possible:

$$f_0(\lambda_i) = f(1) + \sum_{r=0}^{\infty} \lambda_i^{(-1/2)^r} \sigma_0 \left(\lambda_i^{(-1/2)^r} - 1 \right) \tag{5.34}$$

We can now substitute eq. (5.34) into eq. (5.28). Since $f(1)$ is a constant, we can see that it doesn't affect the stress, σ_i, since $f(1) - 1/3 \sum_{n=1}^3 f(1) = 0$.

To complete our discussion, $f_0(\lambda_i)$ and σ_0 will be written a final time, in their final form:

$$f_0(\lambda_i) = \sum_{r=0}^{\infty} \lambda_i^{(-1/2)^r} \sigma_0 \left(\lambda_i^{(-1/2)^r} - 1 \right) \tag{5.35}$$

$$\sigma_i = \frac{1}{III_{\mathbf{V}}}\left(f_0(\lambda_i) - \frac{1}{3}\sum_{n=1}^{3}f_0(\lambda_n)\right) + K\frac{III_{\mathbf{V}} - 1}{III_{\mathbf{V}}} \qquad (5.36)$$

The series expressed above (eq. (5.35)), which calculates a single value of $f_0(\lambda_i)$ from the uniaxial data by summing (over "r") to ∞, is terminated once a reasonable tolerance is met. At the beginning of the LS-DYNA simulation, a sufficient number of $f_0(\lambda_i)$ values are calculated, where each value is calculated from eq. (5.35) and corresponds to a particular value of λ_i. These values of $f_0(\lambda_i)$ are obtained solely from tabulated uniaxial experimental engineering stress *vs.* engineering strain.

As the simulation runs and the material is loaded, the principal stretches are determined and the principal Cauchy stresses are calculated using eq. (5.36), where "i" in eq. (5.36) refers to the eigenvalue 1, 2, or 3 of the Cauchy stress tensor and stretch tensor. Obtaining the Cauchy stress, $\boldsymbol{\sigma}$, from its eigenvalues and eigenvectors involves just a single transformation.

One can consider that this "tabulated" method is possible because of a number of particular characteristics in the original Ogden model (eq. (5.26)). The introduction of $f_0(\lambda_i)$, which eliminates the material constants from the Ogden model (*i.e.* eq. (5.28)) was important, but it was the step from eq. (5.33) to eq. (5.34) that enables this "tabulated" method to work as desired. The particular pattern that was recognized by the aforementioned researchers that developed this "tabulated" method [28], which is expressed in eq. (5.33), along with the observation that summing the right-hand-side of eq. (5.33) cancels most of the terms, were really the key insights to isolate the $f_0(\lambda_i)$ term.

While the method presented, which is referred to as a "tabulated" method, will fit any uniaxial hyperelastic curve, exactly, it also needs to have the capability of handling viscoelastic effects. *MAT_SIMPLIFIED_RUBBER_WITH_DAMAGE does not contain physical viscoelasticity. To handle rate effects, *MAT _SIMPLIFIED_RUBBER_WITH_DAMAGE permits the user to tabulate a <u>single uniaxial unloading curve</u>, as well as a <u>table of uniaxial loading curves</u> that each

correspond to a particular strain rate. Since the total loading depends on strain and strain rate, the unloading relies on a "damage" function.

As described in *A tabulated formulation of hyperelasticity with rate effects and damage* [28], the "damage" function is nonzero once unloading begins. This damage function, d, is some fraction of the "maximum deformation energy," W_{max}, that was attained during the loading history:

$$d = d \left(\frac{W}{W_{max}} \right) \tag{5.37}$$

This damage function is then applied to the deviatoric part only:

$$\sigma_i = (1 - d)(\sigma_i + p) - p \tag{5.38}$$

In eq. (5.38), the stress "σ_i" includes two terms, namely, the spherical part of the stress, p, and the deviatoric part, σ_i'. We recall that this value of p is equal to $K \frac{III_{\mathbf{V}} - 1}{III_{\mathbf{V}}}$.

The left-hand-side of eq. (5.38) is the updated stress. In order to see that the "d" term is applied only to the deviatoric part of the stress, the expression on the right-hand-side can be expanded and a substitution can be made to replace all "σ_i" with $\sigma_i' + p$.

These rate effects are illustrated, pictorially, in Fig. 5.5.

This phenomenological treatment of viscoelastic effects using a purely hyperelastic function to capture loading behavior and a damage function to capture unloading is not a new idea. This was, in fact, studied by Ogden and Roxburgh in 1999 [46]. The true elastic behavior would be the "relaxed equilibrium response," and any viscoelastic model would cause the loading and unloading to diverge from this equilibrium when the material is subjected to realistic loads at finite strain rates. Since *MAT_SIMPLIFIED_RUBBER_WITH_DAMAGE as well as [46] treat the loading and unloading without consideration of viscoelasticity in a physical
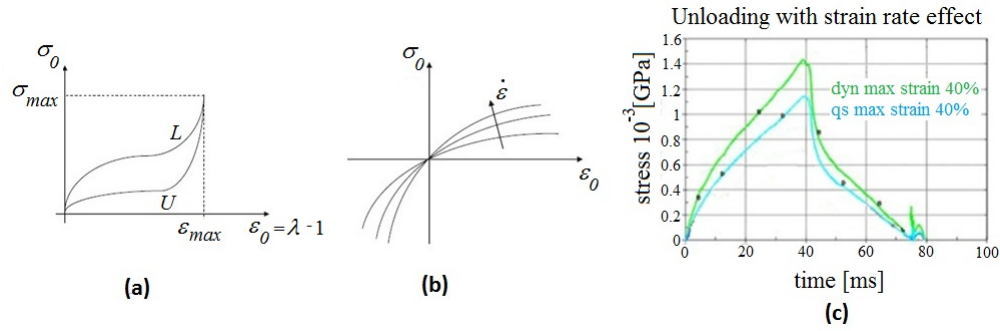
Figure 5.5: *MAT_SIMPLIFIED_RUBBER_WITH_DAMAGE treatment of viscoelastic effects [28]

sense, Ogden and Roxburgh called this formulation "pseudo-elasticity." This is a phrase apparently first coined by Y.C. Fung [16].

The Ogden and Roxburgh paper, however, is not capable of fitting any arbitrary data. They considered only soft rubbers at large strains, and focused in particular on Mullins effect. The programmer is pre-conditioned for the strains expected in Blast Simulator tests, so Mullins effect is not expected. The feature of the programmer material that is so unusual is its decreasing tangent modulus in compression - "small strain softening" [6]. The ability for *MAT_SIMPLIFIED _RUBBER_WITH_DAMAGE to fit uniaxial curves of *any* shape, and retain Ogden hyperelasticity, is essential for programmer modeling.

Fig. 5.5c depicts the axial response of the material from actual simulations. In particular, in Fig. 5.5c, we can see how the unloading response changes depending on strain rate. While *MAT_SIMPLIFIED_RUBBER_WITH_DAMAGE is computationally efficient as well as easy to calibrate from basic uniaxial experimental data, its treatment of viscoelasticity is "simple," and the unloading depicted in Fig. 5.5c may contain significant error at strain rates far removed from the baseline tabulated unloading curve. Indeed, the benefit of using a model that handles viscoelasticity in a physical sense is that the loading and unloading will naturally diverge more from the hyperelastic equilibrium response under higher strain rates as well as reduce to a single hyperelastic equilibrium curve under infinitesimally slow strain rate. Such a model is more likely to remain accurate under

a wide range of strain rates, though this accuracy will depend on the complexity of the viscoelastic treatment within the model.

In general, if the baseline curves (Fig. 5.5a) for the *MAT_SIMPLIFIED _RUBBER_WITH_DAMAGE model are calibrated from a test conducted at a low strain rate and this results in a model that contains unacceptable error at high strain rates, then several options are possible. The baseline could be re-calibrated at some in-between strain rate, although this may not completely resolve the issue. Alternatively, multiple versions of *MAT_SIMPLIFIED_RUBBER_WITH _DAMAGE could be developed that each correspond to different ranges of strain rates. This would be less ideal, and consideration would need to be given to replacing the *MAT_SIMPLIFIED_RUBBER_WITH_DAMAGE model with something more advanced.

While rate effects, in particular on the unloading response, are handled in a simplified way, we can see from Fig. 5.5 that viscoelastic-type behavior is considered in a phenomenological sense. In particular, the unloading in Fig. 5.5a is an essential part of the actual material response as well as the response in the material model. Drop Tower testing provides a means of directly measuring both the loading and unloading response of the programmer under impact loads similar to the kinds of loads that the programmer experiences in the Blast Simulator. The next two sections will discuss the different materials tests that were conducted on the "wall programmer," and will discuss in more detail the manner in which *MAT_SIMPLIFIED_RUBBER_WITH_DAMAGE was characterized from the test data for the purpose of modeling Blast Simulator impacts on walls.

5.4   Programmer material testing

Material models that involve viscoelasticity in a physical sense, are often characterized by performing several different kinds of axial tests. Two kinds of tests, which are common in materials testing, are the Split-Hopkinson Bar (SHPB) Test and the Dynamic Mechanical Analysis (DMA) test. Detailed investigations of

the mechanical properties of polycarbonate and Teflon (PTFE) using SHPB and DMA testing were done by Walley [63], and later by Siviour [56] and Jordan [27], to include, *inter alia*, temperature effects. For our application, temperature effects do not need to be considered due to the relatively constant ambient temperature of the Blast Simulator. Various polyurea and polyurethane materials were tested in a similar manner by Sarva [53] and Yi [66]. Limited dynamic testing has been done for Adiprene L-100, but some SHBP data for this material was obtained by Gray [18]. Unfortunately, the material models that are capable of taking full advantage of SHPB and DMA tests are computationally expensive and absent from the built-in material libraries of commercial FEM codes (a library of user-defined material models can be found in Bergstrom [6]). In addition, SHPB tests are not always effective in providing good data for rubbery materials, especially at relatively low strain rates like the rates that the programmer experiences in the Blast Simulator [58] [18]. Instead, we will consider a particular rubber model that is contained in the LS-DYNA material library, and characterize the model through Drop Tower impact testing.

Drop Tower impact tests provide a lot of information without the need for other kinds of material tests. Whereas the SHPB test measures the loading behavior of the material under a particular [average] strain rate, but gives no information regarding unloading, the Drop Tower impact test provides information on both the loading and the unloading. Nakai and Yokoyama [42] demonstrated that unloading data can be obtained from SHPB tests as well, but this data had the same problem as Drop Tower testing, namely, highly variable strain rate. Strain rate variation is the primary issue in data obtained from Drop Tower testing, as well as in SHPB testing where loading and unloading are measured [42]. Since loading and unloading data were needed for our programmer, the SHPB method by itself offered no advantages over Drop Tower tests. Additionally, Drop Tower tests readily provide loading and unloading data for relatively large strains, and strain rates of order $10^2/s$, while maintaining force equilibrium, which has not been demonstrated with other kinds of test procedures.

The DMA test measures the "storage modulus" and "loss modulus" in order

to determine how the loading and unloading behavior diverge from the relaxed equilibrium (elastic) response, which may not be useful without other kinds of test data, such as the data attained from SHPB testing. The Drop Tower impact test, on the other hand, provides direct loading and unloading data at a particular strain rate. This loading and unloading data is sufficient for phenomenological material models that only need to capture material response within a limited range of strains and strain rates.

The LS-DYNA built-in material model *MAT_SIMPLIFIED_RUBBER_WITH_DAMAGE is well suited for Drop Tower impact test characterization. It is a unique rubber model in that it considers a baseline set of uniaxial experimental data from which it tabulates the loading and unloading behavior. This allows the model to exactly match the baseline set of experimental drop tower test data, for example, and the model will also behave correctly under different modes of loading, since *MAT_SIMPLIFIED_RUBBER_WITH_DAMAGE is derived from the Ogden hyperelastic function [45] [28]. Where loading rates differ from the baseline, *MAT_SIMPLIFIED_RUBBER_WITH_DAMAGE determines the loading behavior by interpolating between different loading curves corresponding to different strain rates, which are supplied by the user. The unloading adjusts, accordingly, through the use of a "damage" formulation. This model does not include failure, and it can be called a "pseudo-elastic" model [16] [46], since it does not include viscoelasticity in any physical sense.

Fitting this material model to DMA data would be quite cumbersome and the model will still remain incapable of correctly capturing behavior at strain rates well below the baseline loading and unloading tabulated data - low rates at which the behavior would approach the relaxed equilibrium (elastic) response. The model may also contain significant error at strain rates much higher than the baseline data set. Thus, while *MAT_SIMPLIFIED_RUBBER_WITH_DAMAGE is computationally efficient and can provide an excellent fit to a single set of experimental data, it is limited to a relatively narrow range of strain rates.

With a particular application in mind and an associated range of strain rates, it makes sense to characterize *MAT_SIMPLIFIED_RUBBER_WITH

_DAMAGE using Drop Tower impact tests. Drop Tower tests provide direct loading and unloading data for a particular strain rate, which is not so easily attained from SHPB or DMA tests, especially for rubbery materials, where the SHPB method is known to be less effective [58] [18]. Since a baseline loading and unloading data is a requirement of *MAT_SIMPLIFIED_RUBBER_WITH_DAMAGE, Drop Tower impact tests will provide the primary data for characterizing the model. The goal is to characterize this material model only for the range of strains and strain rates observed in the "programmer" during Blast Simulator wall tests.

Three compression tests were conducted on a single 50 mm cube (2 in) at a "quasi-static" rate of loading of 10 mmps (.4 inches per second). The resulting data is shown in Fig. 5.6. This data provides insight into the general behavior of this material, namely, a decreasing tangent stiffness is observed in compression, and no damage is observed for strains under 20%. Unloading behavior at such slow strain rates is not of particular interest due to the high average strain rate observed in Blast Simulator tests, and so only the loading was recorded. This quasi-static data is also important since it approximates the relaxed equilibrium response, which is needed to characterize hyper-viscoelastic models - a possible direction of future research.

Drop tests were performed on solid disk specimens that each had a diameter of 15.70 mm (.62 in) and thickness of 10.45 mm (.41 in).

The Drop Tower test mechanism is shown in Fig. 5.7. It consists of a modified Instron 9250HV drop tower accompanied by three different measurement devices: a Phantom V12 high-speed-camera is set to record video of the dynamically deformed sample, a customized load cell is in place to measure the force from the bottom of the sample. In addition, an accelerometer is attached to the drop mass to measure force acting on the top of the sample, similar to the arrangement that is discussed in detail in Hamdan [20]. Comparison of these two forces is necessary to confirm force equilibrium in the sample.

The Instron 9250HV drop tower was modified by adding a bottom anvil that is supported by a hydraulic jack in order to support samples during compressive high-strain rate testing. The drop mass assembly consists of an adjustable weight
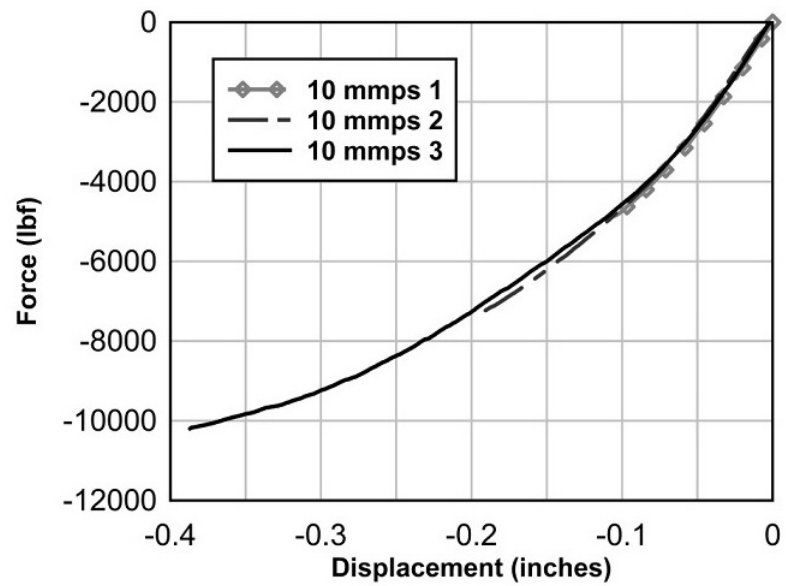
Figure 5.6: Q-S Compression tests of wall programmer cube
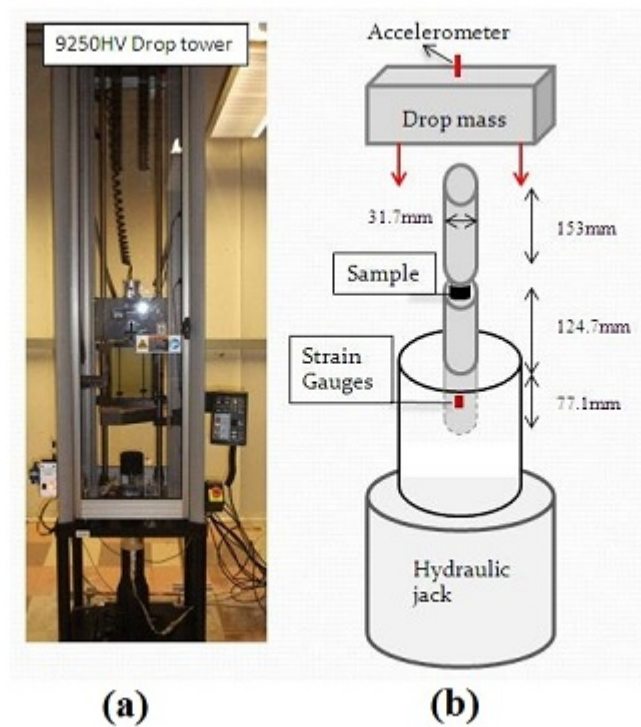
Figure 5.7: (a) UCSD Drop Tower testing apparatus (b) Schematic of Drop Tower assembly [15]

that can be raised to a specific height above the specimen, providing a designated impacting velocity and energy. Drop masses can vary from 2.7 kg to 28.9 kg and the maximum free fall height of the drop tower is 1.25 m, although higher velocities can be achieved with assistance of spring mechanisms available in the Instron 9250HV machine. Images of deformed samples are captured by a Phantom V12 high-speed camera during impact testing to provide a means of estimation of average compressive strains in the sample, along with qualitative information about the shape of the sample, particularly to ensure its uniform axial deformation. This camera can provide 6242 frames-per-second at full 1280X800 widescreen resolution. During this test series the camera was set up to capture 40000 frames-per-second at 512X256 resolution to record deformation images every 25 μs with accuracy up to 0.1 mm [15].

Our customized load cell consists of a shock resisting tool steel (S7) cylinder 31.7 mm in diameter and 77.1 mm in height that is placed beneath the sample. Two strain gauges are placed on opposite sides of this cylinder to record dynamic strains in the steel cylinder, which are converted to the stress history imparted to the tested samples. A piezoelectric accelerometer 8012 (Columbia Research Lab) is attached to the drop mass to measure the acceleration of drop mass in the vertical direction. This sensor can measure accelerations within $\pm$20,000g with calibrated sensitivity of 0.25mv/g. The range of linear frequency response is between 2 Hz to 15 kHz with maximum error of $\pm$5%. The voltage signals from the load cell and the accelerometer are amplified and recorded by a TD-2014 oscilloscope. A trigger device is used to synchronize the three measurements by sending a voltage signal to both the high-speed camera and the oscilloscope when the drop mass is about to touch the top of the steel cylinder that is placed on top of the sample [15].

The purpose of the drop tests was to determine the loading and unloading behavior of the programmer, under strains and strain rates that it experiences in practice. The resulting drop test data is shown in Fig. 5.8. The forces in Fig. 5.8a are obtained by converting signals from the strain gauges to force acting on the bottom of the sample and the displacements are obtained from video images recorded with the high speed camera. The forces applied to the top and bottom

of the sample were very close, demonstrating that force equilibrium was achieved.

It is important to note that the strain rates shown in the figure are average strain rate. Drop tests do not produce constant strain rate like the SHPB tests. In Fig. 5.8a, which depicts the reaction force *vs.* deformation throughout the impact, the strain rates shown in the legend are average strain rate during the loading portion of the impact. Fig. 5.8b shows strain rate over strain. In the test with initial impact velocity of 0.9 mps, the sample is compressed under an initial strain rate of $-70 \ s^{-1}$. The absolute value of strain rate displays monotonic decrease to zero as the engineering strain reaches .18, at which point the sample rebounds back with a strain rate of about $40 \ s^{-1}$.
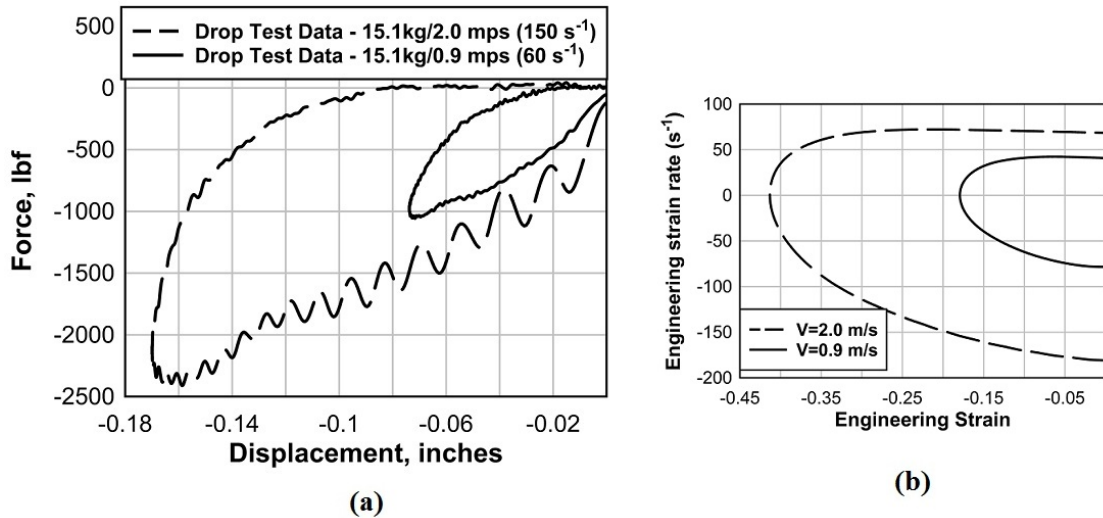
Figure 5.8: Drop testing of wall programmer disks: (a) Plots of force *vs.* deformation (b) Plots of engineering strain rate for each of the two tests

5.5   *MAT_183 programmer model

The theoretical basis for *MAT_183, also known as *MAT_SIMPLIFIED_RUBBER_WITH_DAMAGE was described earlier in this chapter, in detail. It is a nearly incompressible, phenomenological, rubber model that is characterized by tabulated uniaxial data based on Ogden hyperelasticity. The model permits the

user to input a variety of loading curves, but only a single unloading curve.

Since the tabulated experimental data should be uniaxial, a simple "shape factor" [17] is applied to the quasi-static test data and drop test data to account for the barreling effects observed in those tests. The uniaxial curves that are used as input to *MAT_SIMPLIFIED_RUBBER_WITH_DAMAGE are shown in Fig. 5.9. The shape factors corresponding to the respective curves have been applied, resulting in tabulated data that depicts approximate engineering stress *vs.* engineering strain.
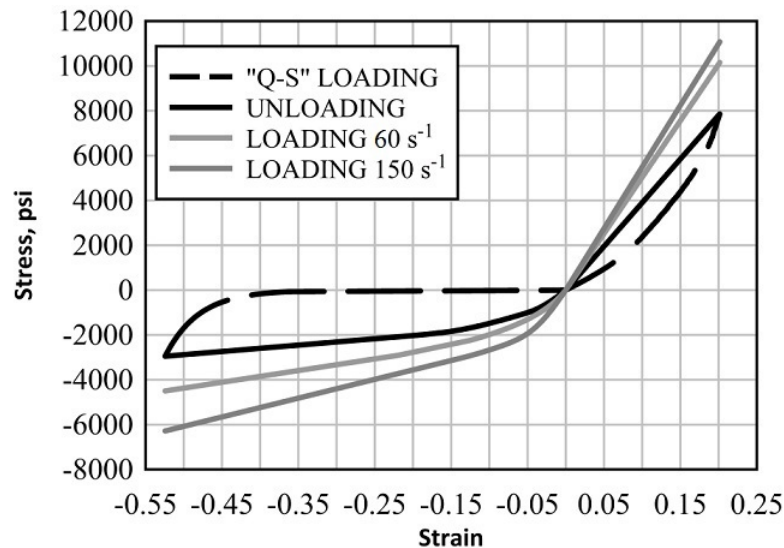
Figure 5.9: Tabulated data used for the wall programmer model

There are a several important comments to make concerning the tabulated data depicted in Fig. 5.9. First, it should be noted that drop tests, unlike Split-Hopkinson Bar Tests, do not apply a constant strain rate to the specimen, and so the strain rates of 60 s^{-1} and 150 s^{-1} shown in Fig. 5.9 were found by averaging. Secondly, the tension data shown in Fig. 5.9 is nonphysical but is required for this material model to run properly. Instabilities can also occur if strains exceed the tabulated data in either compression or tension, and so it should also be noted that the data was extrapolated 50% strain even though strains will not be expected to exceed 25% in Blast Simulator tests. Lastly, the shape of the 150 s^{-1} was slightly modified in order to better simulate the drop tower test, as will be described in

more detail later.

While the "peak" strain rate observed in low-speed Blast Simulator tests is about 2 s^{-1} and the strain rate observed in high-speed Blast Simulator tests can be as high as 200 s^{-1}, the programmer sees a strain rate of zero in every test - at the transition from compression (loading) to decompression (unloading). Thus, it makes sense for the baseline loading data to be near zero ("quasi-static") even if the programmer experiences a high average strain rate in Blast Simulator tests. The loading "baseline" data determines the starting and ending points for the *unloading* data - this is a requirement of the material model.

The unloading data, as explained previously, is the main source of error in this model, as it is purely phenomenological and is limited in its ability to "adjust" to accommodate a wide range of strains and strain rates. For this reason, the unloading shown in Fig. 5.9 does NOT correspond to the same experimental test as the quasi-static loading. Rather, the unloading shown in Fig. 5.9 was determined in an arbitrary fashion that ensures satisfactory unloading behavior for strains around 20% and strain rates around 100 s^{-1}. Validation of this model is required, as will be discussed in the next sections.

5.5.1   Fit to experimental data

Using the *MAT_SIMPLIFIED_RUBBER_WITH_DAMAGE programmer model, characterized with the tabulated data depicted in Fig. 5.9, LS-DYNA simulations were performed for the quasi-static cube test, as well as one of the drop tests. The results are shown in Fig. 5.10 and Fig. 5.11. TYPE 1 solid elements were used, and a coefficient of friction between the sample and the contact surfaces was taken as 0.6. Teflon film was used for additional Drop Tower tests that were performed on this material without any noticeable difference in the results.

The bottom reaction plate in the LS-DYNA simulations of the drop tests is assumed rigid, while in the actual experiments, the plate moved a few millimeters, in some cases. This is likely one reason that the simulations appear slightly "stiff." Due to the large strains experienced by the programmer during the 2 mps drop
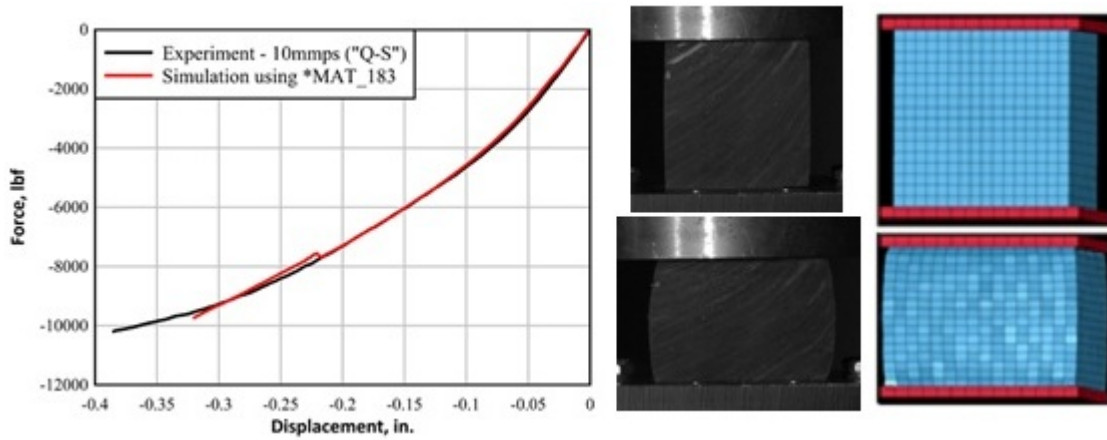
Figure 5.10: Quasi-static experiment and simulation
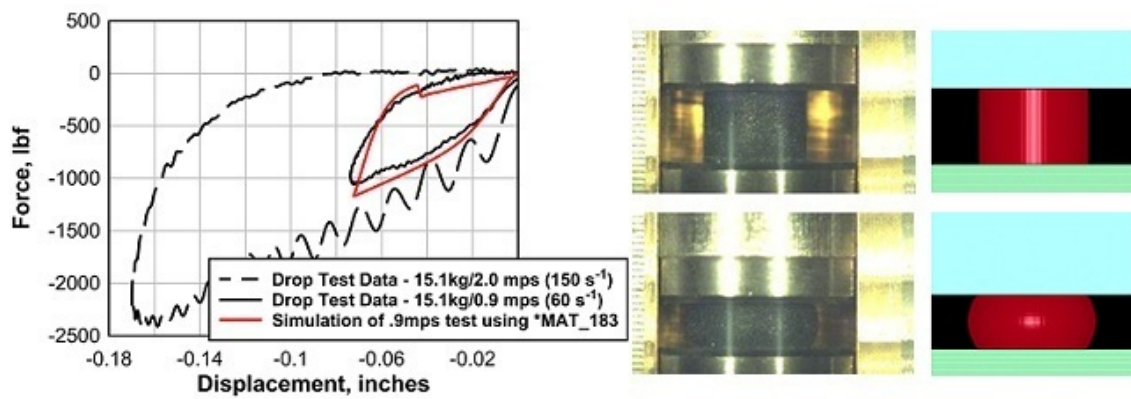
Figure 5.11: Drop-test experiments and simulations

test, the simulation would require a very fine mesh and the use of a more expensive element formulation to avoid mesh distortion. Since such strains do not occur in practice, using the Blast Simulator, a 2 mps simulation was not performed. It is important to note, however, that the 2 mps data is included in the material model (Fig. 5.9) since strain rates of 150 s^{-1}, for example, have been observed in Blast Simulator tests.

Note that within the tabulated data for the material model (Fig. 5.9), approximately the first half of the 150 s^{-1} curve was slightly increased, artificially, because the loading curve during the simulation of the drop tower test was not increasing at a fast enough rate. It turns out that the reason for this behavior during the simulation was due to the Bulk Modulus in the model having a value of 40,000 psi, while it turns out that for Adiprene L-100, a value of 150,000 psi to 380,000 psi would be more realistic. With the correct value of Bulk Modulus, no additional modification to the first half of the curve would have been needed.

Additionally, within the tabulated data for the material model (Fig. 5.9), the second half of the 150 s^{-1} curve was slightly decreased, artificially, because the peak drop tower test force in the simulation was too high. One possible reason for this behavior during the simulation is that *MAT_SIMPLIFIED_RUBBER_WITH_DAMAGE interpolates between tabulated curves, based on strain rate, but we may not have a sufficient number of curves to effectively model severe impacts. In severe impact tests, the strain quickly ramps up to a high value at the beginning of impact and should then decrease to zero at peak deformation, prior to the onset of unloading. With this material model and only three loading curves, it does not appear that the model is interpolating to the baseline (zero strain rate) curve near maximum deformation. Another reason that the drop test force may have been too large in the simulation is due to the assumption of a rigid test frame, as previously described.

It is recommended that material tests (e.x. drop tower tests) be simulated whenever possible in order to tweak the material models (e.x. *MAT_SIMPLIFIED_RUBBER_WITH_DAMAGE) as needed, prior to using the models for their intended application. Of course, even though the simulations correlate well to the

experimental data, as shown in Fig. 5.10 and Fig. 5.11, further validation on this material model, using an arbitrary geometry (*e.g.* "pyramids") is important.

5.5.2 Preliminary validation

While the kind of loading experienced by the Blast Simulator programmer is mostly compressive, the presence of the pyramids on the impact side of the programmer introduces more complex loading. The *MAT_SIMPLIFIED_RUBBER _WITH_DAMAGE programmer material model was characterized from axial experiments, with these axial tests being simulated and directly compared to the test data as one kind of preliminary means of validation. While the strain magnitudes and strain rates experienced in the Blast Simulator are generally within the range of the axial data that has been so far observed, the modes of loading experienced in the Blast Simulator will be more complex.

Since *MAT_SIMPLIFIED_RUBBER_WITH_DAMAGE is based on Ogden hyperelasticity [45], this material model is expected to perform adequately, regardless of the modes of loading. The final validation of this material model will come *via* a comparison between an actual Blast Simulator impact and a computer simulation of the Blast Simulator impact, using material model *MAT_SIMPLIFIED _RUBBER_WITH_DAMAGE with parameters found from Drop Tower tests.

Five blast-simulating tests were conducted on a tapered cylindrical steel specimen provided by the Air Force Research Laboratory (AFRL), with impact velocities ranging from approximately 15 m/s (50 feet per second) to 40 m/s (130 feet per second). The impacting mass, which was composed of an aluminum block attached to a programmer with pyramids, was pushed by the blast generator hydraulics until impact. Three tests involved the use of a single pad mounted to the block, while the final two tests included an additional pad to create a double layer configuration. The test article was loaded in the axial direction of the cylinder and allowed to abandon the test fixture upon impact with the programmer pad. A basic steel stand and three custom pedestals supported the specimen prior to loading. This is described in detail in more detail in [14] [15].

The corresponding simulation was created using LS-DYNA, using TYPE 1

solid elements. The test article was modeled with *MAT_PLASTIC_KINEMATIC, with geometry that was precisely reproduced by Durant [14]. A qualitative comparison of the response of the double programmer pad configuration during impact is displayed in Fig. 5.12. Both the axial compression and lateral expansion seen in the test images are clearly represented in the finite element model [14].
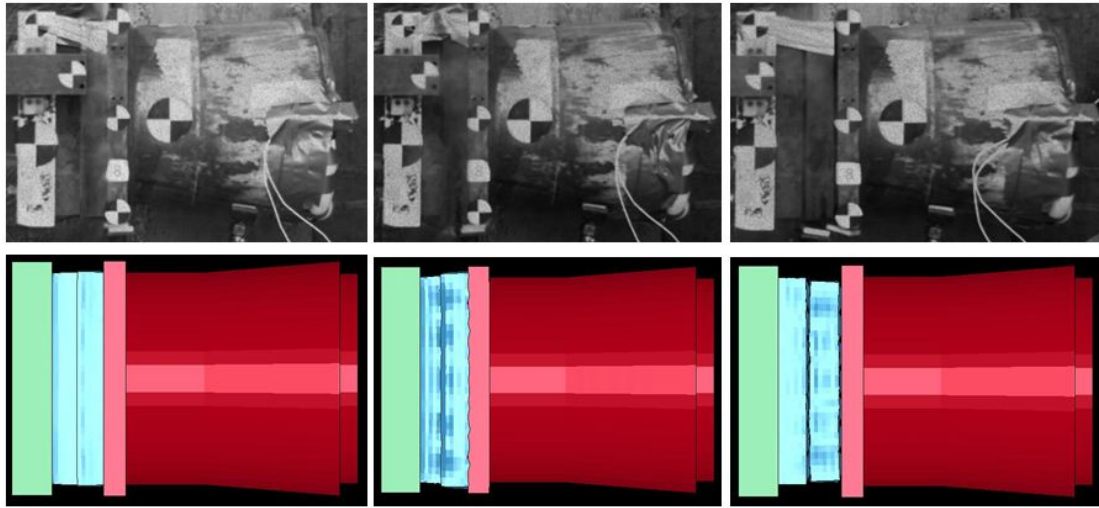
Figure 5.12: Progression of programmer deformation [14]

Durant [14] assigned actual impact velocities observed during the experimental series to the impactor in order to reproduce the collision scenario in the simulation. Outgoing specimen velocity as a function of time was recorded at a specified location on the specimen during the test, using high speed video and motion tracking software. The velocity-time history of the specimen was outputted from the simulation for this same location. A comparison of outgoing specimen velocities for the experimental tests and corresponding LS-DYNA simulations are shown in Fig. 5.13. A test matrix with programmer layering configurations and incoming impact velocities is provided in Table 5.1.

The model produces a good representation of the experimental data both in initial rise and residual outgoing velocity for multiple programmer configurations and incoming impact velocities. More information about this test series can be found in Durant [14]. The slight disagreement between the simulation and experiment under the low velocity impacts and the high velocity impacts
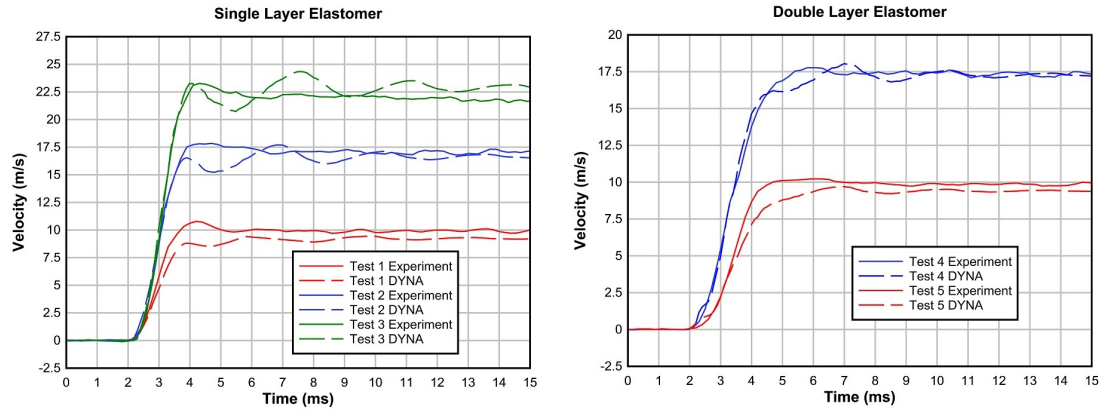
Figure 5.13: Comparison of experimental data and FEM simulations for single and double layer configurations [14]

Table 5.1: Test Matrix [14]

Test	Programmer Configuration	Incoming Velocity
1	Single	16.9 m/s
2	Single	30.2 m/s
3	Single	41.5 m/s
4	Double	31.3 m/s
5	Double	16.8 m/s

is likely due to the *MAT_SIMPLIFIED_RUBBER_WITH_DAMAGE unloading behavior, which we know (e.x. Fig. 5.9) relies on a single set of unloading data. This means that even though the LS-DYNA Blast Simulator programmer has been optimized for the range of strains observed in this test series, the simulation may be less accurate under the extreme impacts. The energy dissipated in these impact events, which is represented by the area enclosed within the loading/unloading response, will be exaggerated for low velocity impacts and artificially smaller for high velocity impacts. This is due to the inability of the *MAT_SIMPLIFIED_RUBBER_WITH_DAMAGE unloading response to correctly "adjust" to a wide range of strains.

The main deficiency of this material model, in other words, is that the Coefficient of Restitution (COR) is too high for high strain rate tests and too low for low strain rate tests. We can, however, assess whether this material model has

been optimized. Consider that further increasing the loading stiffness of the highest strain rate curve, which we can see would improve the loading behavior in the drop tests (e.x. Fig. 5.11), is not beneficial for the Blast Simulator impact tests, since behavior at high strain rates will already be too stiff due to the artificially high COR. As we can see in Fig. 5.13, the behavior under moderate impacts agrees best with the measured data. We can therefore say that the material model has been optimized.

Mesh sensitivity of the programmer pad was also considered. Simulations of the tapered cylindrical steel test article were performed using both of the meshes shown in Fig. 5.14, as well as an in-between mesh. The in-between mesh was adopted. The finest mesh (Fig. 5.14a) had four times the number of elements compared to the adopted mesh, while the coarsest mesh (Fig. 5.14b) had a number of elements four times less than the adopted mesh. The quantitative results are shown in Fig. 5.14c. The coarse mesh does a poor job of simulating the impact, while the adopted mesh had good agreement with the test data. Only slight difference was observed in the response of the test article for the fine mesh, compared to the adopted mesh, which suggests mesh convergence.
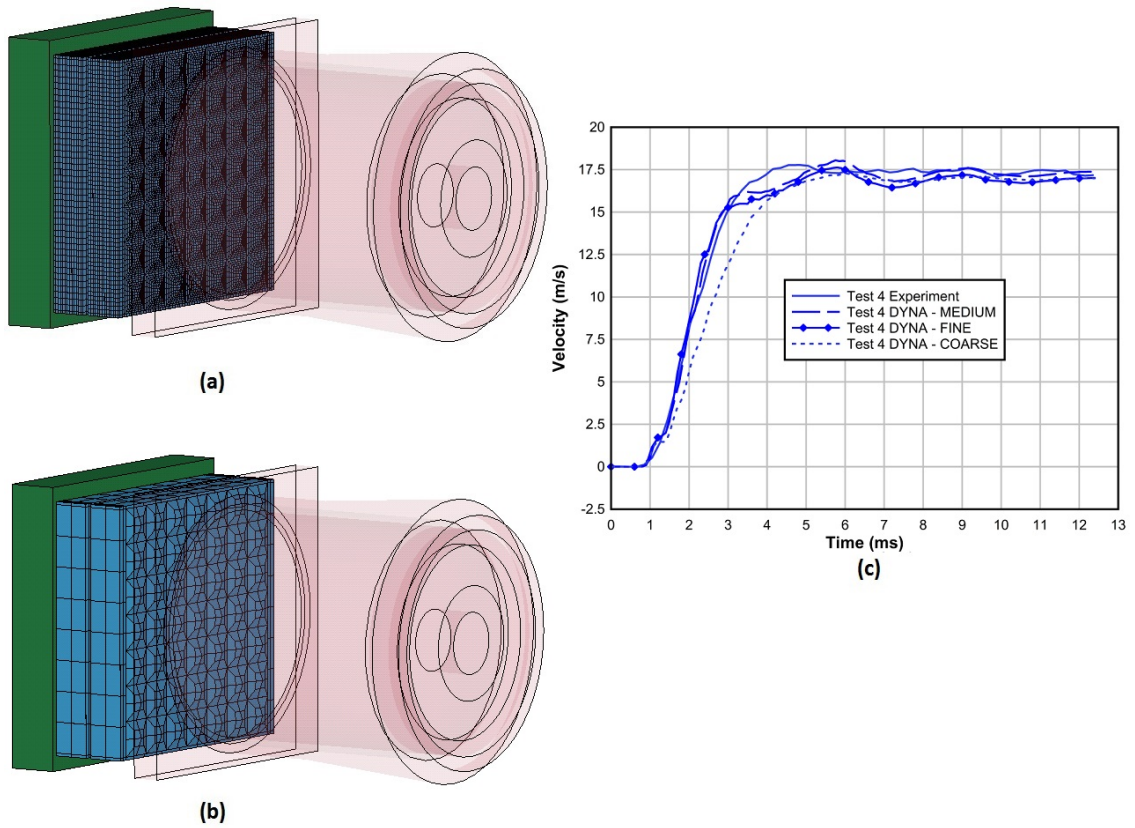
Figure 5.14: (a) Programmer pads with four times the mesh density of the adopted mesh (b) Programmer pads with a mesh density four times less than the adopted mesh (c) Impact results of the three different mesh densities

5.6 *MAT_057 *vs.* *MAT_183

We saw in the previous section that *MAT_183, also known as *MAT_SIMPLIFIED_RUBBER_WITH_DAMAGE, works satisfactorily for the kinds of impacts that the programmer experiences in the Blast Simulator. While it is optimized for moderate impacts, the model can simulate lighter impacts or more severe impacts as well, with sufficient accuracy for our purposes.

We saw that the previous programmer model, *MAT_057, also known as *MAT_LOW_DENSITY_FOAM, which was characterized by Oesterle [44], does not naturally extend to a 3D environment (*i.e.* is not hyperelastic), and is not able to simulate different rate effects for different strain rates. Thus, we expect *MAT_LOW_DENSITY_FOAM to in general perform quite poorly in the simulation of Blast Simulator tests.

For a simple comparison, the two AFRL-sponsored "double-layer" programmer tests, described in the previous section, were simulated in LS-DYNA using *MAT_LOW_DENSITY_FOAM. The same geometries, specimen material parameters, and impact velocities were studied as before. Fig. 5.15 shows a qualitative comparison of the two material models. The bottom three images in Fig. 5.15 show one of the simulations using *MAT_LOW_DENSITY_FOAM, while the top three images in Fig. 5.15 show the same simulation using *MAT_SIMPLIFIED_RUBBER_WITH_DAMAGE. Upon close inspection, it is apparent that the *MAT_LOW_DENSITY_FOAM is experiencing some instabilities and does not appear to be displaying incompressible behavior. We may recall from the beginning of this chapter, in particular Fig. 5.2, that *MAT_LOW_DENSITY_FOAM does not display proper lateral behavior under compression.

Fig. 5.16 shows shows the outgoing specimen velocities as a function of time for the two double-layer programmer tests. For each of the tests, two simulations were performed. As we already saw in the previous section, the simulations using *MAT_SIMPLIFIED_RUBBER_WITH_DAMAGE correspond reasonably well to the experimental (camera) data. We can again see this in Fig. 5.16. The simulations using *MAT_LOW_DENSITY_FOAM gave poor results for all of the AFRL tests.
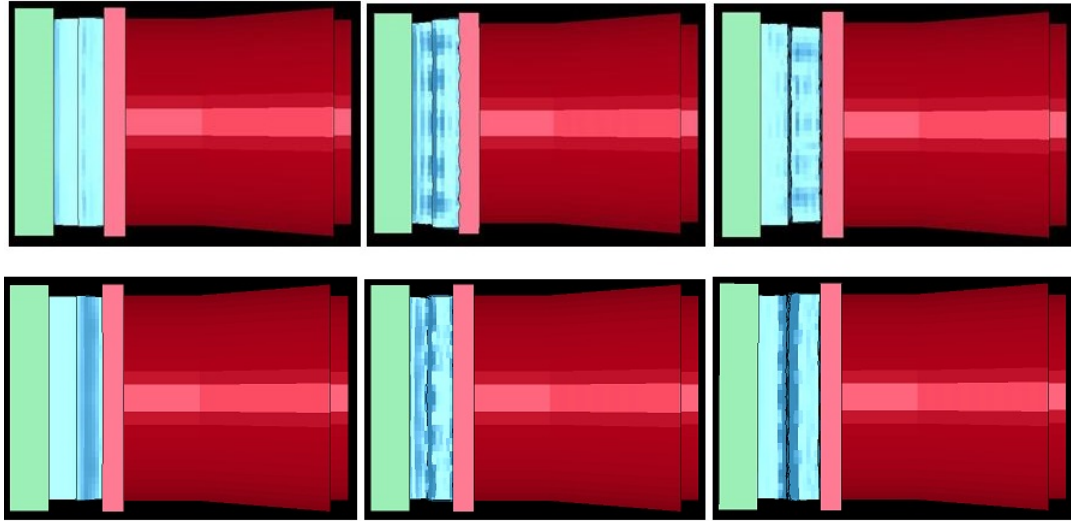
Figure 5.15: Progression of programmer deformation: *MAT_183 (top) and *MAT_057 (bottom)
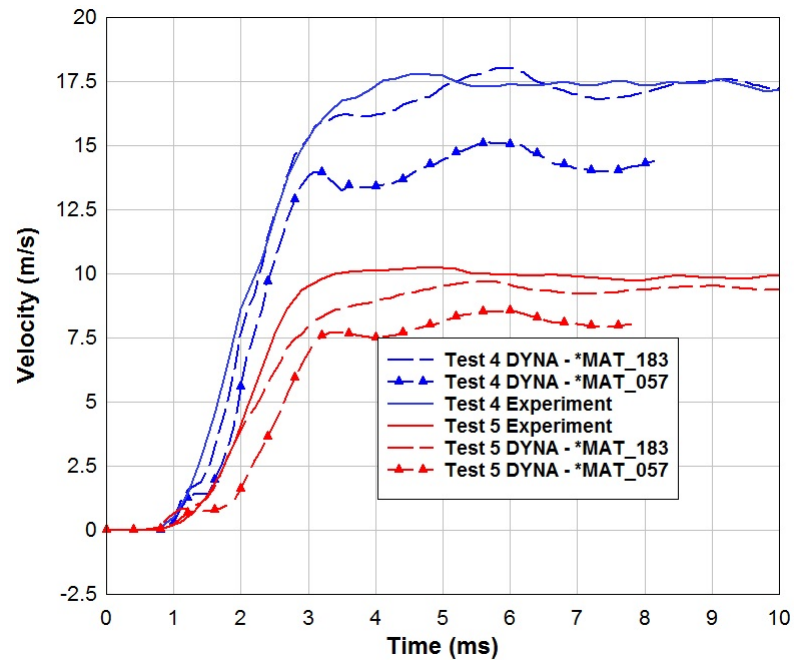
Figure 5.16: Comparison of experimental response *vs.* simulation for two tests

While *MAT_LOW_DENSITY_FOAM may work adequately for a particular narrow range of Blast Simulator tests, it is generally not a good model. *MAT_SIMPLIFIED_RUBBER_WITH_DAMAGE also works adequately for only a certain range of tests, but this range is sufficiently wide to encompass all Blast Simulator testing that is conducted at UCSD. We will be in a better position to critique the *MAT_SIMPLIFIED_RUBBER_WITH_DAMAGE model at the end of the thesis, after we see how the model performs in larger-scale Blast Simulator tests on wall systems. The deficiencies of this model will be revisited later on and recommended future research into programmer material modeling will be discussed.

Chapter 6

Prototype Wall Tests

This chapter will provide detailed descriptions and results for 12 full-size wall tests that were performed at the UCSD Blast Simulator in the Fall of 2011, in collaboration with the company Simpson Gumpertz & Heger (SGH). Descriptions will include construction methods, instrumentation, and design details. Complete pressure-time history demands will be provided, along with displacement-time histories, high-speed images, and close-up photos of damage. The tests will be presented in the order that they were performed.

6.1   Previous research

The general behavior of light gauge wall systems subjected to blast loads has been investigated by Salim [50]. The light gauge walls exhibit significant flexural response resulting in cracking of the interior drywall as shown in Fig. 6.1b, along with structural damage in the studs. Localized buckling as shown in Fig. 6.2 is commonly observed in studs under flexure, as is connection failure [11][51]. One kind of connection failure is shown in Fig. 6.3.

The general behavior of light gauge steel walls in the Blast Simulator was investigated in 2010 and 2011. Two test series were conducted on two distinct light gauge steel wall systems. The first test series, which consisted of ten tests, investigated modes of damage at the connections [22]. This test series was crucial for the development of the connection details that were used in the SGH wall tests

Figure 6.1: (a) Studs prior to blast (b) interior view after blast [50]
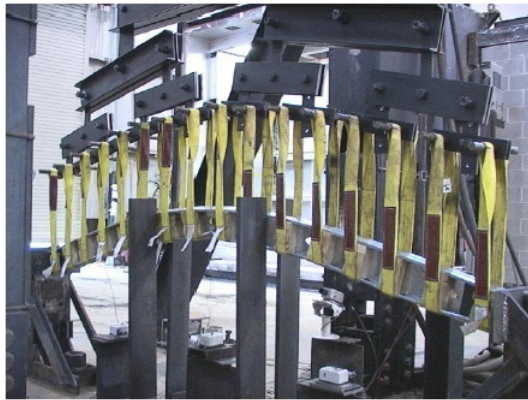
Figure 6.2: Local buckling at access or utility hole observed under flexure [11]

Figure 6.3: Tearing of connection occurs in light gauge sheet [51]

that will be discussed, beginning in the next section. A time-lapse of one of these tests is shown in Fig. 6.4 and the associated connection damage is shown in Fig. 6.5b.
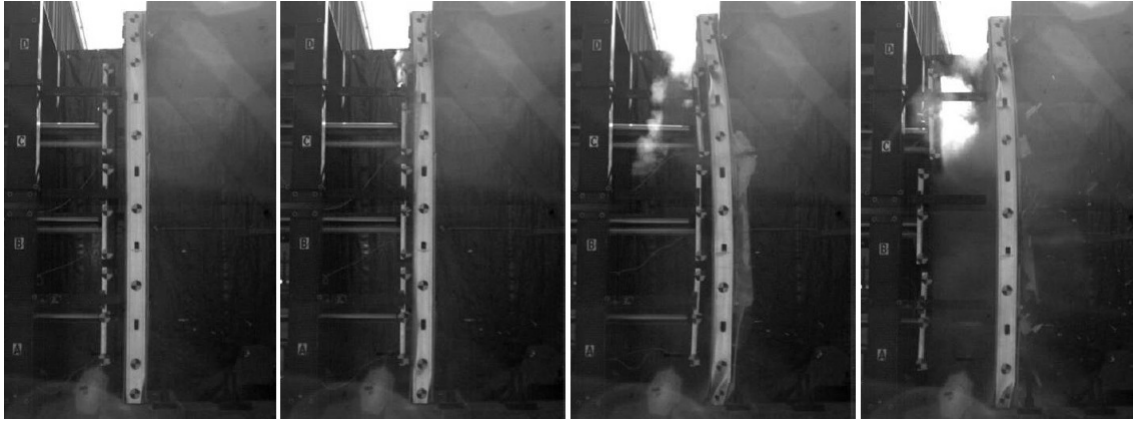
Figure 6.4: Damage evolution of light gauge wall system from first test series [22]

(a)

(b)

Figure 6.5: (a) Initial series 1 "bearing washer" connection (b) Connection failure mechanism involves warping of track and stud webs [22]

The second test series of light gauge walls in the Blast Simulator consisted of four tests. In these tests the walls were supported at the boundaries *via* very simple bearing connections, and the main purpose of these tests was to gain insight into the influence of panel discontinuities and access or utility hole locations. In all four tests, damage occurred at the access holes regardless of the locations of panel discontinuities on the front and back-side of the studs [60]. In order to mitigate damage in the system, which concentrated at these access holes, new methods were employed that attempt to brace the access holes in the SGH wall tests. The SGH

wall tests will be discussed next. A time-lapse of one of the tests from the second series of light gauge wall testing is shown in Fig. 6.6.
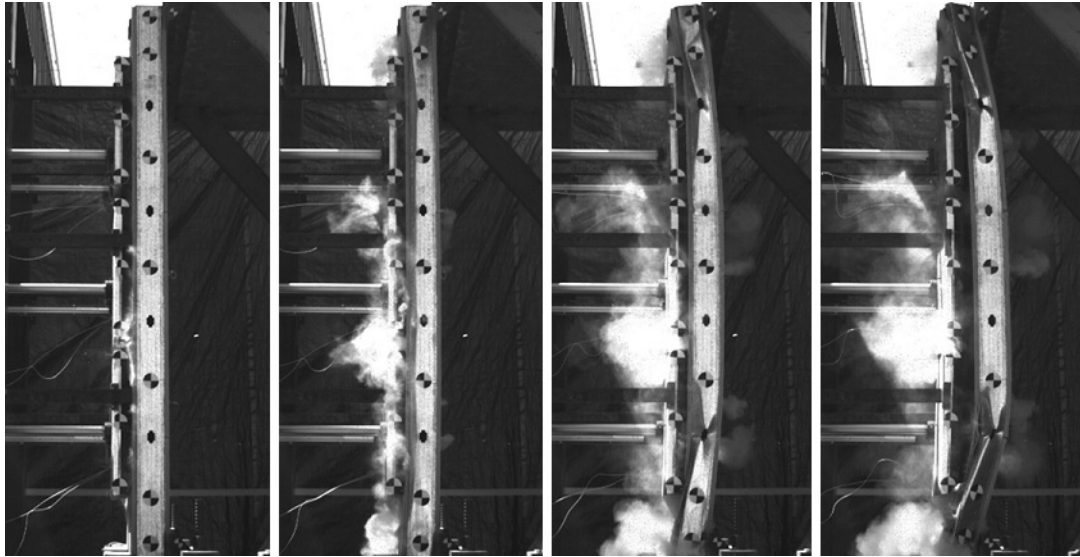
Figure 6.6: Damage evolution of light gauge wall system from second test series

6.2   Prototype wall construction

In a collaboration between UCSD and the engineering firm Simpson Gumpertz & Heger, a test series, entitled SSRE010, was conducted on 4 ft. wide light gauge vanadium-alloy studded walls, using the Blast Simulator. The use of high strength (85 ksi) low alloy vanadium steel (HSLA-V) studs, rather than steel studs, is the primary difference between series SSRE010 and the tests described in Section 6.1. The information gained from the previous tests regarding connection detailing and panel arrangement proved to be valuable and was incorporated into the SSRE010 test series.

While the walls will vary in height, depth, number of studs, *etc.*, the general construction process can be described, as follows. The top and bottom of the vanadium studs sit inside of a "track," which is a 14 gauge steel channel, as shown in Fig. 6.7. Each stud flange is held to the track by a minimum of one 8D screw.

This is commonly called a stud-to-track system (see [30]). Note in Fig. 6.7 that the studs and tracks are only partially assembled, as one track is missing.

Figure 6.7: Preliminary stud-track assembly

The sheathing consists of Sure-board®panels. The front side (impact side) consists of Durock®cement-board that is bonded to 14 gauge steel sheet, while the back-side consists of drywall that is bonded to 22 gauge steel sheet. The panels are attached to the studs by 8D flat head screws, with a minimum screw spacing of 6 inches, as shown in Fig. 6.8.

As shown in Fig. 6.9a, the specimen is placed with some panels absent in order to allow access for connecting the wall system to the concrete deck and concrete footer. Most of the tests consisted of "blast-washer" connections. As shown in Fig. 6.9b, each "blast-washer" is held to the concrete by a 5/8 in. diameter bolt, and spans the entire depth of the studs. The blast-washer-to-footer connection utilizes Hilti Kwik Bolt TZ wedge anchors, while the connection to the deck uses Grade 8 all thread rod. The blast-washers create connections that are "semi-rigid."

As shown in Fig. 6.9c, the final step in the construction is to fully-panel the front and back of the wall. The panels are staggered in a different arrangement on the front-side, compared to the back-side, to avoid having panel discontinuities at the same locations on both sides of the wall. This is done in order to minimize the presence of a "weak-link" through the cross-section of the wall, although it was previously observed (Section 6.1) that the access or utility holes create a weak link that is more significant than the presence of panel discontinuities.
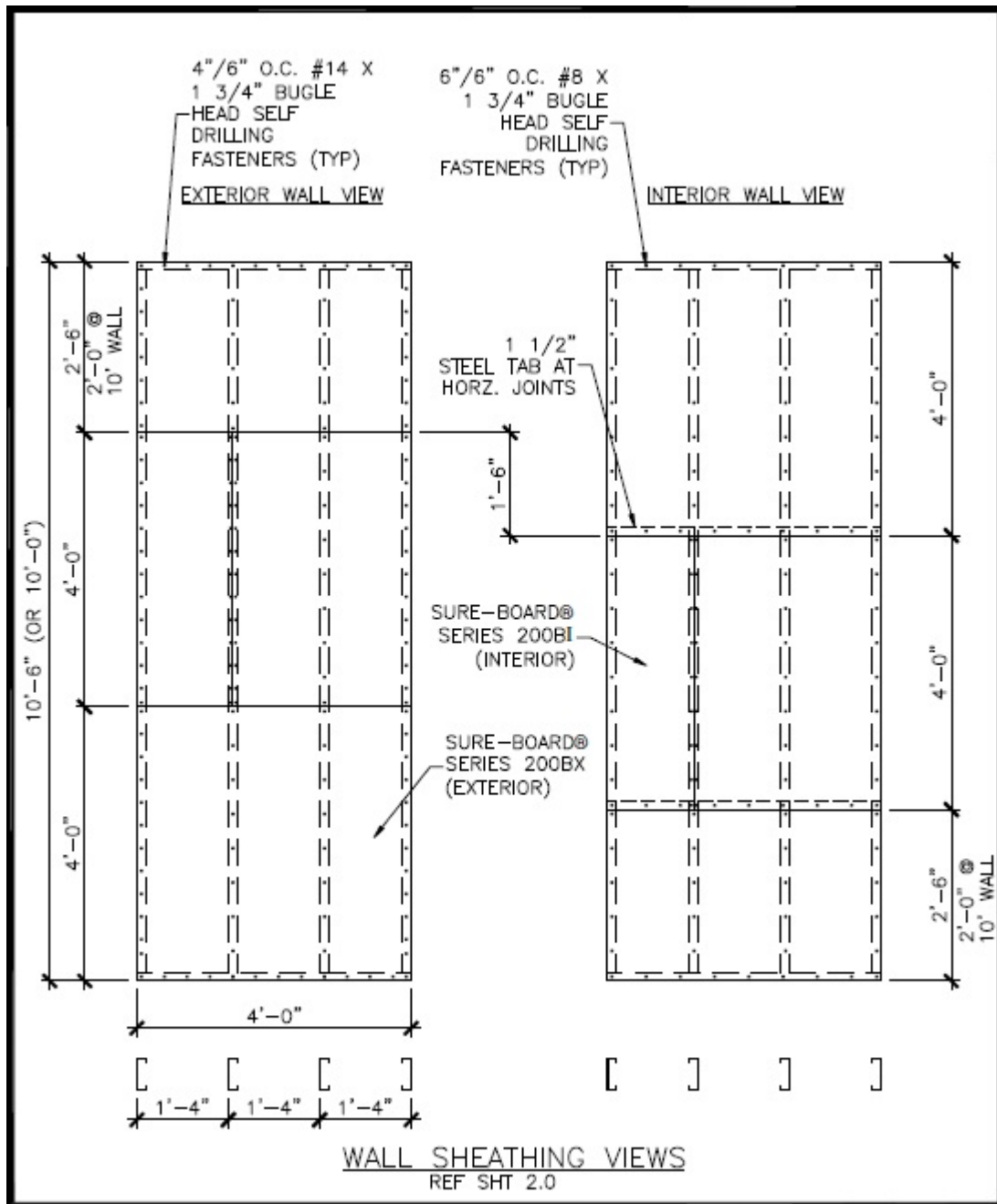
Figure 6.8: Sure-board®wall sheathing views for SSRE010-01
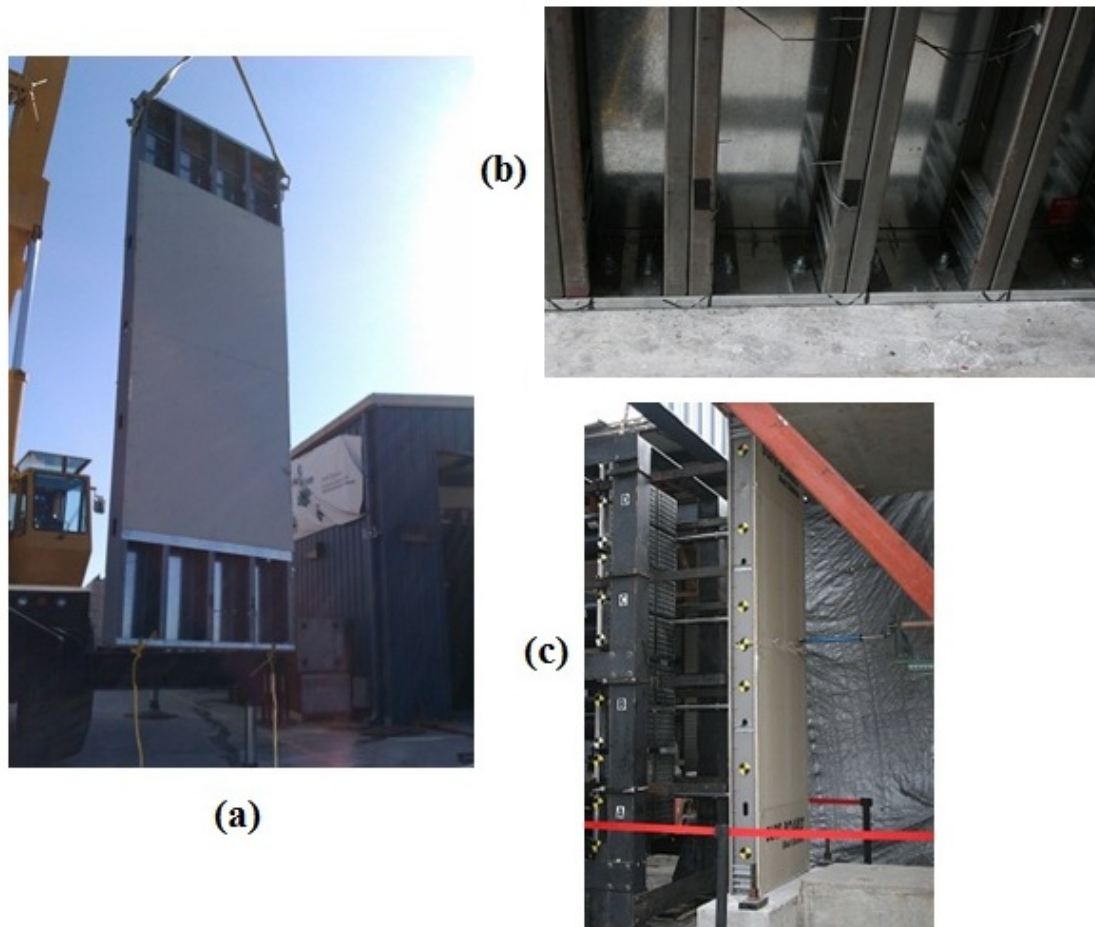
Figure 6.9: (a) Placement of specimen with access to connections (b) Blast-washer connection (c) Completed wall

Other detailing of note include the presence of hardware at the top and bottom of the wall, which prevents the webs of the studs from buckling/crippling at those locations. As shown in Fig. 6.10b, these L-shaped brackets are screwed into the webs of the vertical studs. Nails are driven (shot-pinned) through the bottom tab of the brackets to affix the bracket to the concrete footer at the bottom of the wall or the concrete deck at the top of the wall. Additionally, stiffeners were sometimes placed at access holes in an attempt to prevent buckling in locations along the wall deemed most susceptible or to attempt to control the location of damage initiation in the wall system. An example one such stiffener clip is shown in Fig. 6.10a.

Figure 6.10: (a) Clip placed at utility hole [36] (b) Blast washer and L-shaped bracket installation [22]

6.3 Impact *vs.* uniform pressure

Since the purpose of each wall test is to observe the response of the structure under blast loading, it would be ideal for the Blast Simulator to impart a pressure on the wall that is uniform. For example, the load application should be uniformly distributed along the width of the wall, which is difficult to accomplish, even with the presence of the programmer, since the stiffness of the wall system in this test

series is not uniform along its width. At the locations along the width where the HSLA-V studs are present, it is not surprising to find that the pressure application is greater, in the Blast Simulator, compared to the pressure application from the programmer at locations along the width of the wall in between the studs.
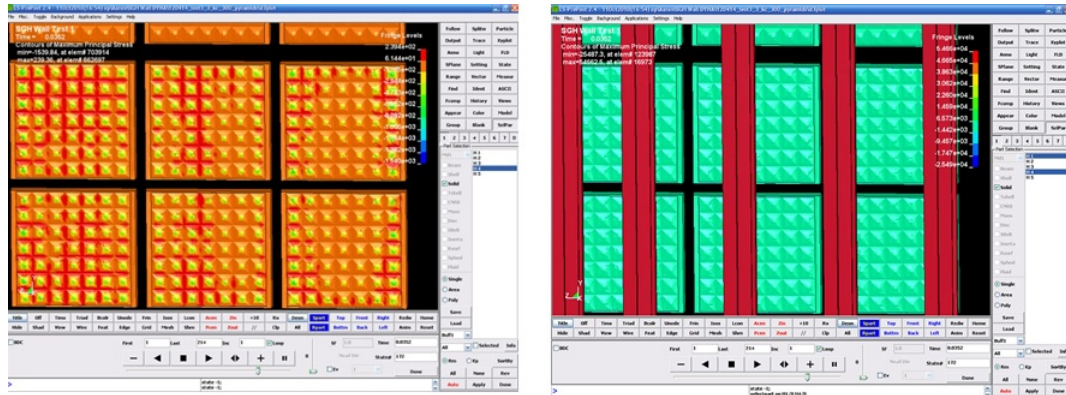
Figure 6.11: Screen-shot illustrating higher stresses in the programmer at the location of studs

This non-uniform load application is shown, pictorially, in Fig. 6.11, which depicts pressure at the front face of the programmer during an LS-DYNA simulation of a Blast Simulator impact. This chapter will focus on the experimental results, where it is important to recognize that the results that will be presented are a simplification. We can recall from Section 4.2.2 that the force imparted to the wall is calculated by taking into consideration the acceleration time history of the impact mass as well as the hydraulics, and it is usually assumed that this force is applied uniformly, though there is no experimental data available to support this. This "equivalent average pressure," which is calculated by dividing the impact mass force by the total programmer area, is done in order to allow for a means of obtaining pressure, and more importantly, specific impulse.

Generally speaking, a value of uniform pressure and its associated specific impulse may correspond to a particular threat level, as discussed in Chapter 3. Since the ability to use the Blast Simulator data to obtain corresponding threat levels is one of the important results in this test series SSRE010, "equivalent average pressure" will be shown in this chapter. This method does need some validation

for the wall systems of SSRE010, since we see in Fig. 6.11 that the load is not in fact uniform. Thus, before showing any results of the Blast Simulator tests, we can investigate how the wall systems of series SSRE010 respond to uniform load, compared to Blast Simulator impacts. In order to perform a direct comparison, LS-DYNA is used, as follows.
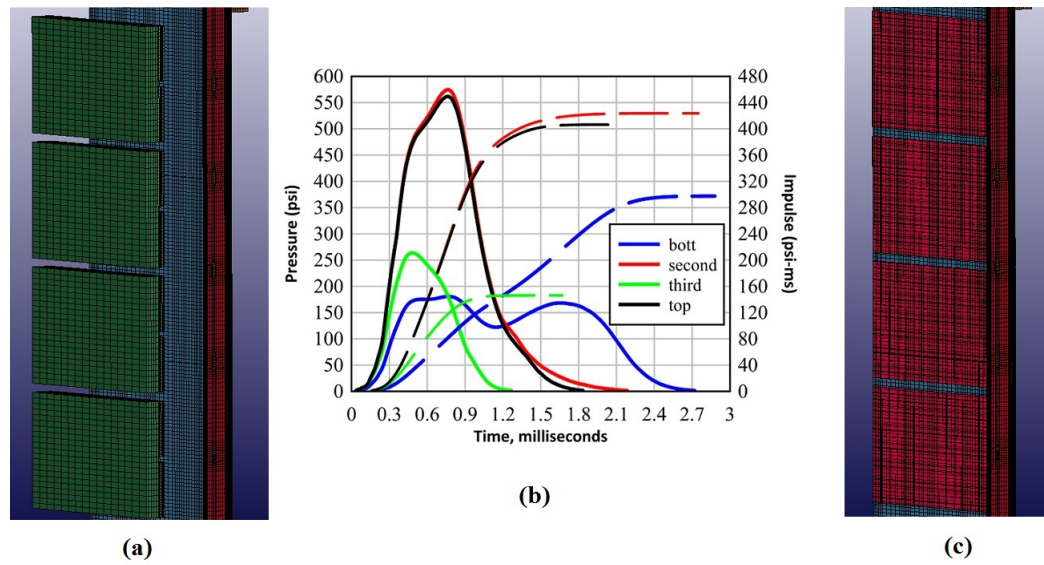
Figure 6.12: (a) LS-DYNA impact (b) "equivalent uniform pressure" for each BG (c) LS-DYNA "direct pressure" application

Fig. 6.12a shows a before view of a moderate severity Blast Simulator impact, and Fig. 6.12b shows the resulting "equivalent average pressure" for each of the four impact masses, which was obtained by exporting the LS-DYNA contact force for each impact mass and then dividing by the total programmer area of a single impact mass. A second LS-DYNA simulation was then performed, where the "equivalent average pressure" for each impact mass was applied directly to the wall, as shown in Fig. 6.12c. Two sets of data were then investigated for the simulations shown in Fig. 6.12a and Fig. 6.12c, namely, 1) the global behavior of the wall in the two simulations was evaluated by considering peak displacement of the studs at varying heights, and 2) local behavior of the panel in between the studs, on the impact side of the wall, was evaluated by considering displacement at mid-height, halfway in-between the inner-most studs (3 ft. from the wall edge).

We can see in Fig. 6.13a,b that the global results agree quite well. We can infer from Fig. 6.14a,b, however, that the panel on the impact side of the wall is receiving smaller force demands in the Blast Simulator impact, compared to a true "equivalent uniform load." One can therefore conclude that the results that will be shown in this chapter and the next one, which use the convenient simplification of "equivalent uniform load," are reasonable so long as only global behavior is of interest when predicting the response of the SSRE010 wall systems to blast threats. If panel damage on the blast-face of the wall is a concern, then the assumption of "equivalent uniform load" is un-conservative, and alternative tests must be performed in order to load the panels more uniformly.

(a)   (b)
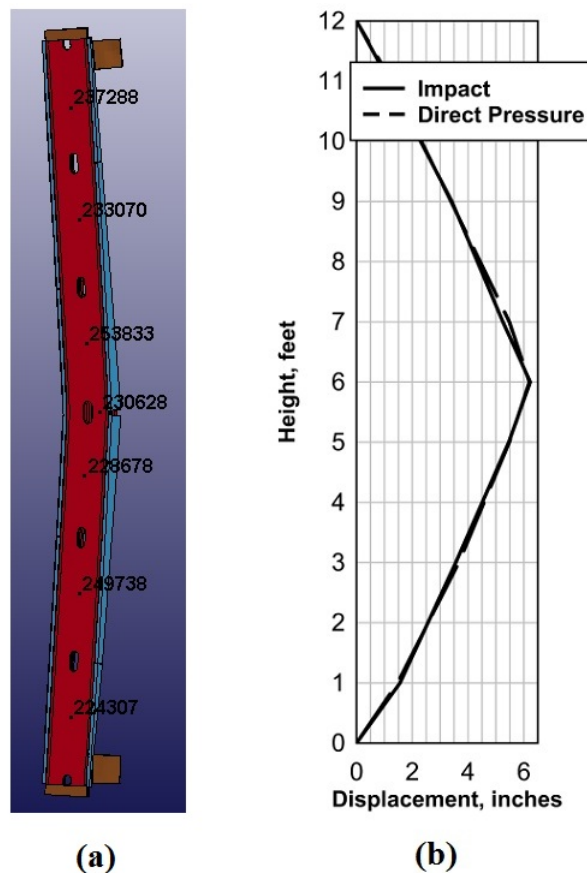
Figure 6.13: (a) Deformed view of LS-DYNA simulation with nodes selected (b) Peak displacement versus height

(a)

Exterior Panel Displacement	
Impact	.25"
Direct Pressure	.5"

(b)
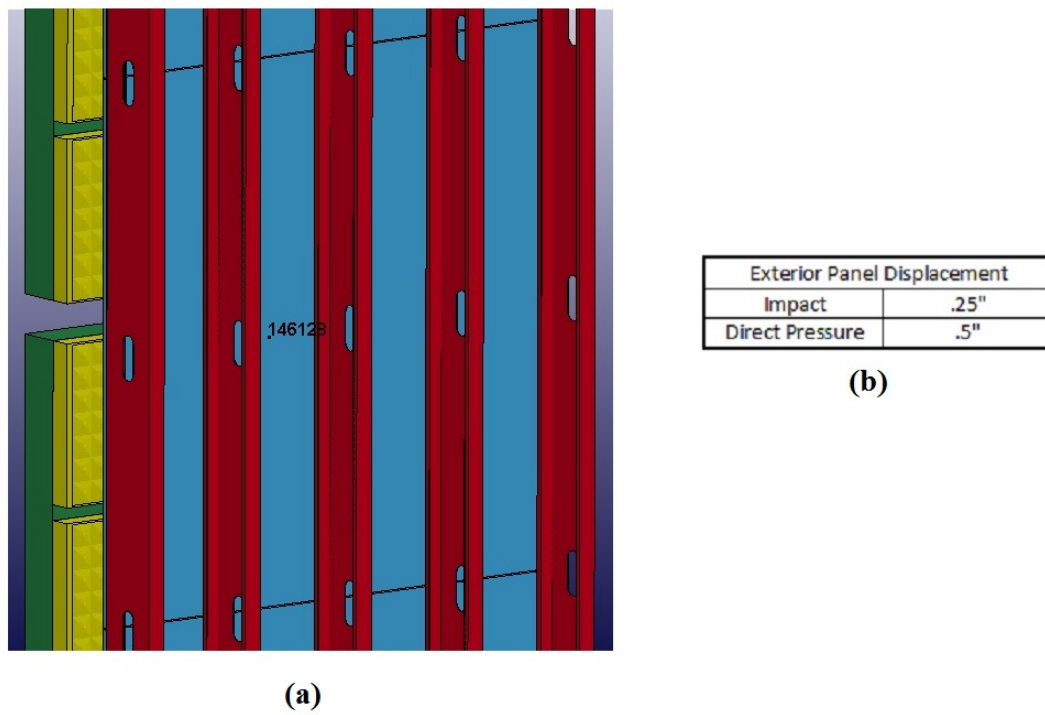
Figure 6.14: (a) Node selected on exterior panel in between studs (b) Comparison of panel deformation for impact *vs.* equivalent direct uniform pressure

6.4 Experimental Description

Test series SSRE010 consisted of seven unique wall specimens, including multiple tests on several of the specimens, which resulted in a total of twelve tests. A summary of test specimens is shown in Table 6.1.

Table 6.1: Test Matrix

Test Number	Stud Material	# Studs	Clear span	Stud thickness	Stud depth	Approximate Spacing	Top Connection	Bottom Connection	CMU	Web braces at access holes	Flange brace at connections
SUREBOARD10	Mild/S	5	9.5ft	16ga	6"	12"	Angle & L- Brackets	Single blast track washer per bay & clip	No	2,4	No
1	HSLA-V	5	9.5ft	16ga	6"	12"	Angle & L- Brackets	Single blast track washer per bay & clip	No	2,4	No
2.1	HSLA-V	10	12ft	12ga	8"	12"	Two blast track washers per bay & clip	Two blast track washers per bay & clip	No	2,4	No
2.2	HSLA-V	10	12ft	12ga	8"	12"	Two blast track washers per bay & clip	Two blast track washers per bay & clip	No	2,4	No
2.3*	HSLA-V	10	12ft	12ga	8"	12"	Two blast track washers per bay & clip	Two blast track washers per bay & clip	No	2,4	No
3.1	HSLA-V	10	12ft	12ga	8"	12"	Angle	Angle	No	2,4	Yes
3.2	HSLA-V	10	12ft	12ga	8"	12"	Angle	Angle	No	2,4	Yes
3.3	HSLA-V	10	12ft	12ga	8"	12"	Angle	Angle	No	2,4	Yes
4.1	HSLA-V	5	12ft	12ga	6"	12"	Two blast track washers per bay & clip	Single blast track washer per bay & clip	No	2,3,4	No
4.2**	HSLA-V	5	12ft	12ga	6"	12"	Two blast track washers per bay & clip	Single blast track washer per bay & clip	No	2,3,4	No
5	HSLA-V	5	12ft	12ga	6"	12"	Single blast track washer per bay & clip	Single blast track washer per bay & clip	Yes	2,3,4	No
6*	HSLA-V	10	12ft	12ga	8"	12"	Two blast track washers per bay & clip and backup angle	Two blast track washers per bay & clip and backup angle	Yes	2,3,4	Yes
7	HSLA-V	4	12ft	16ga	6"	16"	Single blast track washer per stud & clip	Single blast track washer per stud & clip	Yes	2,3,4	No

* Connection failure
** Significant specimen damage prior to test

The general Blast Simulator layout and methodologies used for determining impulse was described previously in Chapter 2. The actuator + piston + impact mass assembly, better known as the Blast Generator (BG) that is used in test series SSRE010 is the "BG25" model, capable of attaining velocities of 25 meters per second. The number of BGs and the weight of the masses varied test-to-test. However, each of the masses used in series SSRE010 consisted of 30in. x 48in. aluminum, in order to span the whole width of the specimen. Six 16in. x 16in. programmer pads were bolted to each aluminum mass.

6.4.1 Instrumentation

Each specimen was instrumented with PCB 20k accelerometers to measure mid-span specimen accelerations. Two inch holes were cut in the interior gypsumboard at the center studs of the wall assembly to provide for a more rigid mounting point for the accelerometers. Penny and Giles LVDT potentiometers were attached to the same mounting points, in some cases, as shown in Fig. 6.15. Targets were also placed on the exterior, camera-facing, stud, in order to measure displacements using high speed video. Strain gauges were present as well, although the survivability rate was low for the strain gauges that were placed on the flanges of the studs, due to the destructive panel placement process.

Figure 6.15: Detailed view of specimen accelerometers and LVDTs

Each impacting mass assembly was instrumented with PCB 10k accelerometers to measure the net force acting on the impact mass. The accelerometers were screwed into pre-drilled holes in the back of the aluminum mass, as shown in Fig. 6.16. A temposonic magnetostrictive transducer is also attached to each mass and measures the displacement of the mass as it is guided by the rails. Three Phantom cameras recorded video of each test. Using TEMA software, BG impact velocities and specimen displacements can be readily obtained. All instrumentation, including the cameras, is time-synchronized.

The post-processing of BG accelerometer and hydraulic data for the purpose
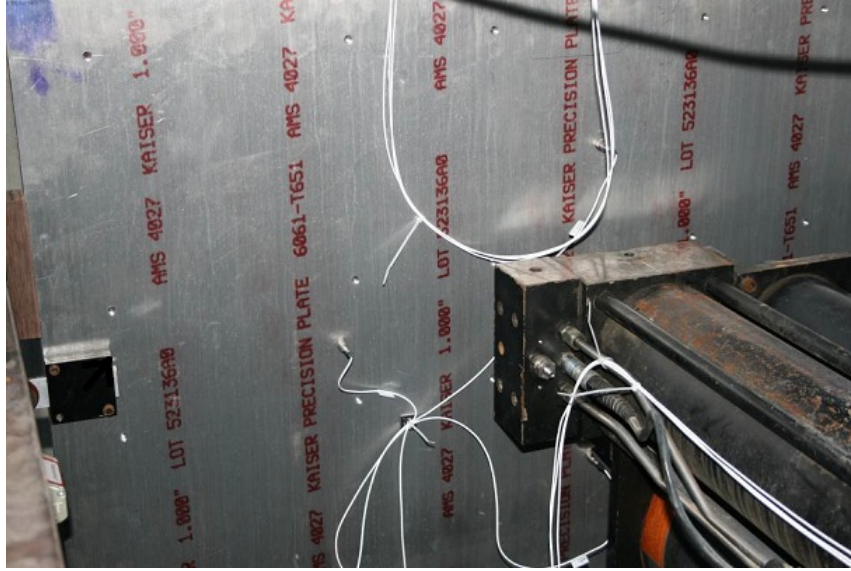
Figure 6.16: View of backside of impact mass.

of obtaining impulse was discussed in detail in Chapter 4. Specimen accelerometers are also present and can be used as an additional means for estimating pressure and impulse. Since the specimen accelerometers in this test series are located at the mid-height of each specimen, the average specimen acceleration time history, $a_s(t)$, can be used to estimate equivalent transferred force in a simplified manner, as follows:

$$p_s(t) = \frac{M_{s,eff}\, a_s(t)}{A_{s,eff}} \tag{6.1}$$

$$M_{s,eff} = m L_{s,eff} \tag{6.2}$$

$$A_{s,eff} = b L_{s,eff} \tag{6.3}$$

In eq. (6.2), m is the mass of one unit length of wall, assuming that the wall is prismatic. In eq. (6.3), b is the width of the wall.

The corresponding specific impulse, $i_s(t)$, can be estimated as well:

$$i_s(t) = \int p_s(t)dt \tag{6.4}$$

Recall that the units of specific impulse will be in $psi - ms$, and it is customary in blast to refer to this quantity simply as "impulse," even though it is not the total impulse, *per se*. In addition, $L_{s,eff}$ will simply be taken as the full height of the wall, and the shear forces at the top and bottom connections of the wall will be ignored. As a result, eq. (6.1) and eq. (6.4) should be used only as rough estimates of the pressure-time history and impulse that are imparted to the specimens. The methodology of Chapter 4, which utilizes hydraulic data and BG accelerometer data is a more precise means of obtaining impulse.

6.5 SGH Sure-board®HSLA-V Experiments

6.5.1 Test SSRE010-01 Results

Test Description

Sure-board®Test SSRE010-01 utilized five 16ga studs (6 in. depth), 12 in. on center, with a clear span of 9.5ft. The target impact velocity for this test was 17 m/s (670 in/s). A 246 lb flyer mass was used, which included the aluminum backing plate, programmer, and rod. The clear span of the specimen was 108 in. and targets to measure displacement were placed at 3 in., 6 in., 12 in., 36 in., 60 in., 84 in., and 117 in. from the footer. A photo showing the initial setup is given in Figure 6.17, and the lower and upper connections are displayed in Figure 6.18 and Figure 6.19. Note that the lower connection utilizes so-called "blast-washers," which permit a small amount of rotation *via* elastic and inelastic bending.

Impacting Mass Behavior

Average pressure and impulse were calculated from the BG accelerometers and hydraulics using the method described in Section 4.2.2. This is depicted in

Figure 6.17: Test SSRE010-01 Initial Setup

Figure 6.18: Test SSRE010-01 Lower Connection

Figure 6.19: Test SSRE010-01 Upper Connection

Figure 6.20.
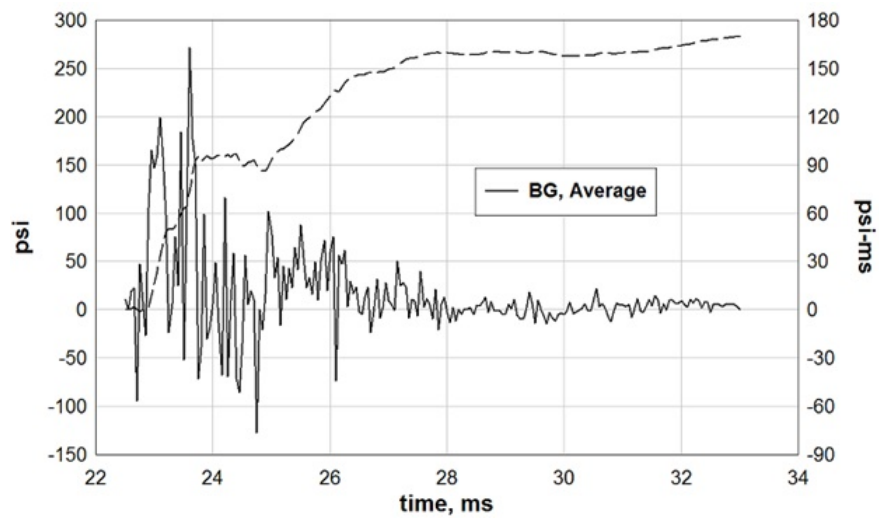
Figure 6.20: Test SSRE010-01 Average Pressure and Impulse

Specimen Behavior

Figure 6.21 shows the response of the specimen recorded with the high speed cameras recorded at approximately 5,000 frames per second. The first frame shows the specimen at initial contact and the second frame shows the specimen at approximate end of contact. The third frame captures the maximum response of the specimen, while the last frame shows the residual deflection of the specimen. Damage occurred primarily at a lower access hole, which is shown in detail in Fig. 6.22.
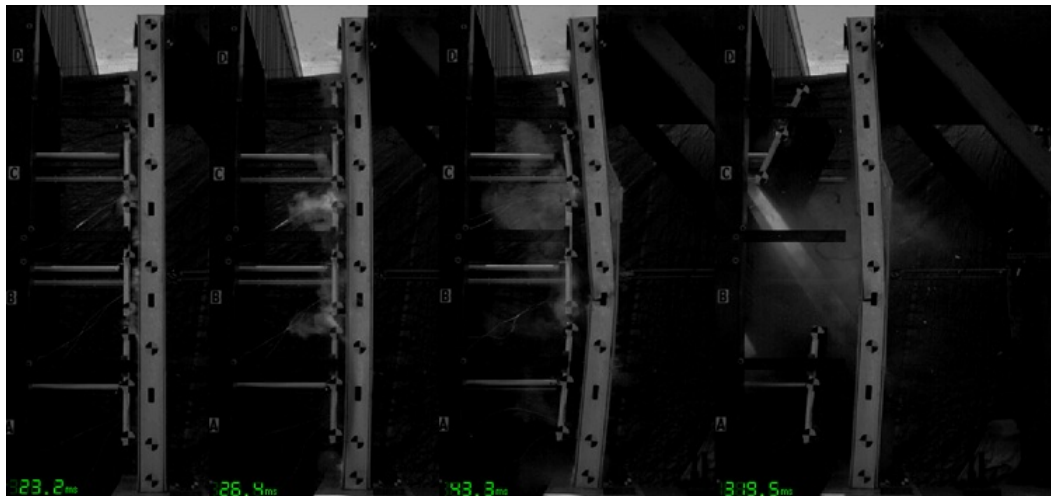
Figure 6.21: Test SSRE010-01 High Speed Video Time-lapse

Displacements were measured using both camera data and a pair of LVDTs behind the specimen. A summary of the maximum, maximum rebound, and residual displacements for each of the specimen target locations is given in Table 6.2. A summary of both methods is shown in Table 6.3.

Additional data, including complete displacement time-histories, individual BG pressures, simplified pressure-time histories, and alternative calculations of impulse, can be found in Appendix E.1.

Figure 6.22: Test SSRE010-01 Primary Damage

Table 6.2: Test SSRE010-01 Camera Displacement Summary

Distance from Wall Base (in)	Maximum Displacement (in)	Maximum Rebound (in)	Residual Displacement (in)
3	.68	.34	.40
12	1.65	.77	.98
36	3.97	1.76	2.48
60	4.73	2.03	3.01
84	2.92	1.30	1.80
108	1.13	.61	.57
117	.50	.38	.13

Table 6.3: Test SSRE010-01 Displacement Summary

Method	Maximum Displacement (in)	Maximum Rebound (in)	Residual Displacement (in)
Camera	4.73	2.03	3.01
Linear Potentiometer	5.28	2.88	2.90
Average	5.01	2.46	2.96

6.5.2 Test SSRE010-02 Results

Test Description

Sure-board®Test SSRE010-02 utilized ten 12ga studs (five "double" studs, 8 in. depth), 12 in. on center. Three tests were performed on this specimen. The target impact velocities for these three tests were 7 m/s (276 in/s), 10 m/s (394 in/s), and 20 m/s (787 in/s). A 246 lb flyer mass was used, which included the aluminum backing plate, programmer, and rod. The clear span of the specimen was 144 in. and targets to measure displacement were placed at 12 in., 36 in., 60 in., 72 in., 84 in., 108 in., and 132 in. from the footer. A photo showing the initial setup is given in Figure 6.23, and the lower and upper connections are displayed in Figure 6.24 and Figure 6.25. Note that the connections utilize so-called "blast-washers," which permit a small amount of rotation *via* elastic and inelastic bending.

Figure 6.23: Test SSRE010-02.1 Initial Setup

Figure 6.24: Test SSRE010-02.1 Lower Connection

Figure 6.25: Test SSRE010-02.1 Upper Connection

Impacting Mass Behavior

Average pressure and impulse were calculated from the BG accelerometers and hydraulics using the method described in Section 4.2.2. These are depicted in Figures 6.26, 6.27, and 6.28.

Specimen Behavior

Figures 6.29, 6.30, and 6.31 show the response of the specimens, recorded with the high speed cameras recorded at approximately 5,000 frames per second.

Figure 6.26: Test SSRE010-02.1 Average Pressure and Impulse

Figure 6.27: Test SSRE010-02.2 Average Pressure and Impulse
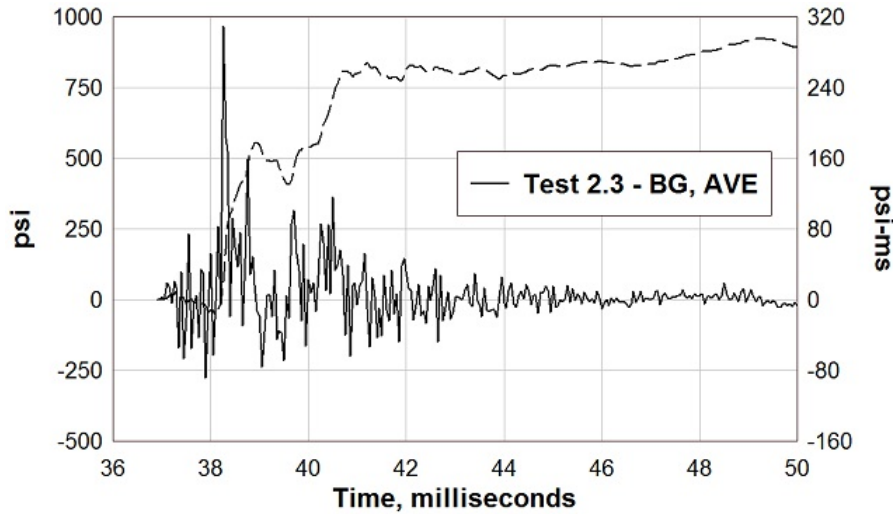
Figure 6.28: Test SSRE010-02.3 Average Pressure and Impulse

The first frame shows the specimen at initial contact and the second frame shows the specimen at approximate end of contact. The third frame captures the maximum response of the specimen, while the last frame shows the residual deflection of the specimen, where applicable. No visible damage occurred in the first test. Damage occurred primarily at the top connection in the second test. The third test failed completely the top connection. A more detailed view of the damage from the second test is shown in Fig. 6.32.

Displacements were measured using camera data and a single LVDT behind the specimen for the first two tests. For the third test, only camera data was available. A summary of the maximum, maximum rebound, and residual displacements for each of the specimen target locations, for the two applicable tests are given in Table 6.4 and Table 6.5.

Additional data can be found in Appendix E.2. This additional data includes complete displacement-time histories, individual BG pressures, simplified pressure-time histories, and an alternative method for estimating impulse.

Figure 6.29: Test SSRE010-02.1 High Speed Video Time-lapse

Figure 6.30: Test SSRE010-02.2 High Speed Video Time-lapse

Figure 6.31: Test SSRE010-02.3 High Speed Video Time-lapse

Figure 6.32: Test SSRE010-02.2 Primary Damage

Table 6.4: Test SSRE010-02.1 Camera Displacement Summary

Distance from Wall Base (ft)	Maximum Displacement (in)	Maximum Rebound (in)	Residual Displacement (in)
1	.56	0.67	0.02
3	1.14	1.37	.05
5	1.48	1.75	.11
6	1.48	1.75	.11
7	1.49	1.72	.13
9	1.16	1.34	.12
11	.63	.67	.25

Table 6.5: Test SSRE010-02.2 Camera Displacement Summary

Distance from Wall Base (ft)	Maximum Displacement (in)	Maximum Rebound (in)	Residual Displacement (in)
1	.89	1.09	.24
3	1.72	1.96	.33
5	2.12	2.56	.38
6	2.13	2.56	.37
7	2.12	2.55	.35
9	1.69	2.06	.33
11	1.11	1.28	.36

6.5.3 Test SSRE010-03 Results

Test Description

Sure-board®Test SSRE010-03 utilized ten 12ga studs (five "double" studs, 8 in. depth), 12 in. on center. Three tests were performed on this specimen. The target impact velocities for these three tests were 7 m/s (276 in/s), 10 m/s (394 in/s), and 20 m/s (787 in/s). A 246 lb flyer mass was used, which included the aluminum backing plate, programmer, and rod. The clear span of the specimen was 144 in. and targets to measure displacement were placed at 12 in., 36 in., 60 in., 72 in., 84 in., 108 in., and 132 in. from the footer. A photo showing the initial setup is given in Figure 6.33, and the lower and upper connections are displayed in Figure 6.34 and Figure 6.35. Note that the top and bottom of the wall is not fixed to the concrete header or footer. Instead, the presence of the angle-shaped structural sections restrict the movement of the top and bottom of the wall.

Figure 6.33: Test SSRE010-03.1 Initial Setup

Figure 6.34: Test SSRE010-03.1 Lower Connection

Figure 6.35: Test SSRE010-03.1 Upper Connection

Impacting Mass Behavior

Average pressure and impulse were calculated from the BG accelerometers and hydraulics using the method described in Section 4.2.2. These are depicted in Figures 6.36, 6.37, and 6.38.
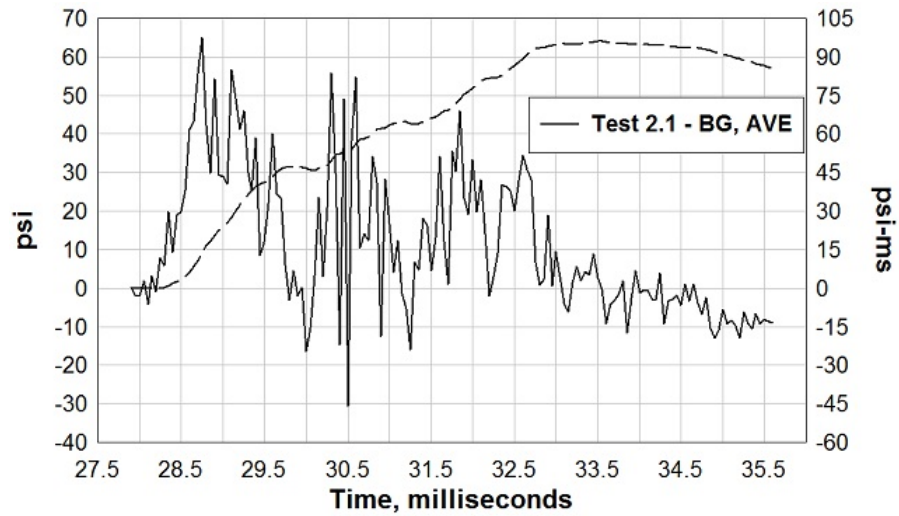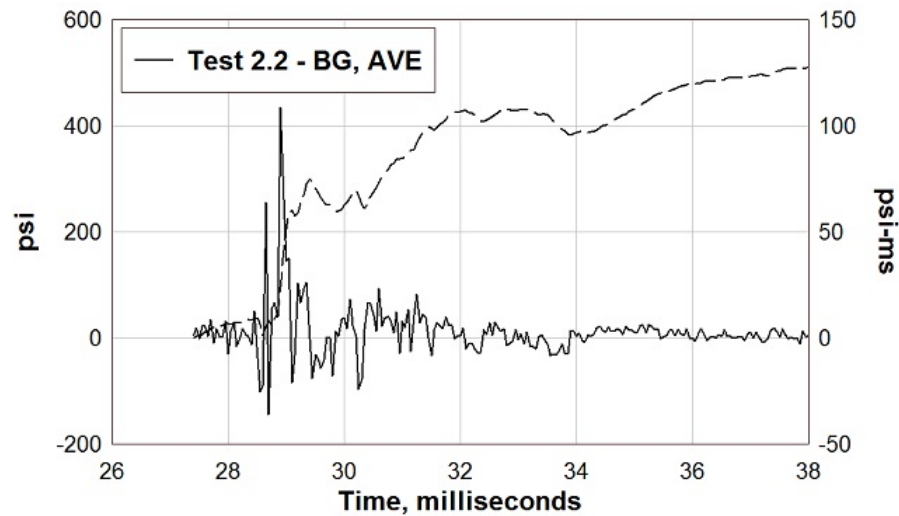
Figure 6.36: Test SSRE010-03.1 Average Pressure and Impulse

Figure 6.37: Test SSRE010-03.2 Average Pressure and Impulse

Figure 6.38: Test SSRE010-03.3 Average Pressure and Impulse

Specimen Behavior

Figures 6.39, 6.40, and 6.41 show the response of the specimens, recorded with the high speed cameras recorded at approximately 5,000 frames per second. The first frame shows the specimen at initial contact and the second frame shows the specimen at approximate end of contact. The third frame captures the maximum response of the specimen, while the last frame shows the residual deflection of the specimen. No visible damage occurred in the first test. Damage occurred primarily in the compression flange at mid-height in the second test. The third test caused significant hinging at mid-height. A more detailed view of the damage from the second and third tests are shown in Figures 6.42 and 6.43.
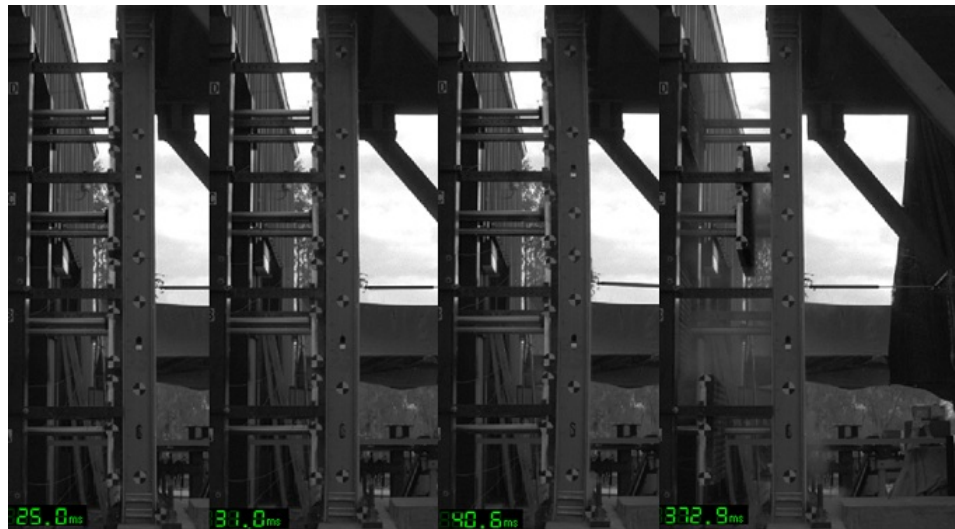
Figure 6.39: Test SSRE010-03.1 High Speed Video Time-lapse

Displacements were measured using camera data and a single LVDT behind the specimen for the first test. For the second and third tests, only camera data was available. A summary of the maximum, maximum rebound, and residual displacements for each of the specimen target locations, for the three tests are given in Table 6.6, Table 6.7, and Table 6.8. Angle displacement is also provided.

Appendix E.3 contains complete displacement-time histories, individual BG pressure-
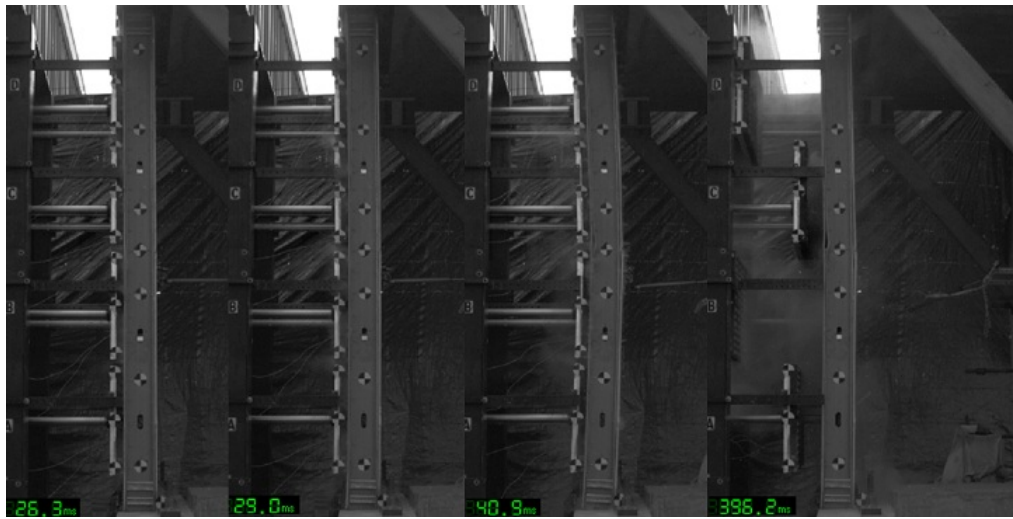
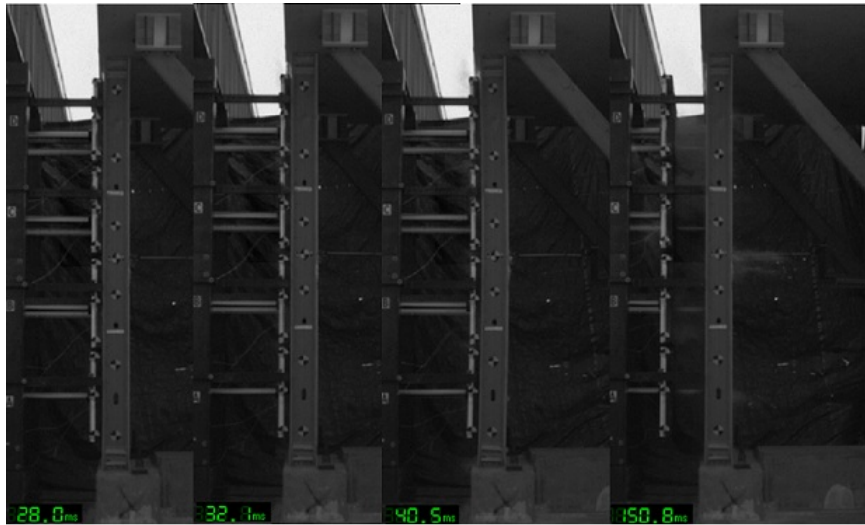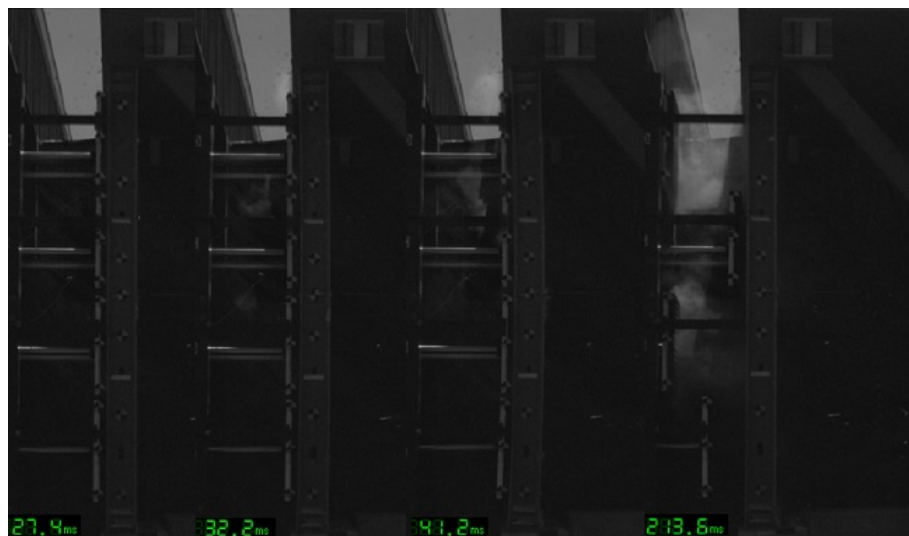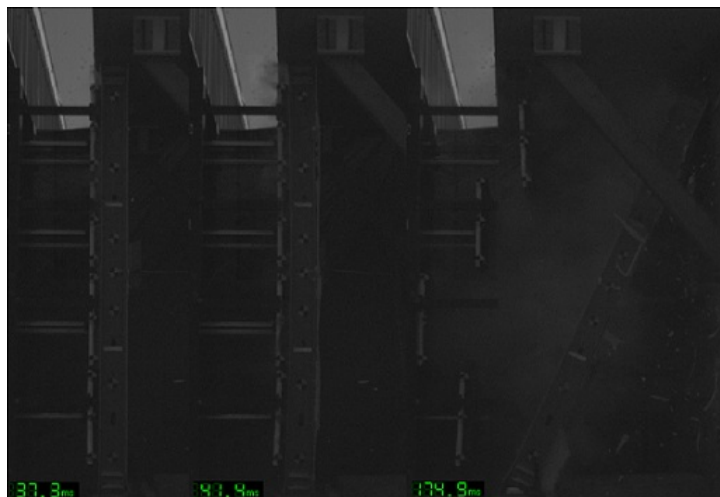**Figure 6.40**: Test SSRE010-03.2 High Speed Video Time-lapse
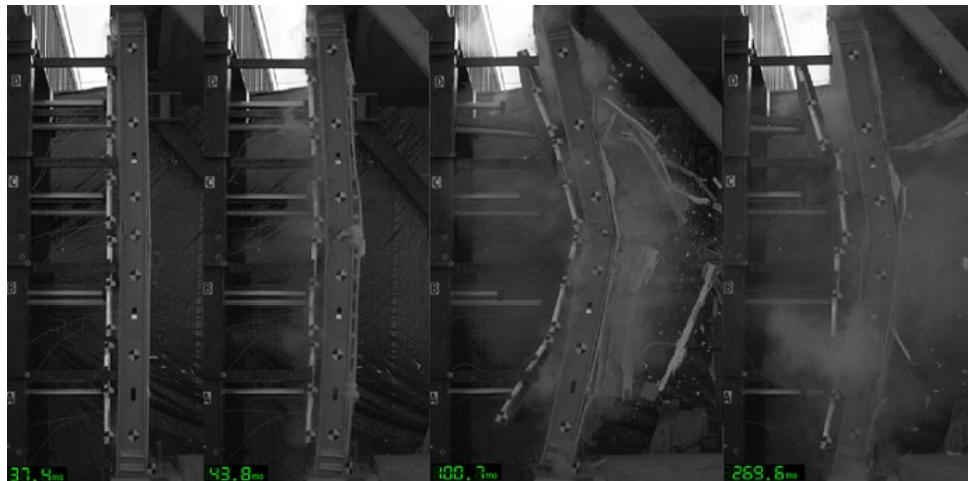
Figure 6.41: Test SSRE010-03.3 High Speed Video Time-lapse

Figure 6.42: Test SSRE010-03.2 Primary Damage

Table 6.6: Test SSRE010-03.1 Camera Displacement Summary

Distance from Wall Base (ft)	Maximum Displacement (in)	Maximum Rebound (in)	Residual Displacement (in)
1	1.07	2.46	0.03
3	1.70	3.10	-.05
5	2.05	3.50	-.17
6	2.12	3.57	-.21
7	2.03	3.46	-.31
9	1.62	3.11	-.49
11	1	2.50	-.65
BOTT ANGLE	.60	.98	.31

Figure 6.43: Test SSRE010-03.3 Damage

Table 6.7: Test SSRE010-03.2 Camera Displacement Summary

Distance from Wall Base (ft)	Maximum Displacement (in)	Maximum Rebound (in)	Residual Displacement (in)
1	.89	2.15	-1.00
3	1.82	1.94	-.70
5	2.54	3.05	-.45
6	2.74	3.05	-.29
7	2.56	2.99	-.44
9	1.91	2.66	-.82
11	1.08	2.14	-1.17
BOTT ANGLE	.44	.44	-.07

Table 6.8: Test SSRE010-03.3 Camera Displacement Summary

Distance from Wall Base (ft)	Maximum Displacement (in)	Maximum Rebound (in)	Residual Displacement (in)
1	2.71	1.49	1.22
3	7.46	NG	NG
5	12.00	3.24	8.76
6	13.70	NG	NG
7	11.61	3.12	8.49
9	7.10	2.27	4.98
11	2.47	1.25	1.44
BOTT ANGLE	.51	.38	.13

time histories, simplified pressure-time histories, and another method for obtaining pressure and impulse using the specimen accelerometers.

6.5.4 Test SSRE010-04 Results

Test Description

Sure-board®Test SSRE010-04 utilized five 12ga studs (6 in. depth), 12 in. on center. Two tests were performed on this specimen. The target impact velocities for these two tests were 14 m/s (551 in/s) and 18 m/s (709 in/s). A 246 lb flyer mass was used, which included the aluminum backing plate, programmer, and rod. The clear span of the specimen was 144 in. and targets to measure displacement were placed at 12 in., 36 in., 60 in., 72 in., 84 in., 108 in., and 132 in. from the footer. A photo showing the initial setup is given in Figure 6.44, and the lower and upper connections are displayed in Figure 6.45 and Figure 6.46. Note that the connections utilize so-called "blast-washers," which permit a small amount of rotation *via* elastic and inelastic bending.

Figure 6.44: Test SSRE010-04.1 Initial Setup

Figure 6.45: Test SSRE010-04.1 Lower Connection

Figure 6.46: Test SSRE010-04.1 Upper Connection

Impacting Mass Behavior

Average pressure and impulse were calculated from the BG accelerometers and hydraulics using the method described in Section 4.2.2. These are depicted in Figures 6.47 and 6.48.
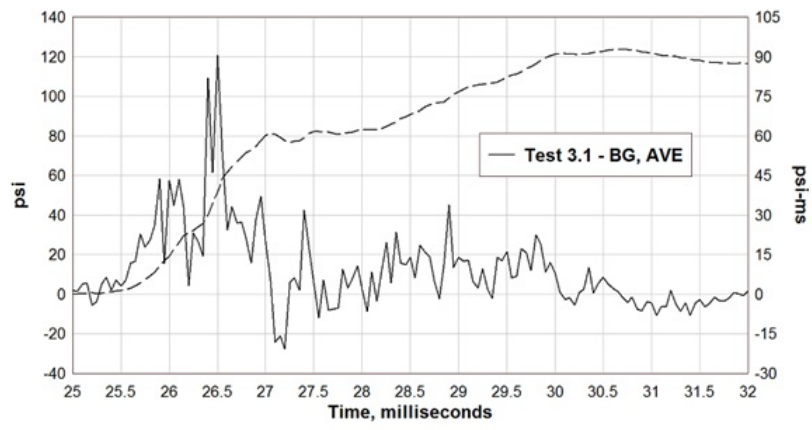

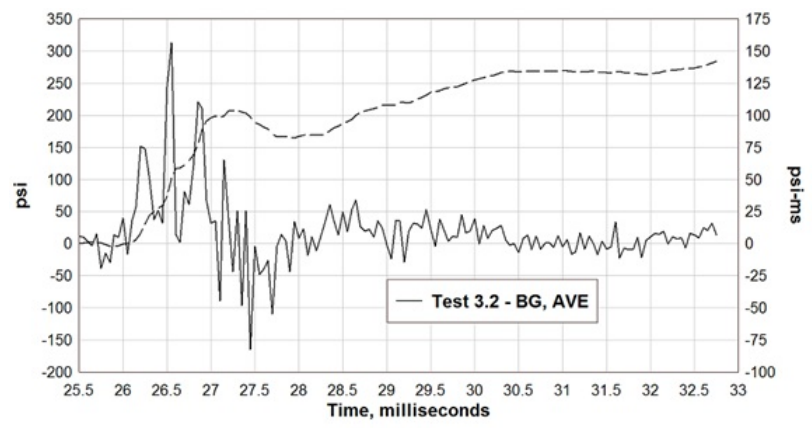**Figure 6.47**: Test SSRE010-04.1 Average Pressure and Impulse

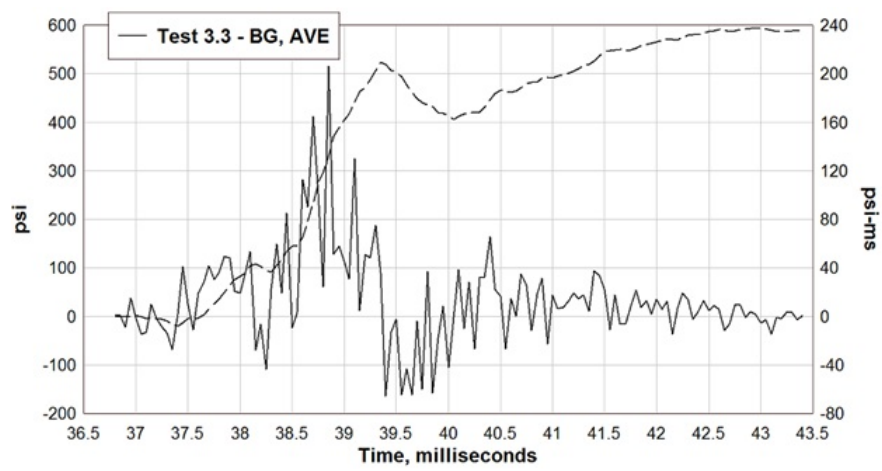**Figure 6.48**: Test SSRE010-04.2 Average Pressure and Impulse

Specimen Behavior

Figures 6.49 and 6.50 show the response of the specimens, recorded with the high speed cameras recorded at approximately 5,000 frames per second. The first frame shows the specimen at initial contact and the second frame shows the specimen at approximate end of contact. The third frame captures the maximum response of the specimen, while the last frame shows the residual deflection of the specimen. Damage occurred primarily at the second access hole in the first test. The second test exacerbated the buckling at this access hole. A more detailed view of the damage from these two tests are shown in Figures 6.51 and 6.52.

Figure 6.49: Test SSRE010-04.1 High Speed Video Time-lapse

Displacements were measured using camera data. A summary of the maximum, maximum rebound, and residual displacements for each of the specimen target locations, for the two tests are given in Table 6.9 and Table 6.10. Note that the target located 11 ft. from the ground was too dark to track in Test SSRE010-04.1 due to weather conditions.

Appendix E.4 includes additional Blast Simulator data for this test. Included in Appendix E.4 are complete displacement-time histories, pressure-time histories for each BG, simplified pressure-time histories, and pressure-time histories approxi-
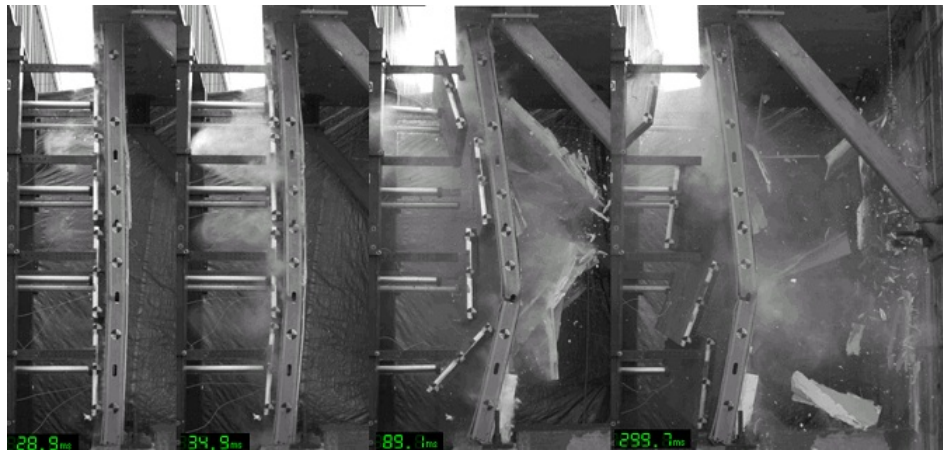
Figure 6.50: Test SSRE010-04.2 High Speed Video Time-lapse

Figure 6.51: Test SSRE010-04.1 Primary Damage

Figure 6.52: Test SSRE010-04.2 Damage

Table 6.9: Test SSRE010-04.1 Camera Displacement Summary

Distance from Wall Base (ft)	Maximum Displacement (in)	Maximum Rebound (in)	Residual Displacement (in)
1	1.57	1.25	.63
3	3.43	2.71	1.44
5	4.59	3.59	1.93
6	4.59	3.59	1.85
7	4.37	3.63	1.66
9	3.25	2.94	1.09
11	N/A	N/A	N/A

Table 6.10: Test SSRE010-04.2 Camera Displacement Summary

Distance from Wall Base (ft)	Maximum Displacement (in)	Maximum Rebound (in)	Residual Displacement (in)
1	4.69	1.63	3.54
3	9.37	3.01	7.15
5	10.81	3.49	8.15
6	9.71	3.32	7.18
7	8.17	3.03	5.85
9	5.52	2.49	3.69
11	2.68	1.74	1.5

mated from specimen accelerometer data.

6.5.5   Test SSRE010-05 Results

Test Description

Sure-board®Test SSRE010-05 utilized five 12ga studs (6 in. depth), 12 in. on center, with a clear span of 12ft. The target impact velocity for this test was 13 m/s (512 in/s). A 500 lb flyer mass was used, which included the aluminum backing plate, programmer, and rod. The clear span of the specimen was 144 in. and targets to measure displacement were placed at 12 in., 36 in., 60 in., 72 in., 84 in., 108 in., and 132 in. from the footer. A photo showing the initial setup is given in Figure 6.53, and the lower and upper connections are displayed in Figure 6.54 and Figure 6.55. Note that the connections utilize so-called "blast-washers," which permit a small amount of rotation *via* elastic and inelastic bending.

Figure 6.53: Test SSRE010-05 Initial Setup

Figure 6.54: Test SSRE010-05 Lower Connection

Figure 6.55: Test SSRE010-05 Upper Connection

Impacting Mass Behavior

Average pressure and impulse were calculated from the BG accelerometers and hydraulics using the method described in Section 4.2.2. This is depicted in Figure 6.56.
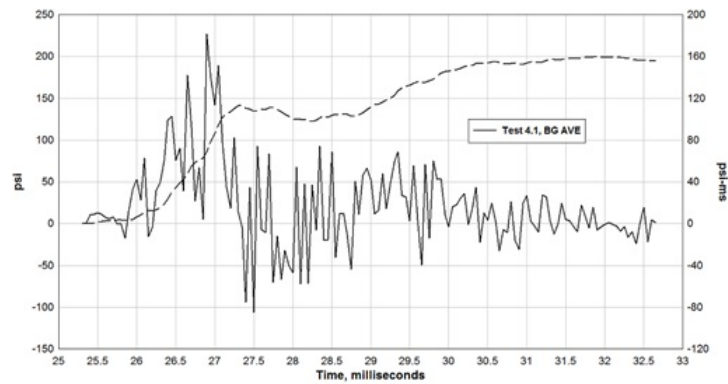

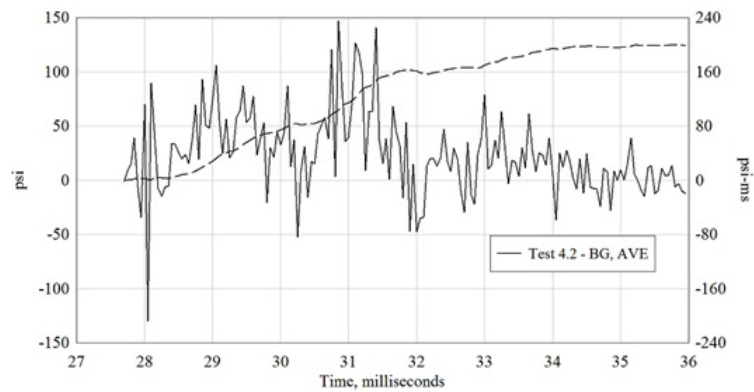**Figure 6.56**: Test SSRE010-05 Average Pressure and Impulse

Specimen Behavior

Figure 6.57 shows the response of the specimen recorded with the high speed cameras recorded at approximately 5,000 frames per second. The first frame shows the specimen at initial contact and the second frame shows the specimen at approximate end of contact. The third frame captures the maximum response of the specimen, while the last frame shows the residual deflection of the specimen. Damage occurred primarily at access hole 3 (mid-height) and at access hole 4. The damaged wall is shown in detail in Fig. 6.58.
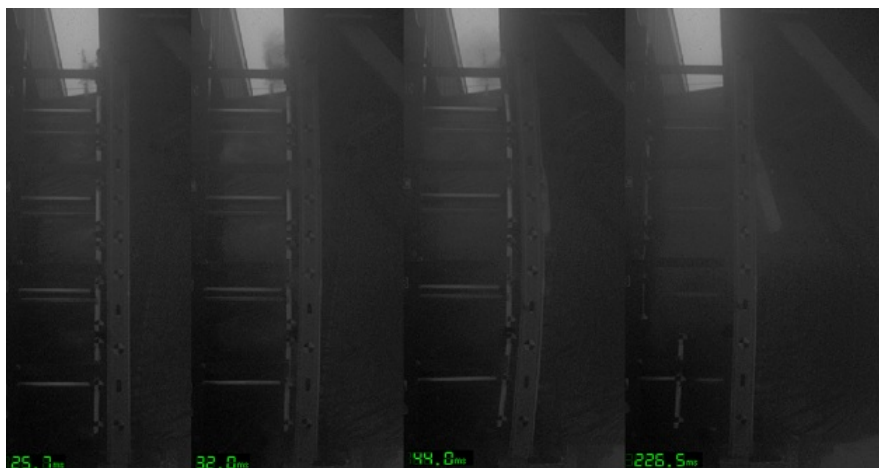

Figure 6.57: Test SSRE010-05 High Speed Video Time-lapse

Displacements were measured using camera data. A summary of the maximum, maximum rebound, and residual displacements for each of the specimen target locations is given in Table 6.11. Note that the obscuring of targets due to the presence of concrete spall results in some missing segments in the displacement histories.

Additional data is provided in Appendix E.5. This additional data includes various additional pressure-time plots, and complete displacement-history data.

Figure 6.58: Test SSRE010-05 Primary Damage

Table 6.11: Test SSRE010-05 Camera Displacement Summary

Distance from Wall Base (ft)	Maximum Displacement (in)	Maximum Rebound (in)	Residual Displacement (in)
1	1.73	n/a*	.98
3	4.35*	n/a	2.58
5	6.37	2.68	4.06
6	7.28	2.95	4.68
7	6.37*	n/a	4.40
9	4.31*	n/a	3.09
11	1.97*	n/a	1.27

*Targets obscured prior to max displacement

6.5.6 Test SSRE010-06 Results

Test Description

Sure-board®Test SSRE010-06 utilized ten 12ga studs (five "double" studs, 8 in. depth), 12 in. on center. The target impact velocity for this test was 17 m/s (669 in/s). A 500 lb flyer mass was used, which included the aluminum backing plate, programmer, and rod. The clear span of the specimen was 144 in. and targets to measure displacement were placed at 12 in., 36 in., 60 in., 72 in., 84 in., 108 in., and 132 in. from the footer. A photo showing the initial setup is given in Figure 6.59, and the lower and upper connections are displayed in Figure 6.60 and Figure 6.61. Note that the connections utilize so-called "blast-washers," which permit a small amount of rotation *via* elastic and inelastic bending. The angles are present as a "back-up" in the event of track failure.

Figure 6.59: Test SSRE010-06 Initial Setup

Figure 6.60: Test SSRE010-06 Lower Connection

Figure 6.61: Test SSRE010-06 Upper Connection

Impacting Mass Behavior

Due to DAQ operator error, the average pressure and impulse were calculated from the LS-DYNA contact force, rather than from the method described in Section 4.2.2, which post-processes BG accelerometer and hydraulic data. This LS-DYNA history is shown in Figure 6.62.
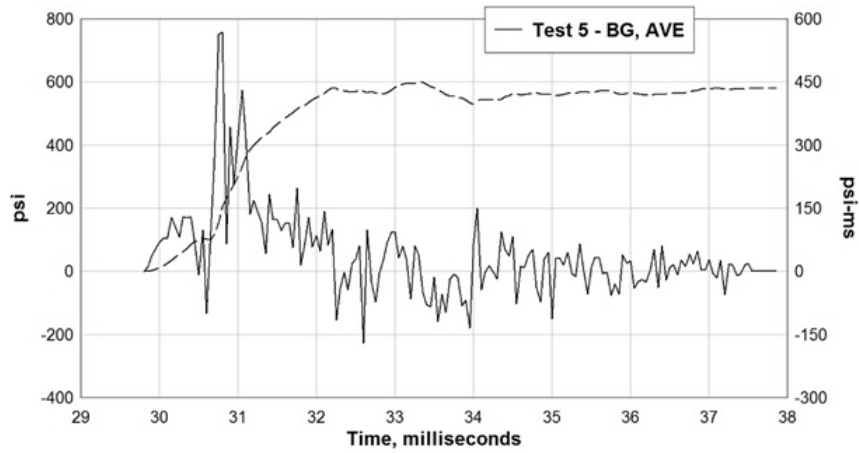

Figure 6.62: Test SSRE010-06 Average Pressure and Impulse

Specimen Behavior

Figure 6.63 shows the response of the specimen recorded with the high speed cameras recorded at approximately 5,000 frames per second. The first frame shows the specimen at initial contact and the second frame shows the specimen at approximate end of contact. The third frame captures the maximum response of the specimen, while the last frame shows the residual deflection of the specimen. Failure occurred at both primary connections, but the back-up angles "caught" the wall, without sustaining much damage. The wall is shown, post-test, in Fig. 6.64.
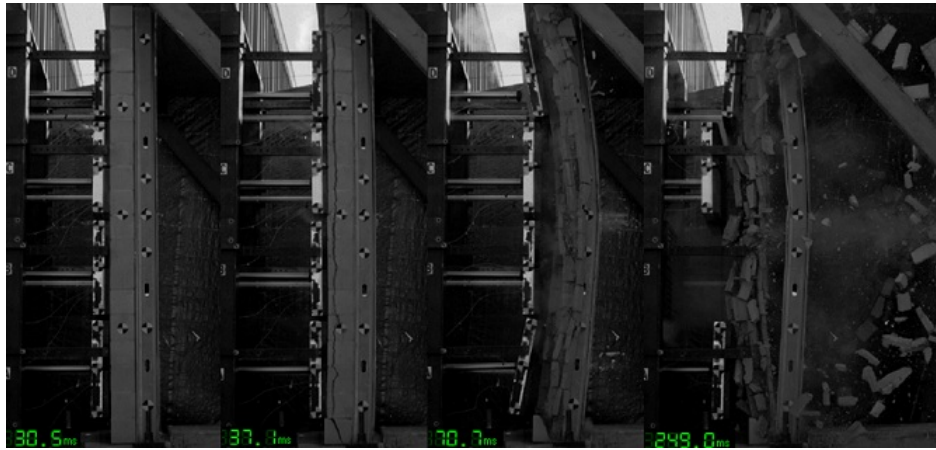

Figure 6.63: Test SSRE010-06 High Speed Video Time-lapse

Displacements were measured using camera data. A summary of the maximum, maximum rebound, and residual displacements for each of the specimen target locations is given in Table 6.12. Note that the obscuring of targets due to the presence of concrete spall results in some missing segments in the displacement histories.

Additional data is provided in Appendix E.6. This additional data includes complete displacement-time histories, a pressure-time history approximated from specimen accelerometers, and a simplified pressure-time history.

Figure 6.64: Test SSRE010-06 Primary Damage

Table 6.12: Test SSRE010-06 Camera Displacement Summary

Distance from Wall Base (ft)	Maximum Displacement (in)	Maximum Rebound (in)	Residual Displacement (in)
1	3.59	n/a	2.24
3	4.11	n/a	2.19
5	4.27	n/a	2.08
6	4.18	n/a	1.94
7	3.95	n/a	1.77
9	3.04	n/a	1.23
11	1.75	n/a	.69

*Connection failure occurred at approximately 60ms

6.5.7 Test SSRE010-07 Results

Test Description

Sure-board®Test SSRE010-07 utilized four 16ga studs (6 in. depth), 16 in. on center, with a clear span of 12ft. The target impact velocity for this test was 10 m/s (394 in/s). A 500 lb flyer mass was used, which included the aluminum backing plate, programmer, and rod. The clear span of the specimen was 144 in. and targets to measure displacement were placed at 12 in., 36 in., 60 in., 72 in., 84 in., 108 in., and 132 in. from the footer. A photo showing the initial setup is given in Figure 6.65, and the lower and upper connections are displayed in Figure 6.66 and Figure 6.67. Note that the connections utilize so-called "blast-washers," which permit a small amount of rotation *via* elastic and inelastic deformation.

Figure 6.65: Test SSRE010-07 Initial Setup

Figure 6.66: Test SSRE010-07 Lower Connection

Figure 6.67: Test SSRE010-07 Upper Connection

Impacting Mass Behavior

Average pressure and impulse were calculated from the BG accelerometers and hydraulics using the method described in Section 4.2.2. This is depicted in Figure 6.68.
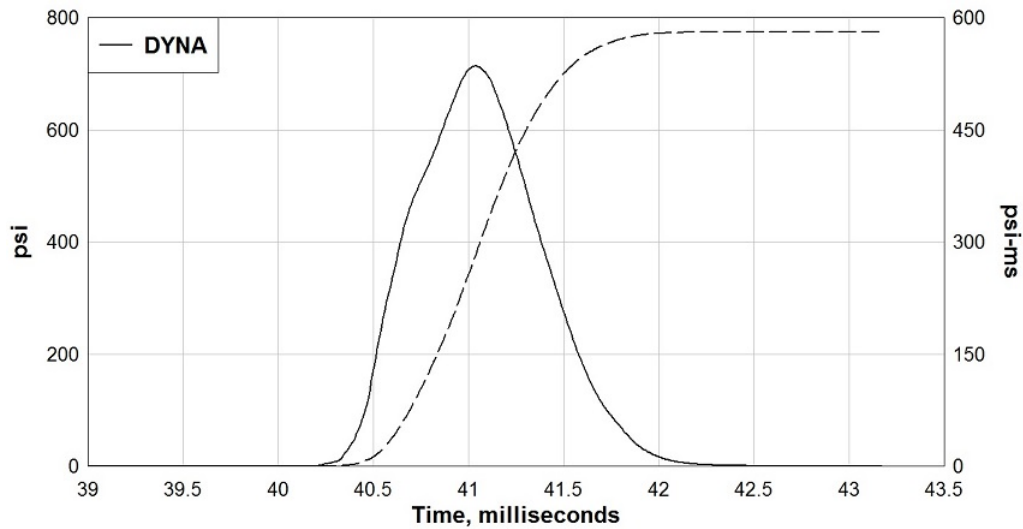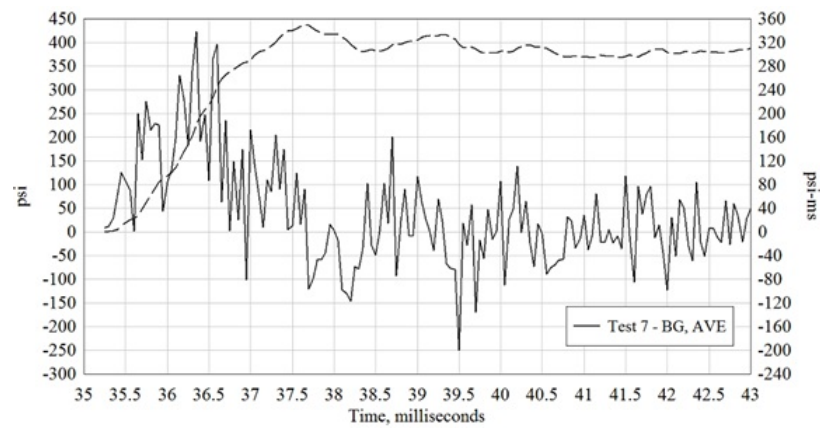
Figure 6.68: Test SSRE010-07 Average Pressure and Impulse

Specimen Behavior

Figure 6.69 shows the response of the specimen recorded with the high speed cameras recorded at approximately 5,000 frames per second. The first frame shows the specimen at initial contact and the second frame shows the specimen at approximate end of contact. The third frame captures the maximum response of the specimen, while the last frame shows the residual deflection of the specimen. Damage occurred primarily at access hole 4. The damage to this access hole is shown in detail in Fig. 6.70.
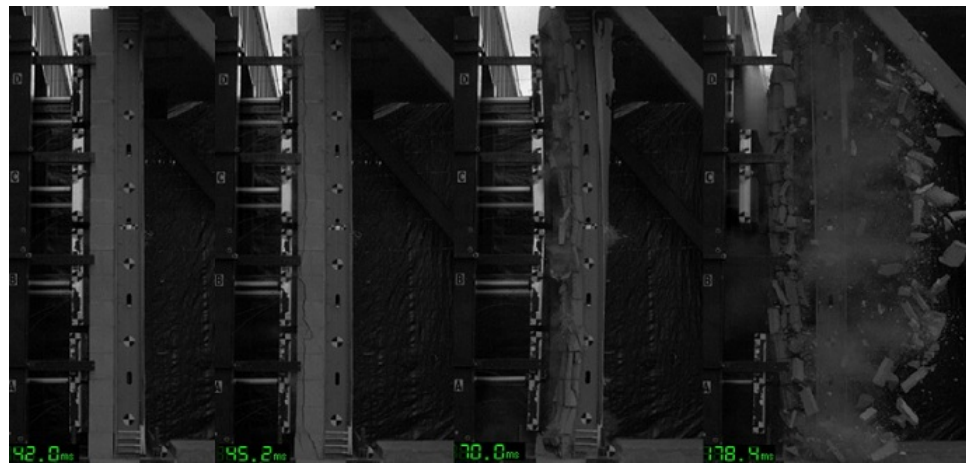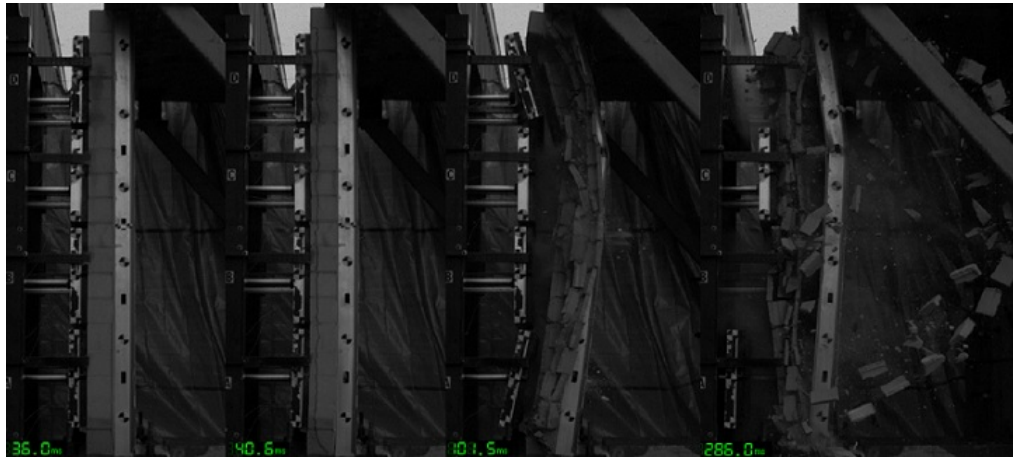

Figure 6.69: Test SSRE010-07 High Speed Video Time-lapse

Displacements were measured using camera data. A summary of the maximum, maximum rebound, and residual displacements for each of the specimen target locations is given in Table 6.13. Note that the obscuring of targets due to the presence of concrete spall results in some missing segments in the displacement histories.

Additional data is provided in Appendix E.7. This additional data includes complete displacement-time histories, individual BG data, and pressure-time histories obtained using various alternative techniques.

Figure 6.70: Test SSRE010-07 Primary Damage

Table 6.13: Test SSRE010-07 Camera Displacement Summary

Distance from Wall Base (ft)	Maximum Displacement (in)	Maximum Rebound (in)	Residual Displacement (in)
1	2.05	n/a*	1.02
3	5.28*	n/a	2.71
5	7.75*	n/a	4.11
6	9.31*	n/a	5.07
7	10.04*	n/a	5.39
9	8.29	4.40	4.33
11	3.25	n/a*	1.46

*Targets obscured prior to max displacement

6.6 Test Series SSRE010 Summary

This chapter documented the response of the experimental series of Sure-Board®wall specimens and Sure-Board®with un-grouted masonry wall specimens subjected to blast-like loadings using the University of California, San Diego Blast Simulator. The "track" style connections exhibited failure in two of the tests, whereas in all other tests damage was observed only at access hole locations throughout the height of the HSLA-V studs. A summary of loads and displacements is presented in Fig 6.14. In general, these prototype walls, which consist of HSLA-V studs, performed significantly better than identical walls that utilize mild steel studs (see [22]). A reduction of required material and lower transportation costs may make up for the increased cost of HSLA-V material compared to mild steel. In general, "The total construction costs of the new steel studsteel sheathing wall system constitutes a 30% savings with respect to the most cost-effective conventional or advanced blast wall system currently available in the market." [36]

6.7 Comparison to Field Tests

As discussed in Section 6.3, the Blast Simulator does not impart a uniform pressure to the wall specimens. Section 6.3 showed that an "equivalent uniform pressure" can be assumed for the purposes of comparing to the pressures and impulses that would be generated from vehicle-borne explosives, so long as the overall response of the wall system is the only parameter that is of interest. Without the presence of masonry, the wall system will exhibit significantly more localized panel deformation on exterior side of the wall under the kinds of uniform pressures generated from actual explosives, compared to Blast Simulator impact. The exterior sheathing suffered only mild damage in Blast Simulator tests. Compare this to the damage that is apparent from field tests of similar severity as shown in Fig. 6.71.

Fig. 6.71 shows the response of a Sure-board®wall when subjected to a 313 psi-ms impulse from a blast test carried out at Tyndall Air Force Base in June of 2012 [36]. While this wall had more robust connections compared to the walls

Table 6.14: Summary of loads and mid-span displacements

Test Number	Peak force [summed from all BGs] F_{s0} (lbf)	#BG	Time duration t_d (ms)	Specific Impulse I (psi-ms)	Mid-height Displacement δ (in)
SUREBOARD10	578,880	3	5.1	125	6.7
1	708,480	3	5.4	160	4.7
2.1	472,320	4	4.7	109	1.5
2.2	1,065,600	4	4.1	143	2.1
2.3*	2,453,760	4	3.3	299	--
3.1	489,600	4	5.1	104	2.1
3.2	898,560	4	4.6	144	2.7
3.3**	1,676,160	4	5.7	273	13.7
4.1	904,320	4	4.7	172	4.6
4.2**	541,440	4	6.0	230	9.6
5	2,592,000	4	3	400	7.7
6*	5,760,000	4	2.5	610	--
7	2,160,000	4	3	320	9.3

* Connection failure
** Significant specimen damage prior to test

Exterior   Interior

Figure 6.71: Significant exterior panel damage from shockwave [36]

tested at UCSD, the wall pictured in Fig. 6.71 was otherwise identical to wall SSRE010-02. Since wall SSRE010-02 exhibited connection failure in Test 2.3, a direct comparison between the Blast Simulator response and field test response is not possible. However, the exterior sheathing that spans in between the studs is clearly subjected to larger demands in the field test, compared to the loading behavior observed during Blast Simulator impact.

Additionally, a test was conducted at Tyndall Air Force Base that included the presence of un-grouted masonry. This specimen was identical to SSRE010-07, namely, 12 feet tall and comprised of 6 inch deep, 12 gauge HSLA-V studs, spaced at 16 inches. The loading was similar as well at just over 300 psi-ms. The response of the wall was nearly identical, with buckling occurring at the top access hole in the actual blast test as well as in SSRE010-07, and peak displacements estimated in both cases to be about 10 inches. Photos of the post-blast condition of the wall are reproduced in Fig. 6.72 from [36].

These two field tests corroborate the experimental data obtained on Sure-board®wall systems using the Blast Simulator. Adequate global response of the walls is achieved in Blast Simulator tests. In particular, when un-grouted masonry is present on the exterior side of the walls (*e.g.* SSRE010-05, SSRE010-06, SSRE010-07), the Blast Simulator impulses and the corresponding responses of the wall systems appears to be nearly identical to that observed in actual blasts. Since Blast Simulator impacts on Sure-board®walls that do not include the presence of masonry tend to impart a load to the studs more directly, compared to the significant local response of the exterior sheathing observed in field tests (Fig. 6.71), additional testing should be performed to assess the performance of the exterior sheathing under blast-like loads. This additional testing is important not only for assessing the sheathing bending behavior, but it is also important for determining adequate stud flange widths, lateral bracing design, and other details or fasteners that are affected by significant sheathing rotation at the locations of the studs. More information relating to field testing on these wall systems using live explosives is provided in Mayes [36] and Aviram [4].

Exterior   Exterior, sheathing partially removed
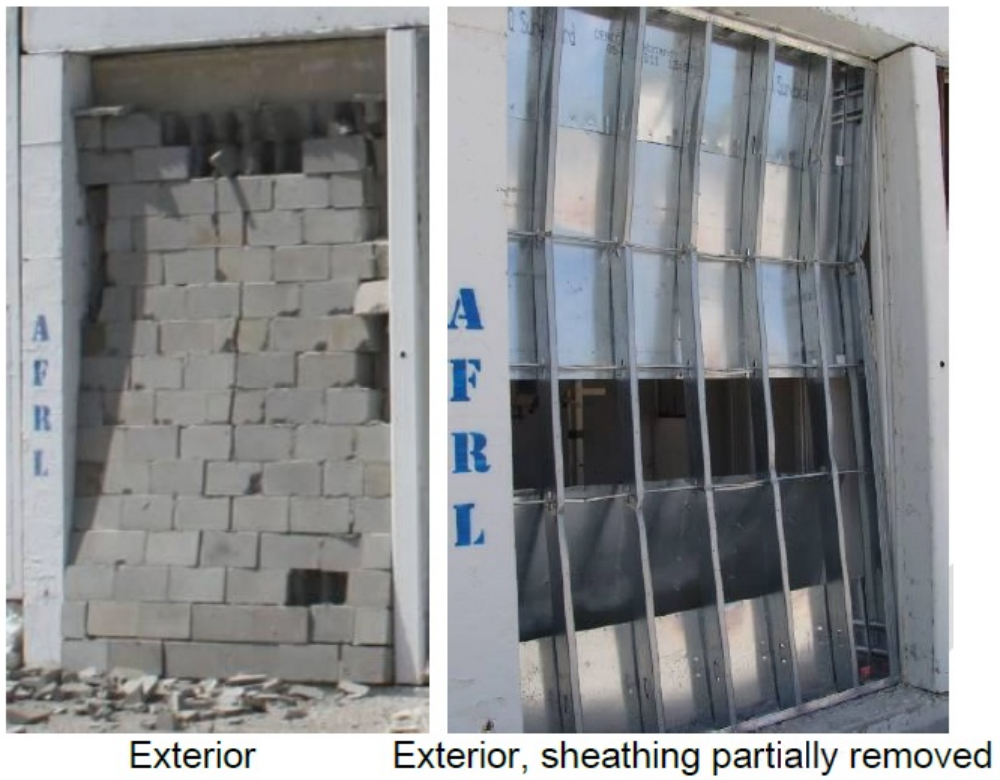
Figure 6.72: Response of un-grouted masonry + Sure-Board®wall specimen to blast [36]

Chapter 7

FEA Models

High-fidelity finite element analysis (FEA) models were created in LS-DYNA [19] for all of the tests that were performed with the exception of test 3.3 and test 4.2, since those tests were performed on walls that already contained significant damage.

7.1   Model descriptions

Each model contained, on average, 750,000 solid elements. The elements were TYPE 1 elements (uniformly reduced integration with hourglass control). Braces at the access or utility holes in the vanadium-alloy studs were represented in the model by boundary condition restraints. Even with these braces, buckling at the access holes was the most common mode of failure, as shown in Fig. 7.1.

At least two elements were present through the thickness of all parts, in order to capture bending. A mesh sensitivity study was performed that looked at, among other things, the number of elements that is required through the thickness of each part in order to capture the response in LS-DYNA (Fig. 7.2), namely, bending of the panels and buckling around the stud access holes.

Fig. 7.2 depicts a 4 in. tall by 5 in. wide section of the wall specimen on the exterior side of an access hole. In Fig. 7.2a, there are three elements through the thickness of the exterior panels, two elements through the thickness of the steel sheet and two elements through the thickness of the studs. Fig. 7.2b shows a finer

Figure 7.1: LS-DYNA buckling of access hole

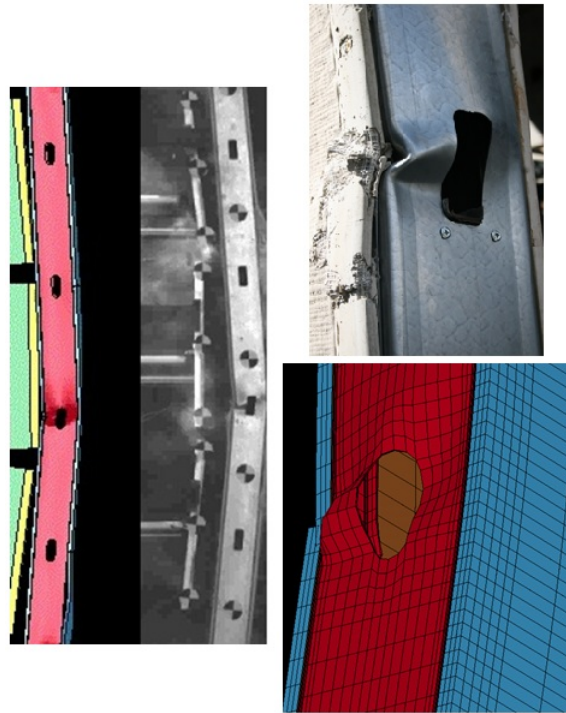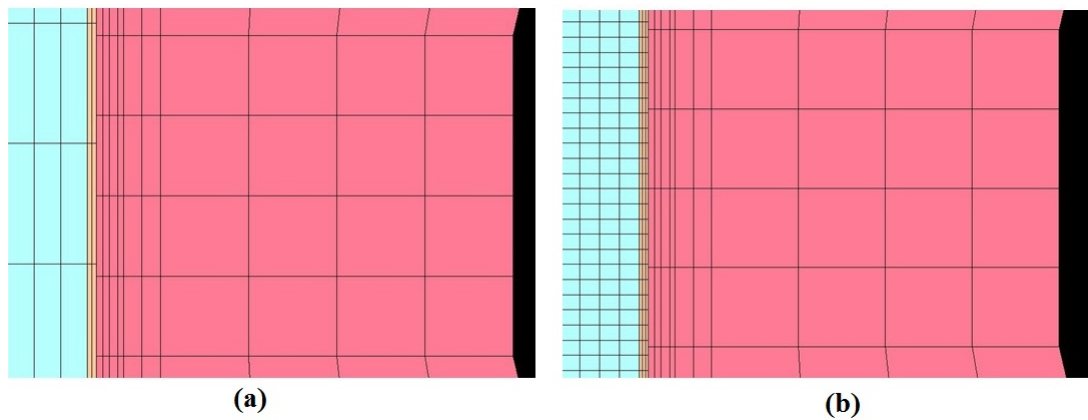**Figure 7.2**: LS-DYNA mesh sensitivity study: (a) Coarse mesh near access hole. From left to right: Exterior cement-board, 14Ga steel sheet, stud with. (b) Finer mesh near access hole.

mesh for the same specimen. No difference in the global or local response of the wall was observed, so the coarser mesh was adopted. Even with the coarser mesh, 750,000 elements were used per simulation, on average, resulting in CPU times of between 1000 and 2000 hours. For example, the average 50 millisecond Blast Simulator computer simulation would have a run-time of about 100 hours on a dedicated 12 processor system.

In most cases, the rigidity of the "blast washers" determines the stiffness of the connections. Thus, the "blast washers" were modeled in a manner that allows for some bending, similar to the way that they are constrained in the experiments. The sheathing, which consisted of a cement/drywall part bonded to steel sheet, was modeled as lightweight concrete with the steel sheet tied *via* merging of nodes. In practice, the sheathing is attached to the vanadium-alloy studs with screws. In the models, this connection is modeled as continuous, using a tie-break contact, and rigid, by setting the tie-break strength to a large value, since shearing or pullout of screws was rarely observed except at the top or bottom connections.

The predominant mode of top or bottom connection failure was screw failure followed by steel track bending and tearing, which occurred in three of the twelve tests. Thus, a tie-break contact was used at the top and bottom connections, in most cases, which contains parameters to control the onset of failure as well as propagation of failure along the path of the tied contact. One of the three tests where connection damage was observed developed only partial failure of the connection, while the other two tests formed a complete mechanism of failure at the connections. The tie-break parameters in the LS-DYNA model were calibrated primarily from the test that exhibited partial failure.

The kind of connection damage that was observed in the experiments appears to be independent of blast washer strength or stud strength. Instead, the connection strength appears to be dependent on track strength, which was unchanged from test-to-test. Thus, the LS-DYNA tie-break strength values at the connections were calibrated based on total shear force capacity. This is a relatively simple, and phenomenological, way of incorporating "stud-track" connection strength into the model, without explicitly modeling the track and all of

its associated hardware. The LS-DYNA tie-break contact that was chosen is
*CONTACT_AUTOMATIC_SURFACE_TO_SURFACE_TIEBREAK. The contact
strength for each of the connections is defined by two simple parameters, "NFLS"
and "SFLS," which correspond to the respective normal and shear stress capacities
of the contact. When $\left(\frac{\sigma_n}{\text{NFLS}}\right)^2 + \left(\frac{\sigma_s}{\text{SFLS}}\right)^2 > 1$, then the contact will break. In Table
7.1, these contact parameters are shown for each of the tests that were simulated
in LS-DYNA.

In addition, the Young's Modulus and the yield strength of the connection
material, the two material parameters that determine the rotational capacity of the
connection, is provided in Table 7.1. Some additional explanation of the values in
Table 7.1 will be provided throughout this chapter. Essentially, the two parameters
that determine the *resistance to failure* of the bottom or the top of a given wall
are determined in a manner so that the total strength capacity of the bottom or
the top of the wall is held constant from test-to-test. The two parameters that
determine the *resistance to rotation* of the bottom or the top of a given wall are
determined in a manner so that the rotational stiffness of the bottom or the top of
the wall is directly proportional to the number of blast washers that were present
in the test.

Table 7.1: Summary of connection parameters for FEA models

Test Number	E (psi)	σ_y (psi)	NFLS	SFLS
1	5,000,000	185,000	6700	13400
2.1, 2.2, 2.3	5,000,000	185,000	2500	5000
3.1, 3.2	N/A	N/A	N/A	N/A
4.1 (top)	10,000,000	370,000	6700	13400
4.1 (bott)	5,000,000	185,000	6700	13400
5	5,000,000	185,000	6700	13400
6	5,000,000	185,000	2500	5000
7	6,250,000	232,000	8400	16800

For some of the tests, a masonry wall was placed in front of the light gauge

steel wall. Mortar was modeled in the joints in between the CMU blocks and at locations of contact between the mortar and the CMU block, the nodes were merged. Thus, failure in the mortar joints is assumed to occur within the actual mortar material. This failure assumption as well as a more detailed description of the masonry wall geometry and mesh can be found in Oesterle [44].

The impact mass assembly, which consists of an aluminum mass with the programmer bolted to front and the piston bolted to the back, was modeled in a simplified manner, since any deformation of the aluminum is assumed negligible. The thickness of the aluminum in the model was taken to be arbitrarily thick, with the density scaled in order to account for the total weight of the aluminum and the piston. The programmer geometry, including the pyramids, was modeled in detail. Rather than modeling the programmer-aluminum bolts, which in practice are countersunk and so should not interfere with the collision, the nodes on the backside of the programmer are merged with the nodes on the front face of the aluminum. This is done in order to achieve connectivity without modeling bolt pretension and friction explicitly in the model.

In the LS-DYNA simulations of the wall tests, the motion of the impact masses are driven by incorporating the net hydraulic pressures into the simulation. As we know, each BG outputs a separate file containing its net hydraulic pressure-time history from the experiment, post-test. Even if the BG inputs are identical for each BG, the actual hydraulic pressure-time histories will vary in some cases quite significantly. So, in the LS-DYNA simulations, each impact mass is driven independently (see Fig. 7.3).

Including the hydraulics into the simulation for each impact mass in this manner is important, although the reasons may not be obvious. For example, treating the impact masses as simple projectiles in LS-DYNA typically will give satisfactory results for the initial impulse, however, double or triple hits may occur in the simulation, which do not typically occur in the actual tests. The hydraulic pressures are tailored in order to decelerate the impact mass beyond the initial contact in order to avoid such double hits. This impact mass behavior occurs naturally in the computer simulation so long as the hydraulic pressure-time histories
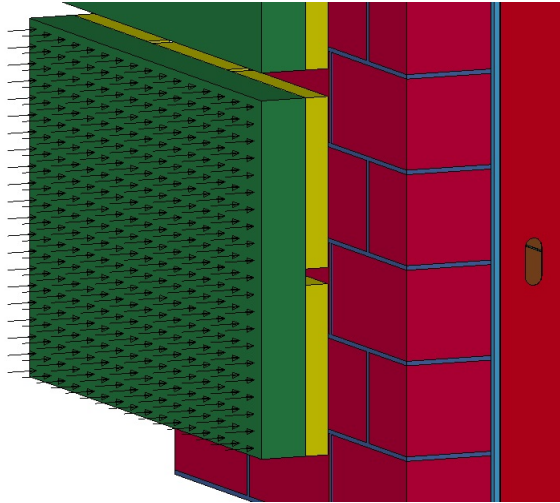
Figure 7.3: Depiction of LS-DYNA hydraulic pressure application. Each impact mass is driven independently.

are included in the simulation, as shown in Fig. 7.3.

Secondly, the masses do not all impact the specimen simultaneously. Although they will impact simultaneously under ideal circumstances, in most cases, the time of initial contact can vary by up to a millisecond, which may be significant since the total duration of impact is typically under five milliseconds. There are many test articles that are investigated in the Blast Simulator that are insensitive to this non-simultaneous impact. Light gauge walls, however, typically exhibit damage in the form of local buckling at a single access hole, and the location of such buckling along the height of the symmetric structure is influenced by the asymmetric loading, even if the loading is only slightly asymmetric. Thus, the order in which the masses impact is crucial. Incorporating the exact hydraulic pressure-time histories for each impact mass, as shown in Fig. 7.3 results in a correct simulation of non-simultaneous, and thus asymmetric, impact loading.

7.2 Material models

This section will describe the material models that were used in LS-DYNA. Unless otherwise stated, the material model that was used for a particular part can

be assumed rigid, either by using a metal model with large stiffness and strength or *MAT_RIGID. The connection materials will be described separately later on.

7.2.1 Programmer

The material of the programmer is Adiprene L-100/MOCA, which is Adiprene that has been cured with MOCA(methylene bis-orthochloroaniline) [48]. The LS-DYNA material model that is used for the programmer is *MAT_183, which is also known as *MAT_SIMPLIFIED_RUBBER_WITH_DAMAGE. This material model produces an exact "fit" to a baseline loading and unloading uniaxial experiment, and the model can be expected to produce good results for any kind of loading so long as the strain rates are close to the strain rate of the baseline test. Computer simulations of Blast Simulator tests will impart large strains in the programmer (up to 30% compression) along with complex loading due to the presence of the pyramids (Fig. 7.4), which is not a problem for the material model *MAT_SIMPLIFIED_RUBBER_WITH_DAMAGE. This is possible because the model is based on a "tabulated" formulation of the Ogden hyperelastic function, while the unloading is tabulated as well and, in general, will unload using a "damage" formulation. This model accommodates material nonlinearity with large deformations, but does not include failure.

To provide a simple means for accommodating strain rates that are different from the baseline, this material model permits a table of tabulated loading curves to be defined. The formulation of *MAT_SIMPLIFIED_RUBBER_WITH_DAMAGE is described in [28], and in detail in section 5.3. The theoretical advantages of this model over the previous programmer model are described in chapter 5, as well as its disadvantages when compared to more expensive models that incorporate viscoelasticity in a physical sense. The experimental data used to characterize the model and other important information relating to general rubber modeling methodologies are also discussed in chapter 5.
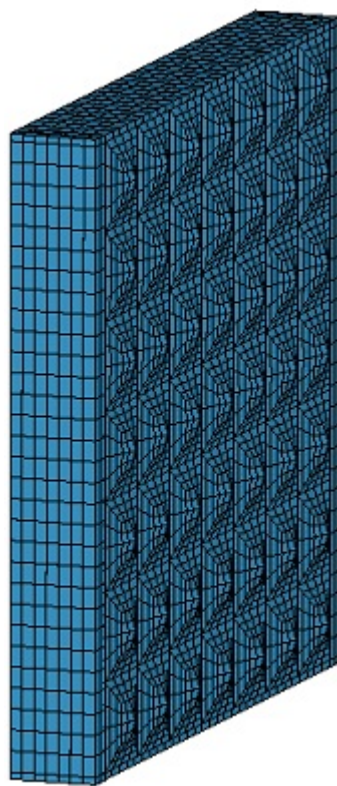
Figure 7.4: Programmer pad mesh

7.2.2 Masonry

The general stress-strain behavior of masonry or concrete under uniaxial compression is shown in Fig. 7.5. In Fig. 7.5, ϵ_u may be taken as .0025 for masonry and .003 for concrete. The uniaxial tensile behavior is quite different, and is sometimes depicted by a curve that plots stress versus crack width. The area under such a curve would be referred to as the fracture energy, G_f, which is the energy required to create a unit crack [44].
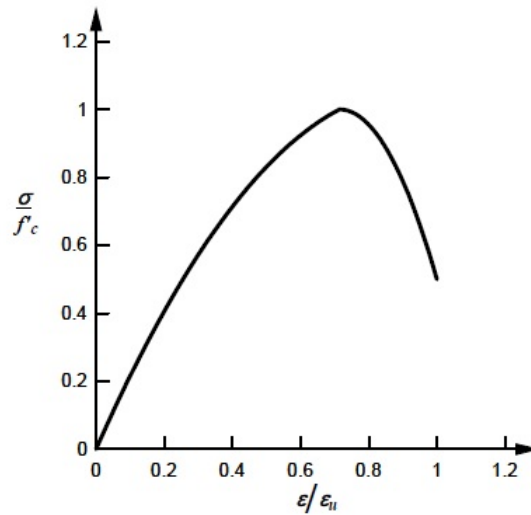

Figure 7.5: Uniaxial compression behavior of concrete [44]

To see how concrete or masonry behaves under biaxial stress, consider Fig. 7.6. The maximum strength of concrete or masonry in biaxial compression will increase according to curve $C - D$ in Fig. 7.6. In this stress state the maximum tensile strain in the direction opposite of the plane that is loaded will also increase [44]. Under biaxial compression-tension, the compressive strength decreases as the tensile stress increases, as depicted by curve $C - E$ in Fig. 7.6.

The increase in strength, due to confinement, of masonry and concrete specimens that are present in wall tests in the Blast Simulator may exceed five times the unconfined strength, and the failure strain may increase by more than a factor of eight [44]. The general failure surface that is used for concrete or masonry is depicted in Fig. 7.7a. Fig. 7.7b depicts a cross section of the failure surface in
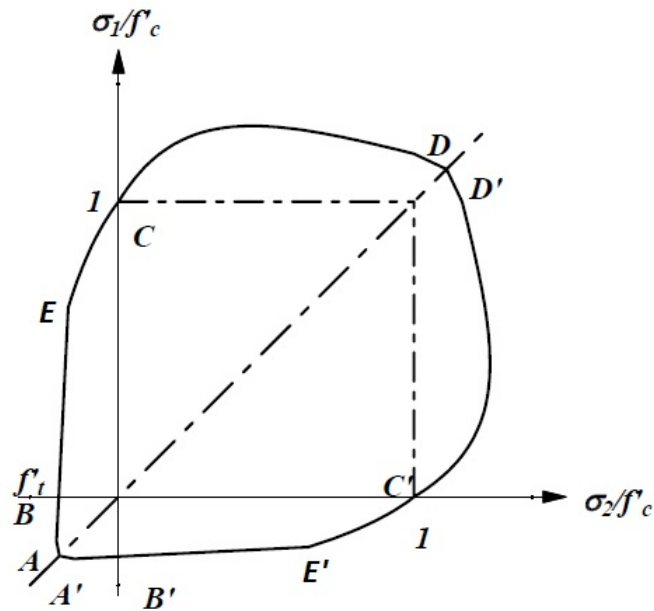
Figure 7.6: Biaxial stress behavior of masonry or concrete [44]

the deviatoric plane (looking down the hydrostat). At higher hydrostatic pressures the shape would be more circular.

As described by William and Warnke [65] and Oesterle [44], this general concrete model defines the failure surface with three stress invariants. The first invariant of the Cauchy stress defines the location of the deviatoric plane along the hydrostat. The second invariant of the deviatoric stress is used to determine the distance from the hydrostat to the failure surface (similar to "J_2" von Mises plasticity, which is used for metals, as we will see later). The third invariant called the angle of similarity, θ, is used to define the shape of the failure surface in the deviatoric plane. Strain rates for concrete and masonry cause different effects on strength for tension *vs* compression. Rate effects on compression may double the strength while the effect on tensile strength can increase by more than six times [44].

The material model that was used for all concrete and masonry elements in the LS-DYNA simulations was *MAT_72 release 3. This model, also called the K&C concrete model, assumes linear infinitesimal, isotropic, behavior that includes
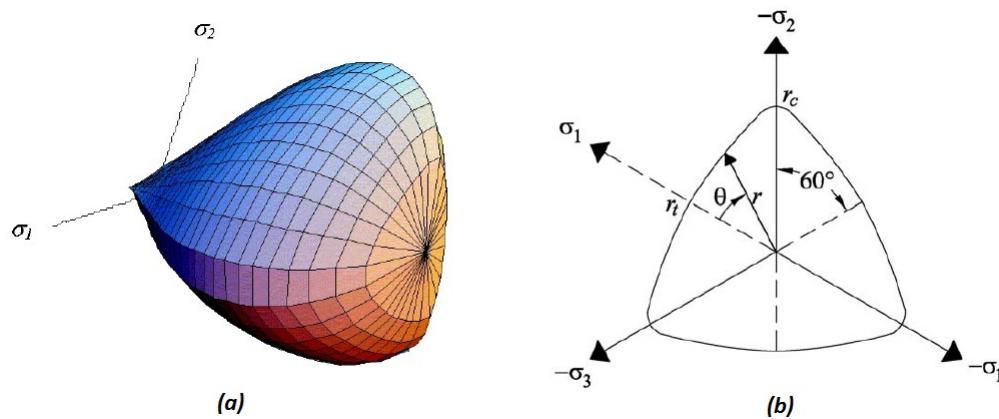
Figure 7.7: (a) Failure Surface of concrete or masonry in principal stress space [41] (b) Cross-section of failure surface in deviatoric plane [44]

rate effects and failure. This model decouples the volumetric and deviatoric parts of the compression response, treating the volumetric part with an equation of state (EOS) that tabulates pressure as a function of volumetric strain and strain rate. The deviatoric compression response is defined by three movable surfaces.

When the masonry or concrete reaches the yield surface, but has not yet reached the maximum failure surface, then the current failure surface is defined by linear interpolation between these two surfaces with the slope of the linear interpolation given by a hardening parameter that varies between 0 and 1. Once the maximum surface is reached, the failure surface is then interpolated between the maximum and residual surfaces with the slope of the linear interpolation given by a softening parameter that varies between 1 and 0 [44]. This can be visualized by inspection of Fig. 7.8, which shows how the behavior of concrete must incorporate plasticity when hydrostatic compression is considered. Additionally, this movable yield surface permits some material nonlinearity in the model - a well-known characteristic of concrete and masonry, even under uniaxial compression - as failure is approached.

Tensile behavior (cracks and crack propagation) is treated mostly separately, primarily using a fracture energy model. Rate effects are generally handled by scaling of the failure surfaces. More information on the theoretical foundations
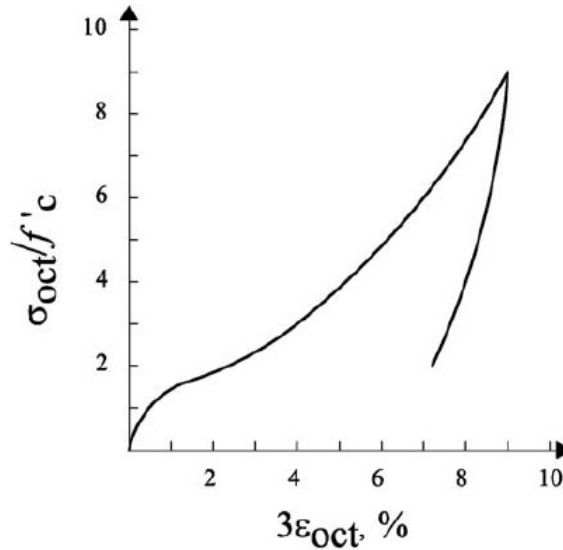
Figure 7.8: Concrete or masonry under hydrostatic compression [44]

of this material model can be found in Oesterle [44]. In practice, the density and uniaxial compressive strength of the concrete or masonry are the only material parameters that need to be input to *MAT_72.

Using *MAT_72, the concrete or masonry will behave as one expects. For example, the capacity will increase with an increase in confinement. Generally speaking, failure occurs *via* "cleavage," where failure surfaces slide over each other in a shearing fashion. This sliding between adjacent planes is prevented so long as the crack width is less than the thickness of the aggregate in the crack. Confinement increases this aggregate interlock and thus helps to prevent cracks from widening. On the other hand, under triaxial confinement (hydrostatic loading), failure can occur *via* plasticity, for example. All of these kinds of failure are considered, at least in a phenomenological sense, in the material model.

The strength of the CMU block material was set at 1,500 *psi*, in accordance with the specified CMU strength from the builders. The density was assumed to be 110 lbs/ft^3, per Oesterle [44]. The mortar strength was taken as 920 *psi*, which is slightly lower than would be expected for Type S mortar. As explained in Oesterle [44], this was done in order to represent the lower tensile strength at the interface between the mortar and the CMU block without modeling this interface explicitly.

In the LS-DYNA model, the interface between the CMU and mortar was "merged" and thus forms a rigid connection.

Erosion may be set to a strain value of .0125, using *MAT_ADD_EROSION, which is quite conservative. Erosion is not generally needed for the constitutive properties of the material model to work correctly, but the simulation of spalling may be of interest in some cases. Caution should generally be taken when implementing erosion, but the presence of erosion with values of .0125 or greater has been verified to give the same structural response for these wall systems as for the simulations without erosion. Fig. 7.9 shows an example of one of the wall simulations using *MAT_ADD_EROSION.
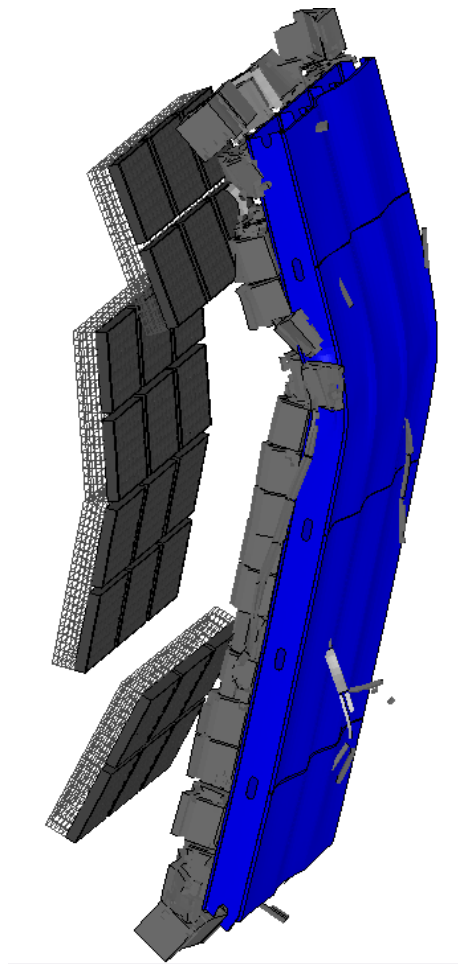

Figure 7.9: LS-DYNA simulation (test 7) with masonry erosion

7.2.3 Steel/Vanadium-Alloy

The steel and vanadium material models are characterized by metal plasticity. Specifically, these materials are modeled in LS-DYNA with *MAT_PLASTIC_KINEMATIC, or *MAT_PIECEWISE_LINEAR_PLASTICITY, where the latter permits the user to input tabulated stress strain data in up to eight linear segments. These models are based on linear, infinitesimal, isotropy with a von-Mises failure surface. The Young's Modulus for steel is about 29,000ksi and the Young's Modulus for Vanadium is about 20,000ksi, although the Modulus of the HSLA-V studs was tested by SGH to be around 29,000ksi.

In index form, the constitutive relation for linear elasticity is:

$$\sigma_{ij} = \lambda\epsilon_{kk}\delta_{ij} + 2\mu\epsilon_{ij} \tag{7.1}$$

If eq. (7.1) is split into its deviatoric and volumetric parts, then eq. (7.1) can be written in the following equivalent way:

$$\sigma_{ij} = \sigma'_{ij} - P\delta_{ij} \tag{7.2}$$

In eq. (7.2), σ'_{ij} is the deviatoric stress and can be written as $\sigma'_{ij} = 2\mu\left(\epsilon_{ij} - \frac{1}{3}\epsilon_{kk}\delta_{ij}\right)$. In eq. (7.2), P is the pressure or volumetric component of the stress. It can be shown that P must be taken as $P = -\left(\lambda + \frac{2}{3}\mu\right)\epsilon_{kk}$ in order to arrive at the simple relation that is expressed in eq. (7.1).

Recall the concrete/masonry yield surface of the previous section (section 7.2.2). The shape of the concrete yield surface cross-section in any given deviatoric plane depends on its location along the hydrostat, as was shown in Fig. 7.7. In other words, damage in the concrete/masonry is a function of the hydrostatic pressure. In concrete/masonry this is handled by first decoupling the volumetric and deviatoric components of the stress as was done above (eq. (7.2)), although the volumetric pressure, P, in the masonry is found from an equation of state formulation. Then, the concrete/masonry material model finds the location of the stress demand in

principal stress space, relative to the yield surface, by calculating the first invariant of the stress and then the second and third invariants of the deviatoric stress.

In metal plasticity the volumetric component of the stress is ignored altogether since the von Mises yield surface is independent of pressure. This independence of hydrostatic pressure is shown pictorially in Fig. 7.10, where we can see that the yield surface has the same cross-sectional shape at every point along the hydrostat. Additionally, in metal plasticity, only the second invariant of the deviatoric stress demand is needed in order to compare to the von Mises yield surface in principal stress space. The third invariant is not needed, for example, since the von Mises yield surface is circular and, therefore, symmetric.

Metal plasticity occurs when:

$$\bar{\sigma} = \sqrt{II_{\sigma'}} \geqslant k \tag{7.3}$$

In eq. (7.3), $\bar{\sigma}$ is the von Mises stress, $II_{\sigma'} = $ "J_2" $= \frac{1}{2}\boldsymbol{\sigma'} : \boldsymbol{\sigma'} = \frac{1}{2}\sigma'_{ij}\sigma'_{ij}$ and $k = \frac{f_y}{\sqrt{3}}$

$II_{\sigma'}$ can also be written in terms of the principal stresses, as follows:

$$II_{\sigma'} = \sqrt{\frac{(\sigma_1 - \sigma_2)^2 + (\sigma_2 - \sigma_3)^2 + (\sigma_1 - \sigma_3)^2}{6}} \tag{7.4}$$

The initial yield surface is defined by following equation:

$$f = \bar{\sigma} - k = 0 \tag{7.5}$$

Eq. (7.4) is derived in [34] and, along with eq. (7.5), is useful for constructing the cylindrical shape of the yield surface in principal stress space. This surface can be described as a cylinder with radius $\sqrt{\frac{2}{3}}k$ that follows the hydrostat in principal stress space, as depicted in Fig. 7.10.

Once yield is reached, plasticity is treated using:

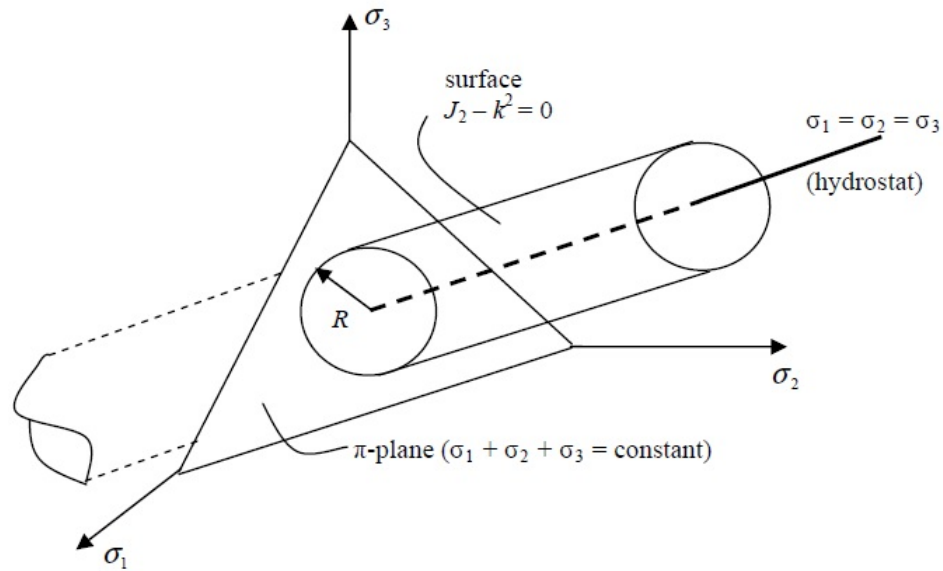$$\dot{f} = \dot{\bar{\sigma}} - H\dot{\bar{\epsilon}}^p \tag{7.6}$$

Figure 7.10: von Mises yield surface [59]

In eq. (7.6), H is proportional to σ/ϵ - *i.e.* H is the hardening parameter. In eq. (7.6), $\dot{\bar{\epsilon}}^p = \sqrt{2\dot{\epsilon}'^p : 2\dot{\epsilon}'^p}$. Furthermore, $\dot{f} = 0$ is enforced using a radial return algorithm [43]. The treatment of plasticity is volume-preserving and independent of applied pressure.

Isotropic (yield surface expanding) or kinematic (yield surface moving) or some combination of each can be specified in *MAT_PLASTIC_KINEMATIC or *MAT_PIECEWISE_LINEAR_PLASTICITY by a single parameter. Isotropic hardening is assumed for the metal materials in this dissertation, although maximum deformations (monotonic) will be of primary interest for the SGH wall specimens, and so kinematic hardening would give identical results. In addition, a table defining the yield stress versus plastic strain can be defined for various levels of strain rate.

Such effects are incorporated into either *MAT_PLASTIC_KINEMATIC or *MAT_PIECEWISE_LINEAR_PLASTICITY by placing a multiplication factor on eq. (7.6). Rate effects are included on all mild steel parts (50 ksi yield). For this purpose, *MAT_PIECEWISE_LINEAR_PLASTICITY is used as described in more detail in Stewart [59]. Specifically, the Cowper-Symonds model is used for

strain rate effects. More information on this can be found in the LS-DYNA theory manual [19]. A more detailed look at the rate-form of eq. (7.5), the stress updating algorithm, and other general information on the LS-DYNA implementation of plasticity can also be found in [19].

Rate effects are absent for the vanadium alloy studs, due to lack of data. To minimize computation, the cheaper *MAT_PLASTIC_KINEMATIC is used for the vanadium studs. This is justified since the studs are relatively high strength (85ksi), where rate sensitivity is known to be reduced [33].

7.2.4   Cement Board and Gypsum Board Sheathing

The exterior side (impact side) of the wall is composed of Sure-board Durock®cement board, and was modeled using the same material model that was used for the masonry mortar. This material model is *MAT_72 release 3, developed by K&C. The compression strength of the cement board was taken to be 400 psi, per [36].

The interior side of the wall is composed of gypsum board "drywall," which offers relatively little structural stiffness. The material model that was used for this part was *MAT_PLASTIC_KINEMATIC, with an arbitrarily low stiffness. The strength was set to a high value so that the gypsum board behaves in a linear and predictable manner. The chosen material model actually displays more flexible behavior compared to using *MAT_NULL. This is likely due to complications such as hourglassing that were observed when *MAT_NULL was used, which were less of an issue when using *MAT_PLASTIC_KINEMATIC with low stiffness.

7.3   Computer Simulations of Wall Tests

The computer simulations will be presented in the order that they were performed, which is different than the order that the wall tests were performed in the Blast Simulator. Of the 12 HSLA-V tests that were performed with the Blast Simulator, 10 were modeled in LS-DYNA. Two of the 12 tests contained significant damage prior to the Blast Simulator impact and so were not modeled.

The idea was to start with the simplest wall test in order to achieve a proper baseline LS-DYNA model, and then build upon this baseline model. The simplest test, which was SSRE010-03.2, was therefore the first test that was validated *via* computer simulation. Models that include "blast washers" contain parameters to control connection failure and connection rotational stiffness. These complexities may introduce some error, so it was important to first validate test SSRE010-03.2, which did not contain blast washers. It was also a moderate impact, which we know can be simulated better than mild or severe impacts due to the limitations of the programmer material model (see chapter 5).

Wall 3 is the only wall that had "simple" bearing-type connections. All of the other walls contained fixity in their connections, typically due to the presence of "blast washer" connections. Among the remaining walls, moderate impacts included tests SSRE010-01, SSRE010-02.2, and SSRE010-04.1. Since test SSRE010-01 contained a special kind of semi-rigid top connection, and since test SSRE010-02.2 exhibited some connection damage, test SSRE010-04.1 was chosen as the second wall test to validate *via* computer simulation.

The next computer simulation that was performed was test SSRE010-01. The main source of error in the simulation of test SSRE010-01 is the rotational stiffness of the top connection. Following these computer simulations, models were created for test SSRE010-05 and SSRE010-07, both of which contained the addition of a masonry wall. The presence of the CMU and mortar material models and the severity of the programmer impacts are the main sources of error. Tests SSRE010-02.1 and SSRE010-03.1 were then performed. The error in these latter two simulations primarily comes from the mild impact from the programmers.

Since the wall specimens SSRE010-03.3 and SSRE010-04.2 were already damaged prior to the impact, they were not modeled. None of the aforementioned nine Blast Simulator wall tests or computer simulations exhibited connection damage. Test SSRE010-02.2 experienced partial connection damage and was thus modeled in order to validate LS-DYNA parameters that control connection damage. Test SSRE010-02.3, which experienced complete connection failure, was modeled, despite the existence of connection and mid-span flange damage prior

to the impact. The main purpose of simulating test SSRE010-02.3 was to show that complete connection failure is easily incorporated into the LS-DYNA models. Lastly, test SSRE010-06 was then modeled, which was the most complicated LS-DYNA model. It was a severe impact that exhibited complete masonry and connection failure.

7.3.1   Test SSRE010-03.2 Simulation

The LS-DYNA model for this wall test employed "TYPE 1" solid elements. Two of the access holes on each stud in the actual wall contained "clips" which were in place to prevent buckling at the access holes. In the LS-DYNA model, the access holes were braced, accordingly, by using boundary conditions. The access holes that were braced are shown in Fig. 7.11.
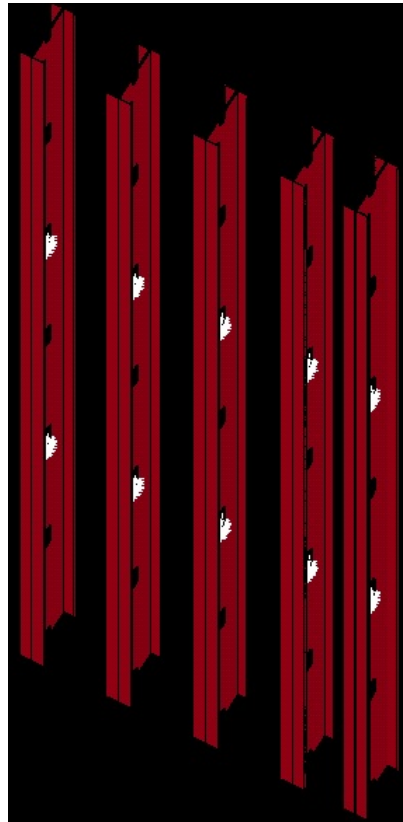
Figure 7.11: LS-DYNA boundary conditions at access holes for test 3.2

The top and bottom of the wall are not connected to the concrete header or footer. Instead, they bear against 6 in. angle sections. This connection, as modeled in LS-DYNA, is shown in Fig. 7.12, where a surface-to-surface contact is used between the wall and the angle, and boundary constraints are placed on the angle. Additionally, at this location, the stud wall is braced against crippling in the actual wall *via* web stiffeners, and is braced, accordingly, in the computer model (not shown).
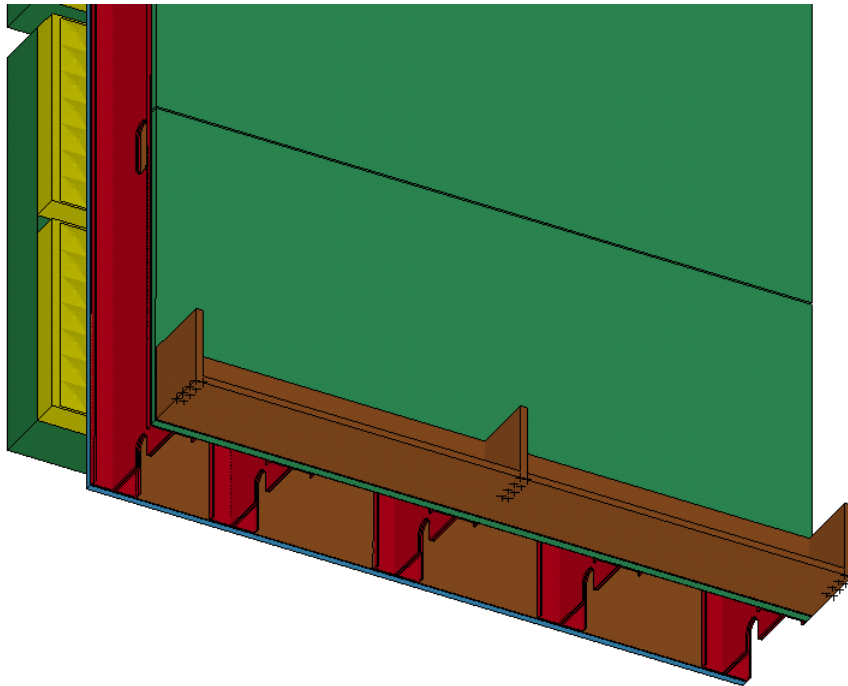

Figure 7.12: LS-DYNA connection fixities for test 3.2

The BGs were modeled in the simulation and were each driven by the net hydraulic pressure as recorded from the Blast Simulator test. A view of the simulation at maximum displacement is shown in Fig. 7.13a alongside a view of the corresponding Blast Simulator test at approximately the same time (Fig. 7.13b). We can observe that flange crippling occurred in the Blast Simulator test at mid-height, which did not occur in the LS-DYNA simulation.

A complete pressure-time history of the LS-DYNA contact force between the BGs and the wall is shown in Fig. 7.14. The total impulse imparted in the
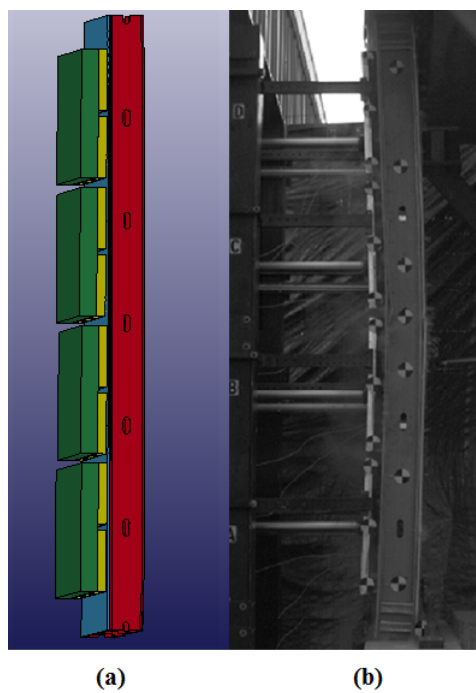
Figure 7.13: Deformed view (a) LS-DYNA simulation of test 3.2 (b) Blast Simulator experiment

LS-DYNA simulation compares quite well with the impulse that was recorded in the experiment, which is also shown in Fig. 7.14, although the time duration of the impulse appears shorter in the LS-DYNA simulation (approximately 3ms in the computer simulation *vs* 4ms in the experiment). This longer recorded duration may be a consequence of the oscillatory behavior of the accelerometers.
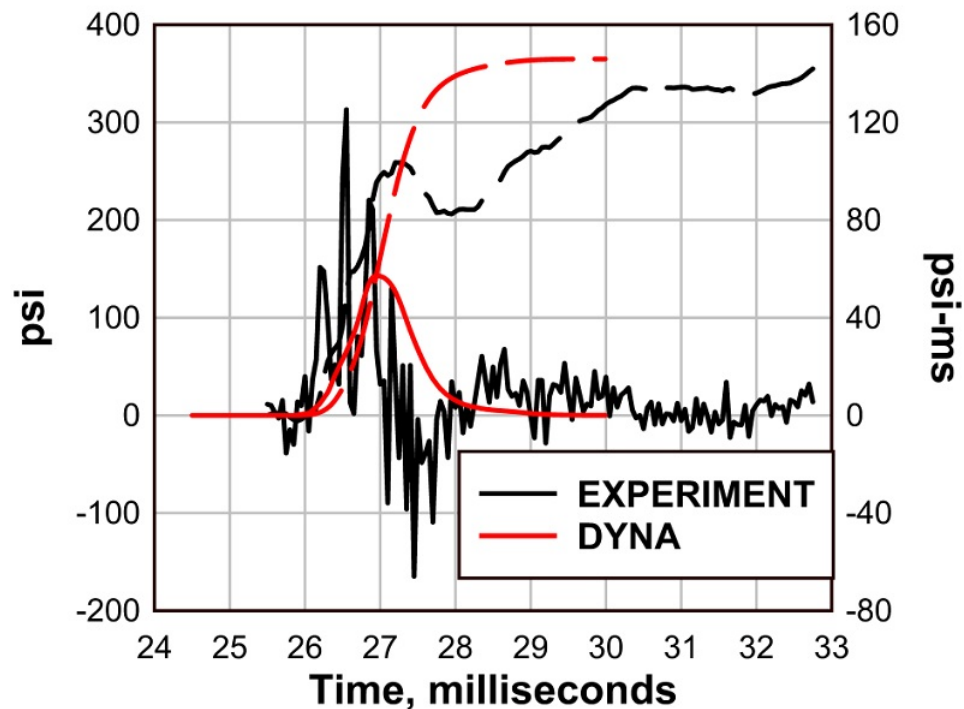

Figure 7.14: Pressure-time history of the LS-DYNA simulation of test 3.2, plotted alongside the average data recorded from the Blast Simulator experiment

The peak displacement *vs* height is shown in Fig. 7.15. We can observe that the mid-height displacement recorded in the experiment is greater than the mid-height displacement observed in the LS-DYNA simulation. This is most likely due to 1) damage that occurred at mid-height in the experiment which did not occur in the computer simulation, and 2) displacement of the 6 in. angles occurred in the experiment of approximately .25 in., which is not permitted in the computer simulation.
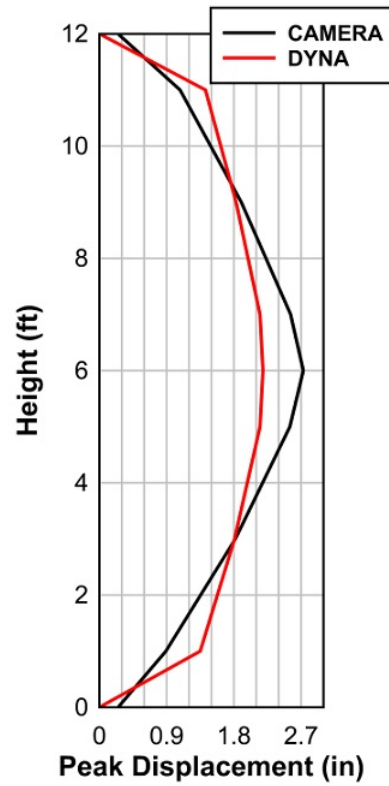
Figure 7.15: Displacement *vs* height of the LS-DYNA simulation of test 3.2, plotted alongside the corresponding camera data from the Blast Simulator experiment

7.3.2 Test SSRE010-04.1 Simulation

The LS-DYNA model for this wall test employed "TYPE 1" solid elements. The three middle access holes on each stud in the actual wall contained "clips" which were in place to prevent buckling at the access holes. In the LS-DYNA model, the access holes were braced, accordingly, by using boundary conditions. The access holes that were braced are shown in Fig. 7.16.
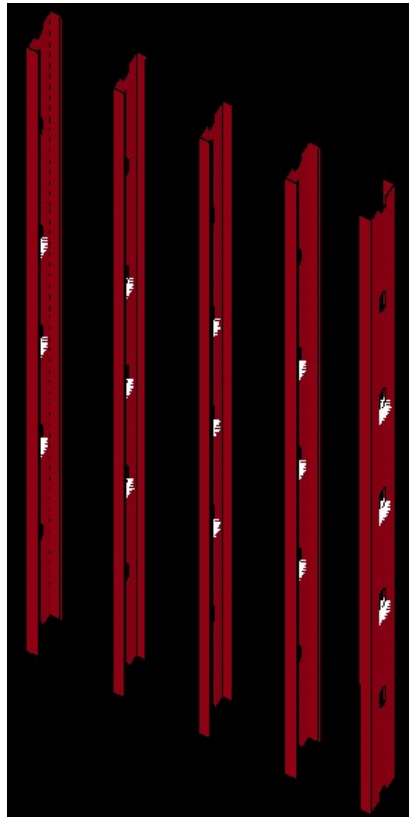
Figure 7.16: LS-DYNA boundary conditions at access holes for test 4.1

The bottom connection and the top connection, as modeled in LS-DYNA, have "blast washer" geometry and boundary conditions, which are shown in Fig. 7.17. For this connection type, a tie-break style contact is used within each connection in LS-DYNA in order to simulate failure if the connection shear forces are sufficiently large. Essentially, the LS-DYNA connection has a certain resistance to translation, and when this resistance is exceeded, the connection will simply fail.

In the actual Blast Simulator tests, this connection failure is a result of track and hardware damage (e.x. shearing and pullout of screws).

In addition, in the LS-DYNA model, boundary constraints are placed only at the interior faces of each connection (Fig. 7.17), in order to allow for sufficient rotation of the connection, which includes elastic and inelastic deformation. The rotational stiffness of the connection is primarily a function of the connection's Young's Modulus and plastic hardening behavior, which were assigned to the LS-DYNA material model of the connection. In the actual Blast Simulator tests, the rotational stiffness of the connection is determined by the number of "blast-washers."
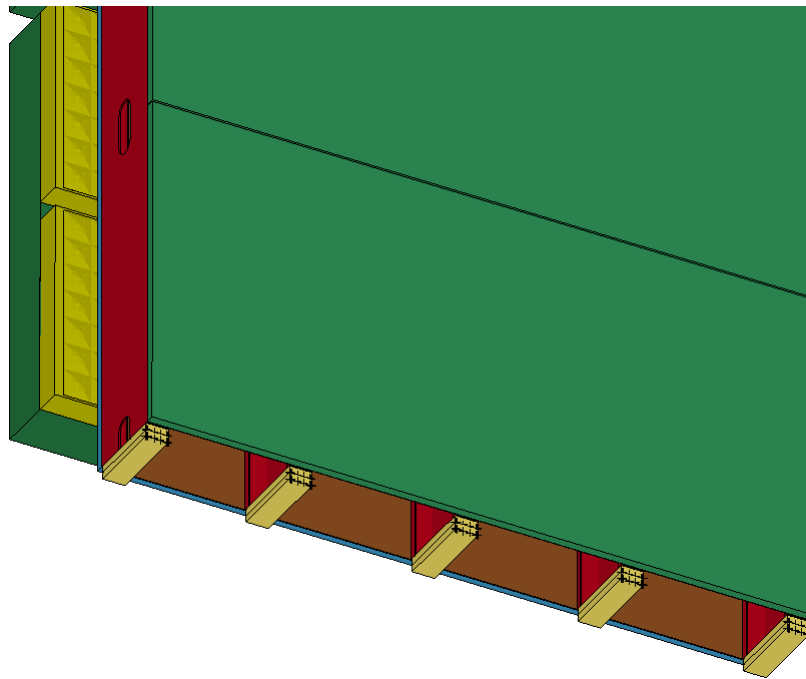

Figure 7.17: LS-DYNA connections for test 4.1

By comparing Fig. 7.17 to the photos and descriptions of the connections that were used in the Blast Simulator tests, we can see that many simplifications are present. The track and screws are not modeled, nor are the blast-washers, except in a phenomenological sense. So, in order to determine the important parameters of the LS-DYNA connections, namely, the tie-break strength and the

Young's Modulus, it is important to first recognize which factors in each Blast Simulator test most influence the connection strength and connection rotational stiffness.

Connection strength is nearly constant in the Blast Simulator tests, since the track does not change from test-to-test, nor does the hardware that connects the track to the wall, except for a single additional screw for each additional stud that is present. Thus, in LS-DYNA, the total shear capacity at the top or the bottom of the wall, which is the sum of the shear capacities of each of the individual connections, should remain constant. The number of individual connections in the LS-DYNA model, and the size of these connections (Fig. 7.17), is not constant, however. Instead, as we can see in Fig. 7.17, the number of individual connections in LS-DYNA is equal to the number of studs, and the length and width of each individual connection is equal to the depth and flange width of the corresponding stud. Since the total shear capacity at the top and the bottom of the wall is constant (and known, from Blast Simulator test SSRE010-02.2), but the number of individual connections in LS-DYNA is not constant, the tie-break strength parameter must be adjusted for each simulation. This tie-break strength parameter is adjusted in a manner such that the total shear capacity at the top or the bottom of the wall remains constant.

Connection rotational capacity in the Blast Simulator tests is primarily a function of the number of blast-washers. The more blast-washers that are used, the more effective the connection will be in resisting rotation. In all Blast Simulator tests, the number of blast washers used at the top or bottom of the wall was either four blast-washers or eight blast-washers. Thus, the overall connection rotational stiffness at the top or bottom of the wall in the LS-DYNA simulations should be one of two values. However, the number of individual connections at the top or bottom of each wall in the LS-DYNA simulations is equal to the number of studs, rather than the number of blast washers. Thus, the Young's Modulus and yield strength of the LS-DYNA connection material must be adjusted, carefully.

For example, the bottom connection in test 4 utilized four blast-washers. Test 1 and test 5, for example, have a blast-washer configuration that is simi-

lar to the bottom connection in test 4 (four blast-washers with five studs). The Young's Modulus that is used for each of the individual connections at the bottom of the wall in the LS-DYNA simulation for test 4 can therefore be considered a baseline value, and the same Modulus would be used for tests 1 and 5. Test 7, while also containing four blast-washers, only has four studs, and so the Young's Modulus that is used in LS-DYNA for the individual connections should be higher in order for the overall connection rotational stiffness to be the same as the other simulations that have four blast-washers.

Another common configuration is eight blast-washers. Test 2 and test 6, for example, have such a configuration (eight blast washers with ten studs). Since the number of blast-washers is doubled in those Blast Simulator tests, one can expect that the connection rotational stiffness should be doubled, compared to the bottom connection of test 4, for example. Since the number of studs is also doubled, however, achieving this stiffer (doubled) rotational stiffness requires that we use the *same* Young's Modulus for the individual connections in the LS-DYNA simulations of test 2 and 6 as in the simulations of tests 1,5, and the bottom connection of test 4. Thus, most of the connections in the LS-DYNA simulations utilize the baseline Young's Modulus value. Test 7 is an exception (four blast-washers with four studs), as previously described. The top connection in the LS-DYNA simulation for test 4 also requires a different Young's Modulus for the individual connections, since this wall has eight blast washers with only four studs. Thus, a very high Young's Modulus is required for the four individual connections at the top of the wall in this simulation. Recall that all of the relevant connection parameters for each of the ten LS-DYNA wall simulations were summarized in Table 7.1.

The BGs were modeled in the simulation of test 4.1 and were each driven by the net hydraulic pressure as recorded from the Blast Simulator test. A view of the simulation at maximum displacement is shown in Fig. 7.18b alongside a view of the corresponding Blast Simulator test at approximately the same time (Fig. 7.18a). The Blast Simulator test 4.2 is also shown for comparison (Fig. 7.18c). We can observe that buckling occurred at the second access hole in the Blast Simulator test, as well as in the LS-DYNA simulation. This buckling occurs in the simulation

(Fig. 7.18b) slightly before the buckling occurs in the experiment (Fig. 7.18a), hence the larger eventual peak displacement in the simulation.
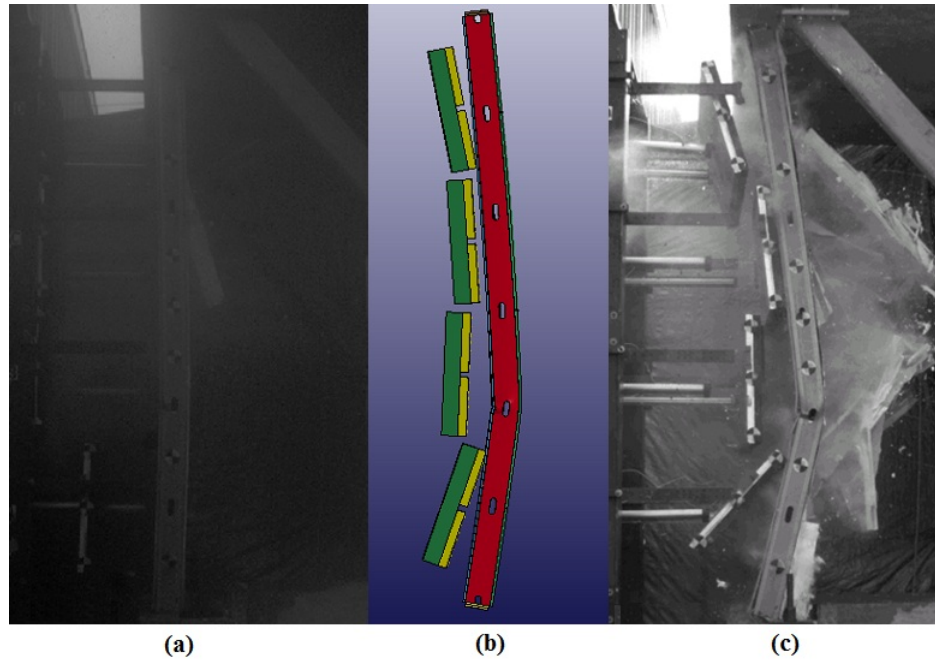

Figure 7.18: Deformed view (a) Blast Simulator test 4.1 (b) LS-DYNA simulation (c) Blast Simulator test 4.2

A complete pressure-time history of the LS-DYNA contact force between the BGs and the wall is shown in Fig. 7.19. The total impulse imparted in the LS-DYNA simulation compares quite well with the impulse that was recorded in the experiment, which is also shown in Fig. 7.19.

The peak displacement *vs* height is shown in Fig. 7.20. We can observe that the mid-height displacement recorded in the experiment is smaller than the mid-height displacement observed in the LS-DYNA simulation. This is most likely due to damage that occurred at the access hole in the computer simulation, which occurred at a later time in the experiment. The displacements recorded for test 4.2 are also shown in Fig. 7.20 for comparison.
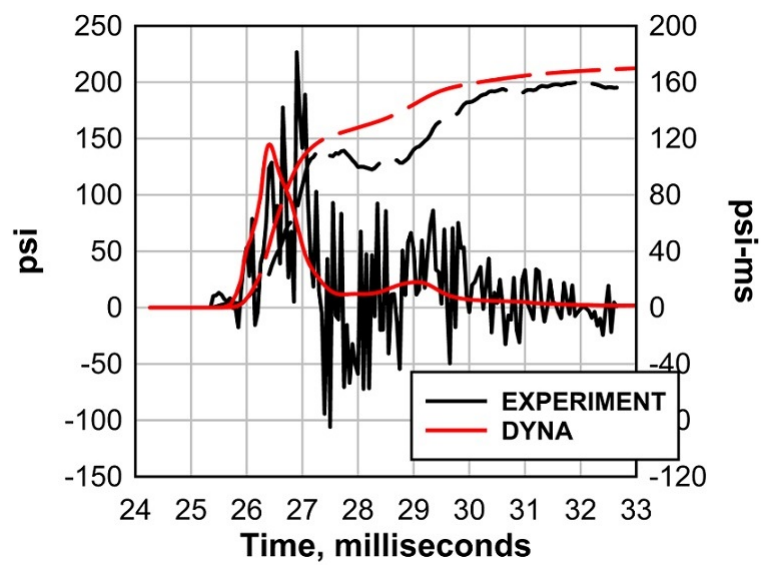
Figure 7.19: Pressure-time history of the LS-DYNA simulation for test 4.1, plotted alongside the average data recorded from the corresponding Blast Simulator experiment
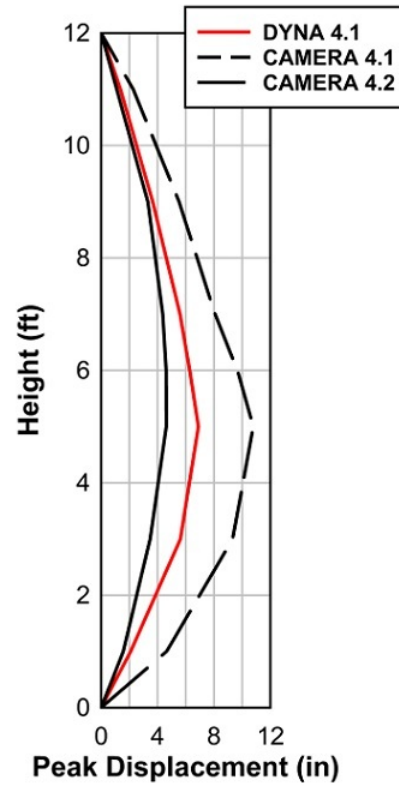
Figure 7.20: Displacement *vs* height of the LS-DYNA simulation 4.1, plotted alongside the corresponding camera data from the Blast Simulator experiments 4.1 and 4.2

7.3.3 Test SSRE010-01 Simulation

The LS-DYNA model for this wall test employed "TYPE 1" solid elements. Two of the access holes on each stud in the actual wall contained "clips" that were in place to prevent buckling at the access holes. In the LS-DYNA model, these access holes were braced, accordingly, by using boundary conditions. The access holes that were braced are shown in Fig. 7.21.
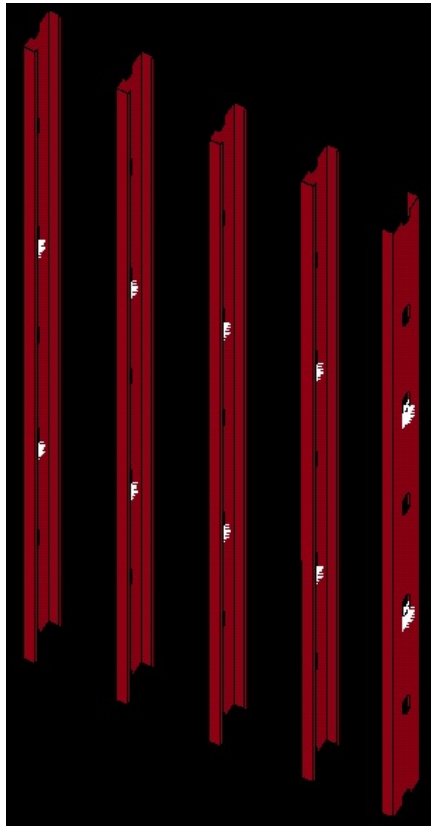
Figure 7.21: Boundary conditions at access holes for the LS-DYNA model of test 1

The bottom connection, as modeled in LS-DYNA, is shown in Fig. 7.22. For this connection type, a tie-break style contact is used within each connection in LS-DYNA in order to simulate failure if the connection shear forces are sufficiently large. Essentially, the LS-DYNA connection has a certain resistance to translation, and when this resistance is exceeded, the connection will simply fail. In the actual

Blast Simulator tests, this connection failure is a result of track and hardware damage (e.x. shearing and pullout of screws).

In addition, in the LS-DYNA model, boundary constraints are placed only at the interior faces of each connection (Fig. 7.22), in order to allow for sufficient rotation of the connection, which includes elastic and inelastic deformation. The rotational stiffness of the connection is primarily a function of the connection material's Young's Modulus and yield strength, which were assigned to the LS-DYNA material model of the connection. In the actual Blast Simulator tests, the rotational stiffness of the connection is determined by the number of "blast-washers."
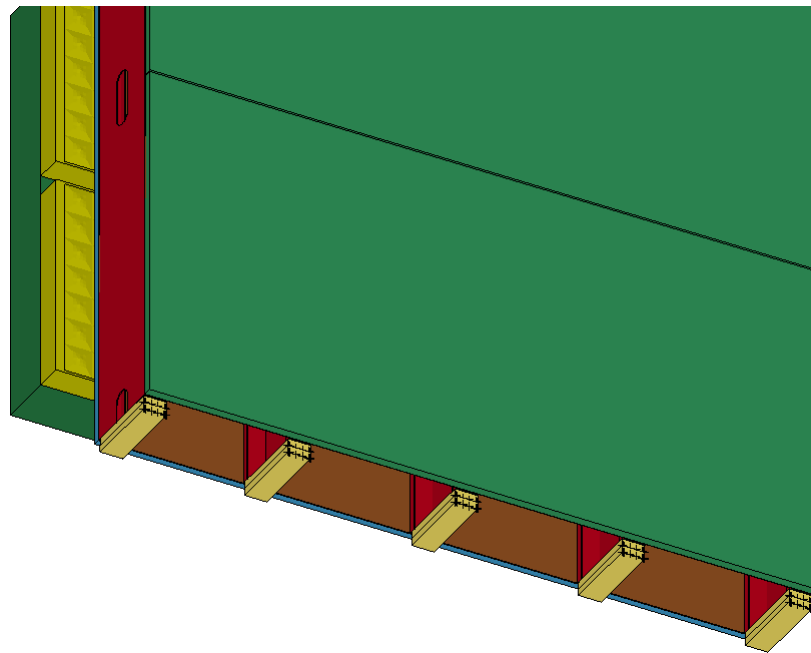
Figure 7.22: LS-DYNA bottom connection for test 1

By comparing Fig. 7.22 to the photos and descriptions of the connections that were used in the Blast Simulator tests, we can see that many simplifications are present. The track and screws are not modeled, nor are the blast-washers, except in a phenomenological sense. The important parameters of the LS-DYNA connections are the tie-break strength and the Young's Modulus, where the tie-break strength and the Young's Modulus in the test 1 simulation are assigned the

same value as the tie-break strength and Young's Modulus for bottom connection of test 4.

We recall that the connection strength is nearly constant in the Blast Simulator tests, since the track does not change from test-to-test, nor does the hardware that connects the track to the wall. Thus, in LS-DYNA, the total shear capacity at this bottom connection, which is the sum of the shear capacities of each of the individual connections, should remain constant. Since this model of the bottom connection has the same number of individual connections as the LS-DYNA model of the bottom connection of test 4 and these individual connections also have the same dimensions, the tie-break strength is assigned the same value for both simulations.

In addition, we also recall that the connection rotational capacity in the Blast Simulator tests is primarily a function of the number of blast-washers. The bottom connection of test 1 and the bottom connection of test 4 have the same number of blast washers (four), and therefore the overall connection rotational stiffness should be the same. So long as the number of individual connections in the LS-DYNA simulations of the bottom connection for test 1 and test 4 are the same, the Young's Modulus of this LS-DYNA connection material should be set to the same value in both simulations in order to achieve the same overall connection rotational stiffness. Indeed, test 1 and test 4 do have the same number of individual connections (five), so the Young's Modulus is, accordingly, assigned the same value in both simulations. In fact, we will see that test 5 also has four blast washers with five studs, and will therefore use the same connection tie-break strength value and the same Young's Modulus as the bottom connection of test 4 and test 1.

We recall that this configuration (four blast-washers with five studs) is common enough that this Young's Modulus value can be considered the "baseline" value. Another common configuration is eight blast-washers. Test 2 and test 6, for example, have such a configuration (eight blast washers with ten studs). Since the number of blast-washers is doubled in those Blast Simulator tests, one can expect that the connection rotational stiffness should be doubled, compared to

the bottom connection of test 4, for example. Since the number of studs is also doubled, however, achieving this stiffer (doubled) rotational stiffness requires that we use the *same* Young's Modulus and yield strength for the individual connections in the LS-DYNA simulations of test 2 and 6 as in the simulations of the bottom connection of test 4, tests 1, and the connections of test 5. Thus, most of the connections in the LS-DYNA simulations utilize the baseline Young's Modulus value. Test 7 is an exception (four blast-washers with four studs), as was the top connection in the LS-DYNA simulation for test 4 (eight blast washers with five studs). Recall that all of the relevant connection parameters for each of the ten LS-DYNA wall simulations were summarized in Table 7.1.

The top connection in test 1 is an entirely different type of connection, which does not utilize blast washers. This connection was shown in Figures 6.17 and 6.19. In LS-DYNA, this connection is fixed.

The BGs were modeled in the simulation of test 1 and were each driven by the net hydraulic pressure as recorded from the Blast Simulator test. We note that only three BGs were present for this test, compared to four BGs in all other tests. A view of the simulation at maximum displacement is shown in Fig. 7.23a alongside a view of the corresponding Blast Simulator test at approximately the same time (Fig. 7.23b). We can observe that buckling occurred at the second access hole in the Blast Simulator test, as well as in the LS-DYNA simulation. This buckling occurs in the simulation (Fig. 7.23a) slightly before the buckling occurs in the experiment (Fig. 7.23b), hence the larger eventual peak displacement in the simulation.

A complete pressure-time history of the LS-DYNA contact force between the BGs and the wall is shown in Fig. 7.24. The total impulse imparted in the LS-DYNA simulation compares quite well with the impulse that was recorded in the experiment, which is also shown in Fig. 7.24.

The peak displacement *vs* height is shown in Fig. 7.25. We can observe that the mid-height displacement recorded in the experiment is smaller than the mid-height displacement observed in the LS-DYNA simulation. This is most likely due to damage that occurred at the access hole in the computer simulation, which
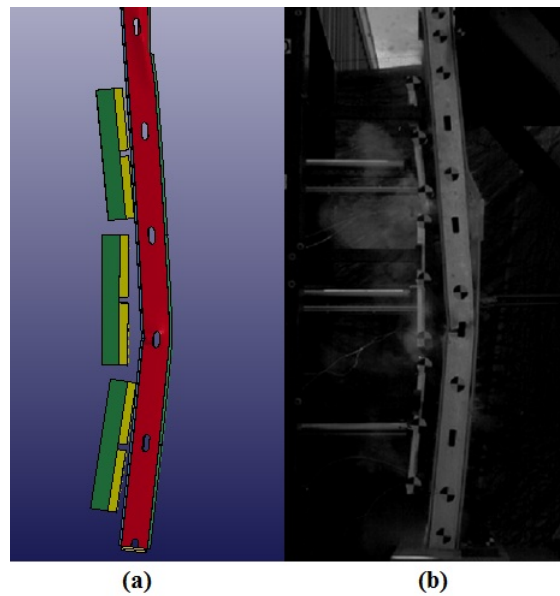
Figure 7.23: Deformed view (a) LS-DYNA simulation of test 1 (b) Blast Simulator test 1
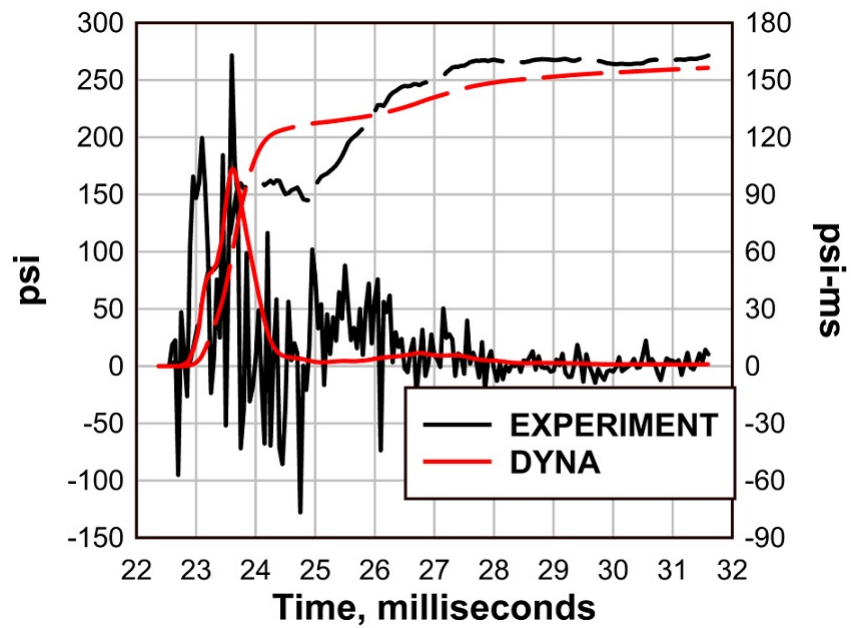

Figure 7.24: Pressure-time history of the LS-DYNA simulation for test 1, plotted alongside the average data recorded from the corresponding Blast Simulator experiment
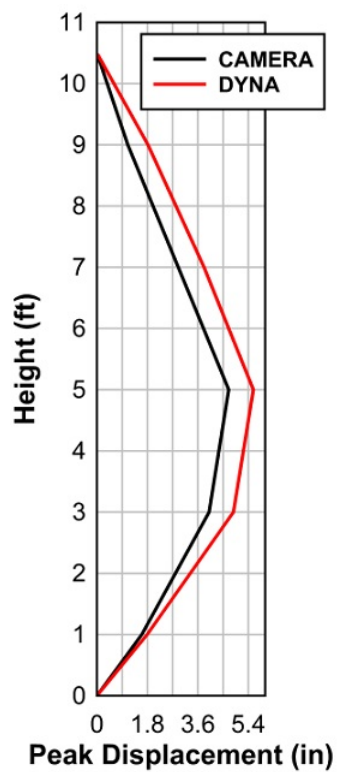
occurred at a later time in the experiment.

Figure 7.25: Displacement *vs* height of the LS-DYNA simulation 1, plotted alongside the corresponding camera data from the Blast Simulator experiment

7.3.4 Test SSRE010-05 Simulation

The LS-DYNA model for this wall test employed "TYPE 1" solid elements. The three middle access holes on each stud in the actual wall contained "clips" which were in place to prevent buckling at the access holes. In the LS-DYNA model, the access holes were braced, accordingly, by using boundary conditions. The access hole that were braced are shown in Fig. 7.26.
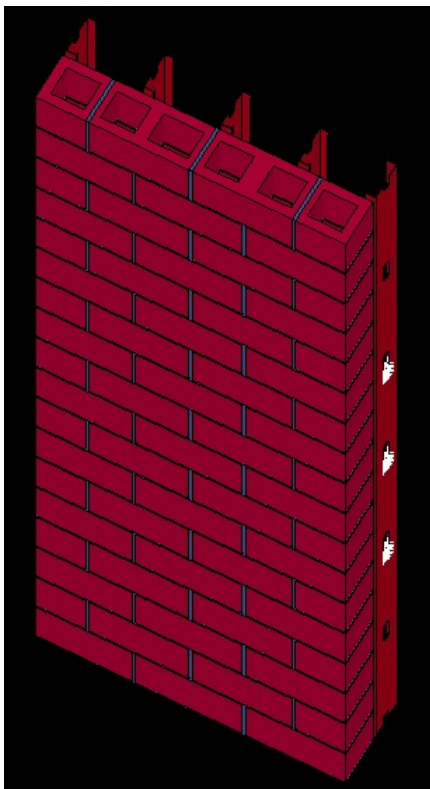
Figure 7.26: LS-DYNA boundary conditions at access holes for test 5

The bottom connection and the top connection, as modeled in LS-DYNA, have identical geometry and boundary conditions, which are shown in Fig. 7.27. For this connection type, a tie-break style contact is used within each connection in LS-DYNA in order to simulate failure if the connection shear forces are sufficiently large. Essentially, the LS-DYNA connection has a certain resistance to translation, and when this resistance is exceeded, the connection will simply fail. In the actual Blast Simulator tests, this connection failure is a result of track and hardware

damage (e.x. shearing and pullout of screws).

In addition, in the LS-DYNA model, boundary constraints are placed only at the interior faces of each connection (Fig. 7.27), in order to allow for sufficient rotation of the connection, which includes elastic and inelastic deformation. The rotational stiffness of the connection is primarily a function of the connection's Young's Modulus and yield strength, which were assigned to the LS-DYNA material model of the connection. In the actual Blast Simulator tests, the rotational stiffness of the connection is determined by the number of "blast-washers."
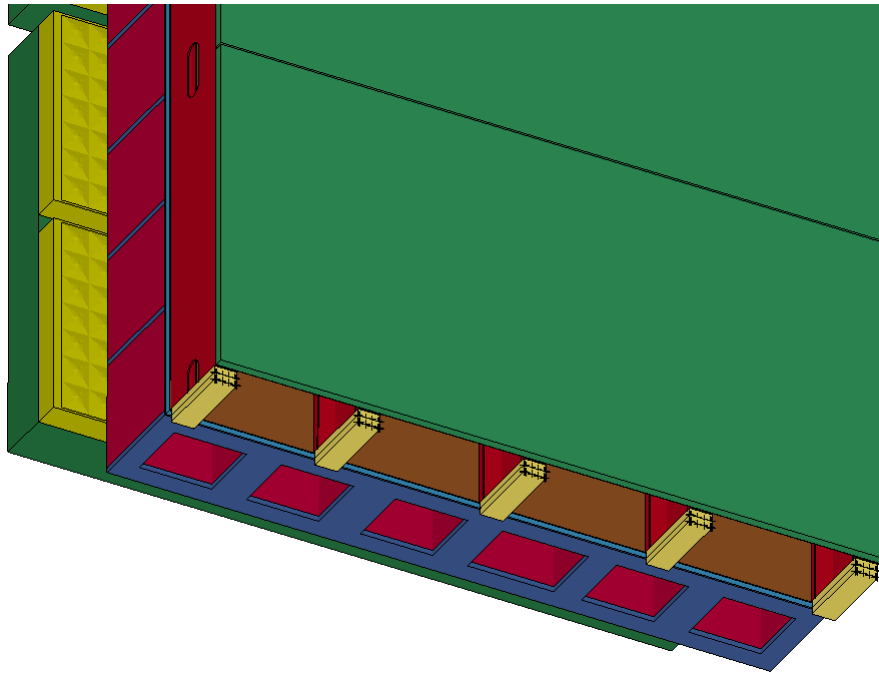
Figure 7.27: LS-DYNA connections for test 5

By comparing Fig. 7.27 to the photos and descriptions of the connections that were used in the Blast Simulator tests, we can see that many simplifications are present. The track and screws are not modeled, nor are the blast-washers, except in a phenomenological sense. The important parameters of the LS-DYNA connections are the tie-break strength and the Young's Modulus. The connection strength was determined based on the track strength, as described in section 7.1. Connection strength is nearly constant in the Blast Simulator tests, since the track does not change from test-to-test, nor does the hardware that connects the track

to the wall, except for a single additional screw for each additional stud that is present. This tie-break strength parameter is adjusted in a manner such that the total shear capacity at the top or the bottom of the wall remains constant. The specific manner in which this tie-break strength is adjusted was described in section 7.1.

Connection rotational capacity in the Blast Simulator tests is primarily a function of the number of blast-washers. The more blast-washers that are used, the more effective the connection will be in resisting rotation, as previously described. The Young's Modulus and yield strength of the LS-DYNA connection material is adjusted, in the manner described in section 7.1 and section 7.3.2. Specifically, test 5 has a blast-washer configuration that is similar to the bottom connection in test 4 (four blast-washers with five studs), as well as the connections of test 1. Thus, the connections of test 5 utilize the same "baseline" material properties. Recall that all of the relevant connection parameters for each of the ten LS-DYNA wall simulations were summarized in Table 7.1.

The BGs were modeled in the simulation of test 5 and were each driven by the net hydraulic pressure as recorded from the Blast Simulator test. In this Blast Simulator test, the South side of the wall buckled at at the access hole near the top of the wall, as shown in Fig. 7.28a. Interestingly, the North side of the wall buckled at the access hole at mid-height, as shown in Fig. 7.28b. A view of the simulation at maximum displacement is shown in Fig. 7.28c. We can observe that buckling occurred at the access hole near the top of the wall in the LS-DYNA simulation, which is consistent with the buckling of the South side of the wall in the experiment. This buckling occurs in the simulation slightly before the buckling occurs in the experiment, hence the larger eventual peak displacement in the simulation.

A complete pressure-time history of the LS-DYNA contact force between the BGs and the wall is shown in Fig. 7.29. The total impulse imparted in the LS-DYNA simulation compares quite well with the impulse that was recorded in the experiment, which is also shown in Fig. 7.29. The total impulse in the simulation is larger, which is expected since the material model of the programmer will tend
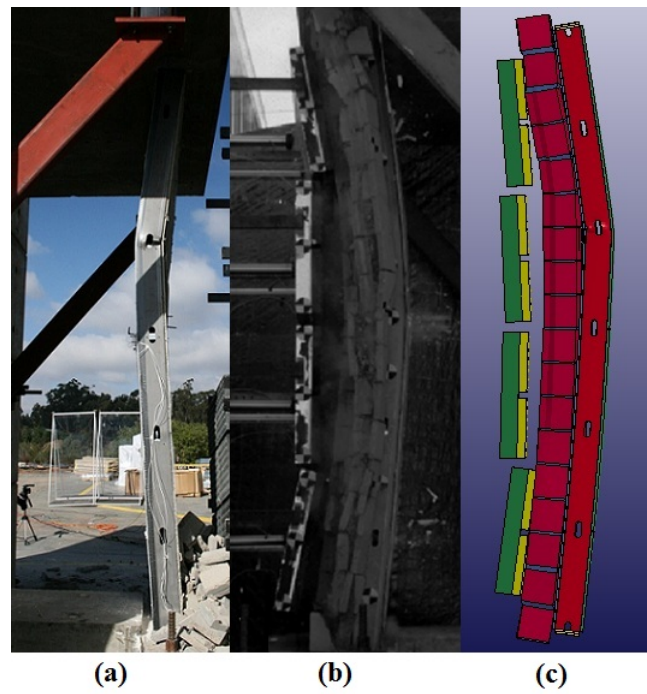
Figure 7.28: Deformed view (a) Blast Simulator test 5: South side of specimen (b) Blast Simulator test 5: North side of specimen (c) LS-DYNA simulation

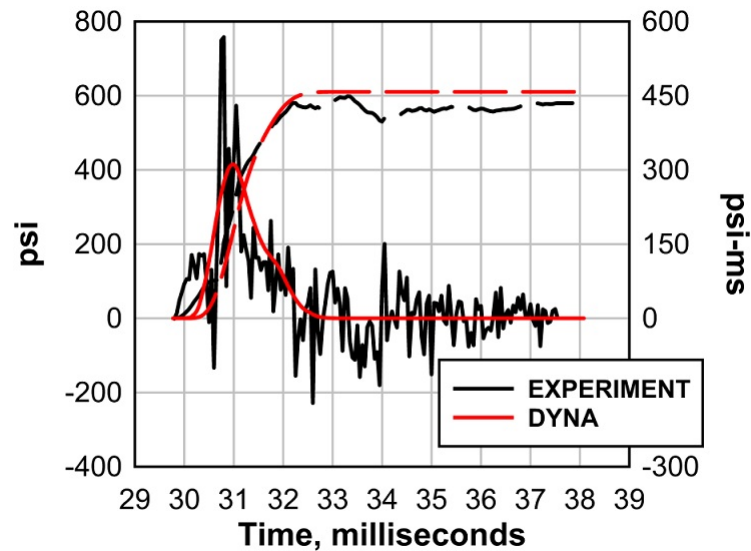to impart an artificially larger impulse than in the actual test, for reasons that are discussed in detail in Ch. 5.

Figure 7.29: Pressure-time history of the LS-DYNA simulation for test 5, plotted alongside the average data recorded from the corresponding Blast Simulator experiment

The peak displacement *vs* height is shown in Fig. 7.30. We can observe that the displacements recorded in the experiment are smaller than the displacements observed in the LS-DYNA simulation. This is most likely due to damage that occurred at the access hole near the top of the wall in the computer simulation, which occurred at a later time in the experiment. The impulse is also larger in the computer simulation, which is most likely a result of the programmer material model. Essentially, the programmer material model was calibrated for moderate impacts as discussed in detail in Chapter 5, whereas this impact was more severe.

Note that the displacements shown in Fig. 7.30 for the experiment are the displacements at a time several milliseconds prior to the peak displacement. The reason for this is that spall from the masonry eventually obscured the view of the camera for most of the locations along the height of the wall, thus preventing an accurate recording of peak displacements. The displacement values shown in Fig. 7.30 for the simulation were similarly chosen for a time several milliseconds prior

to peak, in order to be consistent with the experimental values.

Note also that the experimental displacements that are shown in Fig. 7.30 are of the North side of the wall. The buckling on this side of the wall occurred primarily at the mid-height access hole, whereas the buckling in the simulation occurred primarily at the access hole near the top of the wall. Displacement recordings of the South side of the wall would have better agreement with the LS-DYNA simulation, since the buckling occurred at the access hole near the top of the wall on the South side. However, our cameras were set up only to record displacements on the North side. This is typically sufficient for data collecting purposes as it is unusual for the wall to deform unsymmetrically as it did in this test.
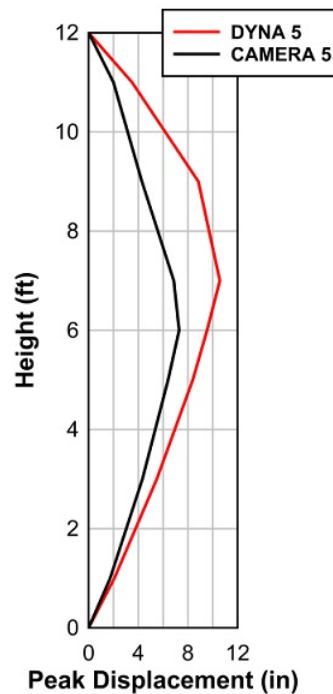
Figure 7.30: Displacement *vs* height of the LS-DYNA simulation 5, plotted alongside the corresponding camera data from the Blast Simulator experiment

7.3.5 Test SSRE010-07 Simulation

The LS-DYNA model for this wall test employed "TYPE 1" solid elements. The three middle access holes on each stud in the actual wall contained "clips" which were in place to prevent buckling at the access holes. In the LS-DYNA model, the access holes were braced, accordingly, by using boundary conditions. The access holes that were braced are shown in Fig. 7.31.
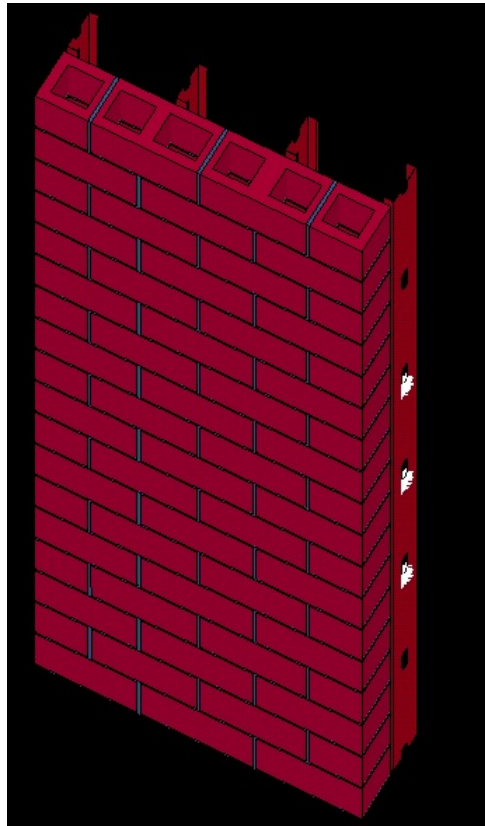
Figure 7.31: LS-DYNA boundary conditions at access holes for test 7

The bottom connection and the top connection, as modeled in LS-DYNA, have identical geometry and boundary conditions, which are shown in Fig. 7.32. For this connection type, a tie-break style contact is used within each connection in LS-DYNA in order to simulate failure if the connection shear forces are sufficiently large. The value of this tie-break and the rationale for determining it was described in section 7.1.

In addition, in the LS-DYNA model, boundary constraints are placed only at the interior faces of each connection (Fig. 7.32), in order to allow for sufficient rotation of the connection, which includes elastic and inelastic deformation. The rotational stiffness of the connection is primarily a function of the connection's Young's Modulus and plastic hardening behavior, which were assigned to the LS-DYNA material model of the connection. In the actual Blast Simulator tests, the rotational stiffness of the connection is determined by the number of "blast-washers."
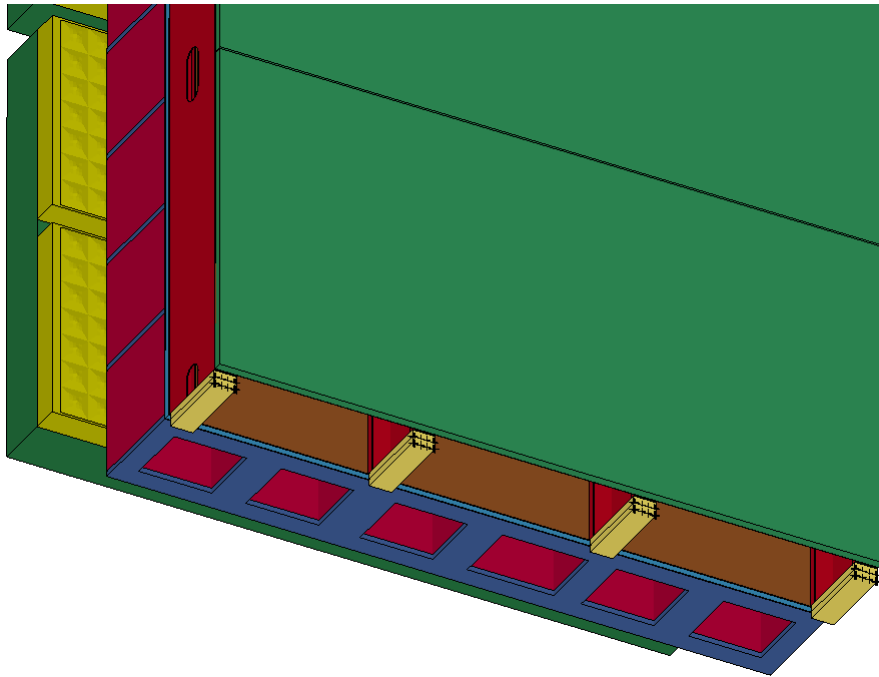
Figure 7.32: LS-DYNA connections for test 7

By comparing Fig. 7.32 to the photos and descriptions of the connections that were used in the Blast Simulator tests, we can see that many simplifications are present. The track and screws are not modeled, nor are the blast-washers, except in a phenomenological sense. So, in order to determine the important parameters of the LS-DYNA connections, namely, the tie-break strength, the Young's Modulus, and the yield strength, it is important to first recognize which factors in each Blast Simulator test most influence the connection strength and connection rotational

stiffness. Track strength and blast washer stiffness are assumed to be the factors in the Blast Simulator tests that control global connection strength and stiffness.

The rationale for determining the LS-DYNA tie-break value for the connections was described in section 7.1, and the values provided in table 7.1. The assumption that is used is that track strength determines the strength of the connection. Connection rotational stiffness, on the other hand, is assumed to be primarily a function of the number of blast-washers. The more blast-washers that are used, the more effective the connection will be in resisting rotation. Recall that all of the relevant connection parameters for each of the ten LS-DYNA wall simulations were summarized in Table 7.1. A detailed explanation addressing the parameters that influence the LS-DYNA connection stiffness, namely, the connection material's Young's modulus and yield strength, is provided in section 7.1 and section 7.3.2. Essentially, since test 7 utilized four blast washers, it should have the same rotational stiffness as test 1, test 5, and the bottom connection of test 4. Due to the way in which the connections are modeled in LS-DYNA, however, the Young's Modulus for each of the LS-DYNA individual connections was set to a higher value, as shown in Table 7.1.

Two of the BG sensors failed during test 7, as described in Section 6.5.7. The BGs were modeled in the simulation of test 7 and were each driven by the net hydraulic pressure as recorded from the Blast Simulator test. Since the hydraulic data for only two of the BGs was known, the remaining two BGs were also driven by these pressures. Obtaining the BG impact velocities from camera data and using *Initial_Velocity_Generation is another option, however, incorporating the hydraulic histories into LS-DYNA is the preferred method due to, *inter alia*, "double-hits" that would occur if the BGs are treated as simple projectiles.

In this Blast Simulator test, the wall buckled at at the access hole near the top of the wall, as shown in Fig. 7.33a. A view of the simulation at maximum displacement is shown in Fig. 7.33b. We can observe that buckling occurred at the access hole near the top of the wall in the LS-DYNA simulation, which is consistent with the buckling of the wall in the experiment. This buckling occurs in the simulation slightly before the buckling occurs in the experiment, hence the

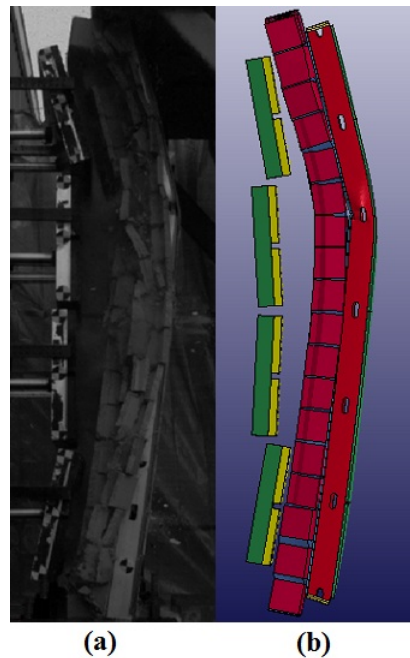larger eventual peak displacement in the simulation.

Figure 7.33: Deformed view (a) Blast Simulator test 7 (b) LS-DYNA simulation

A complete pressure-time history of the LS-DYNA contact force between the BGs and the wall is shown in Fig. 7.34. The total impulse imparted in the LS-DYNA simulation compares quite well with the impulse that was recorded in the experiment, which is also shown in Fig. 7.34. The total impulse in the simulation is larger, which is expected since the material model of the programmer will tend to impart an artificially larger impulse than in the actual test, for reasons that are discussed in detail in Ch. 5.

The peak displacement *vs* height is shown in Fig. 7.35. We can observe that the displacements recorded in the experiment are smaller than the displacements observed in the LS-DYNA simulation. This is most likely due to damage that occurred at the access hole near the top of the wall in the computer simulation, which occurred at a later time in the experiment. The impulse is also larger in the computer simulation, which is most likely a result of the programmer material model, as discussed in detail in Chapter 5.
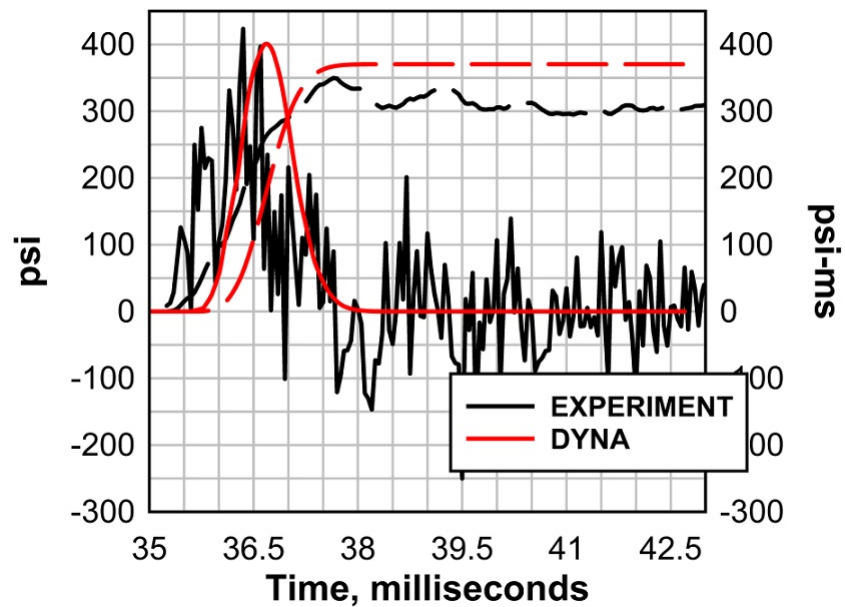
Figure 7.34: Pressure-time history of the LS-DYNA simulation for test 7, plotted alongside the average data recorded from the corresponding Blast Simulator experiment

Note that the displacements shown in Fig. 7.35 for the experiment are the displacements at a time several milliseconds prior to the peak displacement. The reason for this is that spall from the masonry eventually obscured the view of the camera for most of the locations along the height of the wall, thus preventing an accurate recording of peak displacements. The displacement values shown in Fig. 7.35 for the simulation were similarly chosen for a time several milliseconds prior to peak, in order to be consistent with the experimental values.
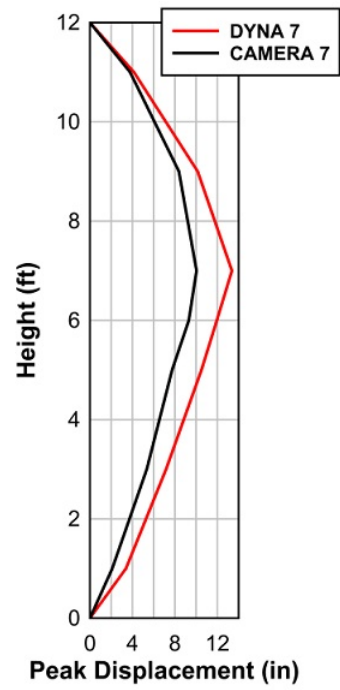
Figure 7.35: Displacement *vs* height of the LS-DYNA simulation 7, plotted alongside the corresponding camera data from the Blast Simulator experiment

7.3.6   Test SSRE010-02.1 Simulation

The LS-DYNA model for this wall test employed "TYPE 1" solid elements. Two of the access holes on each stud in the actual wall contained "clips" that were in place to prevent buckling at the access holes. In the LS-DYNA model, the access holes were braced, accordingly, by using boundary conditions. The access holes that were braced are shown in Fig. 7.36.
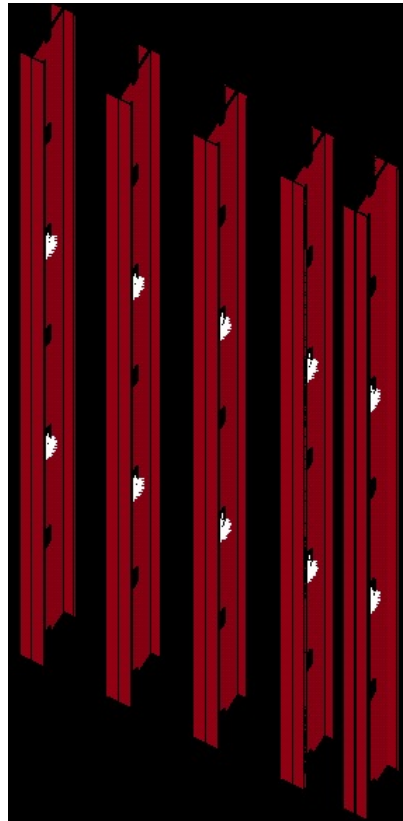
Figure 7.36: LS-DYNA boundary conditions at access holes for test 2.1

The bottom connection and the top connection, as modeled in LS-DYNA, have identical geometry and boundary conditions, which are shown in Fig. 7.37. For this connection type, a tie-break style contact is used within each connection in LS-DYNA in order to simulate failure if the connection shear forces are sufficiently large. Essentially, the LS-DYNA connection has a certain resistance to translation, and when this resistance is exceeded, the connection will simply fail. In the actual

Blast Simulator tests, this connection failure is a result of track and hardware damage (e.x. shearing and pullout of screws followed by track tearing).

In addition, in the LS-DYNA model, boundary constraints are placed only at the interior faces of each connection (Fig. 7.37), in order to allow for sufficient rotation of the connection, which includes elastic and inelastic deformation. The rotational stiffness of the connection is primarily a function of the connection's Young's Modulus, which was assigned to the LS-DYNA material model of the connection. In the actual Blast Simulator tests, the rotational stiffness of the connection is determined by the number of "blast-washers."
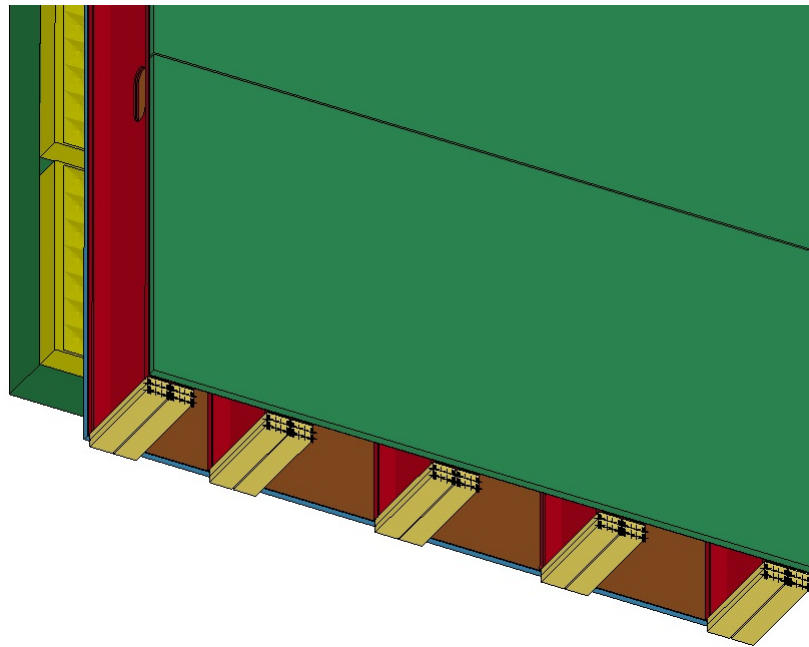
Figure 7.37: LS-DYNA connections for test 2.1

By comparing Fig. 7.37 to the photos and descriptions of the connections that were used in the Blast Simulator tests, we can see that many simplifications are present. The track and screws are not modeled, nor are the blast-washers, except in a phenomenological sense. So, in order to determine the important parameters of the LS-DYNA connections, namely, the tie-break strength and the Young's Modulus, it is important to first recognize which factors in each Blast Simulator test most influence the connection strength and connection rotational

stiffness. These factors were described in section 7.1, along with a list of important LS-DYNA connection parameters in Table 7.1.

Here, the connections in test 2 utilize eight blast-washers and ten studs. Recall that test 1 and test 5, for example, had a blast-washer configuration that consisted of four blast-washers with five studs. Test 2, while containing twice the number of blast washers, also contains twice the number of studs, and so the Young's Modulus and strength that is used in LS-DYNA for the individual connections is set to the same value. To understand why, consider that the rotational stiffness of the test 2 connection should be twice as stiff as the rotational stiffness of the test 5 connection, since the rotational stiffness is proportional to the number of blast washers, and test 2 contained twice as many blast washers as test 5. By setting the LS-DYNA connection stiffness parameters for test 2 equal to the values used in test 5 (see Table 7.1), indeed the global connection stiffness for test 2 will be twice that of test test 5.

The BGs were modeled in the simulation of test 2.1 and were each driven by the net hydraulic pressure as recorded from the Blast Simulator test. A view of the simulation at maximum displacement is shown in Fig. 7.38b alongside a view of the corresponding Blast Simulator test at approximately the same time (Fig. 7.38a). We can observe that no damage occurred in the Blast Simulator test, or in the LS-DYNA simulation.

A complete pressure-time history of the LS-DYNA contact force between the BGs and the wall is shown in Fig. 7.39. The total impulse imparted in the LS-DYNA simulation can be compared to the impulse that was recorded in the experiment, which is also shown in Fig. 7.39. Since this was a light impact, where accelerometer data is known to be oscillatory, and double-hits are difficult to prevent, the data is not particularly clean in comparison to the force data that has been so far shown for the other tests in this chapter. For light impacts like this, the "impulse" can only be roughly approximated.

The peak displacement *vs* height is shown in Fig. 7.40. We can observe that the mid-height displacement recorded in the experiment is larger than the mid-height displacement observed in the LS-DYNA simulation. This is due to error in
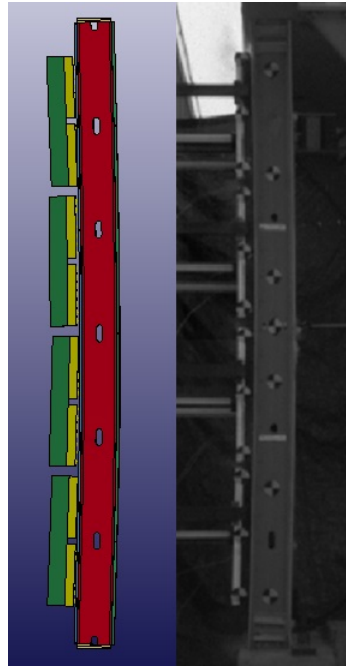
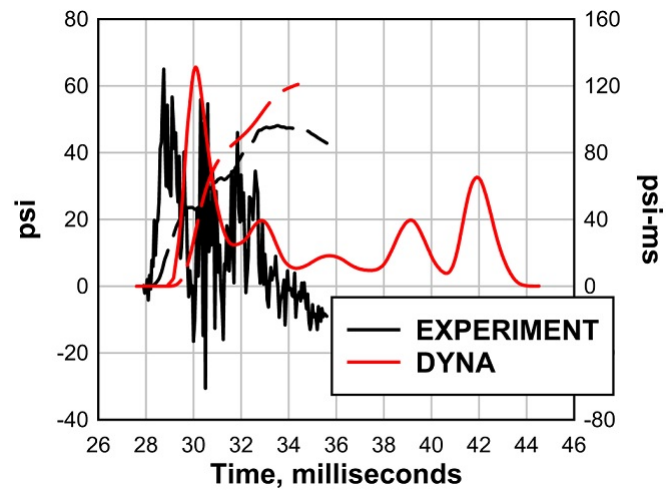**Figure 7.38**: Deformed view (a) Blast Simulator test 2.1 (b) LS-DYNA simulation

Figure 7.39: Pressure-time history of the LS-DYNA simulation for test 2.1, plotted alongside the average data recorded from the corresponding Blast Simulator experiment

the programmer material model, in particular the tendency of the material model to give an artificially low impulse under light impact loads, as described in detail in Ch. 5.
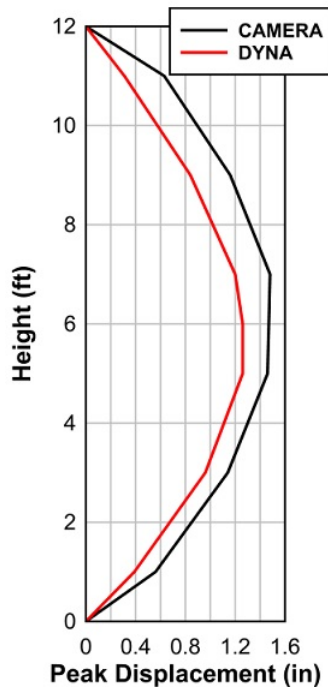

Figure 7.40: Displacement *vs* height of the LS-DYNA simulation 2.1, plotted alongside the corresponding camera data from the Blast Simulator experiment

7.3.7 Test SSRE010-03.1 Simulation

This section will describe the results of the first test that was performed on wall 3. Two subsequent tests were performed on this wall, and the experimental results for all three of these tests can be found in section 6.5.3. An overview of the LS-DYNA model for wall 3 was described in detail previously in section 7.3.1, where the results from the LS-DYNA simulation for test 3.2 were also provided. The results from the LS-DYNA simulation of test 3.1 will be described.

This model employed "TYPE 1" solid elements. Two of the access holes on each stud in the actual wall contained "clips" which were in place to prevent buckling at the access holes. In the LS-DYNA model, the access holes were braced, accordingly, by using boundary conditions as was shown previously in Fig. 7.11.

The top and bottom of the wall are not connected to the concrete header or footer. Instead, they bear against 6 in. angle sections. This connection, as modeled in LS-DYNA, was shown previously in Fig. 7.12. A surface-to-surface contact is used between the wall and the angle, and boundary constraints are placed on the angle. Additionally, at this location, the stud wall is braced against crippling in the actual wall *via* web stiffeners, and is braced, accordingly, in the computer model (not shown).

The BGs were modeled in the simulation and were each driven by the net hydraulic pressure as recorded from the Blast Simulator test. A view of the simulation at maximum displacement is shown in Fig. 7.41a alongside a view of the corresponding Blast Simulator test at approximately the same time (Fig. 7.41b). We can see that no visible damage occurred in either the Blast Simulator test or the LS-DYNA simulation.

A complete pressure-time history of the LS-DYNA contact force between the BGs and the wall is shown in Fig. 7.42. Although contact occurs later in the simulation compared to the experiment, the data in both cases is quite good compared to the oscillatory data of test 2.1. While the LS-DYNA impulse for test 3.1 was expected to be underestimated somewhat due to error in the programmer model under light impact loads, as described Ch. 5, it turned out that the total impulse imparted in the LS-DYNA simulation in test 3.1 compares well with the
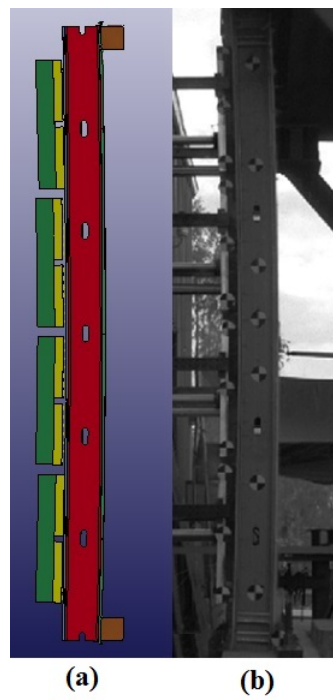
Figure 7.41: Deformed view (a) LS-DYNA simulation of test 3.1 (b) Blast Simulator experiment

impulse that was recorded in the experiment, which is also shown in Fig. 7.42. In the experiment, the 6 in. angles displaced approximately .25 in. This compliance of the boundary restraints, which was not modeled, may have reduced the experimental impulse.
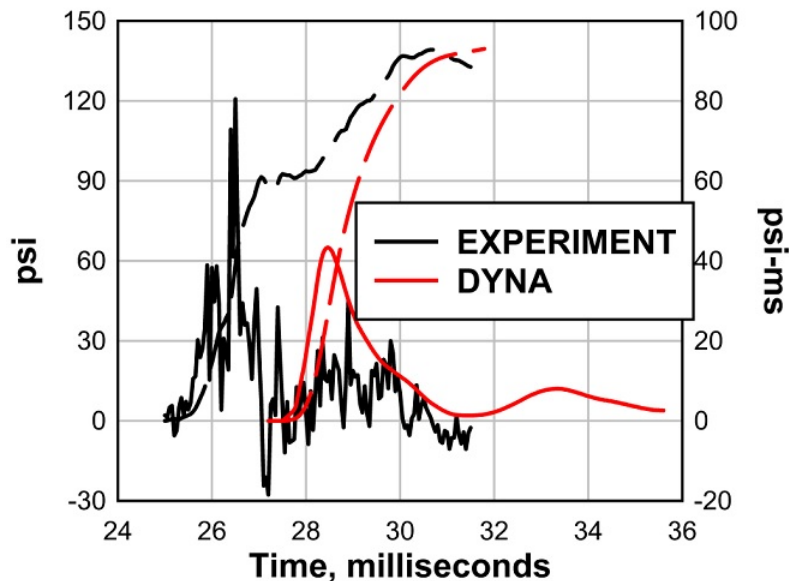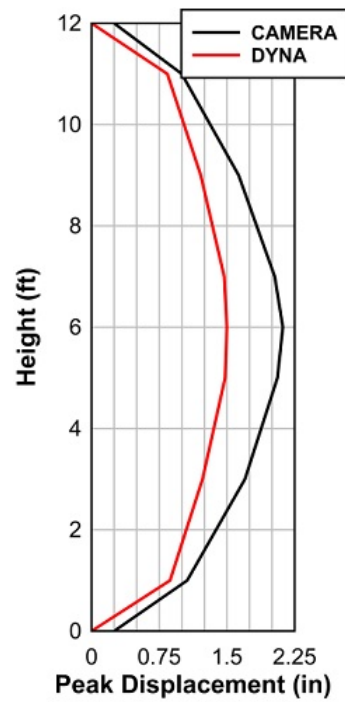

Figure 7.42: Pressure-time history of the LS-DYNA simulation of test 3.1, plotted alongside the average data recorded from the Blast Simulator experiment

The peak displacement *vs* height is shown in Fig. 7.43. We can observe that the mid-height displacement recorded in the experiment is greater than the mid-height displacement observed in the LS-DYNA simulation. This is most likely due to 1) displacement of the 6 in. angles occurred in the experiment of approximately .25 in., which is not permitted in the computer simulation, and 2) the error in the programmer material model, in particular the tendency of the material model to give an artificially low impulse under light impact loads, as described in detail in Ch. 5.

Figure 7.43: Displacement *vs* height of the LS-DYNA simulation of test 3.1, plotted alongside the corresponding camera data from the Blast Simulator experiment

7.3.8   Test SSRE010-02.2, 2.3, 6 Simulation

A detailed description of the LS-DYNA model for wall 2 was given in section 7.3.6. Some description of the LS-DYNA model for test 6 will be described below. The bottom connection and the top connection for test 6, as modeled in LS-DYNA, have identical geometry and boundary conditions, which are shown in Fig. 7.44. For this connection type, a tie-break style contact is used within each connection in LS-DYNA in order to simulate failure if the connection shear forces are sufficiently large. Essentially, the LS-DYNA connection has a certain resistance to translation, and when this resistance is exceeded, the connection will simply fail. In the actual Blast Simulator tests, this connection failure is a result of track and hardware damage (e.x. shearing and pullout of screws). Recall that all of the relevant connection parameters for each of the ten LS-DYNA wall simulations were summarized in Table 7.1.

In addition, in the LS-DYNA model, boundary constraints are placed only at the interior faces of each connection (Fig. 7.44), in order to allow for sufficient rotation of the connection, which includes elastic and inelastic deformation. The rotational stiffness of the connection is primarily a function of the connection's Young's Modulus and yield strength, which were assigned to the LS-DYNA material model of the connection. In the actual Blast Simulator tests, the rotational stiffness of the connection is determined by the number of "blast-washers." The rationale for determining the Young's Modulus and yield strength for each of the simulations was described in detail in section 7.1 and section 7.3.2, and the values provided in Table 7.1.

Recall from chapter 6 that test SSRE010-06 exhibited complete connection failure at the bottom and the top of the wall. Test SSRE010-02.3 exhibited complete connection failure at the top of the wall only. Test SSRE010-02.2 exhibited partial connection failure at the top of the wall. In the LS-DYNA simulation of test 2.2, the tie-break at the top of the wall failed. Although partial connection failure is not difficult to simulate using an LS-DYNA tie-break, a complete connection failure was desired due to lack of data. This suggests that the tie-break values that are used in the LS-DYNA simulations will be slightly conservative. In-
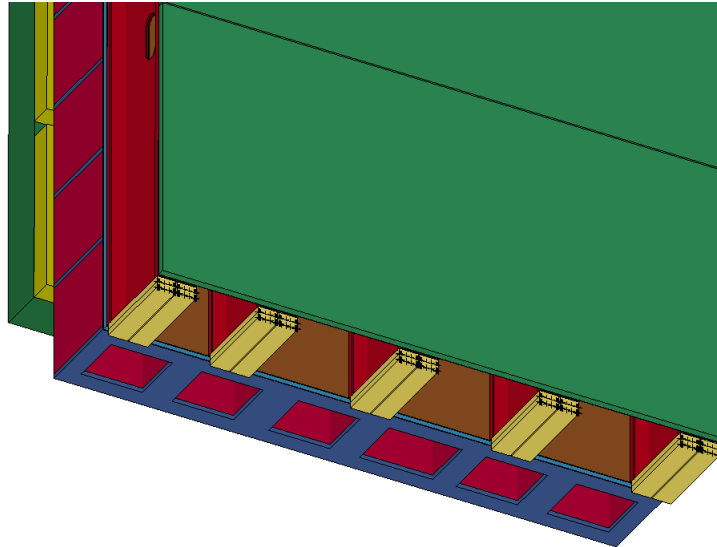
Figure 7.44: LS-DYNA connections for test 6

deed, both connections failed in the LS-DYNA simulation of test 2.3, even though only one of the connections failed in the Blast Simulator test 2.3. The LS-DYNA simulation of test 6 exhibited complete connection failure at both connections, as expect. These LS-DYNA results are depicted in Fig. 7.45. Note that none of the tie-breaks failed in any of the seven previous LS-DYNA simulations, as expected.

Note also in Fig. 7.45c that the impact masses were treated as projectiles in the LS-DYNA simulation due to DAQ operator error, which was described briefly in section 6.5.6. Since no hydraulic data could be obtained from the Blast Simulator test, the impact masses were simply given an initial velocity in the LS-DYNA simulation, hence, the artificially symmetric mass behavior and specimen response as depicted in Fig. 7.45c.
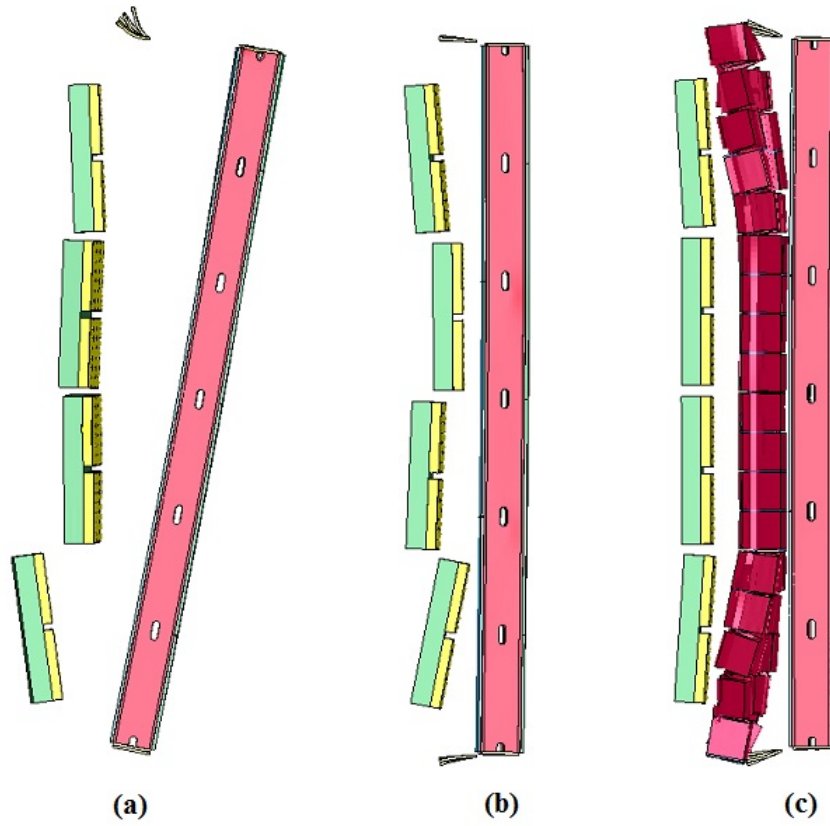
Figure 7.45: (a)LS-DYNA simulation of test 2.2 (b) LS-DYNA simulation of test 2.3 (c) LS-DYNA simulation of test 6

7.4 Summary of FEA simulations

This chapter described the geometries, material models, and other important information relating to the FEA simulations that were performed, which corresponded to the twelve Blast Simulator experiments conducted on the prototype walls of test series SSRE010. Since the two Blast Simulator tests that were performed on walls containing previous significant damage were not modeled, a total of ten LS-DYNA simulations were performed. The results of each of the computer simulations, including impulse demands, peak wall displacements, and LS-DYNA images of deformed shape have been documented. A trend in the LS-DYNA responses is observed that suggests that these computer simulations tend to underestimate the loading for light impacts and overestimate the loading for the more severe impacts.

For example, the impacts in the Blast Simulator on Test 2.1 and 3.1, which did not damage the wall specimens, can be classified as light impacts. For the corresponding LS-DYNA simulations, it was observed that the peak displacements were too small, presumably as a result of impulse demands that were too small. Impulse data from the Blast Simulator is unfortunately not reliable for such light impacts due to accelerometer noise. For the more severe impacts, such as Test 5 and Test 7, the computer simulations very clearly overestimated the load demand and, accordingly, the wall displacements. This was expected, since the material model of the programmer contains a simplified treatment for rate effects. The programmer material model was characterized for moderate impacts, using a Drop Tower test approach as described in chapter 5, and it was the moderate impacts in the simulations of the prototype walls that agreed best.

Despite the inherent error in the new programmer material model, the results certainly agree better than the old programmer model, although no such simulations were performed due to the high computational cost associated with repeating the simulations for this test series using the old programmer model. In this chapter it was observed that the walls generally buckled at the same access hole in the LS-DYNA simulations as in the Blast Simulator tests, despite the apparent randomness associated with access hole buckling observed in the Blast

Simulator tests. The location of buckling appeared to be primarily a result of non-simultaneous impact from the BGs, thus, the ability for the simulations to match the buckling behavior can be largely attributed to the incorporation of the hydraulics into the simulation. Additionally, connection failure was successfully incorporated into the models of the wall specimens. For the three tests where connection damage occurred, connection damage was present in the corresponding computer simulations. For the rest of the tests, connection damage was absent in both the Blast Simulator tests and the computer simulations.

Chapter 8

Conclusions

This chapter will summarize the major findings that have been described in this dissertation. Through several major changes to Blast Simulator data processing and computer simulation, research that involves the testing of wall systems in the Blast Simulator is facilitated and improved. In general, this enables the blast group to perform improved research relating to blast mitigation strategies.

A series of tests that focused on a particular high strength steel stud-sheathing prototype wall systems was investigated in this dissertation. It was demonstrated that the Blast Simulator is capable of generating tailored blast-like impulses on such wall systems and the data collected from this series of tests gave good insight into the responses of the prototype walls to a wide range of blast demands. The impulses delivered by the Blast Simulator were accurately measured through a combination of accelerometer and hydraulic data, and the displacement histories throughout the height of the wall were recorded with time-synchronized high speed cameras.

High fidelity computer simulations were performed for various tests in this dissertations, including the prototype wall test series, which included a new material model for the *programmer*, and a new method for incorporating the *punch* from the hydraulics. The simulations were generally in good agreement with the Blast Simulator tests. In the simulations of the prototype stud-sheathing walls, damage occurred at the correct locations along the heights of each wall, and connection failure was also modeled with reasonable accuracy, exhibited failure, for example,

in the same instances that failure occurred in Blast Simulator testing.

This chapter will conclude with some recommendations for future work.

8.1   Summary and Conclusions

The first major topic that was investigated relates to methods for post-processing data that is obtained from tests conducted in the Blast Simulator. The most important function of the Blast Simulator with regard to wall testing is to apply tailored blast-like loading, and as part of this process it is expected that the outputted data from the Blast Simulator can provide an estimate of the delivered pressures and impulses. In order to obtain a precise estimate for the impulse, the hydraulic pressure data as well as the accelerometer data must be included in the calculation.

A new procedure was thus developed that considers the net hydraulic pressure-time history that acts on the impact mass piston, along with the acceleration-time history from accelerometers mounted on the impact mass. By converting both of these time-synchronized quantities to force, the force-time history delivered to the wall specimen can be calculated. This method was validated in a systematic manner in chapter 4 through LS-DYNA simulations that included hydraulic data, along with results from two simple Blast Simulator tests.

Incorporating the hydraulics into LS-DYNA offers several additional benefits compared to previously used methods for modeling the collision of the impact masses. When the hydraulics are included in LS-DYNA, the *punch* of the hydraulics is included naturally, a key characteristic enabling the Blast Simulator to avoid multiple-hit behavior associated with impact masses that are simple projectiles. Additionally, where multiple, independently-driven, impact masses are used, non-simultaneous impact is simulated naturally in LS-DYNA, so long as the hydraulics are incorporated into the model.

An investigation into some of the properties of the rubber material that is placed at the front of the impact rams (the *programmer*) was a second major topic in this dissertation. A particular LS-DYNA rubber model was chosen, which

is described in detail in chapter 5. This model immediately showed promise as it is one of the newer models in the LS-DYNA material library and was developed originally for the crashworthiness industry. The model is user-friendly since it is characterized solely from tabulated uniaxial stress *vs.* strain data, and unique in that this characterization is performed automatically, without requiring the user to input any material constants. The model maintains reasonable accuracy under any kind if loading since it exhibits behavior that is nonlinear-elastic, accurate to large-strains, and 3D, better known as a hyperelastic. The model is also computationally cheap since it only considers elastic behavior, and the unloading is treated with a damage function. In other words, rate effects are treated through a pseudo-elastic algorithm instead of a viscoelastic one.

The rubber model was characterized using quasi-static and drop tower testing for the particular range of strains and strain rates that are typically observed in Blast Simulator tests. In order to validate the model, the LS-DYNA simulations of the quasi-static and drop tower tests were performed. Additionally, a series of LS-DYNA simulations were performed corresponding to a Blast Simulator test series that was relatively simple and involved impacts with a range of severity that is representative of typical Blast Simulator testing. All LS-DYNA simulations that used the new rubber model provided satisfactory results when compared to experimental data, although the results of the tests where impact was moderate agreed best.

Finally, a major test series on a prototype high strength steel wall system was conducted in the Blast Simulator. This wall system was tested as a stand-alone system and was also tested in a configuration that included un-grouted masonry, since the prototype wall can be used as a retrofitting strategy for existing structures that are vulnerable to blast. The prototype wall system contained many unique features, including light gauge studs composed of a high strength low-allow vanadium steel, and a special kind of cement-board exterior sheathing. Ten LS-DYNA simulations were performed corresponding to the ten relevant tests that were conducted in the Blast Simulator on these walls.

There were many challenges associated with the construction of the walls,

the experimental data processing, and the computer simulations. The second half of the dissertation, namely, chapter 6 and chapter 7, was devoted to these topics. The results of one Blast Simulator test in particular was compared to a corresponding field test that used explosives. Since the walls were identical and the loading nearly identical, this pair of tests was of particular interest. We observed that the responses of the walls were nearly identical, further demonstrating the capability of the Blast Simulator in delivering blast-like loading. The computer simulations of this test and the other nine tests also agreed closely, although several known sources of error remain, which will be discussed in the final section of this thesis.

8.2   Recommendations for Future Work

One of the challenges of post-processing accelerometer data in order to obtain impact forces is accelerometer "noise." This was discussed in Chapter 4. It is possible that this "noise" is a result of either oscillations within the BG mass or in the accelerometer itself. One direction of future research could investigate possible "filters" on the accelerometer or on the accelerometer data, which can eliminate some or all of the "noise" without fundamentally changing the important data. Fig. 8.1 shows one kind of physical filter that we tried.

Typically, the threads of the accelerometers are screwed into the aluminum BG mass directly, but in Fig. 8.1 a rubber washer was placed at the interface between the accelerometer and the aluminum mass. This rubber washer actually exacerbated the undesirable oscillations in the data. Suffice to say, filtering is a complex topic that requires significant theoretical and experimental investigation. Alternatively, better accelerometers could be tested, such as the piezoresistive type or capacitive type (see Brown [9], Dong [13], Acar [1]). While these kinds of accelerometers could potentially provide less noisy data, they are generally more expensive and less durable.

A major source of error in the computer simulations of Blast Simulator tests has always been the programmer material model. While this material model has been significantly improved through the use of *MAT_SIMPLIFIED_RUBBER_

Figure 8.1: Rubber washer placed at interface between accelerometer and aluminum mass

WITH_DAMAGE, as described in detail in Chapter 5, there is still room for improvement.

In particular, there is a commercial software called MCalibration, created by Bergstrom [6], which allows the user to create User-Defined-Materials (UMAT) for polymers, which can be easily exported to LS-DYNA. The most powerful polymer model that is currently available is the Parallel-Network-Model (PNM). Whereas none of the built-in material models in LS-DYNA were able to perfectly "fit" the loading and unloading data from all of the programmer drop tower tests, we can see in Fig. 8.2 that a perfect fit is possible using MCalibration. In order to export this UMAT to LS-DYNA, a license must be purchased from Bergstrom [6].

MCalibration contains a library of hyperelastic and viscoelastic material models. Once a hyperelastic material model and a viscoelastic material model are chosen, MCalibration will undertake an automated iteration procedure in order to determine the material constants that give the best fit. The perfect "fit" shown in Fig. 8.2 is possible for two reasons. First, a hyperelastic material model called *Arruda-Boyce hyperelasticity with Small-Strain-Softening* is contained in the MCalibration library, which is the only material model that is able to fit the unusual shape (decreasing loading tangent modulus) of our data. This ma-
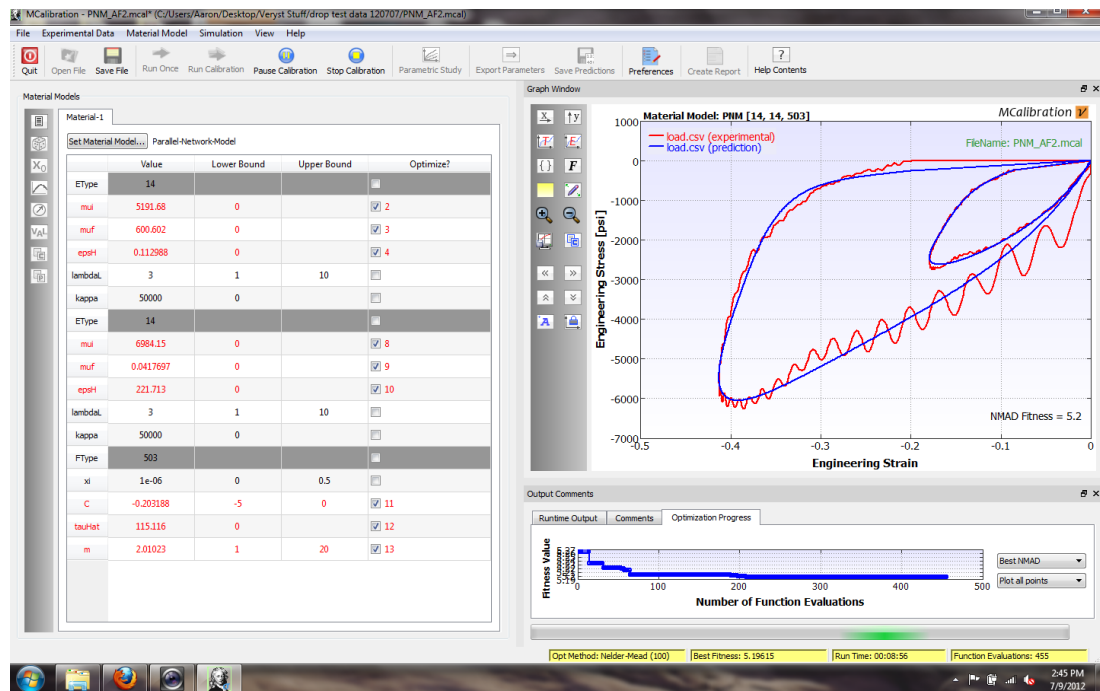
Figure 8.2: Characterization of a "Parallel-Network-Model" based on programmer drop tower test data

terial model is not available in the built-in LS-DYNA material library. Secondly, rate effects are handled through a nonlinear viscoelastic model called *Bergstrom-Boyce viscoelasticity*. Unlike the phenomenological handling of rate effects in *MAT_SIMPLIFIED_RUBBER_WITH_DAMAGE, as described in Chapter 5, the PNM model from MCalibration can handle a much broader range of loading and unloading strain rates, including the ability to simulate quasi-static loading and unloading.

Another source of error in the LS-DYNA simulations of the light gauge high strength low alloy vanadium steel (HSLA-V) stud wall tests was the modeling of the connections. The connections were modeled in the simplest possible way while capturing the actual connection's rotational stiffness, the actual strength of the connection, and also capturing the bracing of the studs against crippling and local web buckling. A more detailed effort into connection modeling was undertaken as well, primarily with the objective of validating the more simple connection model. This more detailed connection is shown in Fig. 8.3a, where we can see that the "track" was modeled as well as the "Blast Washers." We can see how this connection permits some rotation in Fig. 8.3b, in the same way that rotation occurs in the actual tests, *namely*, due bending of the track and blast washers, as shown in Fig. 8.4.

(a) (b)
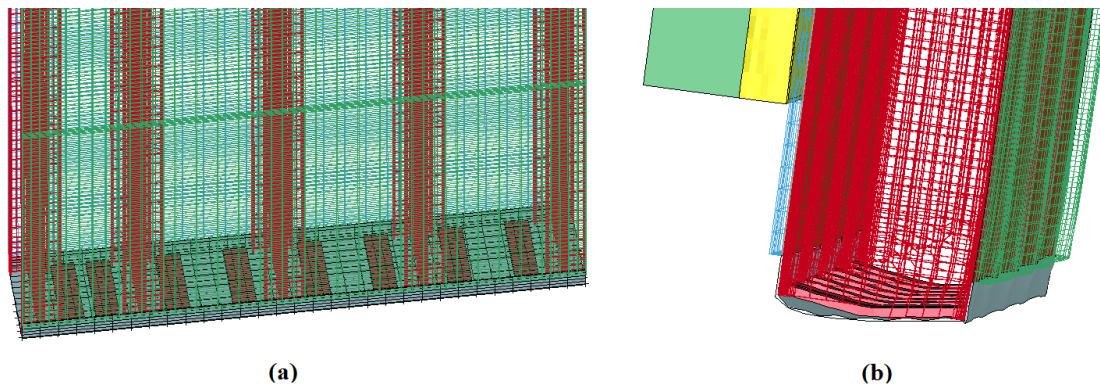
Figure 8.3: (a) LS-DYNA connection that includes blast "track" and "washers" (b) Rotation of connection similar to rotation observed in experiments

While this model is more complex (and computationally expensive), requir-

Figure 8.4: Photo showing rotation of connection similar to rotation observed in LS-DYNA simulation

ing two additional contact assignments and two additional material assignments, it offers no real advantages over the simplified connection presented in previous chapters. In order to improve upon the connection failure model presented in previous chapters, the screws that sandwich the flanges of the track between the composite panels and the studs would need to be modeled, since connection failure in the actual tests is initiated by the shearing or pullout of the track's screws. In the connection model shown in Fig. 8.3, the flanges of the track are simply "tied" to the studs, and since the "tie-breaks" were set to very large values, any detailed modeling of the panels at the location of the connections would offer no additional resistance to failure. A more complex model would consider localized bending of the panels at the location of the track, which would require a significant increase in the complexity of the geometry.

Additionally, the webs of the studs are braced against local buckling or crippling *via* a tied contact to the track, which is present for the back half of the track. In the actual connection, a "clip" is present in order to brace the stud webs against buckling, which may be modeled, since clip failure was observed in the Blast Simulator tests where the connections failed.

Other simplifications of the connection shown in Fig. 8.3 include the assignment of restraints to a portion of the bottom of the track, whereas in the actual connection, "wedge anchors" were used in order to anchor the connection to a concrete footer. Wedge anchor failure is not considered at all in the model. Contact between the front flange of the track and the blast washers, which may

have a minor influence on the behavior of the connection at failure is also not considered. Lastly, incorporating tearing of the track into the model, a mode of failure that was observed in two of the Blast Simulator tests, would require a significant increase in the complexity of the track's material model.

An investigation into the properties of some of the other materials that were used in the wall tests could be another direction of future research. While the static strengths of the HSLA-V material, the steel sheet material, and the cement board panel material were all provided by SGH, no tests were done to investigate the influence of rate effects on those materials. The cement board material model and the steel sheet material model incorporated rate effects but the accuracy of those models is unknown. The HSLA-V material model did not include any rate effects.

Appendix A

A.1 Design Table

Table A.1 Dynamic increase factors (DIF) for design of reinforced concrete and structural steel elements

Type of stress	Concrete	Reinforcing bars		Structural steel	
	f_{dcu}/f_{cu}	f_{dy}/f_y	f_{du}/f_u	f_{dy}/f_y^*	f_{du}/f_u
Bending	1·25	1·20	1·05	1·20	1·05
Shear	1·00	1·10	1·00	1·20	1·05
Compression	1·15	1·10	—	1·10	—

* Minimum specified f_y for grade 50 steel or less may be enhanced by the average strength increase factor of 1·10.

226

A.2   Design Table

BLAST EFFECTS ON BUILDINGS

Deformation limits

	Protection category			
	1		2	
	θ	μ	θ	μ
Reinforced concrete beams and slabs	2°*	Not applicable	4°†	Not applicable
Structural steel beams and plates‡	2°	10	12°	20

Handwritten annotations: "protect ppl" above column 1, "protect structure" above column 2.

* Shear reinforcement in the form of open or closed 'blast links' must be provided in slabs for $\theta > 1°$. Closed links (shape code 74 to BS 4466) [4] must be provided in all beams.

† Support rotations of up to 8° may be permitted when the element has sufficient lateral restraint to develop tensile membrane action. Further guidance regarding the tensile membrane capacity of reinforced concrete slabs may be found in TM5-1300 [3].

‡ Adequate bracing must be provided to assure the corresponding level of ductile behaviour.

A.3   Design Table

Dynamic design stresses for reinforced concrete

Type of stress	Protection category	Dynamic design stress	
		Concrete f_{dc}	Reinforcing bars f_{ds}
Bending	1	f_{dcu}	f_{dy}
	2	f_{dcu}	$f_{dy} + (f_{du} - f_{dy})/4$
Shear	1	f_{dcu}	f_{dy}
	2	f_{dcu}	f_{dy}
Compression	1 and 2	f_{dcu}	f_{dy}

Appendix B
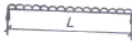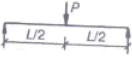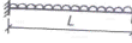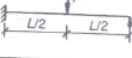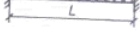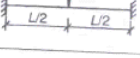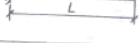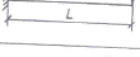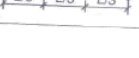
B.1 Design Table

Transformation factors for one-way elements (after US Department of the Army Technical Manual, TM5-1300. Design of structures to resist the effects of accidental explosions, 1990)

Edge conditions and loading diagrams	Range of behaviour	Load factor K_L	Mass factor K_M	Load–mass factor K_{LM}
(uniform load, L)	Elastic	0·64	0·50	0·78
	Plastic	0·50	0·33	0·66
(point load P, L/2 L/2)	Elastic	1·0	0·49	0·49
	Plastic	1·0	0·33	0·33
(uniform load, L)	Elastic	0·58	0·45	0·78
	Elasto-plastic	0·64	0·50	0·78
	Plastic	0·50	0·33	0·66
(point load P, L/2 L/2)	Elastic	1·0	0·43	0·43
	Elasto-plastic	1·0	0·49	0·49
	Plastic	1·0	0·33	0·33
(uniform load, L)	Elastic	0·53	0·41	0·77
	Elasto-plastic	0·64	0·50	0·78
	Plastic	0·50	0·33	0·66
(point load P, L/2 L/2)	Elastic	1·0	0·37	0·37
	Plastic	1·0	0·33	0·33
(uniform load, L)	Elastic	0·40	0·26	0·65
	Plastic	0·50	0·33	0·66
(point load P, L)	Elastic	1·0	0·24	0·24
	Plastic	1·0	0·33	0·33
(P/2 P/2, L/3 L/3 L/3)	Elastic	0·87	0·52	0·60
	Plastic	1·0	0·56	0·56

B.2 Design Table

Ultimate unit resistances for one-way elements (as per Table)

Edge conditions and loading diagrams	Ultimate resistance
L	$r_u = \dfrac{8M_P}{L^2}$
P $L/2 \quad L/2$	$R_u = \dfrac{4M_P}{L}$
L	$r_u = \dfrac{4(M_N + 2M_P)}{L^2}$
P $L/2 \quad L/2$	$R_u = \dfrac{2(M_N + 2M_P)}{L}$
L	$r_u = \dfrac{8(M_N + M_P)}{L^2}$
P $L/2 \quad L/2$	$R_u = \dfrac{4(M_N + M_P)}{L}$
L	$r_u = \dfrac{2M_N}{L^2}$
P L	$R_u = \dfrac{M_N}{L}$
$P/2 \quad P/2$ $L/3 \quad L/3 \quad L/3$	$R_u = \dfrac{6M_P}{L}$

B.3   Design Table

Table B.3 *Elastic, elasto-plastic and equivalent elastic stiffnesses for one-way elements (as per Table* ⬛⬛)

Edge conditions and loading diagrams	Elastic stiffness, K_e	Elasto-plastic stiffness, K_{ep}	Equivalent elastic stiffness K_E
(simply supported, UDL, L)	$\dfrac{384EI}{5L^4}$	—	$\dfrac{384EI}{5L^4}$
(simply supported, P at midspan, $L/2$, $L/2$)	$\dfrac{48EI}{L^3}$	—	$\dfrac{48EI}{L^3}$
(propped cantilever, UDL, L)	$\dfrac{185EI}{L^4}$	$\dfrac{384EI}{5L^4}$	$\dfrac{160EI^*}{L^4}$
(propped cantilever, P at midspan, $L/2$, $L/2$)	$\dfrac{107EI}{L^3}$	$\dfrac{48EI}{L^3}$	$\dfrac{106EI^*}{L^3}$
(fixed-fixed, UDL, L)	$\dfrac{384EI}{L^4}$	$\dfrac{384EI}{5L^4}$	$\dfrac{307EI^*}{L^4}$
(fixed-fixed, P at midspan, $L/2$, $L/2$)	$\dfrac{192EI}{L^3}$	$\dfrac{48EI\dagger}{L^3}$	$\dfrac{192EI^*}{L^3}$
(cantilever, UDL, L)	$\dfrac{8EI}{L^4}$	—	$\dfrac{8EI}{L^4}$
(cantilever, P at free end, L)	$\dfrac{3EI}{L^3}$	—	$\dfrac{3EI}{L^3}$
(simply supported, $P/2$ and $P/2$ at third points, $L/3$, $L/3$, $L/3$)	$\dfrac{56\cdot4EI}{L^3}$	—	$\dfrac{56\cdot4EI}{L^3}$

* Valid only if $M_N = M_p$.
† Valid only if $M_N < M_p$.

Appendix C

C.1   Design Table
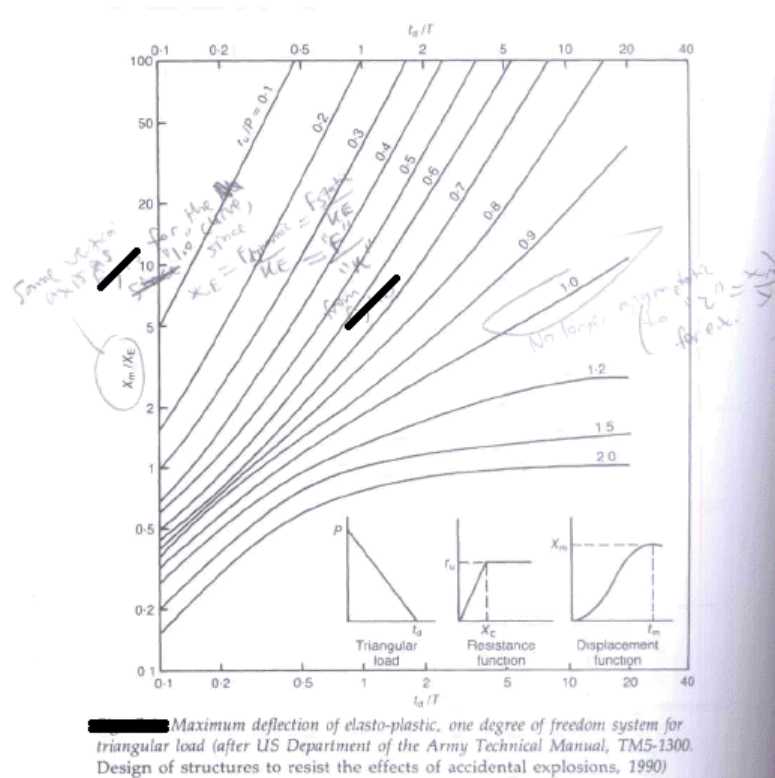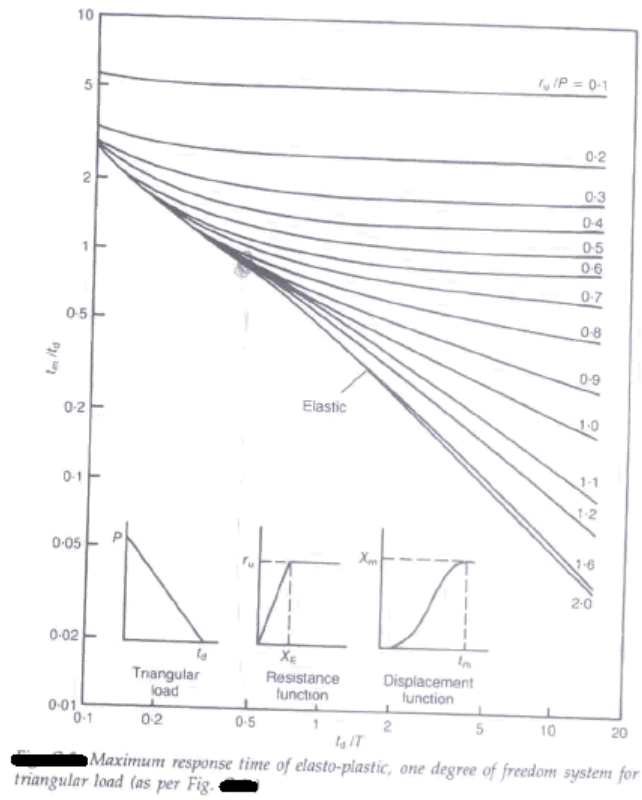
Maximum deflection of elasto-plastic, one degree of freedom system for triangular load (after US Department of the Army Technical Manual, TM5-1300, Design of structures to resist the effects of accidental explosions, 1990)

C.2   Design Table

Maximum response time of elasto-plastic, one degree of freedom system for triangular load (as per Fig. ▩**)**

C.3   Design Table
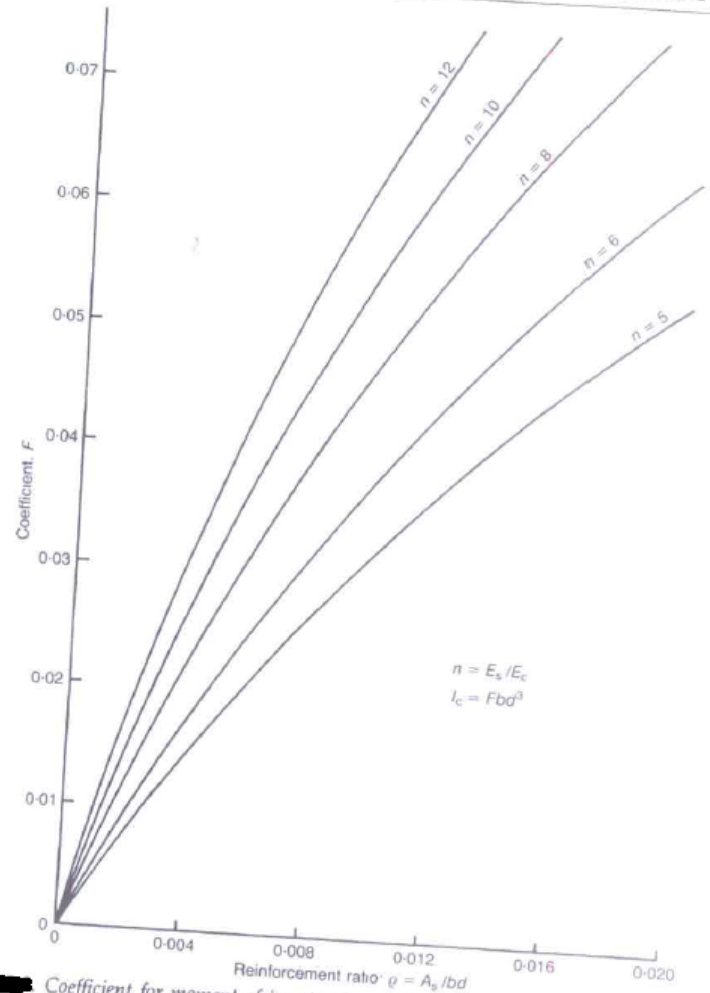
Coefficient for moment of inertia of cracked sections with equal reinforcement on opposite faces [3]

Appendix D

D.1 Derivation: $\frac{dI_B}{d\mathbf{B}}$, $\frac{dII_B}{d\mathbf{B}}$, $\frac{dIII_B}{d\mathbf{B}}$

$$\text{Since } I_B = tr\mathbf{B} = B_{kk}, \quad \frac{dI_B}{d\mathbf{B}} = \frac{\partial B_{nn}}{\partial B_{kl}}\mathbf{e_k e_l} = \delta_{nk}\delta_{nl}\mathbf{e_k e_l} \qquad \text{(D.1)}$$

$$\frac{dII_B}{d\mathbf{B}} = \frac{d\left[\frac{1}{2}[(tr\mathbf{B})^2 - tr(\mathbf{B^2})]\right]}{d\mathbf{B}} = \frac{1}{2}\big[2tr\mathbf{B}\underbrace{\frac{d(tr\mathbf{B})}{d\mathbf{B}}}_{\text{chain rule}} - \frac{d(tr(\mathbf{B^2}))}{d\mathbf{B}}\big]$$

$$= \frac{1}{2}\big[2tr(\mathbf{B})\mathbf{I} - \underbrace{\frac{d(tr(\mathbf{B^2}))}{d\mathbf{B}}}_{\text{see below}}\big]$$

$$\frac{d(tr\mathbf{B^2})}{d\mathbf{B}} = \frac{d(B_{ij}B_{ji})}{d\mathbf{B}} = \frac{\partial(B_{ij}B_{ji})}{\partial B_{mn}}\mathbf{e_n e_m} = \underbrace{\frac{\partial B_{ij}}{\partial B_{mn}}B_{ji}\mathbf{e_n e_m} + \frac{\partial B_{ji}}{\partial B_{mn}}B_{ij}\mathbf{e_n e_m}}_{\text{product rule}}$$

$$= \delta_{im}\delta_{jn}B_{ji}\mathbf{e_n e_m} + \delta_{jm}\delta_{in}B_{ij}\mathbf{e_n e_m} = B_{ji}\mathbf{e_j e_i} + B_{ij}\mathbf{e_i e_j} = 2B_{ij}\mathbf{e_i e_j}$$

$$\text{So, } \frac{dII_B}{d\mathbf{B}} = \frac{1}{2}[2tr(\mathbf{B})\mathbf{I} - 2B_{ji}\mathbf{e_i e_j}] = I_B\mathbf{I} - \mathbf{B} \qquad \text{(D.2)}$$

We know $III_B = det\mathbf{B}$; but we need a better expression for III_B before we derive $\frac{dIII_b}{d\mathbf{B}}$.

We know from the Cayley-Hamilton Theorem: $\mathbf{B}^3 - I_B\mathbf{B}^2 + II_B\mathbf{B} - III_B\mathbf{I} = 0$;

$tr(\mathbf{B}^3 - I_B\mathbf{B}^2 + II_B\mathbf{B} - III_B\mathbf{I}) = tr(0)$

$tr(\mathbf{B}^3) - \underbrace{tr(I_B\mathbf{B}^2)}_{I_Btr(\mathbf{B}^2)} + \underbrace{tr(II_B\mathbf{B})}_{II_Btr\mathbf{B}} - \underbrace{tr(III_B\mathbf{I})}_{III_B*3} = 0$

$tr(\mathbf{B}^3) - tr(\mathbf{B})tr(\mathbf{B}^2) + \frac{1}{2}[(tr\mathbf{B})^2 - tr(\mathbf{B}^2)]tr\mathbf{B} = III_B * 3$

$tr(\mathbf{B}^3) - tr(\mathbf{B})tr(\mathbf{B}^2) + \underbrace{\frac{1}{2}tr(\mathbf{B})(tr\mathbf{B})^2}_{1/2(tr\mathbf{B})^3} - \frac{1}{2}tr(\mathbf{B})tr(\mathbf{B}^2) = III_B * 3$

$\frac{1}{3}\left[tr(\mathbf{B}^3) - \frac{3}{2}tr(\mathbf{B})tr(\mathbf{B}^2) + \frac{1}{2}(tr\mathbf{B})^3\right] = III_B$

$\frac{dIII_B}{d\mathbf{B}} = \frac{d\left(1/3tr(\mathbf{B}^3)\right)}{d\mathbf{B}} - \frac{d\left(1/2tr(\mathbf{B})tr(\mathbf{B}^2)\right)}{d\mathbf{B}} + \frac{d\left(1/6(tr\mathbf{B})^3\right)}{d\mathbf{B}}$

$= \frac{d\left(1/3tr(\mathbf{B}^3)\right)}{d\mathbf{B}} \underbrace{- \frac{d\left(1/2tr(\mathbf{B})\right)}{d\mathbf{B}} * tr(\mathbf{B}^2) - \frac{d(tr(\mathbf{B}^2))}{d\mathbf{B}} * \frac{1}{2}tr\mathbf{B}}_{\text{product rule}} + \underbrace{\frac{d(1/6(tr\mathbf{B})^3)}{d\mathbf{B}}}_{\frac{1}{6}\frac{d((tr\mathbf{B})^2tr\mathbf{B})}{d\mathbf{B}}}$

$= \frac{1}{3}\frac{d(tr(\mathbf{B}^3))}{d\mathbf{B}} - \frac{1}{2}tr(\mathbf{B}^2)\underbrace{\frac{d(tr\mathbf{B})}{d\mathbf{B}}}_{\mathbf{I}} - \frac{1}{2}\underbrace{tr(\mathbf{B})}_{I_B}\underbrace{\frac{d(tr(\mathbf{B}^2))}{d\mathbf{B}}}_{2\mathbf{B}}$

$\overbrace{+ \frac{1}{6}tr(\mathbf{B})\underbrace{\frac{d((tr\mathbf{B})^2)}{d\mathbf{B}}}_{2tr(\mathbf{B})\frac{d(tr\mathbf{B})}{d\mathbf{B}}} + \frac{1}{6}(tr\mathbf{B})^2 * \underbrace{\frac{d(tr\mathbf{B})}{d\mathbf{B}}}_{\mathbf{I}}}^{\text{product rule}}$

$= \frac{1}{3}\underbrace{\frac{d(tr(\mathbf{B}^3))}{d\mathbf{B}}}_{\text{see below}} - \frac{1}{2}tr(\mathbf{B}^2)\mathbf{I} - \frac{1}{2}I_B(2\mathbf{B}) + 1/3(tr\mathbf{B})^2\mathbf{I} + 1/6(\underbrace{tr\mathbf{B}}_{I_B})^2\mathbf{I}$

where $\frac{d(tr(\mathbf{B}^3))}{d\mathbf{B}} = \frac{\partial[B_{kl}B_{lm}B_{mk}]}{\partial B_{ji}}\mathbf{e_i}\mathbf{e_j}$

$= \frac{\partial B_{kl}}{\partial B_{ji}}B_{lm}B_{mk}\mathbf{e_i}\mathbf{e_j} + B_{kl}\frac{\partial B_{lm}}{\partial B_{ji}}B_{mk}\mathbf{e_i}\mathbf{e_j} + B_{kl}B_{lm}\frac{\partial B_{mk}}{\partial B_{ji}}\mathbf{e_i}\mathbf{e_j}$

$= \delta_{kj}\delta_{li}B_{lm}B_{mk}\mathbf{e_i}\mathbf{e_j} + \delta_{lj}\delta_{mi}B_{kl}B_{mk}\mathbf{e_i}\mathbf{e_j} + \delta_{mj}\delta_{ki}B_{kl}B_{lm}\mathbf{e_i}\mathbf{e_j}$

$= B_{im}B_{mj}\mathbf{e_i}\mathbf{e_j} + B_{kj}B_{ik}\mathbf{e_i}\mathbf{e_j} + B_{il}B_{lj}\mathbf{e_i}\mathbf{e_j} = 3\mathbf{B}^2$

So,

$\frac{dIII_B}{d\mathbf{B}} = \frac{1}{3}(3\mathbf{B}^2) - \frac{1}{2}tr(\mathbf{B}^2)\mathbf{I} - \frac{1}{2}I_B(2\mathbf{B}) + \frac{1}{2}I_B^2\mathbf{I}$

$= \mathbf{B}^2 - I_B\mathbf{B} - \frac{1}{2}(tr(\mathbf{B}^2) - I_B^2)\mathbf{I}$

$$= \mathbf{B}^2 - I_B\mathbf{B} + II_B\mathbf{I} , \quad \text{Since } II_B = \frac{1}{2}\left(I_B^2 - tr(\mathbf{B}^2)\right) \qquad \text{(D.3)}$$

D.2   Blatz-Ko Foam

Consider the following strain energy function, which is a simplified version of the Blatz-Ko function [7]:

> note: It has been assumed that the material is compressible, with a Poisson Ratio $\nu = .25$

$$\phi = \frac{1}{2}\mu \left(2III_B^{1/2} + II_B III_B^{-1} - 5 \right)$$

We can derive the constitutive equation for $\boldsymbol{\sigma}$ in terms of μ and $\mathbf{B}$ as follows:

$$\frac{\partial \phi}{\partial I_B} = 0 \qquad \frac{\partial \phi}{\partial II_B} = \frac{1}{2}\mu III_B^{-1} \qquad \frac{\partial \phi}{\partial III_B} = \frac{1}{2}\mu(III_B^{-1/2} - II_B III_B^{-2})$$

Substituting into eq. (5.15), re-written below:

$$\boldsymbol{\sigma} = \frac{2}{det\mathbf{B}^{1/2}}[(III_B \frac{\partial \phi}{\partial III_B} + \frac{\partial \phi}{\partial II_B} II_B)\mathbf{I} + \frac{\partial \phi}{\partial I_B}\mathbf{B} - III_B \frac{\partial \phi}{\partial II_B}\mathbf{B}^{-1}]$$

We then get:

$$\boldsymbol{\sigma} = \frac{2}{det\mathbf{B}^{1/2}}[(III_B * \frac{1}{2}\mu(III_B^{-1/2} - II_B III_B^{-2}) + \frac{1}{2}\mu III_B^{-1} * II_B)\mathbf{I} - III_B * \frac{1}{2}\mu III_B^{-1} * \mathbf{B}^{-1}]$$

This reduces to:

$$\boldsymbol{\sigma} = \frac{1}{det\mathbf{B}^{1/2}} * \mu(III_B^{1/2}\mathbf{I} - \mathbf{B}^{-1})$$

or

$$\boldsymbol{\sigma} = \mu \left(\mathbf{I} - III_B^{-1/2}\mathbf{B}^{-1} \right)$$

> μ is analogous to the "shear modulus." However, in order to simplify experimentation, a simple uniaxial test is often performed in order to determine μ for materials that follow the above Blatz-Ko function.

*MAT_BLATZ-KO_RUBBER is available in LS-DYNA and is an incompressible version of the original Blatz-Ko model [7].

D.3 Mooney-Rivlin Rubber

Consider a rectangular block under tensile stress in X_1 direction (simple extension test) that causes the stretch in that direction of amount λ_1. Assume the material of the block is an incompressible "Mooney-Rivlin" rubber with:

$$\phi = \frac{1}{2}\mu\left[\left(\frac{1}{2}+\beta\right)(I_B-3) + \left(\frac{1}{2}-\beta\right)(II_B-3)\right] \tag{D.4}$$

where μ and β are material constants.

Incompressible $\rightarrow \boldsymbol{\sigma} = -\rho_0\mathbf{I} + 2[(\frac{\partial\phi}{\partial I_B})\mathbf{B} - (\frac{\partial\phi}{\partial II_B})\mathbf{B}^{-1}]$

We need to figure out a $x \longleftrightarrow X$ mapping. We can do this as follows:

$x_1 = \lambda_1 X_1$
$x_2 = \lambda_2 X_2$
$x_3 = \lambda_2 X_3 \quad (\lambda_3 = \lambda_2 \text{ due to isotropy})$

$$\mathbf{F} = \begin{bmatrix} \lambda_1 & 0 & 0 \\ 0 & \lambda_2 & 0 \\ 0 & 0 & \lambda_2 \end{bmatrix}$$

$det\mathbf{F} = \lambda_1\lambda_2^2 = 1 \longrightarrow \lambda_2 = \frac{1}{\sqrt{\lambda_1}}$

$$\longrightarrow \mathbf{B} = \mathbf{F}\cdot\mathbf{F}^T = \begin{bmatrix} \lambda_1^2 & 0 & 0 \\ 0 & \frac{1}{\lambda_1} & 0 \\ 0 & 0 & \frac{1}{\lambda_1} \end{bmatrix}$$

Now, let's find an expression for σ_{11}, since we presumably have this experimental data.

$\frac{\partial\phi}{\partial I_B} = \frac{1}{4}\mu + \frac{1}{2}\mu\beta \quad ; \quad \frac{\partial\phi}{\partial III_B} = 0 \quad ; \quad \frac{\partial\phi}{\partial II_B} = \frac{1}{4}\mu - \frac{1}{2}\mu\beta$

$\boldsymbol{\sigma} = -\rho_0\mathbf{I} + 2\left[(\frac{1}{4}\mu + \frac{1}{2}\mu\beta)\mathbf{B} - (\frac{1}{4}\mu - \frac{1}{2}\mu\beta)\mathbf{B}^{-1}\right]$

$\sigma_{11} = -\rho_0 + \mu[(\frac{1}{2} + \beta)\lambda_1^2 - (\frac{1}{2} - \beta)\frac{1}{\lambda_1^2}]$

$\sigma_{22} = \sigma_{33} = -\rho_0 + \mu[(\frac{1}{2} + \beta)\frac{1}{\lambda_1} - (\frac{1}{2} - \beta)\lambda_1] = 0$ (we can assume this)

$\longrightarrow \rho_0$ now known $\longrightarrow \sigma_{11} = \mu\frac{\lambda_1^3 - 1}{\lambda_1}[\frac{1}{2} + \beta + (\frac{1}{2} - \beta)\frac{1}{\lambda_1}]$

We essentially have one equation with two unknown constants. We would like to have another equation - *i.e.* ideally we would like to have data from another experimental test.

Consider a simple shear test, of amount φ, in the direction X_1:
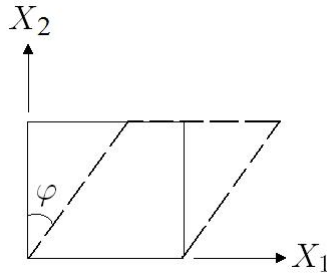
Figure D.1: Simple shear

If $k = tan\varphi, \quad x_1 = X_1 + kX_2 \quad ; \quad x_2 = X_2 \quad ; \quad x_3 = X_3 \quad ; \quad \sigma_{33} = 0$

$$\boldsymbol{\sigma} = -\rho_0\mathbf{I} + 2\left[\underbrace{(\frac{1}{2} + \beta)\frac{\mu}{2}}_{a}\mathbf{B} - \underbrace{(\frac{1}{2} - \beta)\frac{\mu}{2}}_{b}\mathbf{B}^{-1}\right] \quad \text{(found previously)}$$

$$\mathbf{F} = \begin{bmatrix} 1 & k & 0 \\ 0 & 1 & 0 \\ 0 & 0 & 1 \end{bmatrix}$$

$$\mathbf{B} = \mathbf{F} \cdot \mathbf{F}^T = \begin{bmatrix} k^2 + 1 & k & 0 \\ k & 1 & 0 \\ 0 & 0 & 1 \end{bmatrix}$$

$$\mathbf{B}^{-1} = \begin{bmatrix} 1 & -k & 0 \\ -k & 1+k^2 & 0 \\ 0 & 0 & 1 \end{bmatrix}$$

$\sigma_{12} = 2(a+b)k \longleftarrow$ no ρ_0 because $\rho I_{12} = 0$ due to $\mathbf{I}$ being a diagonal matrix

These Mooney-Rivlin examples were shown to illustrate the complexity involved in obtaining unique material constants from multiple material experiments. What was shown is that an axial test would give you σ_{11} and "λ_1" while a shear test would give you σ_{12} and "k." These would be unique for a particular Mooney-Rivlin rubber and once these data are known, then there are two equations in σ_{11}, σ_{12} and one can solve for the two unknowns: μ and β.

In practice, uniaxial data is often used by itself and all material constants are determined based solely on uniaxial data. Defining a hyperelastic material based solely on uniaxial data is essentially how *MAT_SIMPLIFIED_RUBBER _WITH_DAMAGE works, as we saw in a previous chapter. The Mooney-Rivlin model can similarly be characterized using axial data. Both the Mooney-Rivlin model and the Ogden model are good rubber models and both are widely used. From the perspective of an engineer that merely wants to characterize their material model, we saw the benefit of using a "tabulated" approach with *MAT_SIMPLIFIED_RUBBER_WITH_DAMAGE compared to the cumbersome approach described here in the Appendix with the classic Mooney-Rivlin model. Additionally, note that this Mooney-Rivlin model does not consider rate effects at all.

Appendix E

E.1 Additional SSRE010-01 Data

The force-time history for each BG has been converted to pressure, and is shown in Figure E.1.
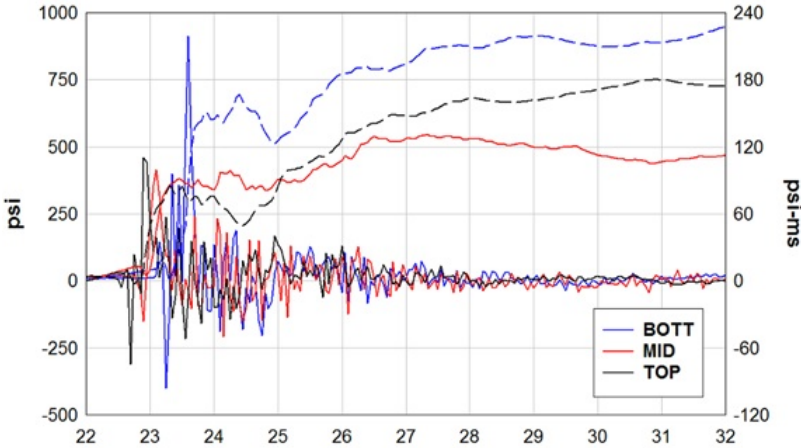
Figure E.1: Test SSRE010-01 Pressure and Impulse for each BG

A simplified exponential force-time history is provided, using the method described in Section 4.2.2. Specifically, eq. (4.2) was used as the basis for generating this curve. This simplified force-time history is shown in Fig. E.2 and was found, here, from the equation:

$$F(t) = 164psi * 3BGs * 48in. * 30in. * [1 - (t - 22.75ms)/5.4ms]e^{-(t-22.75ms)/1.22}$$
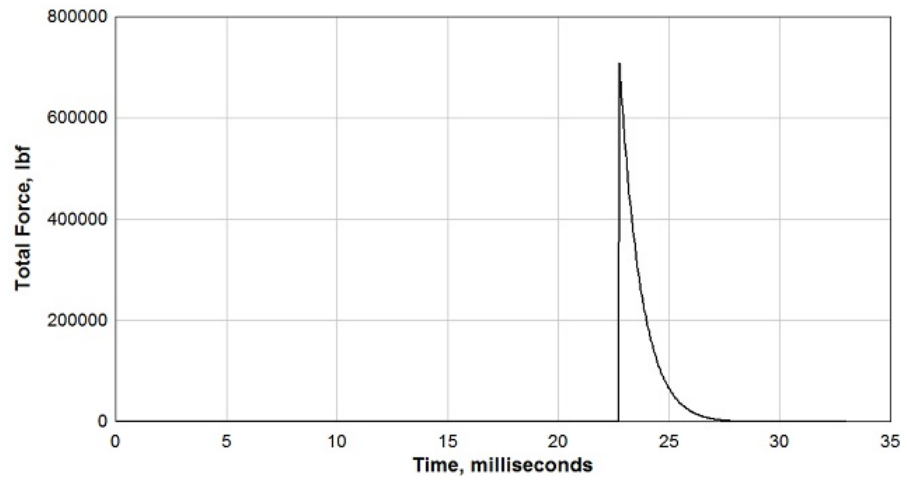
Figure E.2: Test SSRE010-01 Simplified Pressure and Impulse for each BG

Displacements were measured using both camera data and a pair of LVDTs behind the specimen. Displacement-time histories from these two methods are displayed in Figure E.3 and Figure E.4.

Accelerations of the specimen were also used to approximate the transferred pressure and impulse on the back (non-impact) side of the wall. Figure E.5 shows the pressure and impulse curves that can be obtained from averaging these specimen accelerometer readings, with minimal post-processing. The values shown in Fig. E.5 ignore any shear in the specimen during the collision and so will tend to underestimate the pressure and impulse imparted to the specimen.
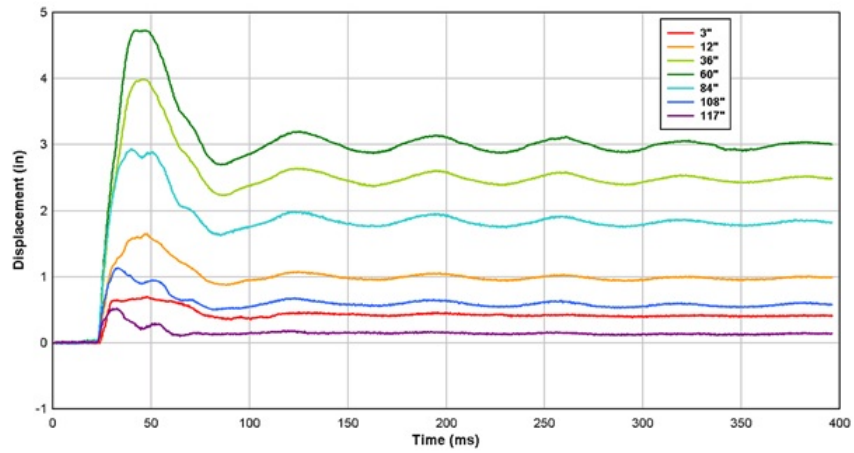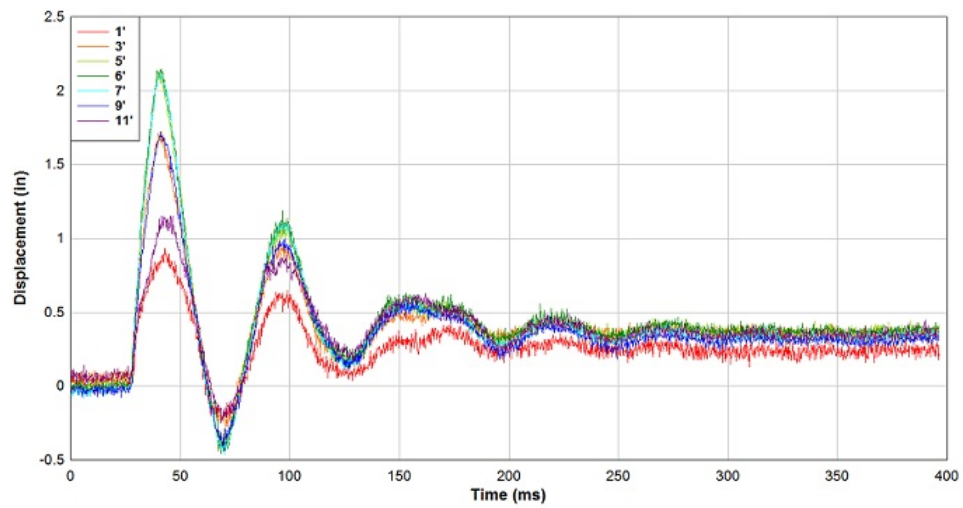
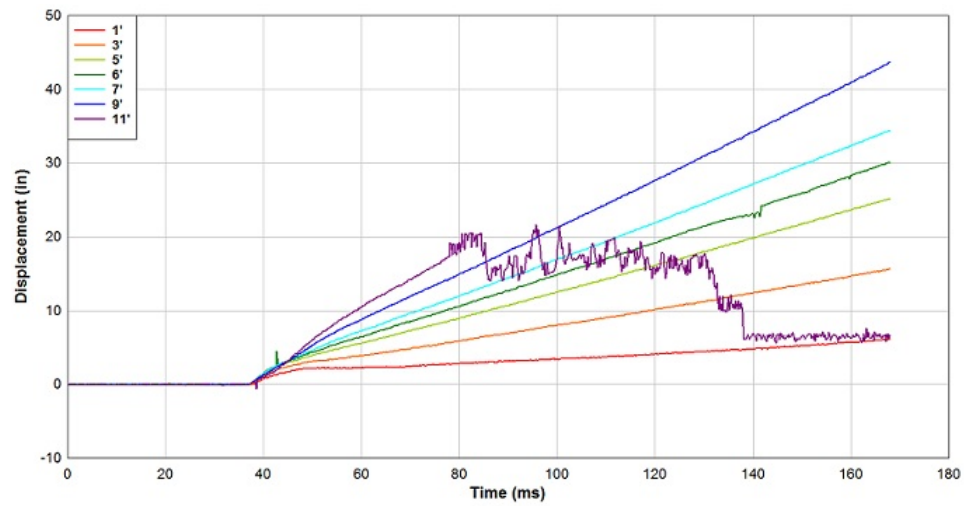**Figure E.3**: Test SSRE010-01 Target Displacements
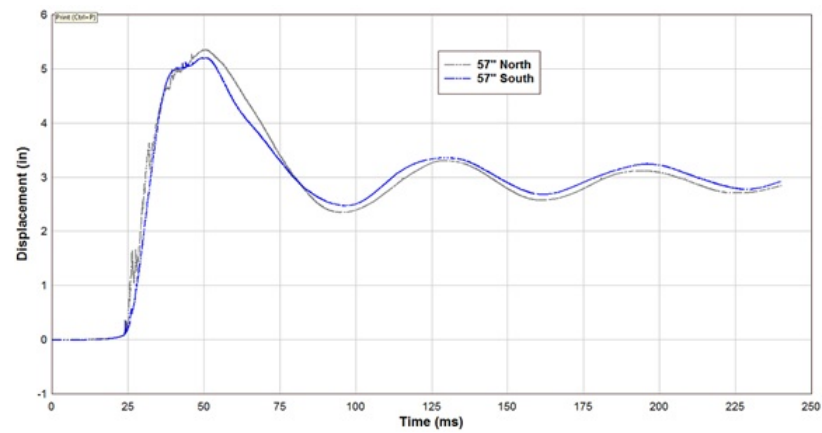
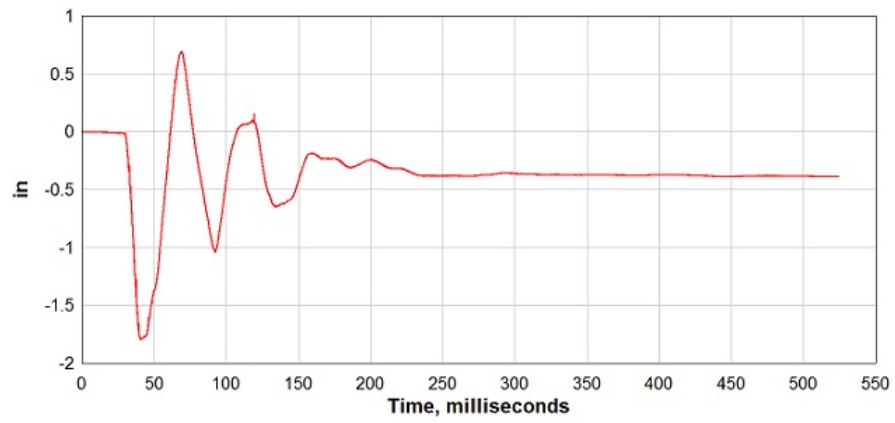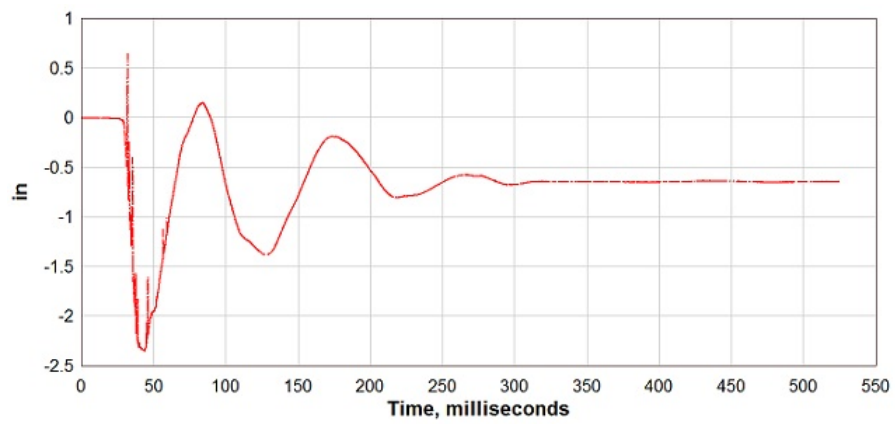**Figure E.4**: Test SSRE010-01 LVDT Displacements
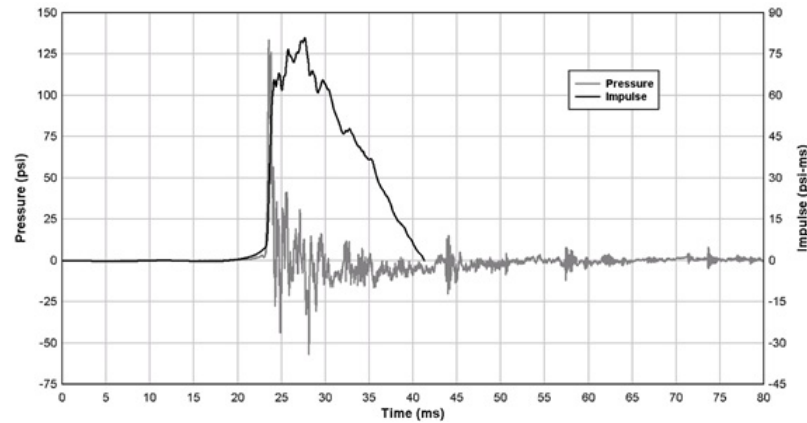
Figure E.5:   Test SSRE010-01 Pressure and Impulse from Specimen Accelerometers
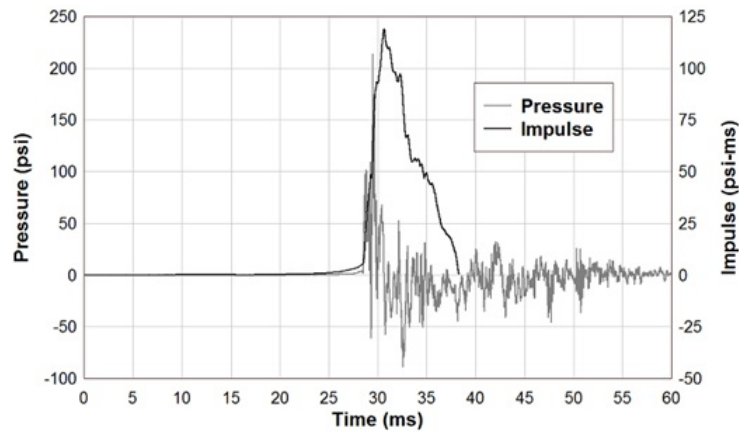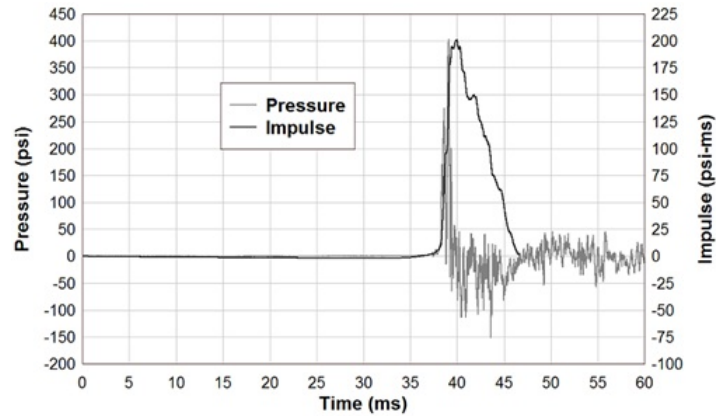
E.2   Additional SSRE010-02 Data

The force-time history for each BG has been converted to pressure and is provided in Figures E.6, E.7, and E.8.
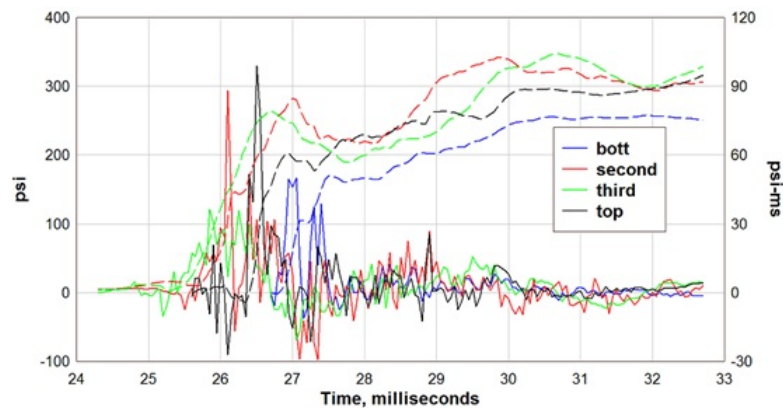
Simplified exponential force-time histories are provided, using the method described in Section 4.2.2. Specifically, eq. (4.2) was used as the basis for generating these curves. These simplified force-time histories are shown in Figures E.9, E.10, and E.11, and were found, here, from the following three equations:

$$F(t) = 82psi * 4BGs * 48in. * 30in. * [1 - (t - 22.80ms)/4.7ms]e^{-(t-22.80ms)/2.26}$$

$$F(t) = 185psi * 4BGs * 48in. * 30in. * [1 - (t - 27.78ms)/4.1ms]e^{-(t-27.78ms)/0.98}$$

$$F(t) = 426psi * 4BGs * 48in. * 30in. * [1 - (t - 37.33ms)/3.3ms]e^{-(t-37.33ms)/0.93}$$

Displacements were measured using camera data and a single LVDT behind the specimen for the first two tests. For the third test, only camera data was available.

Displacement-time histories from the camera are shown in Figures E.12, E.13, and E.14. Displacements from the LVDT are shown in Figure E.15 and
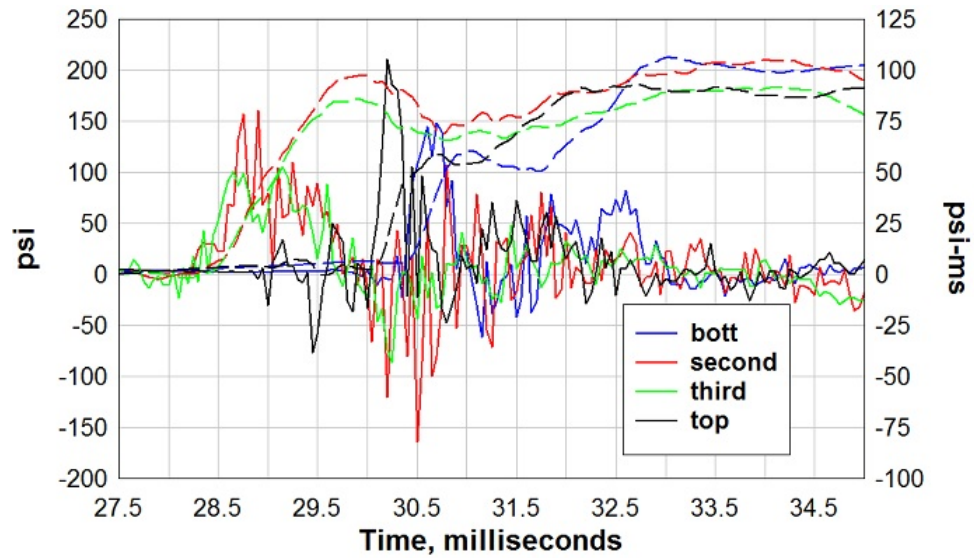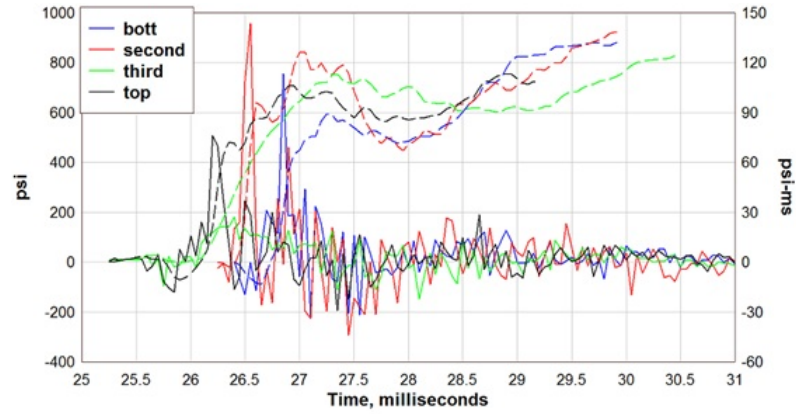
Figure E.6: Test SSRE010-02.1 Pressure and Impulse for each BG
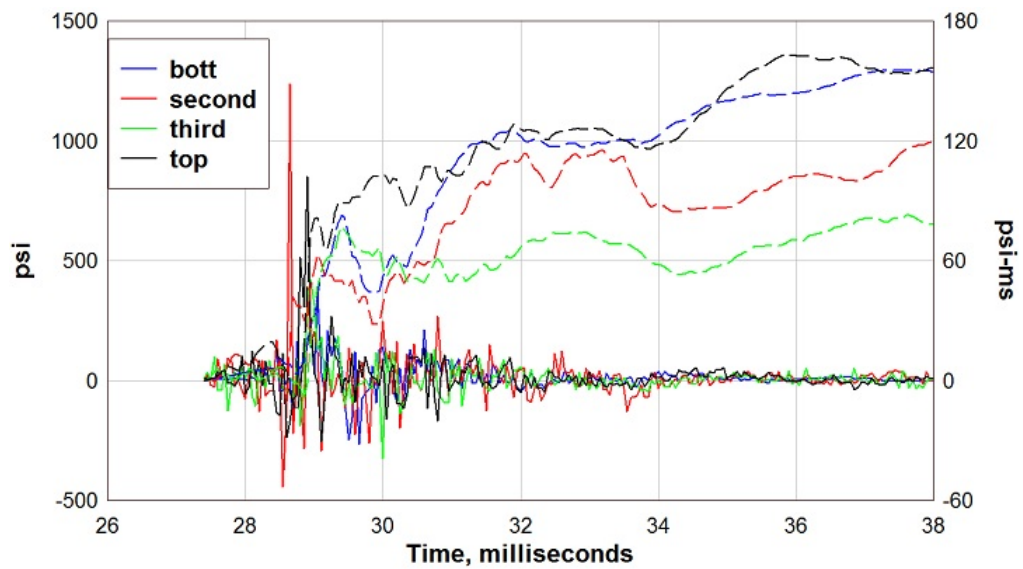
Figure E.7: Test SSRE010-02.2 Pressure and Impulse for each BG
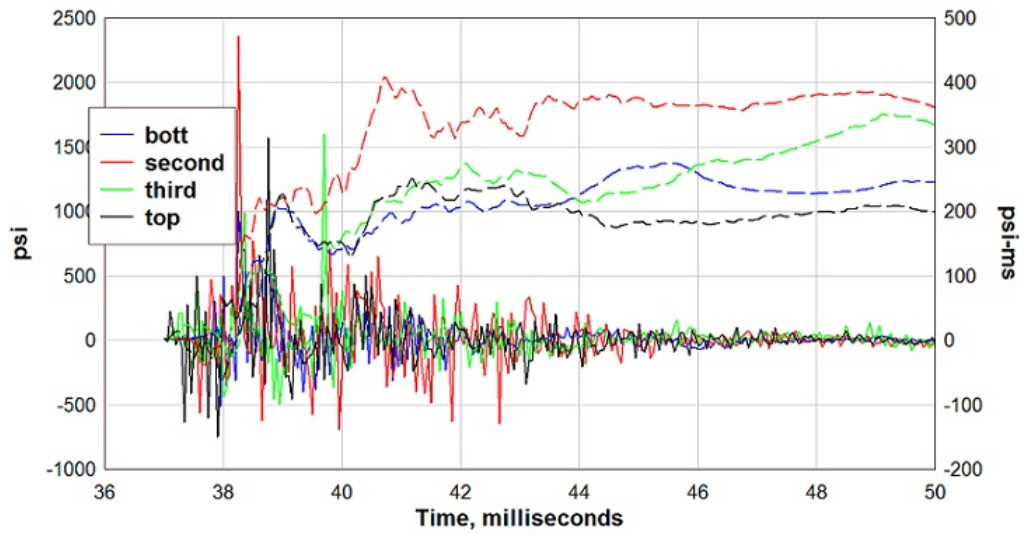
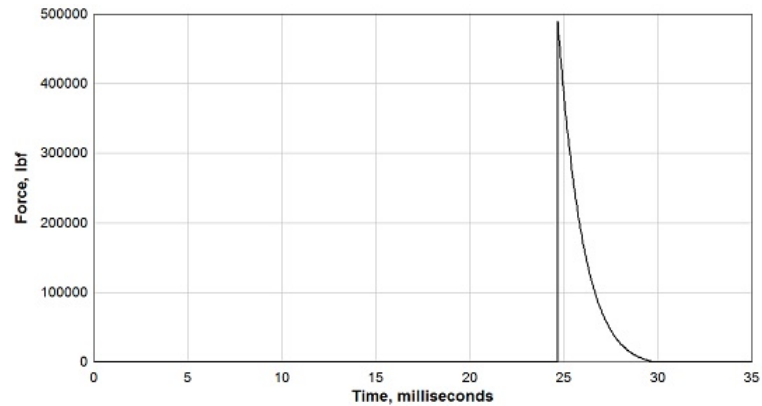**Figure E.8**: Test SSRE010-02.3 Pressure and Impulse for each BG
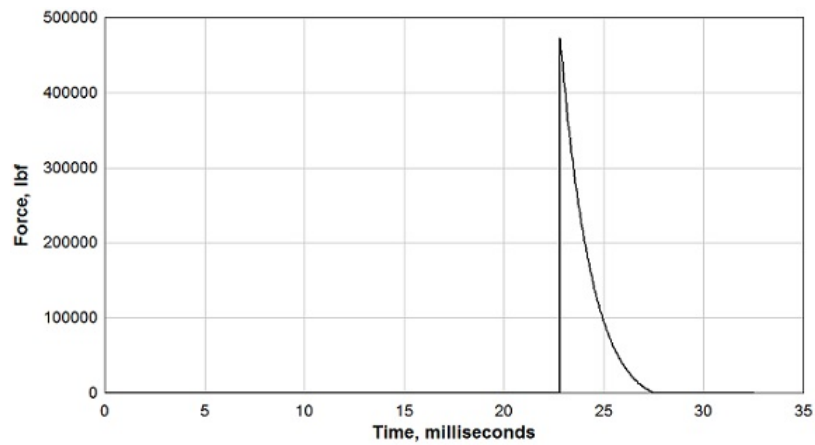
Figure E.9: Test SSRE010-02.1 Simplified Pressure and Impulse
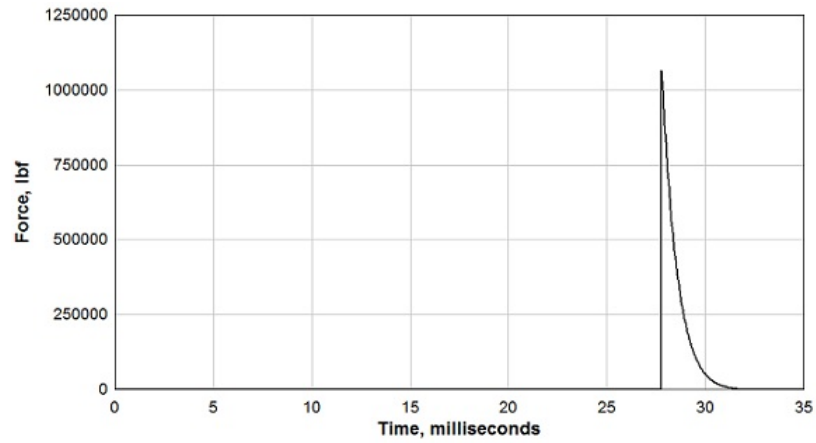
Figure E.10: Test SSRE010-02.2 Simplified Pressure and Impulse
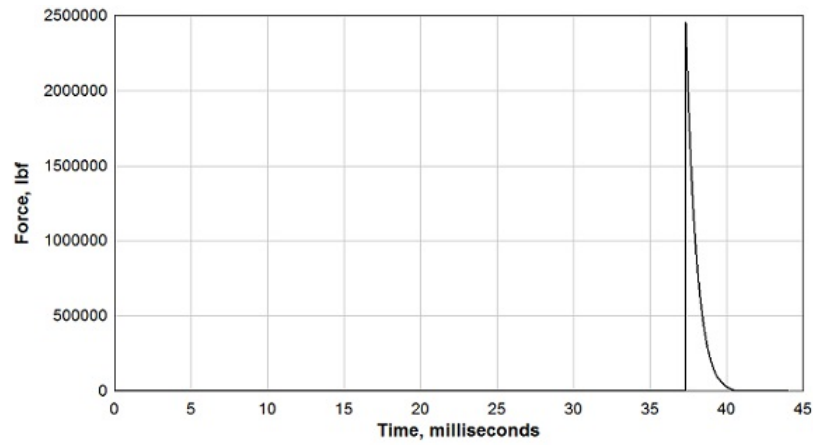
Figure E.11: Test SSRE010-02.3 Simplified Pressure and Impulse

E.16.
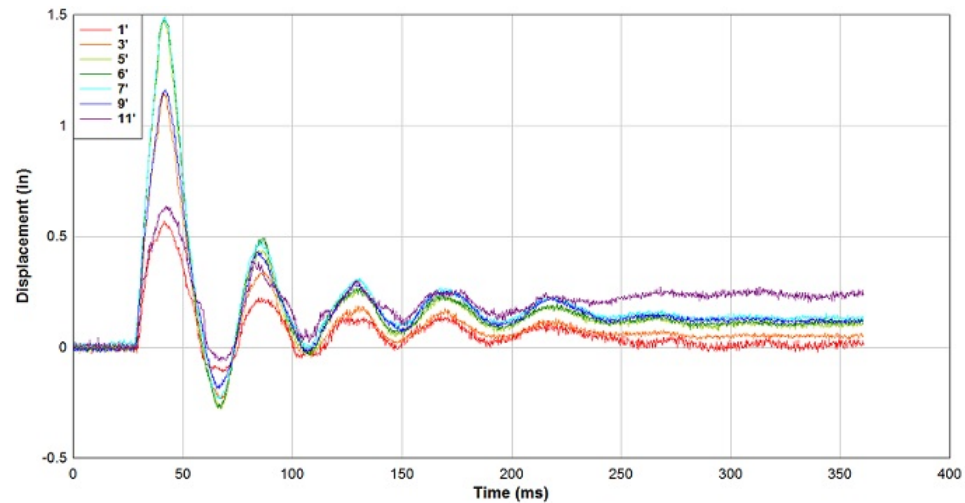
Figure E.12: Test SSRE010-02.1 Target Displacements

Accelerations of the specimen were also used to approximate the transferred pressure and impulse on the back (non-impact) side of the wall. Figures E.17, E.18, and E.19 show the pressure and impulse curves that can be obtained from averaging these specimen accelerometer readings, with minimal post-processing. The values shown in these figures ignore any shear in the specimen during the collision and so will tend to underestimate the pressure and impulse imparted to the specimen.

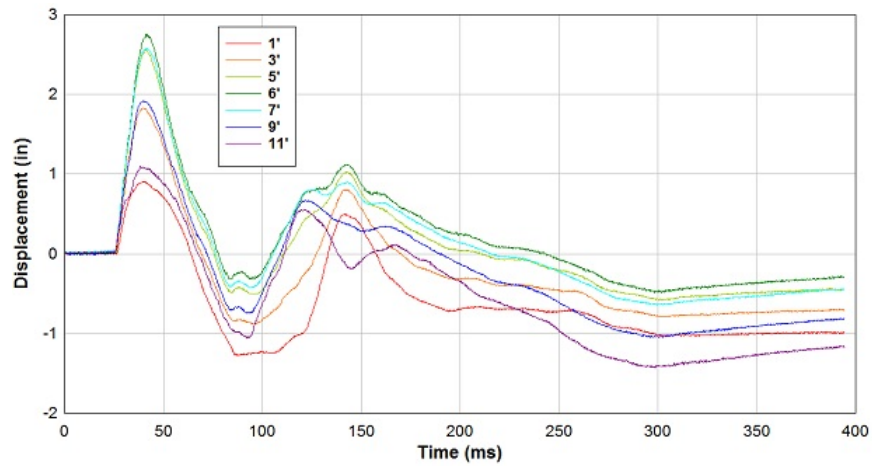**Figure E.13**: Test SSRE010-02.2 Target Displacements

Figure E.14: Test SSRE010-02.3 Target Displacements

Figure E.15: Test SSRE010-02.1 LVDT Displacements

Figure E.16: Test SSRE010-02.2 LVDT Displacements
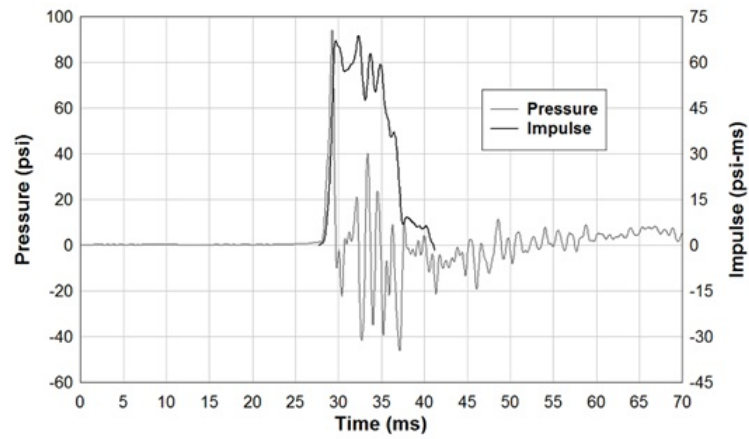
Figure E.17: Test SSRE010-02.1 Pressure and Impulse from Specimen Accelerometers

Figure E.18: Test SSRE010-02.2 Pressure and Impulse from Specimen Accelerometers

Figure E.19: Test SSRE010-02.3 Pressure and Impulse from Specimen Accelerometers

E.3 Additional SSRE010-03 Data

The force-time history for each BG has been converted to pressure and is provided in Figures E.20, E.21, and E.22.

Figure E.20: Test SSRE010-03.1 Pressure and Impulse for each BG

Simplified exponential force-time histories are provided, using the method described in Section 4.2.2. Specifically, eq. (4.2) was used as the basis for generating these curves. These simplified force-time histories are shown in Figures E.23, E.24, and E.25, and were found, here, from the following three equations:

Figure E.21: Test SSRE010-03.2 Pressure and Impulse for each BG
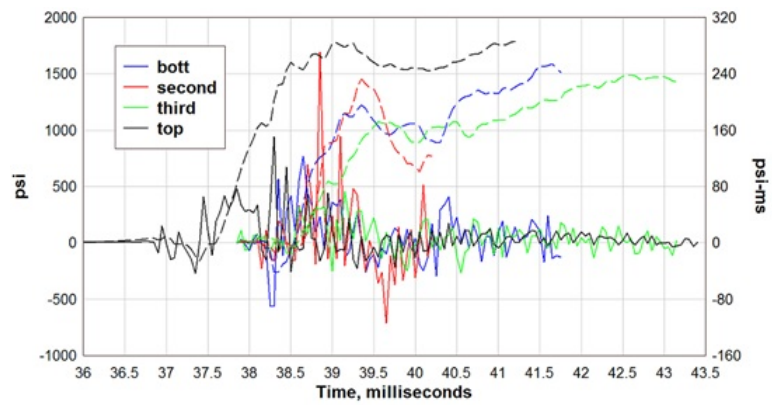
Figure E.22: Test SSRE010-03.3 Pressure and Impulse for each BG

$$F(t) = \quad 85psi * 4BGs * 48in. * 30in. * [1 - (t - 24.68ms)/5.1ms]e^{-(t-24.68ms)/1.8}$$

$$F(t) = 156psi * 4BGs * 48in. * 30in. * [1 - (t - 25.33ms)/4.6ms]e^{-(t-25.33ms)/1.21}$$

$$F(t) = 291psi * 4BGs * 48in. * 30in. * [1 - (t - 38.03ms)/5.7ms]e^{-(t-38.03ms)/1.14}$$

Figure E.23: Test SSRE010-03.1 Simplified Pressure and Impulse
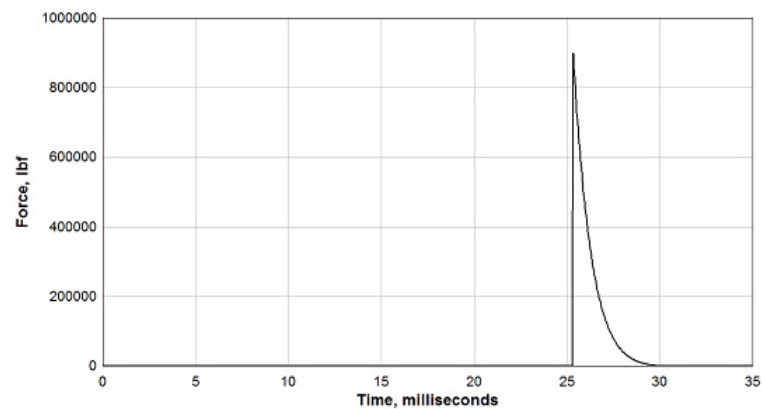
Figure E.24: Test SSRE010-03.2 Simplified Pressure and Impulse

Displacements were measured using camera data and a single LVDT behind the specimen for the first test. For the second and third tests, only camera data was available. Displacement-time histories from the camera are shown in Figures E.26, E.27, and E.28. Displacements from the LVDT is shown in Figure E.29.
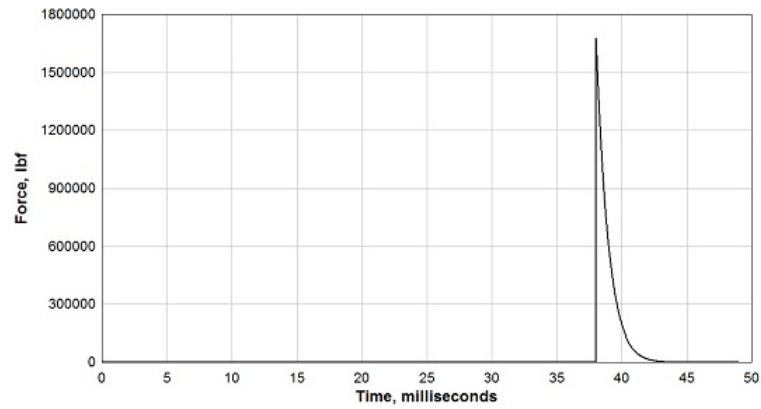
Figure E.25: Test SSRE010-03.3 Simplified Pressure and Impulse
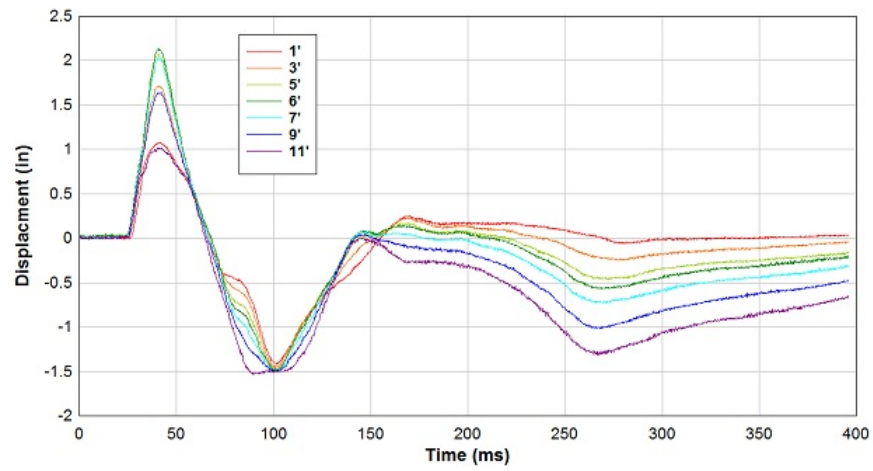
Figure E.26: Test SSRE010-03.1 Target Displacements

Figure E.27: Test SSRE010-03.2 Target Displacements
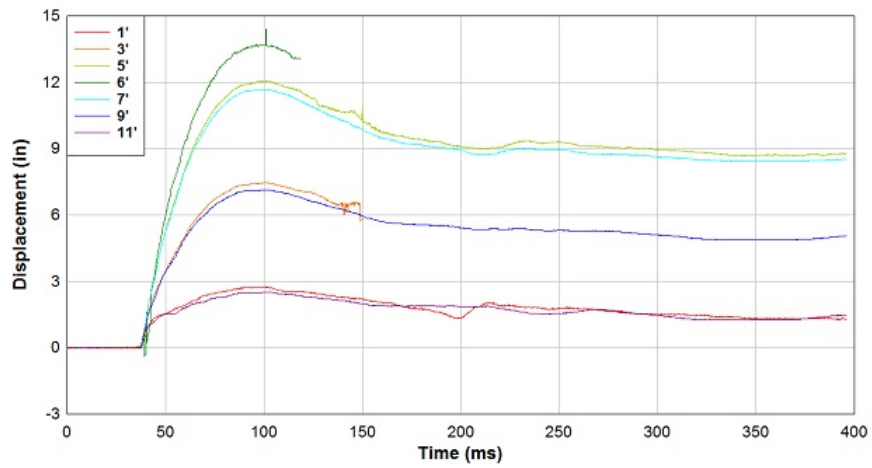
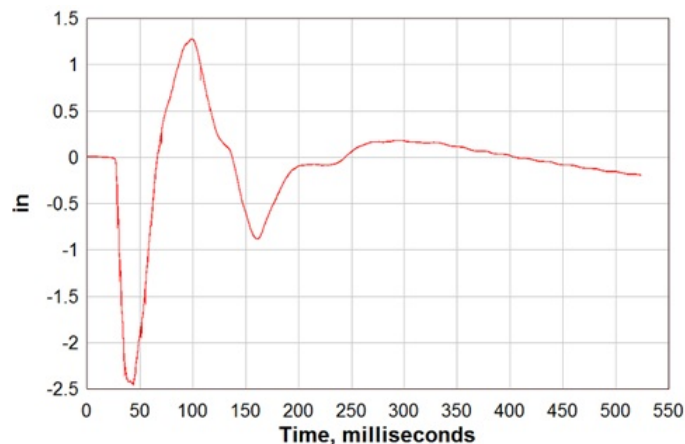**Figure E.28**: Test SSRE010-03.3 Target Displacements

Figure E.29: Test SSRE010-03.1 LVDT Displacements

Accelerations of the specimen were also used to approximate the transferred pressure and impulse on the back (non-impact) side of the wall. Figures E.30, E.31, and E.32 show the pressure and impulse curves that can be obtained from averaging these specimen accelerometer readings, with minimal post-processing. The values shown in these figures ignore any shear in the specimen during the collision and so will tend to underestimate the pressure and impulse imparted to the specimen.
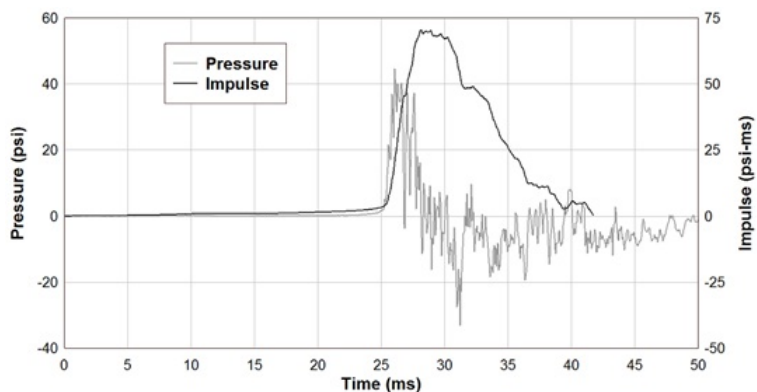
Figure E.30: Test SSRE010-03.1 Pressure and Impulse from Specimen Accelerometers
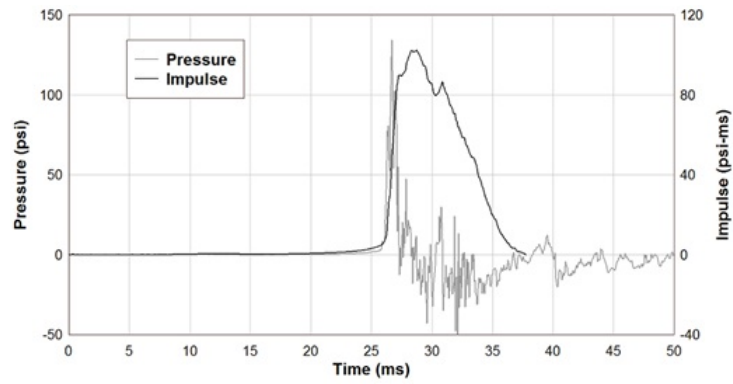
Figure E.31: Test SSRE010-03.2 Pressure and Impulse from Specimen Accelerometers
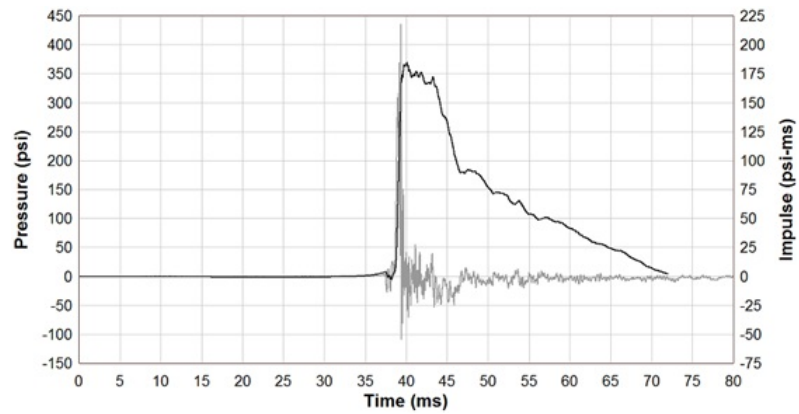

Figure E.32: Test SSRE010-03.3 Pressure and Impulse from Specimen Accelerometers

E.4   Additional SSRE010-04 Data

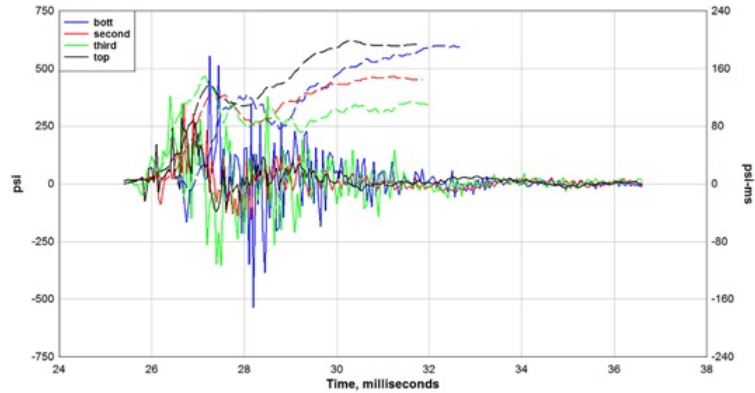The force-time history for each BG has been converted to pressure and is provided in Figures E.33 and E.34.

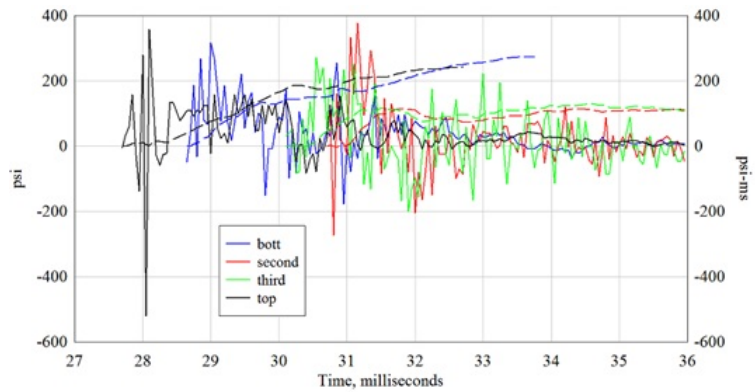**Figure E.33**: Test SSRE010-04.1 Pressure and Impulse for each BG

Figure E.34: Test SSRE010-04.2 Pressure and Impulse for each BG

Simplified exponential force-time histories are provided, using the method described in Section 4.2.2. Specifically, eq. (4.2) was used as the basis for generating these curves. These simplified force-time histories are shown in Figures E.35 and E.36, and were found, here, from the following two equations:

$$F(t) = 157psi * 4BGs * 48in. * 30in. * [1 - (t - 25.93ms)/4.7ms]e^{-(t-25.93ms)/1.58}$$

$$F(t) = \quad 94psi * 4BGs * 48in. * 30in. * [1 - (t - 28.03ms)/6ms]e^{-(t-28.03ms)/8.85}$$
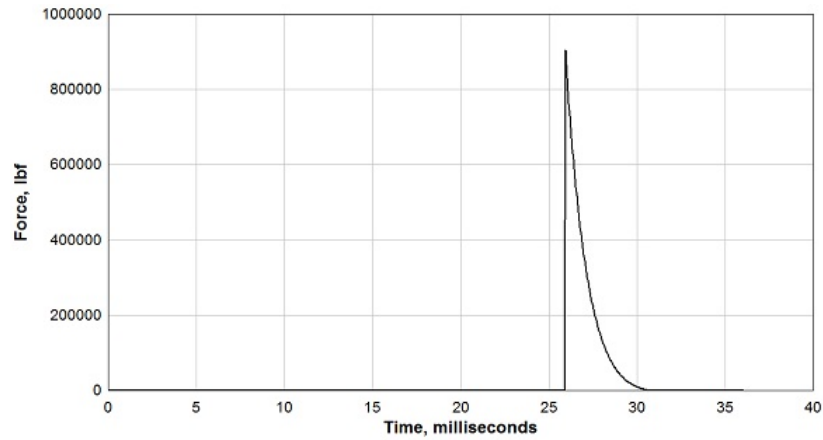

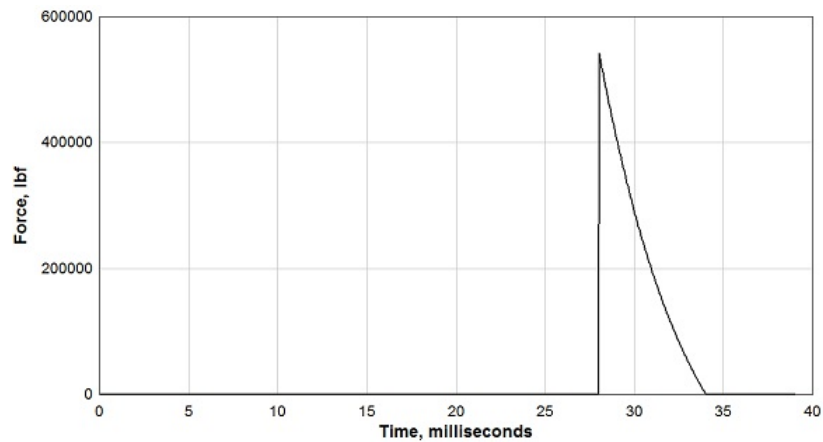**Figure E.35**: Test SSRE010-04.1 Simplified Pressure and Impulse

Figure E.36: Test SSRE010-04.2 Simplified Pressure and Impulse

Displacements were measured using camera data. Displacement-time histories from the camera are shown in Figures E.37 and E.38.
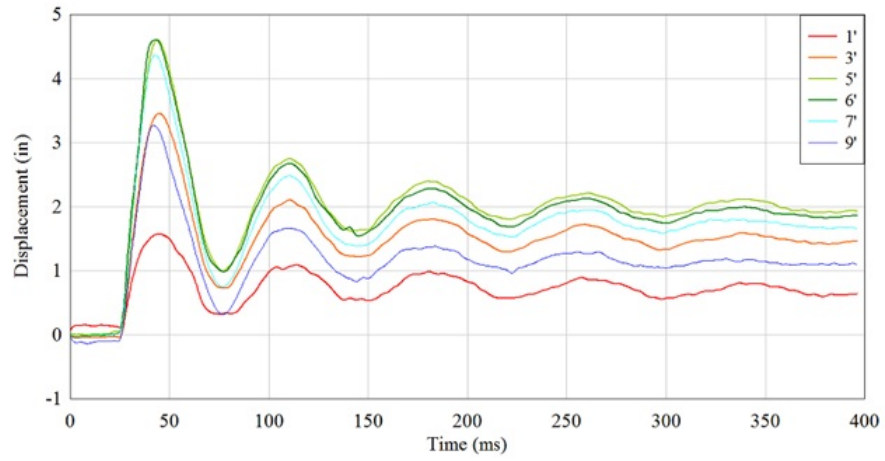
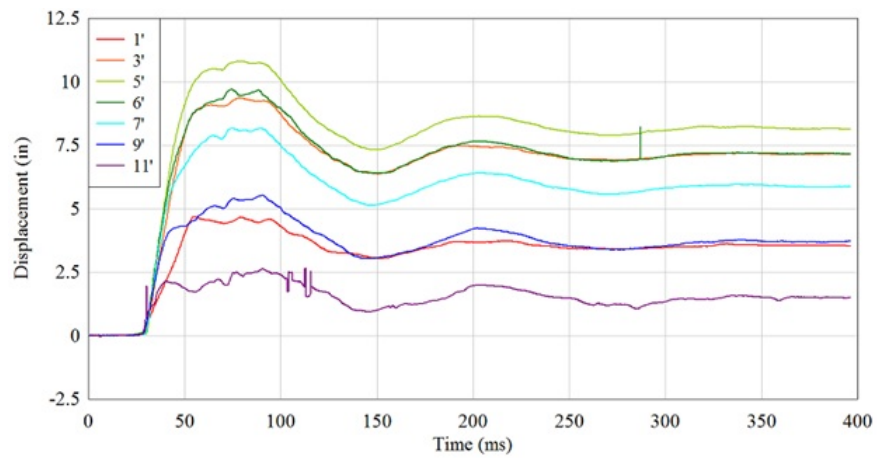**Figure E.37**: Test SSRE010-04.1 Target Displacements

Figure E.38: Test SSRE010-04.2 Target Displacements

Accelerations of the specimen were also used to approximate the transferred pressure and impulse on the back (non-impact) side of the wall. Figures E.39 and E.40 show the pressure and impulse curves that can be obtained from averaging these specimen accelerometer readings, with minimal post-processing. The values shown in these figures ignore any shear in the specimen during the collision and so will tend to underestimate the pressure and impulse imparted to the specimen.
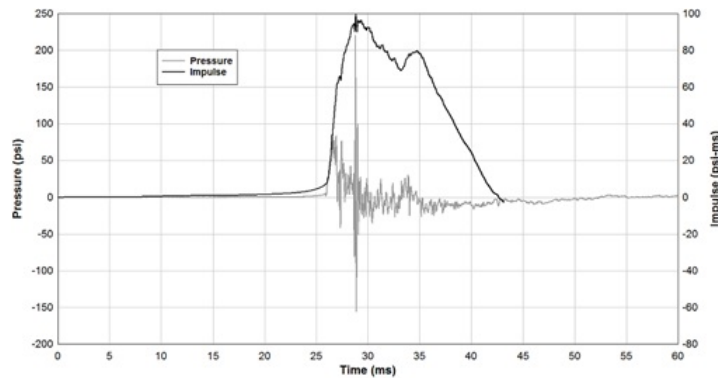

Figure E.39: Test SSRE010-04.1 Pressure and Impulse from Specimen Accelerometers
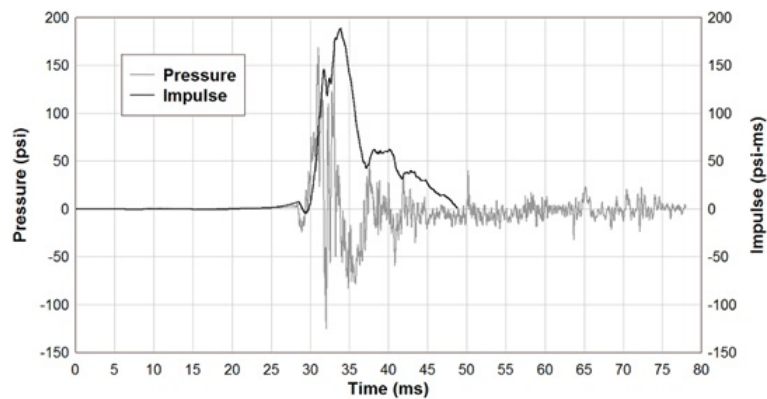

Figure E.40: Test SSRE010-04.2 Pressure and Impulse from Specimen Accelerometers

E.5   Additional SSRE010-05 Data

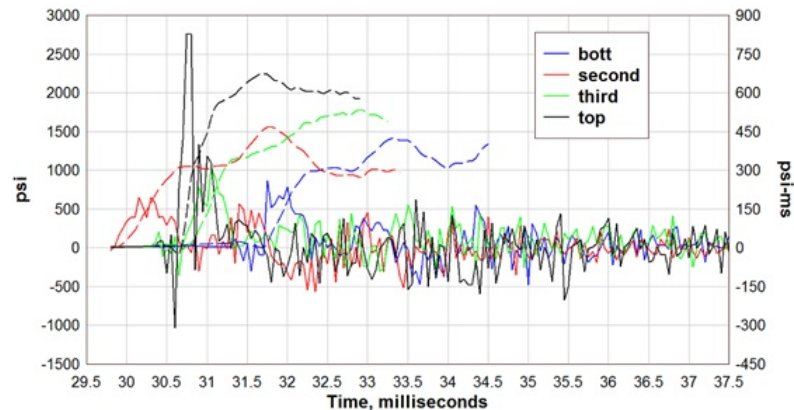The force-time history for each BG has been converted to pressure and is provided in Figure E.41.

Figure E.41: Test SSRE010-05 Pressure and Impulse for each BG

A simplified exponential force-time history is provided, using the method described in Section 4.2.2. Specifically, eq. (4.2) was used as the basis for generating this curve. This simplified force-time history is shown in Fig. E.42 and was found, here, from the equation:

$$F(t) = 450psi * 4BGs * 48in. * 30in. * [1 - (t - 30.08ms)/3ms]e^{-(t-30.08ms)/1.5}$$

Displacements were measured using camera data. Displacement-time histories are displayed in Figure E.43.

Accelerations of the specimen were also used to approximate the transferred pressure and impulse on the back (non-impact) side of the wall. Figure E.44 shows the pressure and impulse curves that can be obtained from averaging these specimen accelerometer readings, with minimal post-processing. The values shown in

Figure E.42: Test SSRE010-05 Simplified Pressure and Impulse

Figure E.43: Test SSRE010-05 Target Displacements

Fig. E.44 ignore any shear in the specimen during the collision and so will tend to underestimate the pressure and impulse imparted to the specimen.
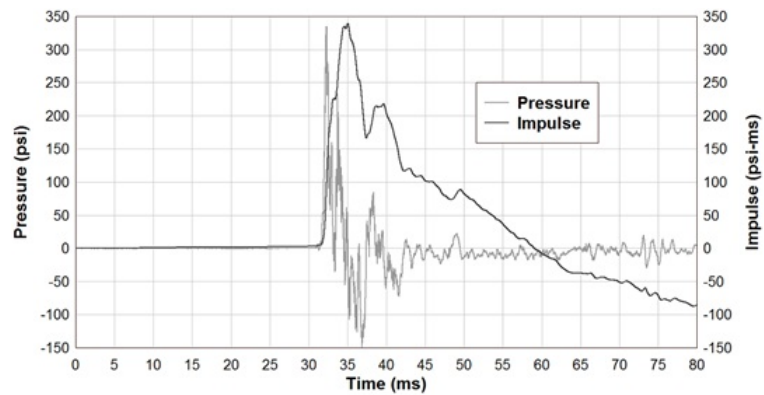
Figure E.44: Test SSRE010-05 Pressure and Impulse from Specimen Accelerometers

E.6 Additional SSRE010-06 Data

A simplified exponential force-time history is provided, using the method described in Section 4.2.2. Specifically, eq. (4.2) was used as the basis for generating this curve. This simplified force-time history is shown in Fig. E.45 and was found, here, from the equation:

$$F(t) = 1000psi * 4BGs * 48in. * 30in. * [1 - (t - 41.98ms)/2.5ms]e^{-(t-41.98ms)/.79}$$

Figure E.45: Test SSRE010-06 Simplified Pressure and Impulse

Displacements were measured using camera data. Displacement-time histories are displayed in Figure E.46.

Accelerations of the specimen were also used to approximate the transferred pressure and impulse on the back (non-impact) side of the wall. Figure E.47 shows the pressure and impulse curves that can be obtained from averaging these specimen accelerometer rea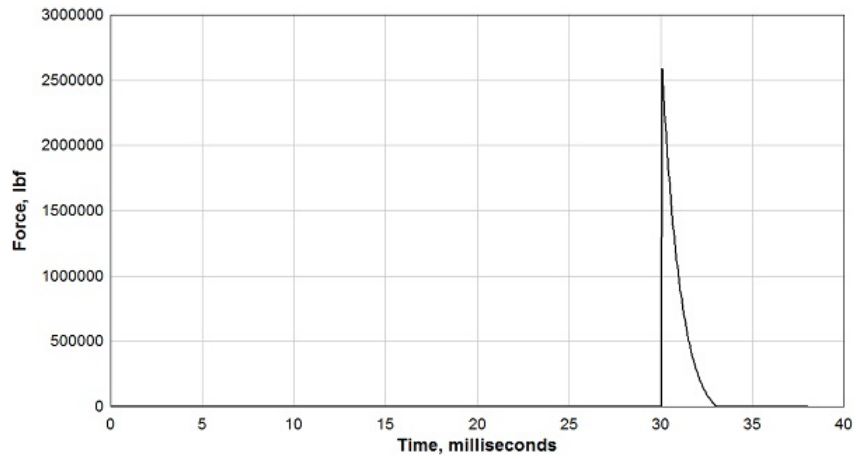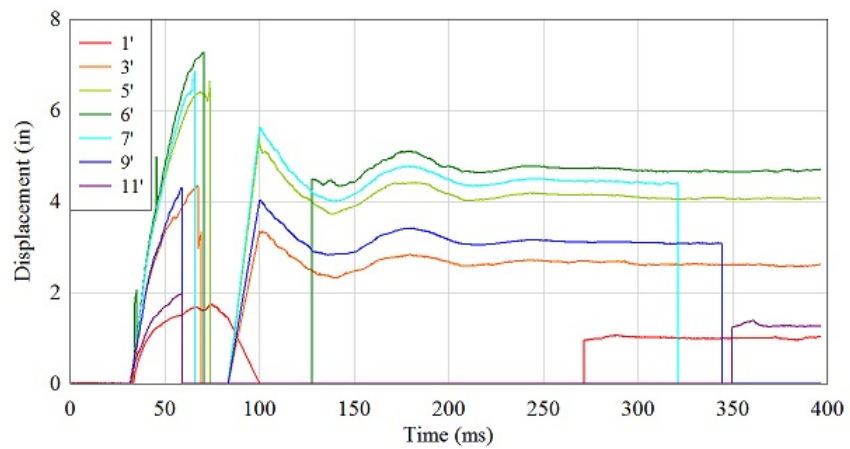dings, with minimal post-processing. The values shown in Fig. E.47 ignore any shear in the specimen during the collision and so will tend to
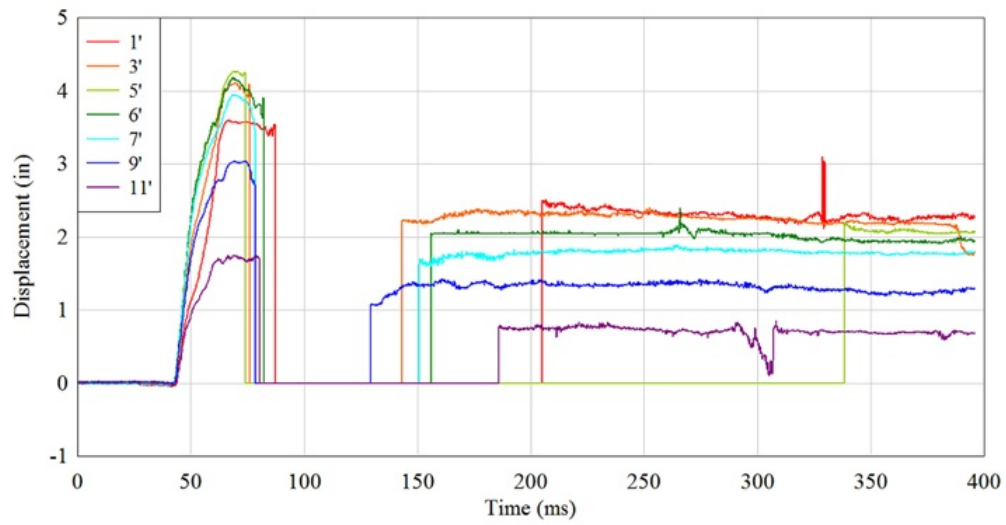
Figure E.46: Test SSRE010-06 Target Displacements

underestimate the pressure and impulse imparted to the specimen.
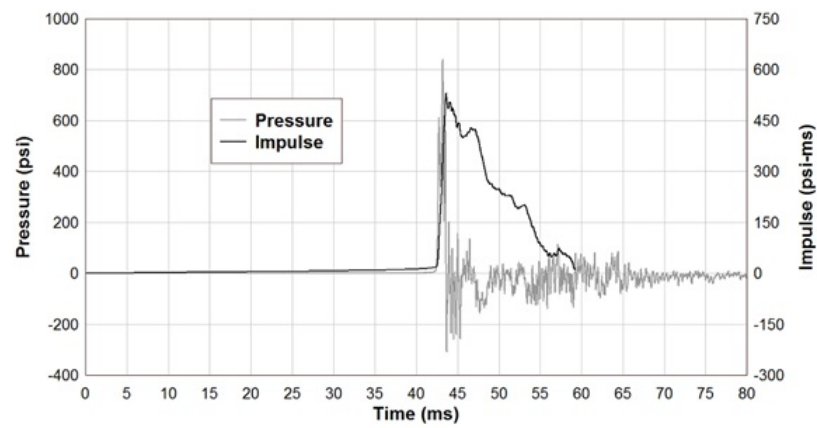
Figure E.47: Test SSRE010-06 Pressure and Impulse from Specimen Accelerometers

E.7 Additional SSRE010-07 Data

The force-time histories for the BGs (two BG hydraulic sensors failed during this test) have been converted to pressure and are given in Figure E.48.
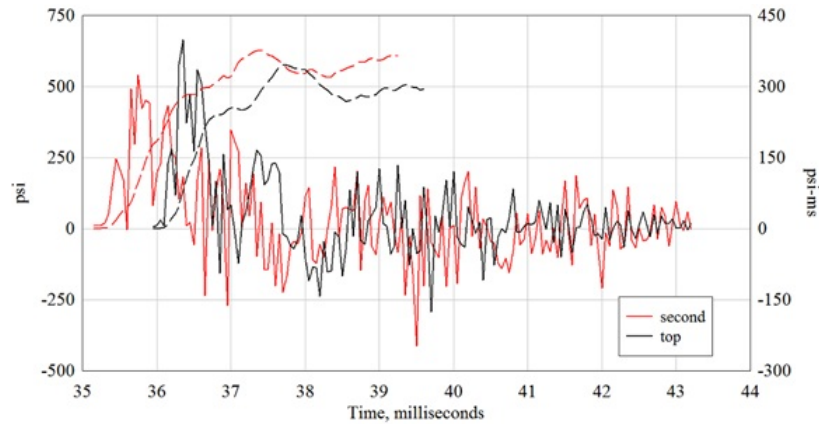
Figure E.48: Test SSRE010-07 Pressure and Impulse for each BG

A simplified exponential force-time history is provided, using the method described in Section 4.2.2. Specifically, eq. (4.2) was used as the basis for generating this curve. This simplified force-time history is shown in Fig. E.49 and was found, here, from the equation:

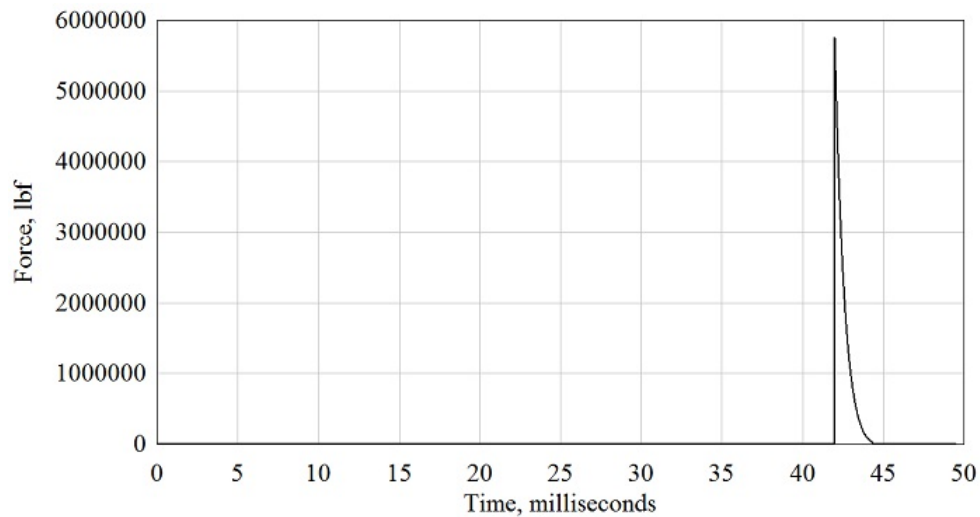$$F(t) = 375psi * 4BGs * 48in. * 30in. * [1 - (t - 35.98ms)/3ms]e^{-(t-35.98ms)/1.34}$$

Displacements were measured using camera data. Displacement-time histories are displayed in Figure E.50.

Accelerations of the specimen were also used to approximate the transferred pressure and impulse on the back (non-impact) side of the wall. Figure E.51 shows the pressure and impulse curves that can be obtained from averaging these specimen accelerometer readings, with minimal post-processing. The values shown in

Figure E.49: Test SSRE010-07 Simplified Pressure and Impulse

Figure E.50: Test SSRE010-07 Target Displacements

Fig. E.51 ignore any shear in the specimen during the collision and so will tend to underestimate the pressure and impulse imparted to the specimen.

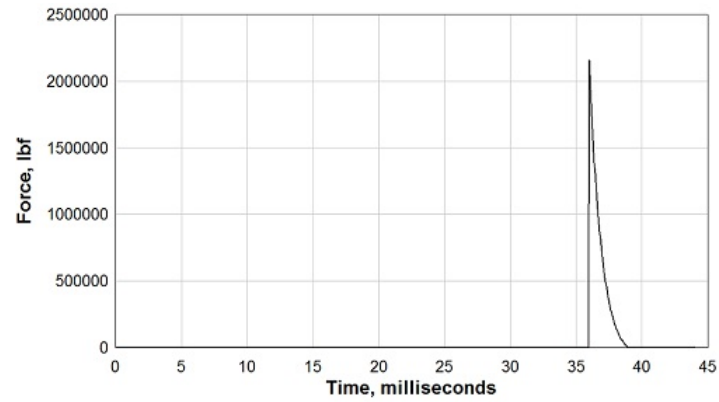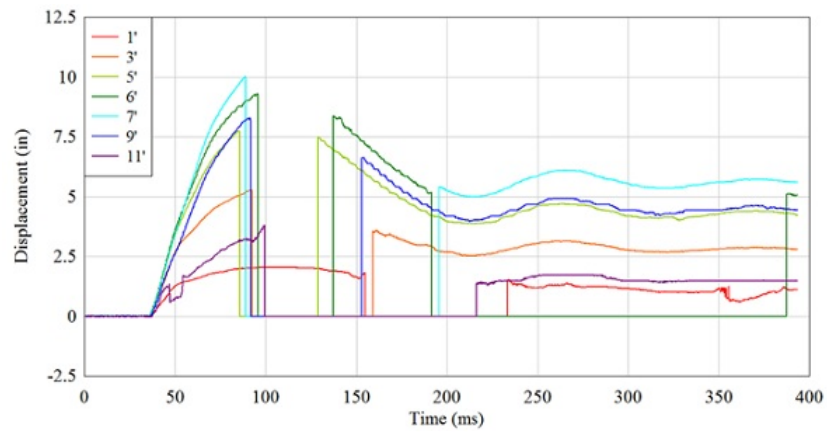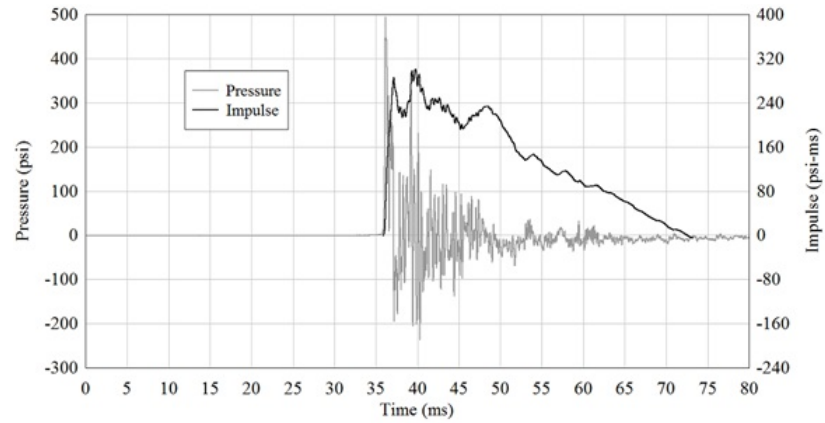**Figure E.51**: Test SSRE010-07 Pressure and Impulse from Specimen Accelerometers

Bibliography

[1] Cenk Acar and Andrei M Shkel. Experimental evaluation and comparative analysis of commercial variable-capacitance mems accelerometers. *Journal of Micromechanics and Microengineering*, 13(5):634, 2003.

[2] Ellen M. Arruda and Mary C. Boyce. A three-dimensional constitutive model for the large stretch behavior of rubber elastic materials. *Journal of the Mechanics and Physics of Solids*, 41(2):389 – 412, 1993.

[3] Robert J. Asaro and Vlado A. Lubarda. *Mechanics of Solids and Materials*. Cambridge University Press, Cambridge, UK, 2006.

[4] Ady Aviram, Ronald L Mayes, and Ronald O. Hamburger. Enhanced blast-resistance of an innovative high strength steel stud wall system. In *SEAOC Proceedings*, 2012 Structural Engineers Association of California Convention, Santa Fe, NM, 2012.

[5] W. E. Baker. *Explosions in air, by Wilfred E. Baker*. University of Texas Press Austin, 1973.

[6] Jorgen Bergstrom. *PolyUMod User's Manual*. Veryst Engineering, LLC, Needham, MA, v.1.8.7 edition, 2009.

[7] Paul J. Blatz and William L. Ko. Application of finite elastic theory to the deformation of rubbery materials. *Transactions of the Society of Rheology*, 6(1):223–252, 1962.

[8] NK Bourne. A 50 mm bore gas gun for dynamic loading of materials and structures. *Measurement Science and Technology*, 14(3):273, 2003.

[9] T Gordon Brown, Bradford Davis, David Hepner, Jonah Faust, Craig Myers, C Muller, Thomas Harkins, M Holis, and B Placzankis. Strap-down microelectromechanical (mems) sensors for high-g munition applications. *Magnetics, IEEE Transactions on*, 37(1):336–342, 2001.

[10] David Cormie, Geoff Mays, and Peter Smith. *Blast Effects on Buildings: Second Edition*. Thomas Telford, London, GB, 2009.

[11] Beverly P. DiPaolo, Hani A. Salim, Trent Townsend, and James L. Davis. A study on static and dynamic responses of exterior cold-formed steel stud framing walls for enhanced blast resistance. 2003.

[12] Beverly P DiPaolo and Stanley C Woodson. An overview of research at ERDC on steel stud exterior wall systems subjected to severe blast loading. In *ASCE Structures Congress*, pages 18–20, 2006.

[13] Peitao Dong, Xinxin Li, Heng Yang, Haifei Bao, Wei Zhou, Shengyi Li, and Songlin Feng. High-performance monolithic triaxial piezoresistive shock accelerometers. *Sensors and Actuators A: Physical*, 141(2):339 – 346, 2008.

[14] Bradley J. Durant. Blast simulator testing for high-g shock environment characterization. Master's thesis, University of California, San Diego, 2013.

[15] A. Freidenberg, C.W. Lee, B. Durant, V.F. Nesterenko, L.K. Stewart, and G.A. Hegemier. Characterization of the Blast Simulator elastomer material using a pseudo-elastic rubber model. *International Journal of Impact Engineering*, 60(0):58 – 66, 2013.

[16] Y. C. Fung. *On the pseudo-elasticity of living tissues*. Permagon Press, New York, NY, S.N. Nasser edition, 1980.

[17] A N Gent and P B Lindley. The compression of bonded rubber blocks. *Proceedings Of The Institution Of Mechanical Engineers*, 173(3):111–122, 1959.

[18] GT Gray and WR Blumenthal. Split-hopkinson pressure bar testing of soft materials. *Materials Park, OH: ASM International*, 8:488–496, 2000.

[19] J.O. Hallquist. *LS-DYNA theory manual*. Livermore Software Technology Corporation, Livermore, CA, 2006.

[20] S Hamdan and GM Swallowe. The strain-rate and temperature dependence of the mechanical properties of polyetherketone and polyetheretherketone. *Journal of materials science*, 31(6):1415–1423, 1996.

[21] Gilbert Hegemier, Frieder Seible, Karen Arnett, Tonatiuh Rodriguez-Nikl, Mike Oesterle, Janet Wolfson, M. Gram, and A. Clark. *The UCSD Blast Simulator*. Proceedings of the 77th Shock and Vibration Symposium, Monterey, CA, 2006.

[22] Gilbert A. Hegemier, Lauren K. Stewart, and Peter N. Huson. Blast simulator tests of sure-board series 200b wall system. *Protective Technologies Group Test Report*, 2011.

[23] Anne Hoger. A second order constitutive theory for hyperelastic materials. *International Journal of Solids and Structures*, 36(6):847 – 868, 1999.

[24] Peter Noble Huson. *Experimental and Numerical Simulations of Explosive Loading on Structural Components: Composite Sandwich Connections.* PhD thesis, University of California, San Diego, 2012.

[25] David Hyde. *DPlot: Graph Software for Scientists and Engineers.* HydeSoft Computing, LLC, Vicksburg, MS, 2011.

[26] JS Johnsen, HR Karimi, and KG Robbersmyr. The harp: a vehicle crash test apparatus for full-scale crash test experiments. *The International Journal of Advanced Manufacturing Technology*, 63(9-12):1073–1080, 2012.

[27] Jennifer L Jordan, Clive R Siviour, Jason R Foley, and Eric N Brown. Compressive properties of extruded polytetrafluoroethylene. *Polymer*, 48(14):4184–4195, 2007.

[28] S. Kolling, P. Bois, D. Benson, and W. Feng. A tabulated formulation of hyperelasticity with rate effects and damage. *Computational Mechanics*, 40:885–899, 2007. 10.1007/s00466-006-0150-x.

[29] Daniel Lacroix and Ghasan Doudak. Behaviour of typical light frame wood stud walls subjected to blast loading. In *WCTE Proceedings*, World Conference of Timber Engineering, Aukland, NZ, 2012.

[30] JW Larson. Aisi codes, standards, and design guides on cold-formed steel framing. In *Building Integration Solutions*, pages 1–11. ASCE, 2006.

[31] Zhi Xin Liu, Lei Lou, and Yun Sheng Yang. Study on one kind of test method of simplified side impact using sled test. *Advanced Materials Research*, 301:1249–1253, 2011.

[32] Vlado A. Lubarda. *Elastoplasticity Theory.* CRC Press, Boca Raton, FL, 2002.

[33] William E. Luecke, J. David McColskey, Christopher N. McCowan, Stephen W. Banovic, Richard J. Fields, Timothy Foecke, Thomas A. Siewert, and Frank W. Gayle. *Federal Building and Fire Safety Investigation of the World Trade Center Disaster: Mechanical Properties of Structural Steel.* National Institute of Standards and Technology, Washington, DC, 2005.

[34] Lawrence. E. Malvern. *Introduction to the Mechanics of a Continuous Medium.* Prentice-Hall, Inc., Upper Saddle River, NJ, 1969.

[35] M Massenzio, A Maupas, A Bennani, S Ronel, P Joffrin, and E Jacquelin. Study of a device for controlling the pulses of sled testing. *International Journal of Crashworthiness*, 12(3):311–318, 2007.

[36] Ronald L. Mayes, Ady Aviram, Kyle Douglas, and Ronald O. Hamburger. *Use of HSLA-V Steel Studs for Blast-Resistant Walls.* Simpson Gumpertz and Heger, Inc., San Francisco, CA, 2012.

[37] G.C. Mays and P.D. Smith. *Blast Effects on Buildings.* Thomas Telford, New York, NY, 2001.

[38] J.M. McGlaun, S.L. Thompson, and M.G. Elrick. Cth: A three-dimensional shock wave physics code. *International Journal of Impact Engineering*, 10(1-4):351 – 360, 1990.

[39] M. Mooney. A theory of large elastic deformation. *Journal of Applied Physics*, 11(9):582 –592, sep 1940.

[40] RA Morris, JR Crandall, and WD Pilkey. Multibody modelling of a side impact test apparatus. *International Journal of Crashworthiness*, 4(1):17–30, 1999.

[41] Yvonne D. Murray. Users manual for LS-DYNA concrete material model 159. 2007.

[42] K Nakai and T Yokoyama. High strain-rate compressive behavior and constitutive modeling of selected polymers. In *EPJ Web of Conferences*, volume 26. EDP Sciences, 2012.

[43] Sia Nemat-Nasser. Rate-independent finite-deformation elastoplasticity: a new explicit constitutive algorithm. *Mechanics of Materials*, 11(3):235 – 249, 1991.

[44] Michael G. Oesterle. *Blast Simulator Wall Tests: Experimental Methods and Mitigation Strategies for Reinforced Concrete and Concrete Masonry.* PhD thesis, University of California, San Diego, 2009.

[45] R. W. Ogden. Large deformation isotropic elasticity - on the correlation of theory and experiment for incompressible rubberlike solids. *Proceedings of the Royal Society of London. A. Mathematical and Physical Sciences*, 326(1567):565–584, 1972.

[46] R. W. Ogden and D.G. Roxburgh. Pseudo-elastic model for the Mullins effect in filled rubber. *Proceedings of the Royal Society of London. A. Mathematical, Physical, and Engineering Sciences*, 455:2861–2877, 1999.

[47] R. S. Rivlin. Large elastic deformations of isotropic materials. i. fundamental concepts. *Philosophical Transactions of the Royal Society of London. Series A, Mathematical and Physical Sciences*, 240(822):pp. 459–490, 1948.

[48] Tonatiuh Rodriguez-Nikl. *Experimental Simulations of Explosive Loading on Structural Components: Reinforced Concrete Columns with Advanced Composite Jackets*. PhD thesis, University of California, San Diego, 2006.

[49] H Salim, P Muller, and R Dinan. Response of conventional steel stud wall systems under static and dynamic pressure. *Journal of performance of constructed facilities*, 19(4):267–276, 2005.

[50] H.A. Salim and P.T. Townsend. Explosion-resistant steel stud wall system. 2004.

[51] Hani A. Salim, Robert Dinan, Sam A. Kiger, Philip Trent Townsend, and Jonathan Shull. Blast-retrofit wall systems using cold-formed steel studs. 2003.

[52] J. Sallay and G. Gurtman. Characterization of blast simulator programmers. *SAIC*, 2008.

[53] Sai S. Sarva, Stephanie Deschanel, Mary C. Boyce, and Weinong Chen. Stress strain behavior of a polyurea and a polyurethane from low to high strain rates. *Polymer*, 48(8):2208 – 2213, 2007.

[54] G.K. Schleyer, M.J. Lowak, M.A. Polcyn, and G.S. Langdon. Experimental investigation of blast wall panels under shock pressure loading. *International Journal of Impact Engineering*, 34(6):1095 – 1118, 2007.

[55] J.C. Simo and T.J.R. Hughes. *Computational inelasticity*. Springer, 1998.

[56] C.R. Siviour, S.M. Walley, W.G. Proud, and J.E Field. The high strain rate compressive behaviour of polycarbonate and polyvinylidene difluoride. *Polymer*, 46(26):12546 – 12555, 2005.

[57] P.D. Smith and J.G. Hetherington. *Blast and Ballistic Loading of Structures*. Butterworth-Heinemann Ltd, Oxford, GB, 1994.

[58] Bo Song and Weining Chen. Split hopkinson pressure bar techniques for characterizing soft materials. *Latin American Journal of Solids and Structures*, 2:113–152, 2005.

[59] Lauren K. Stewart. *Testing and Analysis of Structural Steel Columns Subjected to Blast Loads*. PhD thesis, University of California, San Diego, 2010.

[60] Lauren K. Stewart, Brad Durant, Aaron Freidenberg, Gilbert Hegemier, and Frieder Seible. Continued blast simulator testing: Wall panel test report, fortocrete. *Explosive Loading Laboratory CDRL Deliverable*, 2011.

[61] Douglas Sunshine, Ali Amini, and Mark Swanson. Overview of simplified methods and research for blast analysis. *Journal of Structural Engineering*, 2004.

[62] Ton Versmissen, Richard Schram, and Steve McEvoy. The development of a load sensing trolley for frontal offset testing. *International Journal of Crashworthiness*, 12(3):235–245, 2007.

[63] S.M. Walley and J.E. Field. Strain rate sensitivity of polymers in compression from low to high rates. *DYMAT*, 1(3):211 – 227, 1994.

[64] Daniel Whisler, Antony Chen, Hyonny Kim, Peter Huson, and Robert Asaro. Methodology for exciting dynamic shear and moment failure in composite sandwich beams. *Journal of Sandwich Structures and Materials*, 14(4):365–396, 2012.

[65] K.J. William and E.P. Warnke. *Constitutive Model for the Triaxial Behavior of Concrete.* Proceedings of the International Association of Bridge and Structural Engineers, Seminar in Concrete Subjected to Triaxial Stresses, Bergamo, IT, 1975.

[66] J. Yi, M.C. Boyce, G.F. Lee, and E. Balizer. Large deformation rate-dependent stress strain behavior of polyurea and polyurethanes. *Polymer*, 47(1):319 – 329, 2006.

[67] Abdullatif K Zaouk and Dhafer Marzougui. Development and validation of a US side impact moveable deformable barrier FE model. In *3rd European LS-DYNA Users Conference, Page*, volume 14, 2001.